Biomimetic Tympanic Membrane Grafts

Citation

Permanent link

Terms of Use

Share Your Story

HARVARD UNIVERSITY

Graduate School of Arts and Sciences

DISSERTATION ACCEPTANCE CERTIFICATE
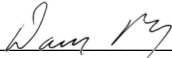
The undersigned, appointed by the

Harvard John A. Paulson School of Engineering and Applied Sciences
have examined a dissertation entitled:

"Biomimetic Tympanic Membrane Grafts"

presented by: Nicole Leah Black

Signature _____

Typed name: Professor J. Lewis

Signature _____

Typed name: Professor D. Mooney

Signature _____

Typed name: Professor J. T. Cheng

Signature _____

Typed name: Dr. Aaron Remenschneider

September 30, 2020

BIOMIMETIC TYMPANIC MEMBRANE GRAFTS

A dissertation presented

by

NICOLE LEAH BLACK

to

The John A. Paulson School of Engineering and Applied Sciences

In partial fulfillment of the requirements for the degree of Doctor of Philosophy in the subject of

Engineering Sciences

Harvard University

Cambridge, Massachusetts

September 2020

Dissertation Advisor: Dr. Jennifer A. Lewis   Nicole Leah Black

Biomimetic Tympanic Membrane Grafts

ABSTRACT

The tympanic membrane (TM), commonly known as the eardrum, is a thin tissue that captures sound waves from the environment and transmits them to the ossicles of the middle ear. Importantly, its circumferential and radial collagen fiber architecture enables efficient sound-induced motion over a wide range of frequencies that match the human cochlea's dynamic range (20 – 20,000 Hz). While its delicate structure serves a crucial acousto-mechanical role in sound conduction, the fragile TM can be damaged by exposure to impulse blast waves, chronic ear infections, or trauma. While small TM perforations may heal spontaneously, many perforations do not heal on their own. When damaged, the TM is no longer efficient at transducing sound pressure waves into mechanical motion and hearing loss results. Moreover, perforated TMs permit pathogens to enter the middle ear space, resulting in infection, pain and dizziness. Surgical repair of the TM, also known as tympanoplasty, uses grafted materials harvested from the patient to close the perforation and restore proper sound conduction to the ossicular chain. Unfortunately, commonly used graft materials, such as temporalis fascia, cartilage, fat, and dermis, do not degrade nor remodel after implantation. These reconstructed TMs also lack the native circumferential and radial collagenous architecture and, thus, are less efficient at sound conduction. As a result, healing and hearing outcomes in tympanoplasty patients are often poor.

The overarching goal of this Ph.D. thesis is to create biomimetic TM grafts with anisotropic architecture that overcome the current tympanoplasty challenges described above. Specifically, this research focuses on novel TM designs, synthesis of biodegradable, biocompatible materials, 3D printing, and *in vitro* and *in vivo* characterization of their performance. In this dissertation, the parameters for an "ideal TM graft" are first described followed by a discussion of the research carried out to achieve the stated goal of improved TM grafts and tympanoplasty outcomes.

We first investigated the TM structure via histopathology to determine the circumferential and radial fiber arrangement in the human TM. Inspired by the native TM, we created synthetic TM grafts via 3D

printing of three polymeric inks: polydimethylsiloxane (PDMS), poly(lactic acid) (PLA), and polycaprolactone (PCL). Their printed circular/radial architectures were infilled with a hydrogel solution to create a confluent graft capable of transmitting sound. Next, we carried out *in vitro* acoustic testing via laser Doppler vibrometry (LDV) and digital opto-electronic holography (DOEH) to obtain high frequency and spatial resolution of sound-induced motion. We find that these first-generation biomimetic TM grafts exhibited high fidelity in their sound-induced motion compared to inconsistent motion patterns in harvested autologous fascia grafts. Through simple modal motion patterns at low frequencies and complex, organized motion patterns at high frequencies, biomimetic composite grafts were able to transmit sound in a manner similar to the unloaded native TM. We also find that their sound-induced motion varies with graft material and architecture, demonstrating their tunability via 3D printing. We then explored the mechanical properties of the printed and infilled grafts as well as their propensity to enable cellular ingrowth and remodeling. Biomimetic TM grafts exhibited lower hysteresis compared to fascia grafts under repeated loading. We find that fibroblasts seeded onto these grafts deposit collagen I in the infill region. However, cellular remodeling occurred isotropically due to limitations in both material properties and in the isotropic nature of the infilled region between printed features.

To further optimize the performance of biomimetic TM grafts, we synthesized a biomaterial ink that enables post-implantation anisotropic remodeling in a controlled fashion, guided by the deterministic architecture defined during 3D printing. This biomaterial was designed with a tunable biodegradation rate, mechanical properties that mimic the native TM and facilitate manipulation during placement, and biocompatibility with relevant cell types. Specifically, we created a thermoplastic poly(ester urethane urea) (PEUU) elastomer blended with a fugitive poly(ethylene glycol) (PEG) component to form porous PEUU (P-PEUU) grafts upon leaching PEG species from the graft material. We characterized the rheological and printing behavior of this ink, alongside control PEUU, PCL, and porous PCL (P-PCL) inks, and optimized these parameters for high operating temperature-direct ink writing (HOT-DIW). After fabricating these second-generation TM grafts, we measured their Young's Moduli, *in vitro* degradation, *in vitro* proliferation of fibroblast and keratinocyte cells, topography, and alignment of fibroblasts along the print path under various print conditions. Specifically, the mean Young's modulus of P-PEUU specimens that were printed parallel to the tension testing direction ($E_\parallel$ = 33.7 ± 2.8 MPa) is 142% that of those printed orthogonal to

the tension testing direction the ($E\perp$ = 23.8 ± 1.5 MPa). Grafts from P-PEUU inks aligned fibroblasts and extracellular deposited collagen I to a greater extent than grafts from both PEUU and P-PCL inks printed with the same speed and filament width, while PCL grafts and melted P-PEUU grafts did not show any degree of fibroblast alignment or extracellular collagen alignment. Notably, increasing the print speed from 5 mm/s up to 20 mm/s while maintaining identical filament width leads to higher cellular and collagen I alignment in P-PEUU grafts. Together, these observations revealed that our synthetic P-PEUU ink is well suited for creating biomimetic TM grafts that may induce anisotropic remodeling.

Next, we investigated the acoustic and mechanical responses of the biomimetic TM grafts (based on P-PEUU) with the goal of optimizing their architecture to best match native TM properties *in vivo*. Specifically, printed grafts were patterned in a 50 circular and 50 radial (50C/50R) architecture as well as a 50 circular only (50C) architecture. Control TM grafts composed of human fascia and a porcine small intestinal submucosa, which are commonly used in tympanoplasty, were used as controls. Based on LDV and DOEH *in vitro* acoustic tests, we find that these biomimetic TM grafts exhibited superior sound-induced motion compared to both control grafts as well as to circular-only P-PEUU grafts and isotropic versions of the same printed grafts (melted to "erase" their 50C/50R architecture) with identical thickness. Biomimetic P-PEUU grafts showed simple modal motion patterns at low frequencies that increase to more complex motion patterns at higher frequencies, similar to isolated human TM tissue. Finally, we carried out *in vivo* studies on biomimetic P-PEUU grafts and control grafts implanted into chinchilla models of chronic TM perforations. After 3 months, chinchillas implanted with biomimetic P-PEUU 50C/50R grafts exhibit higher healing rates and superior hearing outcomes compared to control grafts (human fascia and Biodesign® porcine small intestinal submucosa). The structure of these biomimetic TM grafts is partially degraded via ingrowth of native cells and host vasculature, as determined by post-mortem histology. The P-PEUU grafts were well tolerated and non-toxic to the surrounding tissue and the delicate structures within the inner ear.

In summary, we have developed biomimetic TM grafts through the integration of design, biomaterial synthesis, and additive manufacturing with improved performance compared to native (control) grafts. We have validated their functionality through a combination of *in vitro* and *in vivo* experiments. The work presented in this Ph.D. dissertation provides a strong foundation for translating these biomimetic TM grafts into human patients for use in tympanoplasty and possibly well beyond.

Table of Contents

Acknowledgements

Although this section physically represents only approximately 3% of the total page length of this Ph.D. dissertation, mentally and emotionally, it represents 100% of the reason why this dissertation exists. I am incredibly thankful for everyone who has played a part in my life over the past 6 years. Particularly when undergoing so many work and life adjustments over the past 6 months due to COVID-19, these individuals have provided crucial support both in and out of the lab.

Firstly, I would like to thank my amazing husband, Michael Pettit, for everything you have done to support me during graduate school. I have been a graduate student for a majority of the 8.5 years we have been together, and you have been there alongside me every step of the journey. From driving me in during early hours and picking me up late at night, to helping me learn statistical analysis techniques and proofreading my writing, you have gone above and beyond to support this work. And, given how much you have patiently listened me discuss the challenges and opportunities of this project over the years, I am fairly certain that you could give my defense presentation at this point. You have never stopped reminding me that I can accomplish this. Thank you so much Mary, Tom, Daniel, and Mary E. Pettit for being amazing in-laws and providing a family life for me here in Boston.

Secondly, I want to thank my parents, Deborah and Daniel Black, for fostering my curiosity and interest in science over the years. From caving under my constant requests to buy the "nerdy" STEM toys and to enable me to attend local STEM-focused camps, you have never faltered in your support of my eventual career in science, despite insisting that most of my science homework was above your level of help. I appreciate your patience in letting me make a mess the kitchen on an almost weekly basis with various slime, soap, and other experiments. During graduate school, you have never faltered in your patience and support. Watching dad battle adult acute lymphoblastic leukemia from my third year of graduate school onward has put my struggles with failed experiments into a broader context. Even when you were spending long nights in the hospital the first few months, you always somehow worried about me and expressed how you were partially battling so hard to make it to my Ph.D. graduation. I have tried my best to even remotely meet your extremely high opinions of my intellect.

Thirdly, I would like to thank my sister, Amanda Haggerty, for always being very protective of me. You have always encouraged me to unashamedly be myself and to stand up for my ideas. Thank you so

much for being a wonderful mother to Colin, Dylan, and Tyler. My nephews are my constant inspiration, and I am looking forward to instilling a love of science in them as they grow older. Dylan and Tyler, I am very sorry that I have missed your early months to finish this dissertation and due to COVID-19, but I am looking forward to meeting you shortly.

Next, I would like to thank my incredible thesis advisor, Jennifer Lewis, for your constant support and encouragement over the years. Thank you so much for taking a chance on me to join your lab 6.5 years ago, when I was ready to go into a consulting job and suddenly received the National Science Foundation Graduate Research Fellowship. I appreciate that you always expect the very best from your students, as it has inspired me to leave my comfort zone and learn so many new techniques and to look at problems through news lenses. Over the course of my Ph.D., you have provided crucial advice and guidance, both from a scientific lens and general life advice. Seeing how you manage so many diverse projects while prioritizing your students' goals has been inspirational. I could not ask for a better role model. You have always cared deeply amount my long-term goals and in helping me find opportunities to accomplish these goals, particularly on a translational level. It has been a pleasure getting to know you and Lori on a personal level, and I hope our professional and personal relationship continues to strengthen for many years even after I have graduated.

To Aaron Remenschneider (my committee member) and Elliott Kozin— words cannot adequately express how much you both mean to me. You have both been so incredibly instrumental to the success of this project and to my confidence as a scientist and engineer. Ever since our first meeting 5.5 years ago in the Lewis Lab Design studio, you have treated me with the utmost respect and belief. You always listen diligently to my thoughts and ideas, whatever they may be, and your support is unparalleled. Aaron, ever since we spent a week together in Denmark for the Middle Ear Mechanics and Research and Otology conference during my first summer of graduate school, I knew that we were research soulmates (and not just because you agree that international conferences should be fully experienced in academia). Your thoughtfulness, kindness, and ambition are unparalleled. Elliott, you have been such a steadfast force in my life, and your propensity for embracing innovation has been incredibly encouraging. In particular, your enthusiasm for rejecting the status quo and making real change in the Otolaryngology field is contagious. Whenever I see a new device or approach, I now always think "would Aaron and Elliott think this is really

the best way to do this?". I am proud to have worked closely with you both over the years, and I am excited to continue pushing forward all of our great ideas. I always leave discussions with you both feeling energized and hopeful. I rarely believe in destiny, but in this case, I do believe it was destiny that I met both of you.

To Tao Chen (my committee member), thank you so much for all of your guidance and support over the past 5.5 years. You are an amazing teacher—patient, kind, and thorough. You are an amazing teacher and always take the time to bring me up to speed on new research approaches and scientific principles. I feel like I can ask you anything, and you will always answer with respect. I greatly appreciate your diligence in reviewing many of our abstracts, proposals, and more recently, my thesis drafts. You are such a wonderful person, and I am looking forward to continued interactions with you.

To David Mooney (my committee member), thank you so much for your support and great advice over the years. Since taking your Advanced Tissue Engineering course during my second year of graduate school, you have been such an inspiration to me and to my future career goals. I highly respect all of the breakthroughs that you have made in the fields of biomaterials and tissue engineering, and I try to emulate the approach that you take in your lab making sure that these innovations make it past the lab and into helping real patients. You always ask wonderful questions, and it has been such an honor working under your Immunomaterials platform at the Wyss Institute.

Thank you to my Harvard Fluid Mechanics professor and Qualifying Exam committee member, James Rice, who asked whether I could create a superhuman eardrum. At the time, I thought this question was a bit preposterous, but now it seems actually feasible. Thank you for planting the seed in my mind.

To all of the professors who have supported and encouraged my work—particularly John Rosowski, Heidi Nakajima, Sunil Puria, and Bertrand Delgutte —thank you all so much for always supporting my ideas and for making me feel like a valued part of the Eaton-Peabody Labs and Speech and Hearing Bioscience and Technology (SHBT) Program communities. Despite feeling like a black sheep at Mass. Eye & Ear during my first year working on this project, you have all made me feel as though not only do I belong in this research environment, but that I am a valued leader and scientist. I consider myself a proud member of the SHBT and Eaton-Peabody Laboratories communities, and I will do my best to contribute back to all that this community has given me over the years.

To Scott Slimmer, you deserve your own paragraph because of everything you have done for me (and the entire lab) over the years. Your organization and thoroughness are qualities that I try to emulate in every professional interaction. Without you, the lab would certainly not be nearly as successful. To be honest, I do not even know what your job description encompasses because you do so much for everyone. Also, I feel like my health insurance should have been sending you payments as an unofficial counselor over the years. You are an amazing listener and friend.

To all of my labmates in the Lewis Lab, I cannot express enough how inspired I am by each and every one of you every day. While you are all extremely smart individuals, your enthusiasm, creativity, and leadership qualities make you all truly unique. I am so impressed by the work done by each and every one of you, and I am thankful for the support I have received from all of you. In particular, I would like to thank Emily Davidson, Daniele Foresti, Mike Lis, Arda Kotikian, Ed Guzman, Sydney Gladman, Joseph Muth, Claas Visser, Dahlia Amato, Ryan Truby, and Alex Chortos for all of your materials science guidance over the years. As someone coming into graduate school with relatively little polymer experience, you have all helped me tremendously. Additionally, I would like to thank the entire Lewis Lab bioteam. You have provided a truly unique and supportive community over the years, and despite my work differing from our lab's primary approach of bioprinting, you have always made me feel like I belong. In particular, I would like to thank David Kolesky, Mark Skyler-Scott, Kim Homan, Dan Reynolds, John Ahrens, Kathi Kroll, and Aric Lu for always being delightful personalities to work alongside in lab and always giving the absolute best advice. Thank you so much in particular to Rob Weeks for creating the printing setup that made Chapters 4 and 5 possible. Finally, thank you to Mariana Mata for all of your hands-on help with cell culture and immunostaining, particularly during stressful COVID-19 and thesis writing times. You are such a sweet and thoughtful person, and I appreciate your help.

To all of my labmates and colleagues at Mass. Eye & Ear, you have all become such great friends, and your enthusiasm for auditory research is partially why I have stuck with this project over the years. Dhrumi Gandhi, you are a wonder woman. Your roles as chief chinchilla-wrangler, and histology-expert are just a small part of everything you have done for our project. Thank you to my other amazing labmates, including Iman Ghanad, Melissa Castillo-Bustamante, Renata Knoll, Danielle Trakimas, Sam Barber, and

Rory Lubner for all that you have done to assist with this thesis project and our other tympanic membrane projects over the years. I am so grateful for all of your support and contributions to this work.

One pivotal part of my graduate school experience has been in mentoring younger students, particularly in completing their own independent projects. Thank you so much to Max Cotler, Sabrina Liu, Dominique Voso, Sabino Maldonado, Javier Morales, Minh-Chau Le, Arin Stowman, Stacy Jo, Jen Zhu, Juhee Goyal, Efe Karaca, Cindy Liu, and Naomi Berhane for all of your contributions and for always inspiring me to put a fresh perspective on problems. I would also like to thank Michelle Walsh, whom I have worked alongside since her senior year of high school, and who played a pivotal role in the polymer ink formulations. Additionally, I would like to especially thank Renee Friedman, whose relationship grew from a sophomore in the Introduction to Biomaterials class, to several semesters of research, and finally as your senior design advisor. Thank you to Marta Pawluczuk for your assistance with acoustic testing protocols and for always believing in the translational potential of this project. Thank you to Eva Cai for all of your enthusiasm for solving problems in the ear and for your thorough dissertation edits. I am also thankful to have mentored Moritz Mond on his ETH-Zurich Master's thesis over the past 6 months. I am incredibly grateful for the progress you have made for our team in using computation modeling approaches to investigate tympanic membrane perforations and in helping set up our new 3D printer in Longwood.

Thank you to everyone at the Wyss Institute for Biologically Inspired Engineering at Harvard for believing in this project and enabling progress from our very first funding source. In particular, thank you to Ed Doherty, Paul Resnick, Angelika Fretzen, Don Ingber, Ayis Antoniou, Matt Makarewicz, Michael Carr, Troy Leonard, and Deirdre Hume for your constant support. Thank you also to Michael Lewandowski, Jack Alvarenga, Oktay Uzun, and Tom Ferrante for the fantastic equipment trainings and scientific advice.

This translational potential of this project would not be possible without the constant advice of Chris Petty, Peter Sollins, Jay Culverwell, Christine, Christine Taft, and Aru Ananthanarayanan at the Harvard Office of Technology Development and Mass General Brigham Innovation. I am extremely proud to have contributed to 5 filed patents and 3 additional reports of invention during my graduate school years. You have all made this experience pleasant and fun! I am excited to work with you in the future.

Another pivotal part of my graduate school experience was as the coordinator of the Harvard College Women's Center Women in STEM (WiSTEM) Mentorship Program over the past 4 years. All of the

staff have been incredibly instrumental in my development as a leader. In particular, Heidi Wickersham— you have been an amazing role model. Bridget Duffy, you are one of the kindest and most selfless souls that I have ever met. I am so proud to have watched the WiSTEM program grow, and I am also very thankful for all of the mentors, mentees, and the Harvard staff members I have met in this role.

To the other members of the SEAS Committee on Diversity, Inclusion, and Belonging (DIB), it has been such a pleasure working alongside you. In particular, I would like to thank Alexis Stokes, John Girash, Kathryn Hollar, Ben Freedman, Brandon Tilghman, and Veronica Santana for being such an incredible inspiration. Coordinating SpeakSEAS and the Virtual Graduate Student Panel were huge accomplishments. I plan to bring forth the enthusiasm you have all brought to the DIB committee into my future career.

I would like to thank all of the incredible, lifelong friends that I have met at Harvard who have not yet been mentioned, including Weilu Shen, Jessica Sagers, Dana Boebinger, Darcy Frear, Stephen McInturff, Mischa Jurkiewicz, Jan Iyer, Olivia Murton, Jeanne Gallée, Eden Tanner, Blakely O'Connor, Michael Kreder, Anna Schneidman, Nina Sinatra, Melinda Malley, Lisa Lee, Cathy Zhang, Reena Paink, Steffi Sunny, Michael Kreder, Kim Noij, Kirupa Suthukar, Rachel Romeo, Salwa Masud, Peter Bowers, Jenny Zuk, Sara Beach, Justin Fleming, Chris Buswinka, John Lee, Kevin Sitek, Kyle Vining, Sam Peppou-Chapman, Joseph Choy, Tyler Brown, and all of your respective significant others that Mike & I have been thankful to become close with over the years. Thank you to my dear friends since high school, Becca Pace, Ashley Arscheene, Kate Syms, and Jenna Ross, for being my biggest cheerleaders throughout life. You are some of the kindest and most thoughtful friends that anyone could ever have. I am so excited to see you all at my Ph.D. defense and to hopefully celebrate when I am able to see you all again.

Chapter 1

Introduction

The human body contains a wide variety of tissues whose performance relies upon the cellular composition and spatial arrangement. In some cases, human tissues exhibit cellular alignment that imparts a desired anisotropic response. For example, the alignment of muscle cells along a given axis enhances both their performance and intercellular communication [1,2]. Similarly, the alignment of neurons is crucial for propagation of electrical signals in the intended direction. Cells can also deposit extracellular matrix proteins, whose alignment can also confer unique properties. For example, in the temporomandibular joint (TMJ), collagen II fibers contained in the hyaline cartilage are arranged in a manner such that the central region is significantly stiffer than the medial and lateral regions [3]. This anisotropic stiffness allows the TMJ cartilage to withstand complex mastication motions. Of specific interest to my doctoral research, the tympanic membrane (TM) contains a complex circumferential and radial collagen architecture, which allows it to vibrate in harmonious modes of motion at both low and high frequencies. This extracellular matrix (ECM) architecture enables the TM to effectively convert a wide range of airborne sound pressures into mechanical energy, which are delivered to the inner ear to permit normal hearing [4-7].

Unfortunately, many soft tissues are damaged through trauma or pathological conditions. They are typically repaired or replaced using a tissue graft that may be autologous (obtained from the same individual), allogenic (obtained from another of the same species), xenogeneic (obtained from another species), or synthetic (obtained from a non-living source). While many grafts effectively bridge the missing tissue, most do not fully recapitulate the native tissue structure or function. For example, TM grafts composed of fascia, fat, and dermis tissue used to repair the TM are largely isotropic and hence, do not exhibit the same acousto-mechanical properties as the native TM. The ideal tissue grafts for TM repair should closely match the anisotropic properties of the damaged tissue. It is therefore important to fully understand the anisotropic properties of the native TM and their functional implications. Additionally, understanding how these properties may change as the tissue graft integrates into the body is also important for understanding long-term functional outcomes following surgery.

1

1.1   Dissertation Scope

The principal goal of my Ph.D. dissertation is to create a bioresorbable, 3D printable elastomeric graft that recapitulates the structure and properties of the native TM thereby improving the treatment of chronic TM perforations. Specifically, we focused on the effects of material composition as well as circular and radial architecture on their sound-induced motion, healing, and hearing outcomes following tympanoplasty procedures. In the first aim, three biomaterial inks of polydimethysiloxane (PDMS), poly(lactic acid) (PLA), and polycaprolactone (PCL) are formulated for direct ink writing, an extrusion-based 3D printing method, of customized TM grafts. Grafts are printed with architectures of 8 circular and 8 radial lines (8C/8R) or 16 circular and 16 radial lines (16C/16R) and then infilled with a collagen-fibrin hydrogel. We analyze the impact of the sound-induced motion of these printed grafts and controls (e.g, fascia) using laser Doppler vibrometry (LDV) and digital opto-electronic holography (DOEH). We also analyzed their mechanical resiliency and propensity for *in vitro* cellular ingrowth. While improvement is sound-induced motion are observed, these first-generation TM grafts lacked the ability to remodel into an anisotropic tissue during in vitro studies with fibroblasts. Additionally, there were concerns that the collagen-fibrin infill comprised of animal proteins may promote an immunogenic response once implanted. Finally, while grafts with a PDMS backbone exhibited elastomeric properties and high resiliency, they would not biodegrade.

In the second aim, we synthesized a thermoplastic, biodegradable poly(ester urethane urea) (PEUU) with a low melting temperature. We used high operating temperature-direct ink writing (HOT-DIW) printing to create 3D printed grafts that mimic the TM's native circular and radial architecture and thickness. PEUU and PCL (control) inks of similar molecular weight are created with and without poly(ethylene glycol) (PEG), which is subsequently removed after printing to form both porous PCL (P-PCL) porous PEUU (P-PEUU). PCL, P-PCL, PEUU, P-PEUU grafts are printed in 50C/50R architectures with an outer diameter of 8 mm. These grafts roughly match the diameter of a chinchilla TM, the model animal used in the final aim. Their mechanical properties, biodegradation rate, cell viability, and cellular alignment were explored. Based on these observations, we determined that the P-PEUU material served as the optimal material from those investigated for biomimetic TM grafts to be used in tympanoplasty procedures.

In the third aim, the hearing and healing outcomes of biomimetic P-PEUU 50C/50C grafts were compared to two commonly used tympanoplasty graft materials, fascia and Biodesign® Otologic Repair

Graft, via *in vitro* and *in vivo* characterization methods. LDV and DOEH testing methods were used to determine the sound-induced velocity of biomimetic and control grafts as well as uncoupled human cadaveric TM tissue. As controls, isotropic P-PEUU 50C/50R and 50C grafts were produced by melting the printed architectures and their properties were compared to their anisotropic counterparts. To investigate *in vivo* hearing and healing outcomes, chronic perforations were created in chinchilla TMs, and transbullar underlay tympanoplasty procedures were performed with P-PEUU 50C/50C grafts, autologous fascia grafts, and Biodesign® grafts. Healing outcomes were assessed via endoscopic photos and histological sectioning 3 months post-healing. Additionally, hearing thresholds 3 months post-healing were compared to initial hearing thresholds via distortion product otoacoustic emissions (DPOAE) and auditory brainstem response (ABR) measurements, and these threshold differences are compared between groups. Finally, potential ototoxic effects of the materials were explored via cochlear histopathology.

1.2   Dissertation Organization

In **Chapter 2**, relevant literature on the structure and function of the TM, properties of ideal TM grafts, normal TM remodeling, the causes and impact of TM perforations on hearing, autologous and non-autologous TM grafts, and relevant manufacturing approaches are reviewed. In **Chapter 3,** the impact of material and architecture on sound-induced motion is explored for 3D printed, biomimetic TM grafts. In **Chapter 4**, second-generation biomimetic TM grafts are created by 3D printing a thermoplastic, biodegradable PEUU ink and characterized. In **Chapter 5,** *in vitro* acoustic testing and *in vivo* implantation studies are conducted on biomimetic P-PEUU grafts alongside control materials. Finally, the conclusions and major findings from my Ph.D. work are provided in **Chapter 6**.

Chapter 2

Literature Review

2.1   Motivation and Scope

While the tympanic membrane (TM) plays a crucial role in sound conduction, it can frequently become damaged, requiring repair via a tympanoplasty procedure. Unfortunately, currently used tympanoplasty graft materials, including autologous and non-autologous tissue grafts are inefficient, partially due to their inability to recapitulate the complex anisotropic circumferential and radial architecture that enables sound conduction. It is therefore paramount to understand the role of the TM and the drawbacks of current tissue engineering approaches before undertaking design of novel biomimetic TM grafts. In this chapter, the role of the TM in the auditory pathway is explored, with an emphasis on the role of the circumferential and radial architecture. Additionally, the overall thickness, stiffness, and dimensional measures of the TM are outlined alongside histological sectioning to provide guidance for the design of biomimetic TM grafts. Next, the afflictions leading to chronic TM perforations are explored, particularly in the context of the impact of TM perforations of various sizes and locations on sound-induced motion. The mechanism for spontaneous healing of TM perforations are explored, alongside current tympanoplasty procedural approaches and challenges for chronic TM perforations that do not spontaneously heal. A discussion of autologous and non-autologous TM grafts is then provided, including the drawbacks of various graft materials. The properties of an "ideal TM graft" are outlined with justification for each design goal. Finally, the role of 3D printing in creating anisotropic tissues is explored, paving the way for specific designs, materials, and fabrication approaches described in the remainder of my Ph.D. thesis.

2.2   The Sense of Hearing

Hearing arises from the ability of an organism to sense vibrations traveling through a medium (e.g., air or water). The tissues and organs of hearing are complex and delicate. When they are damaged, they must be repaired to preserve one's quality of life, since hearing plays a vital role in communication, safety, and socialization. Sound energy is produced when an object vibrates repeatedly at a specific frequency. In response to these vibrations, microscopic air particles adjacent to the object exert pressure on the surrounding air particles, forming a propagating wave of particle vibration in compression and rarefaction.

The frequency at which these vibrations occur is measured in Hertz (Hz), or number of waves passing a given point per second. The intensity of this pressure on surrounding particles is the amplitude, or loudness, of the sound wave and is typically measured in sound pressure level in units of decibels (dB), which are on a logarithmic scale [8]. Together, the values of frequency and amplitude describe the resultant sound wave.

The propagation of sound waves from the environment to the brain is a complex process involving multiple steps of transmission and transformation of energy (**Figure 2.1**). Generally, the human ear is sensitive to sounds in the range of 20 – 20,000 Hz [9-11], with variations due to genetics, age, and previous sound exposure. When sound pressure waves approach the outer ear, the auricle funnels these sound waves to the concha, or the cavity at the entrance of the external auditory canal (EAC) Once inside the EAC, the amplitude of the sound wave can be enhanced through resonance in a frequency-dependent fashion [12]. Next, sound waves reach the middle ear, which contains the TM (eardrum) and the ossicles. The TM is a thin tissue approximately 8.5 to 10.2 mm in diameter [13] that separates the external environment from the middle ear space. The TM vibrates in response to sound waves, transforming sound energy into mechanical vibration of the ossicles. Both standing and traveling waves on the surface of the TM are transformed into mechanical displacement of the tissue. This sound-induced displacement is transferred to the ossicular chain through the manubrium of the malleus, then from the malleus to the incus and finally to the stirrup-shaped stapes. The ossicles are the smallest bones in the human body, with the malleus measuring at an average of 8.15 mm, the incus at 4.7 mm, and the stapes at 3.5 mm in their longest directions [14]. The footplate of the stapes sits on top of the oval window membrane of the cochlea, a snail-shaped organ of the inner ear containing two ducts filled with perilymphatic fluid.
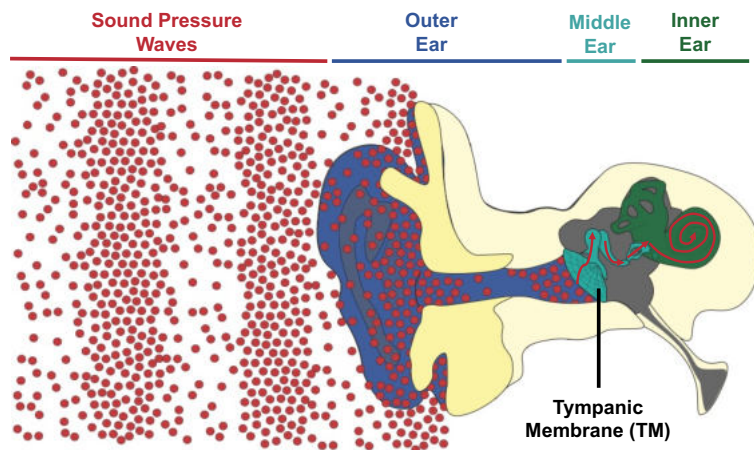
Figure 2.1. Transmission of sound waves through the human ear. Sound pressure waves in red propagate from the environment into the outer ear in dark blue. In the middle ear in teal, the TM converts this sound energy into mechanical motion of the ossicles. Then, the organ of Corti within the cochlea (green) mechanotransduces fluid motion into electrical impulses that are sent to the brain.

The mechanical vibrations of the stapes are transformed into a fluid wave in the scala vestibuli of the cochlea. This fluid wave propagates from the base to the apex of the cochlea, moving the basilar membrane that separates the scala vestibuli from the scala tympani. These fluid waves cause mechanical motion of the basilar membrane. The basilar membrane possesses location-dependent stiffness, causing high-frequency vibrations to move it strongest near the base of the cochlea, while low-frequency vibrations move it closest to the apex. The basilar membrane is integrated into a sensory epithelial tissue, known as the organ of Corti, containing sensory hair cells. The stereocilia hairs of these cells project into the scala media. Outer hair cells amplify low-level sound while also emitting their own sounds, termed otoacoustic emissions. Inner hair cells transform the fluid vibrations into electrical signals via deflection in the tip links, resulting in depolarization of the cell and activation of the adjacent spiral ganglion neurons (SGNs) in the modiolus, or center, of the cochlea. The SGNs conduct the electrical signals to the auditory efferent neurons and in turn, the auditory brainstem where sound is further relayed to the auditory cortex. Throughout this process, frequency and amplitude are conveyed in each energy format.

2.3   Tympanic Membrane Anatomy and Function

2.3.1   Tympanic Membrane Structure

The TM has a complex structure that contributes to its ability to convert sound pressure waves into mechanical vibration. The TM has a slight conical nature, with the apex at the umbo. The two major components are the pars tensa and pars flaccida (**Figure 2.2**). Most of the TM is comprised by the pars tensa, with the pars flaccida being a small triangle above the malleus. The pars tensa averages 79 – 97 µm in thickness, with smallest thickness in the central area between the umbo and fibrocartilagenous annulus that surrounds the TM [15]. The pars flaccida is thicker, at approximately 100 – 120 µm [15]. Both of the pars tensa and flaccida layers contain a trilaminar structure, which can be visualized by histological processing of a cross-section of the human TM (**Figure 2.3**) [16].
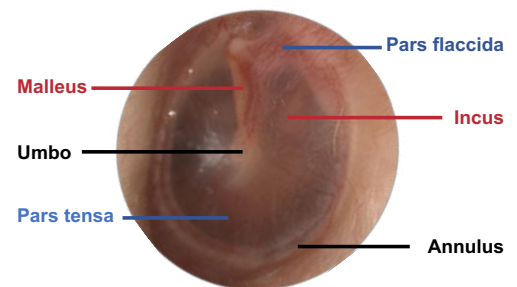
Figure 2.2. Features of the human TM. The two major components of the TM are the pars tensa and the pars flaccida. The TM is surrounded by a fibrocartilaginous annulus. Through the TM, the malleus and incus bones can be seen. The malleus is connected to the TM via the umbo at its center. The fibrocartilaginous annulus holds the TM taut in position at the end of external auditory canal. (image credit: Aaron Remenschneider).
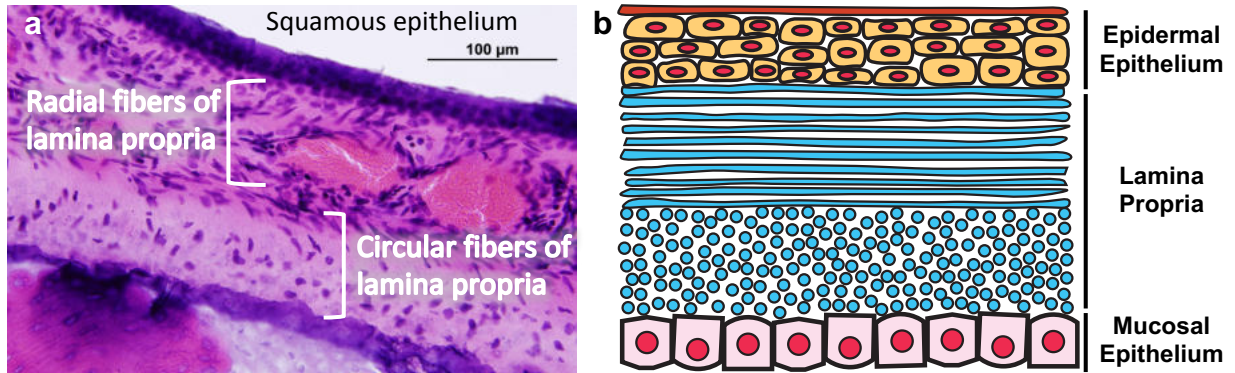
Figure 2.3. Cross-sectional view of the TM. (a) Histological section of a normal human TM stained with hematoxylin and eosin (H&E) Proteins are in pink and cell nuclei are in blue [16]. (b) Cross-sectional schematic of the trilaminar structure of the human TM.

Developmentally, the TM is a unique tissue situated at the air-air interface in the body between the external environment and the middle ear space, which is connected indirectly to the environment via the Eustachian tubes and nasal cavity. The three major layers of the TM arise from different tissue types—the lateral epithelial layer from ectoderm, the middle lamina propria from mesoderm, and the inner mucosal layer from endoderm. Lineage tracing of cells in mouse models has led to a better understanding of the formation of this air-air interface and tissue layers [17]. There are three widely contested models to explain the formation of this air-filled epithelium. In the first model, the intact endoderm wraps around the ossicles. In the second model, the endoderm breaks to allow this tissue to move around the ossicles. In the final model, a cavity is created from mesenchymal tissue. These three models, along with a combination model of the three, are represented in **Figure 2.4**.
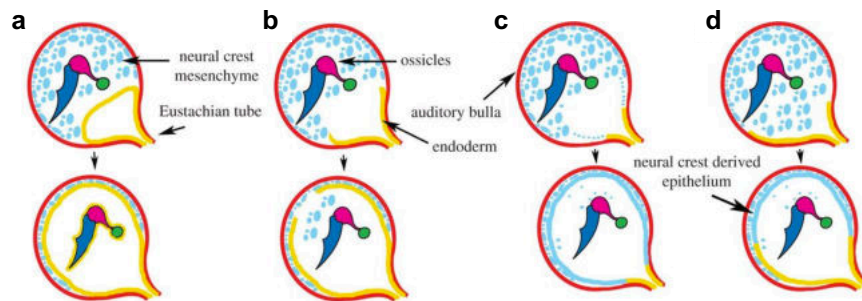
Figure 2.4. Proposed processes of creating an air-filled space. (a) Invasion of the endoderm as a sheet of tissue wrapping around the ossicles. (b) Break of the endoderm to allow the tissue to move around the ossicles. (c) No invasion of the endoderm but creation of a cavity by retraction and transformation of the mesenchyme. (d) Process based on lineage tracing showing a dual origin of the middle ear lining incorporating some of the ideas from the previous three models [17].

7

The lateral, or outer-facing layer consists of a thin epidermal epithelium with keratinocytes forming a protective barrier from the environment. From top to bottom, the epidermis consists of a stratum corneum, a stratum granulosum, a stratum spinosum, and a stratum basale [18]. The keratinocytes in the stratum basale divide and migrate upward to the stratum granulosum and stratum corneum. The cells in the stratum corneum regularly slough off the surface of the TM and into the EAC, migrating in a radial manner from the umbo outward [19] (**Figure 2.5**). Using an ink dot technique, researchers have demonstrated that the average migratory rate of keratinocytes is approximately 131 µm/day in children, with the highest rate at the umbo [20]. Other researchers studied this migratory rate in gerbils and found it to be dependent on age, with the fastest rate observed for young gerbils (3- 6 months old) at 116 µm/day and the slowest rate in older gerbils (24 – 30 months old) at 86 µm/day, [21] suggesting slower TM regeneration in older animals. In addition to keratinocytes, immunohistochemical analysis has revealed the presence of progenitor cells in the epidermis that cover the manubrium, annulus, and malleus of the TM [22,23]. Live cell imaging of explanted mouse TMs was used to investigate the migration patterns of these cells, demonstrating that they follow a superior-inferior path from the malleolar folds between the pars tensa and pars flaccida [24]. These cell-tracking experiments demonstrate a shedding and migration of the cells in this layer that allow for continuous turnover of cells during homeostasis [25].
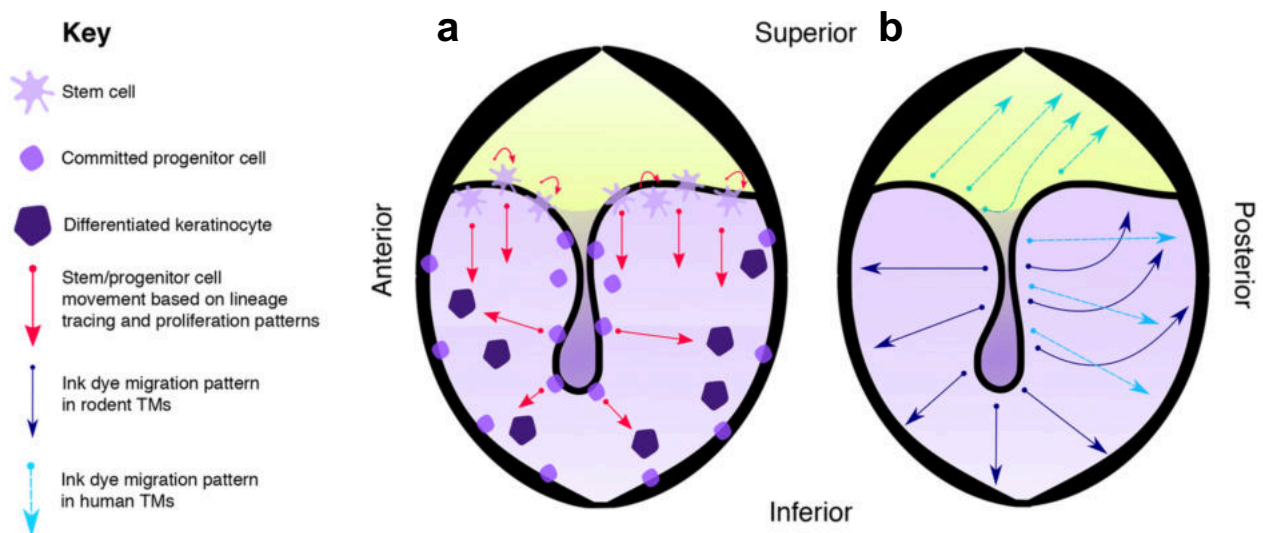
Figure 2.5. Migration of cells on the epidermal layer of the TM. (a) Location and movement of stem/progenitor cells based on lineage tracing experiments and proliferation assays. (b) Migration patterns of keratinocytes based on ink dye labeling experiments in rodents and humans [19].

Below the epidermal layer of the TM lies the lamina propria— the thickest layer. This connective tissue layer consists mainly of collagen fibers. Specifically, in the pars tensa, there is a collagen layer with fibers oriented in a radial orientation outward from the manubrium. Below this radial layer, there is a layer of collagen fibers formed in a circumferential circular and parabolic orientations around the TM. Scanning electron microscopy of the human TM demonstrates the arrangement of collagen fibers in this layer [4] (**Figure 2.6**). Most of these fibers consist of collagen II and III, with collagen I near the annulus. It is believed that these banded, mature collagen fibers are produced by fibroblasts and that the orientation of fibroblasts during development determine the resultant direction of collagen fibers in these layers. Type IV collagen, laminin, and elastin can also be found in the TM. While the keratinocyte-based epidermal tissue is constantly remodeled, the collagen network remains largely unchanged during one's life [26].
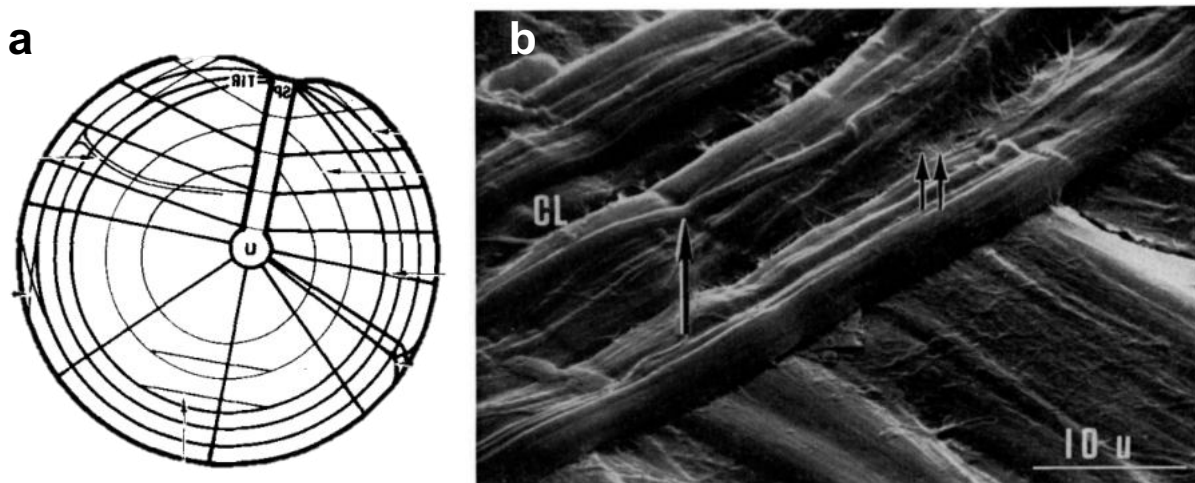
Figure 2.6. Fibrous structure of the human TM. (a) Sketch of the fiber orientation in the TM, containing circumferentially and radially oriented fibers. (c) Scanning electron microscopy (SEM) image of a human TM demonstrating the arranged circumferential and radial fibers [4].

Directly lateral and medial to these collagenous layers lies two layers of capillaries and nerves [27]. During middle ear inflammation, these blood vessels in the pars tensa become easily distinguishable [28]. The lamina propria layer also contains mast cells derived from progenitor cells in bone marrow. Mast cells are often contained in connective tissue. The human TM is estimated to contain approximately 300 mast cells/mm^2, and it is believed that stimulation of the TM triggers the release of neuropeptides that cause vasodilation of the capillary network and mast cell degranulation [29]. Degranulation is a cellular process that releases antimicrobial molecules, such as heparin, proteoglycans, histamine, and multiple enzymes. In the

lateral surface of the TM, innervation comes from the auriculotemporal nerve, arising from the mandibular nerve. In the medial layer, innervation comes from the glossopharyngeal nerve. Due to the TM's complex innervation, damage, inflammation, or exposure to extreme temperatures can cause ear pain, or otalgia [30], which contributes to the production of middle ear effusion in damaged TMs [31]. Overall, the TM is considered to be one of the most sensitive tissues in the body.

The final and medial-most layer of the TM is the mucosal epithelium. This mucosa is continuous across the entire surface area of the middle ear space. These cells take on a flattened, non-ciliated cuboidal form. However, there are sparse ciliated mucosal cells in the epithelial lining of the middle ear space, commonly located at the hypotympanum and the opening to the Eustachian tubes [32]. The mucosal cells of the middle ear produce mucus, particularly in inflammation and in Eustachian tube dysfunction whereby the middle ear pressure cannot properly equalize [33]. In this process, the middle ear epithelium attempts to capture pathogens via mucus and drain them from the Eustachian tubes.

2.3.2   Viscoelastic Mechanical Properties of the Tympanic Membrane

Like most soft tissues, TM is a viscoelastic material— that is, the force needed for deformation depends upon both the rate of deformation (viscous component) and the amount of deformation (elastic component). Importantly, the complex modulus [$E^*(\omega) = E_1(\omega)[1 + i\ \eta(\omega)]$] of the overall TM has been measured at between 10 – 100 MPa depending upon the testing method, frequency, and the direction along which it is tested [34-38]. De Greef *et al.* developed a Finite Element (FE) model of these viscoelastic properties via holography measurements across the TM surface coupled with laser Doppler vibrometry measurements of umbo velocity [35]. They determined that the viscous elements of the TM provide relatively low damping, and that there is significant variation in the complex modulus of the TM between specimens (**Figure 2.7**). For their first model (TB 1), G* had a magnitude value of 10 MPa at 70 Hz, growing to 13 MPa at 20 kHz, while the second model (TB 2), G* had a magnitude value of 40 MPa at 70 Hz, growing to 52 MPa at 20 kHz. Overall, the stiffness of the TM slightly increases with increasing frequency of displacement. As the TM transduces sound pressure waves at a wide range of frequencies into mechanical motion, this relationship is important to understanding the sound-induced motion of the TM at across frequencies.

	TM	Manubrial fold	Lateral process	Anterior ligament	Malleus
E [MPa]	10–40	10% of TM	16000	21[a]	16000[b]
v	0.3[c]	0.49	0.3[d]	0.3[d]	0.3[d]
η	0.01–0.13	Same as TM	0	Same as TM	0
ρ [kg/m³]	1200[d]	1200[d]	2200[e]	1200[d]	2200[e]
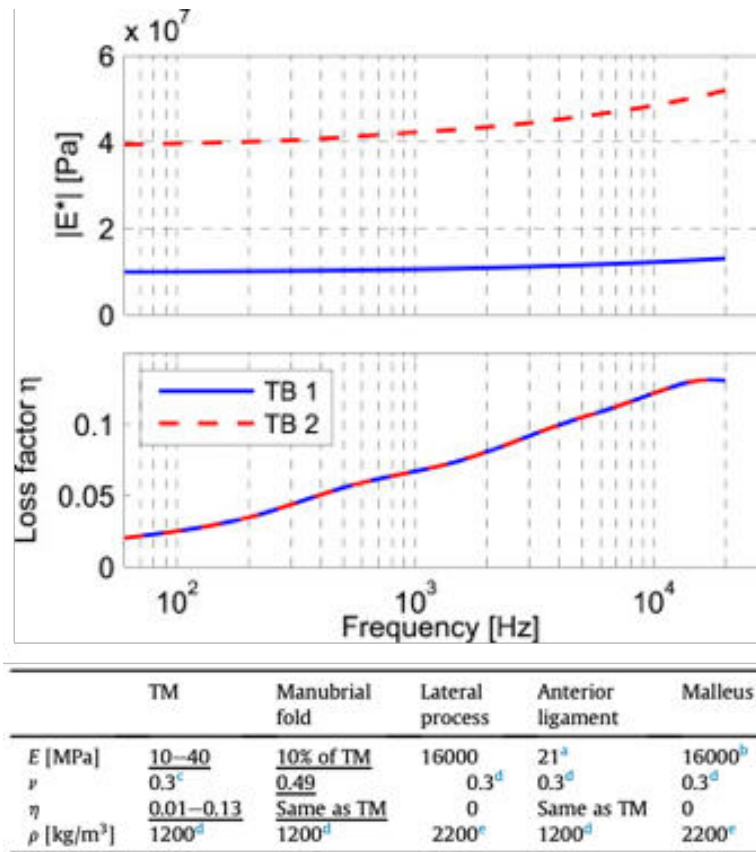
Figure 2.7. Complex modulus magnitude (E*) and phase values of the TM used for the two model data sets. Both magnitude curves differ merely by a multiplication factor, while the phase data is equal. Bottom table shows material properties of Young's modulus (E), Poisson's ratio (v), loss factor (η) and density (ρ) [35]**.**

Given the variability in measurements and relative low contribution of the viscous component to the complex modulus compared the elastic component, several research groups have measured the elastic modulus in the quasi-static regime through testing methods such as tension and bending tests. Decraemer *et al.* reported results for uniaxial tension testing of the human TM, showing that the experimental stress–strain relationship had a small slope at small strains that gradually increased to a large constant slope at high strains, with the Young's modulus, E = 23 MPa [36]. Looking at exclusively the collagen structure in the lamina propria, Fay *et al.* analyzed previous literature utilizing both bending and tension tests, creating a model for the relative shear modulus (G) across the angle of the TM [38]. In their model, an angle of 0° corresponds to a loading direction aligned with the radial collagen fibers, while an angle of 90° corresponds to a loading direction aligned with the circumferential collagen fibers (**Figure 2.8**). They found that, for tension testing, G varies between a local minimal modulus off-axis from either the circumferential or radial

11

directions (G = 148 MPa) and a maximal modulus in the direction of radial collagen fibers (G = 391 MPa). Alternatively, for bending testing, G varies between a minimal modulus in the circumferential direction (G = 14 MPa) and a maximal modulus off-axis from either the circumferential or radial directions (G = 143 MPa). Overall, the TM is stiffer in the radial direction than the circumferential direction, with variation in between due to the anisotropic structure of the TM. It is important to note that these tests only model the impact of the collagen fibers in the lamina propria of the TM and do not consider the impact of the lateral epithelial layer or medical mucosa to the overall mechanical behavior of the TM.
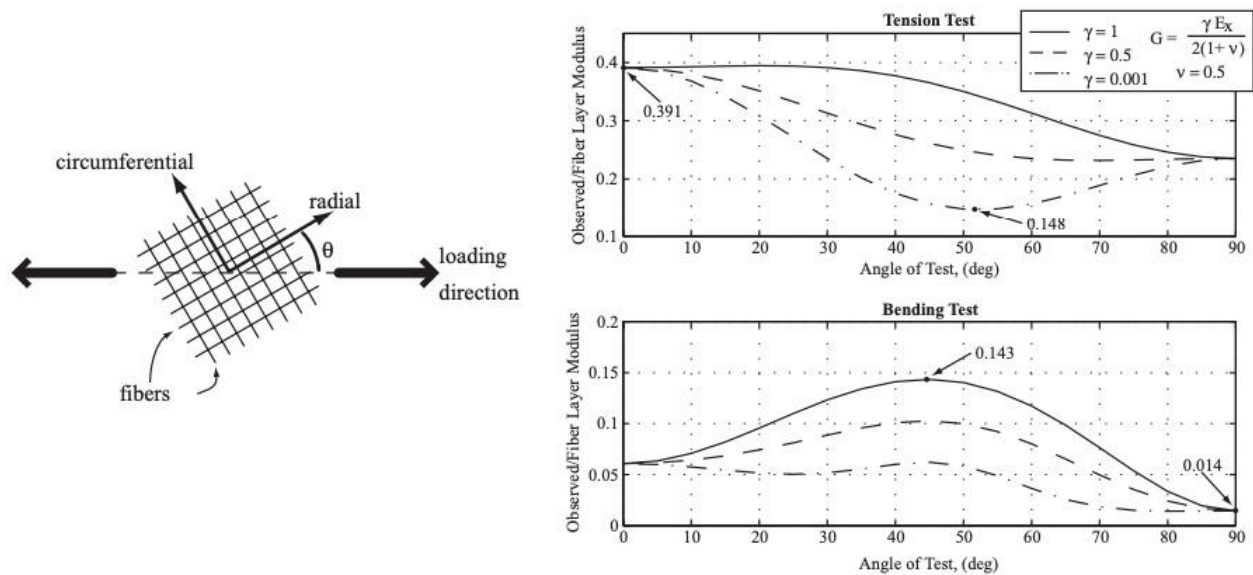
Figure 2.8. Anisotropic shear modulus, G, of the collagenous lamina propria of the TM. Left: material patch of the TM and its orientation with respect to the direction of the applied test load. The effect of angle on the results of a tension or bending test. Right: what would be observed as the elastic modulus of the TM using an isotropic assumption divided by the elastic modulus of the underlying fiber layer. The top graph shows the ratio for a tension test while the bottom is the ratio for bending tests. G is the shear modulus and is varied through the parameter, g. The three curves show the response as the shear modulus is varied from a large value similar to the fiber stiffness (solid lines) to a very soft value comparable to loose connective tissue (dot–dashed lines). v is the Poisson ratio and E_x is the layer on-axis elastic modulus [38].

2.2.2 Sound-Induced Motion of the Tympanic Membrane

Although all three layers of the TM play an important role in its homeostasis and barrier functions separating the environment from the middle ear space, the ability for the TM to effectively conduct sound waves from the environment is a unique feature of the membrane. Importantly, the middle ear (TM and

ossicles) acts as an impedance matcher. Acoustic impedance (Z) functions similarly to resistance in electric circuits or dampening in mechanical systems and is given by:

$$Z = \frac{P}{U} \qquad (1)$$

where P is the sound pressure and U is the sound volume velocity. However, specific acoustic impedance is the more common way to define the impedance of a particular tissue, as it relates to the particle velocity instead of volume velocity and is thus independent of a known surface area. Note, the units of impedance are given as $kg \cdot m^{-4} \cdot s^{-1}$, while the units of specific acoustic impedance are given as $kg \cdot m^{-2} \cdot s^{-1}$ (or rayl).

Temperature and density are important factors in the acoustic impedance of a given material. An increase in temperature is correlated to a decrease in acoustic impedance. For air at 0°C, the specific acoustic impedance is roughly 428 rayl. Increasing air temperature to 25°C results in a decrease in specific acoustic impedance to roughly 409 rayl. By contrast, an increase in the fluid density is results in an increase in acoustic impedance. For example, water at 25°C has a specific acoustic impedance of 1.408×10^6 rayl. Soft tissues and blood are in a similar range, generally between 1.34×10^6 rayl and 1.63×10^6 rayl. Bone is even higher due to its high density, at around 7.8×10^6 rayl [39]. Finally, the specific acoustic impedance of perilymph fluid in the cochlea is significantly higher than that of air. If pressure waves from the air directly contacted the oval window of the cochlea, these pressure waves would be reflected and not transmitted into the cochlea due to the impedance mismatch between air and perilymph fluid in the cochlea, with cochlear impedance being significantly higher than that of air. Thus, only about 0.1% of incident energy would be transmitted to the cochlea.

The TM vibrates in response to sound across a broad range of frequencies, because, partly due to its air-air interface, it is able to more closely match the impedance of air. It converts the low-pressure, high-displacement vibrations in the environment into high-pressure, low-displacement vibrations for cochlear fluids. The middle ear increases the pressure from the TM to stapes through three processes, as demonstrated in **Figure 2.9**. The first is through the transmission of force from a large TM to the oval window with a significantly smaller diameter. The surface area of the TM is approximately 20x (~26 dB increase) the surface area of the stapes footplate [40]. Secondly, the pars tensa of the TM is in the shape of a shallow cone, with the manubrium of the malleus extending along one radius to the apex of the cone. Thus, larger displacement of the TM surface results in smaller displacement at the umbo with a ratio of approximately

13

2:1 (~6 dB increase). The third process is the level action of the three ossicles, whereby the ratio of length of the malleus to the incus is approximately 1.3:1 (~2 dB increase). This process increases the force of the mechanical motion but decreases the velocity at the stapes. Overall, these processes cause a pressure gain of almost 50-fold (~34 dB increase) between the environment and the oval window.
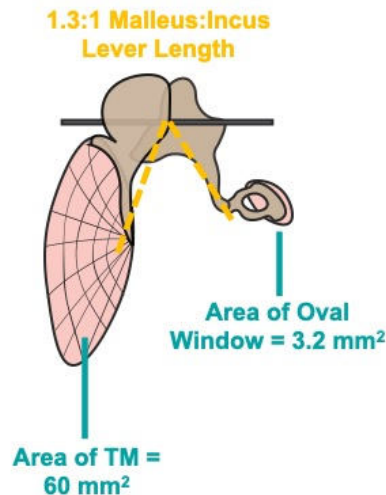
Figure 2.9. Impedance matching action of the middle ear. The middle ear acts to increase the pressure and decrease the displacement of acoustic vibrations through two major mechanisms. The first is through the approximately 20:1 ratio between the area of the TM and that of the oval window to the cochlea, as shown in teal. The second is the 1.3:1 ratio between the level arms of the malleus and incus, as shown in yellow.

The impedance of the TM is affected by contributions from the middle ear and cochlea due to their close connection. Overall, this system exhibits a frequency-dependent impedance, meaning that certain frequencies exhibit less "resistance" to sound transmission than others. The acoustic impedance of the entire middle ear (Z_{me}) is influenced by the admittance of the middle ear cavity (Y_{cav}), admittance of the ossicles and TM, which are modeled as five simple harmonic oscillators in parallel (Y_M) and the impedance of the cochlea (Z_c) [41-43] as given by:

$$Z_{me} = \frac{1}{Y_{cav}} + \frac{1}{Y_M} + Z_c \tag{2}$$

The acoustic impedance of the entire middle ear is also dependent on the frequency of the acoustic pressure waves. Researchers used the model from **Figure 2.10** along with parameters for these components, including density and the speed of sound, to estimate the impedance. The results from this model are shown in **Figure 2.11**, which shows the acoustic input impedance of 6 ears as measured and

modeled [41]. In all ears, this input impedance has a slope of approximately -6 dB/octave, starting at around 10^8 kg·m^{-4}·s^{-1} at 200 Hz and decreasing to approximately 10^6 kg·m^{-4}·s^{-1} at 6000 Hz. As this frequency increases, the middle ear has more influence on impedance due to its resonant frequency at around 1500 Hz, changing the magnitude slope while the phase becomes less negative. The major resonant frequency of the TM corresponds to the sounds best transmitted by the TM. These resonances show up as local minima in the magnitude response plots and local maxima in the phase response plots. Specifically, the magnitude notch results from reflected out-of-phase waves from the TM.
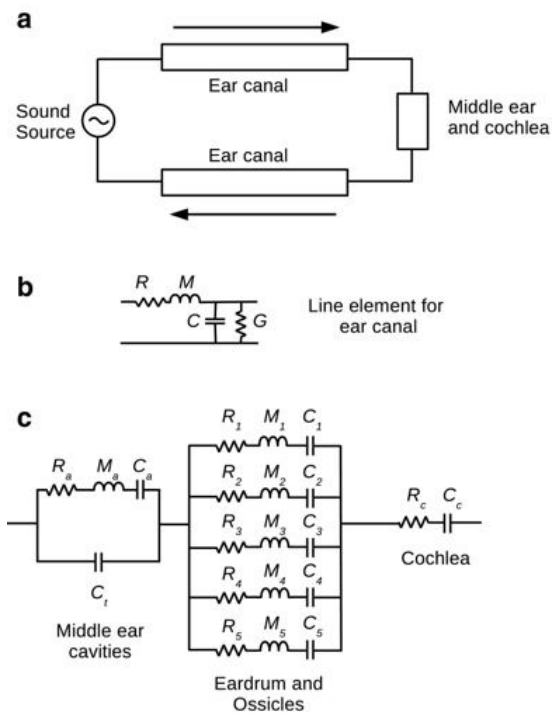
Figure 2.10. Example circuit diagram for the model of the ear. The ear is modeled as a one-dimensional lossy transmission line (ear canal) terminated by a distributed load impedance, the middle ear and cochlea. This model is shown with the two paths for the transmission line, a wave going in and a wave coming out, terminated by the load impedance. The line element for the transmission line is shown in b, consisting of a series impedance and a shunt admittance. The series impedance consists of resistance (R) and mass (M), the shunt admittance consists of conductance (G), and compliance (C). The eardrum and ossicles are represented by a bank of resonant filters, and the cochlea is represented by an RC circuit [41].

While the middle ear has an important role in impedance matching, acoustic vibrations can still traverse from the environment to the cochlea via the skull and tissues in the head. Additionally, during acoustic coupling, sound is transferred from the TM directly to the oval and round windows of the cochlea via the air in the middle ear space. However, sound pressure levels reaching the cochlea through bone conduction alone will be significantly lower than through ossicular coupling or even acoustic coupling. The ratio between the sound intensity (I_2/I_1) transmitted from one medium with acoustic impedance (Z_1) to a second medium with acoustic impedance (Z_2) is given by:

$$\frac{I_2}{I_1} = \frac{4Z_1Z_2}{(Z_1+Z_2)^2}$$

(3)

In a normal ear, sound reaching the cochlea via bone conduction is thought to be insignificant.
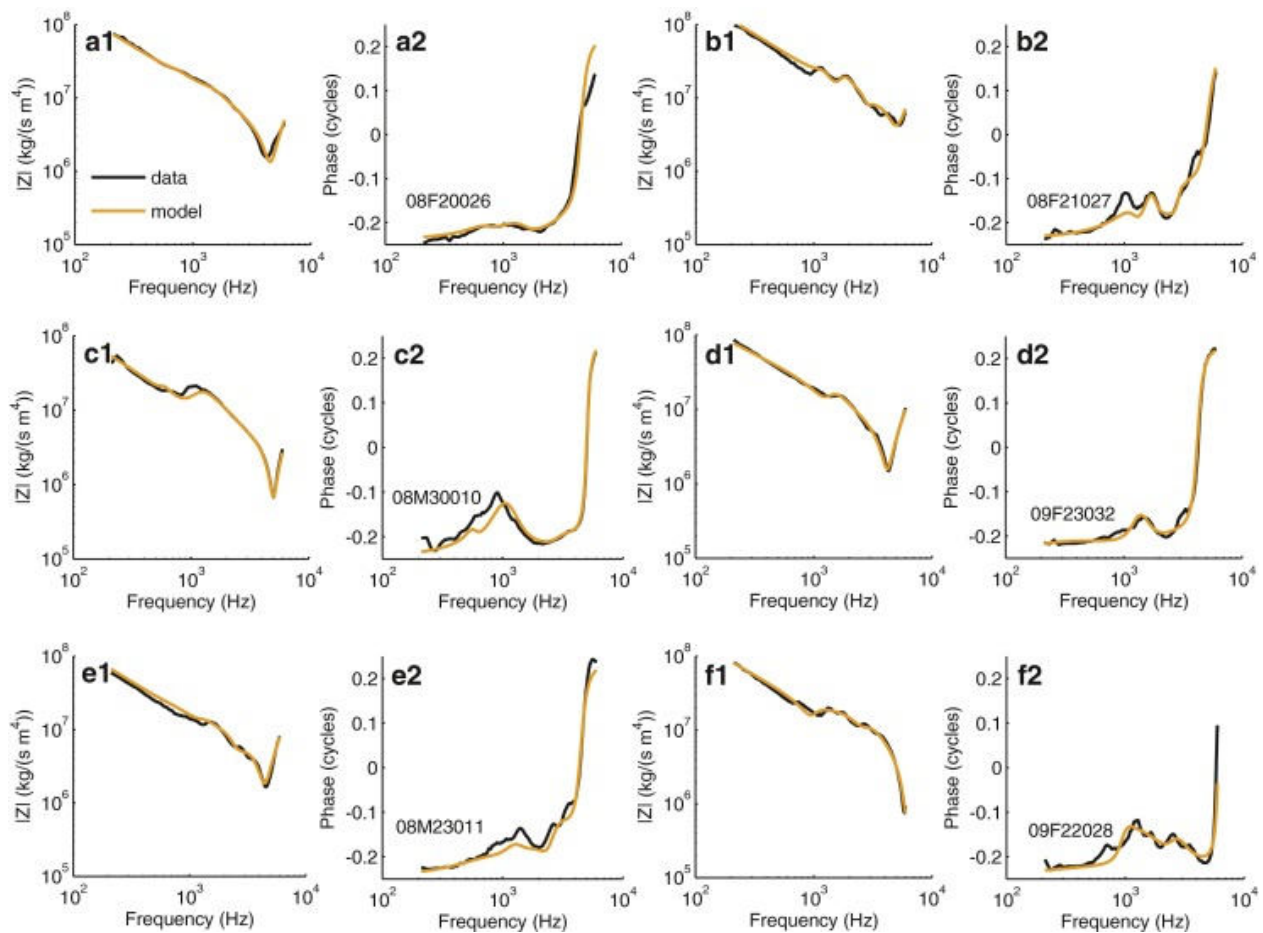
Figure 2.11. Acoustic input impedance: (1) magnitude and (2) phase data. [Note: Model fit from Figure 2.8 to the data for six ears a-f.] [41].

The mastoid bone is part of the temporal bone of the skull made of air-filled mastoid cells. These cells are thought to help protect the ear, particularly during trauma by absorbing pressure [44]. Additionally, the mastoid cells can help regulate pressure between the middle ear and the environment, particularly in cases of Eustachian tube dysfunction [45]. Even with air-filled cells, the mastoid bone still has a significantly higher impedance than the environment. Thus, with the impedance matching potential of the middle ear, sound intensity should be perceived as greater via air conduction (through the ear canal) than bone conduction (through the mastoid bone). These possible pathways for sound conduction to the cochlea are shown in **Figure 2.12** [46].
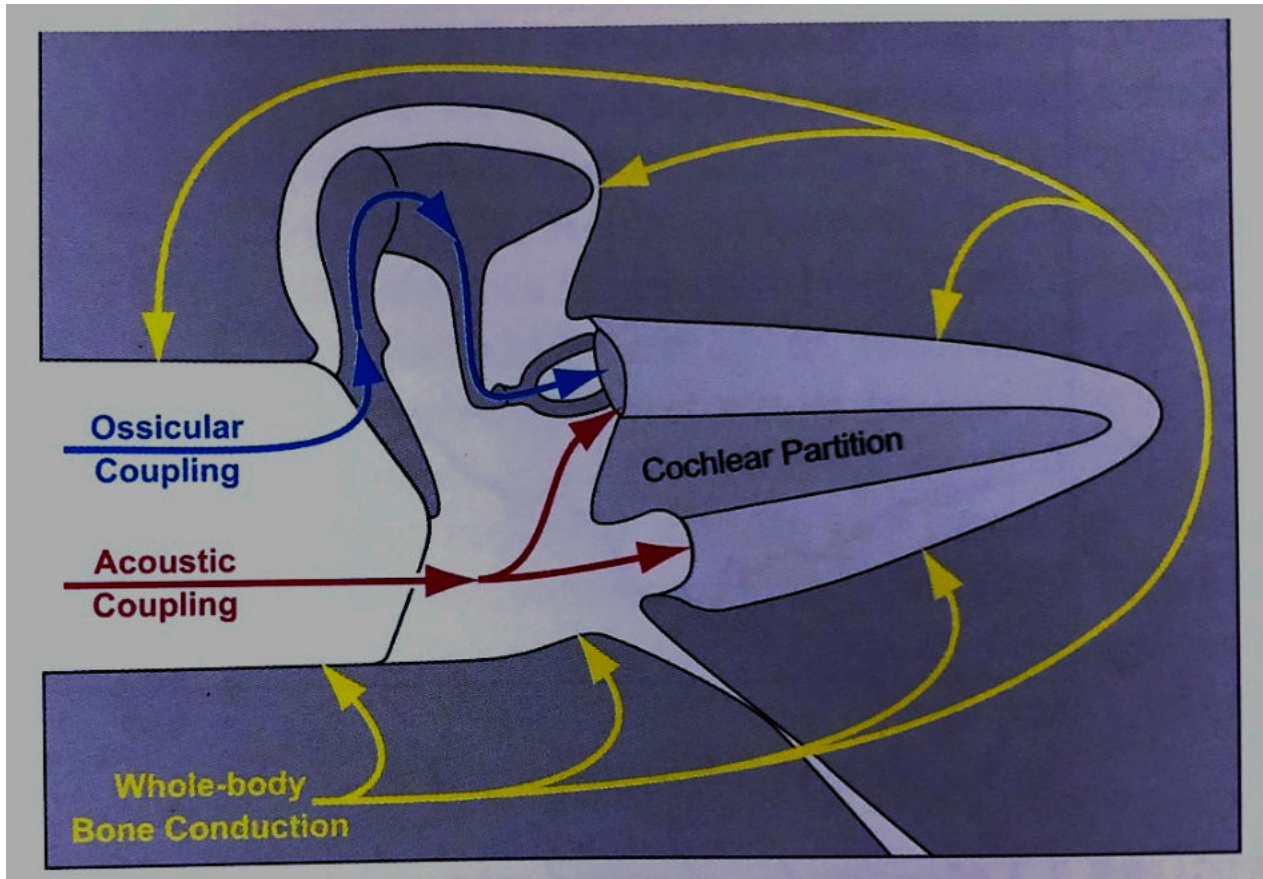
Figure 2.12. Diagram of sound conduction routes from the environment to the cochlea. [Note: The arrow in blue shows coupling through the TM and ossicular chain. The arrows in red shows acoustic coupling directly from the TM to the oval and round window. Finally, the yellow arrows indicate bone conduction routes from the skull and other tissues to the cochlea.] [46].

2.3.3 Importance of Anisotropy and Complex Motions of the Tympanic Membrane

Conductive hearing loss occurs when sound waves are unable to pass properly through the external and middle ear. This could be caused by TM damage, ossicular damage, fluid in the middle ear, inflamed tissues from an infection, or even a buildup of earwax in the ear canal. In contrast, sensorineural hearing loss occurs due to damage to the cochlea, auditory nerve, or brain. Conductive hearing loss is often treatable through surgical approaches. In contrast, sensorineural hearing loss, which is usually caused by genetic factors, aging, and/or noise exposure, is less surgically treatable. In such cases, hearing loss is typically treated with hearing aids which increase the sound pressure level reaching the TM through analog or digital sound amplification.

By extrapolating the principles of impedance-matching, a behavioral audiogram can assess whether a patient's hearing loss is caused by conductive factors or by sensorineural factors. By testing across frequencies, an audiogram compares hearing thresholds between air conduction using over the ear headphones (crosses, X) and bone conduction through a bone transducer over the mastoid (brackets,]). The presence of an air-bone gap (ABG) (**Figure 2.13**), or a significant difference between the sound pressure level required for hearing between air conduction headphones and bone conduction headphones, can indicate conductive hearing loss [47]. In conjunction with an audiogram, otoscopic or endoscopic examination of the ear canal and TM enables diagnosis of implicated pathologies, such as impacted wax, perforation of the TM, or ossicular fixation.
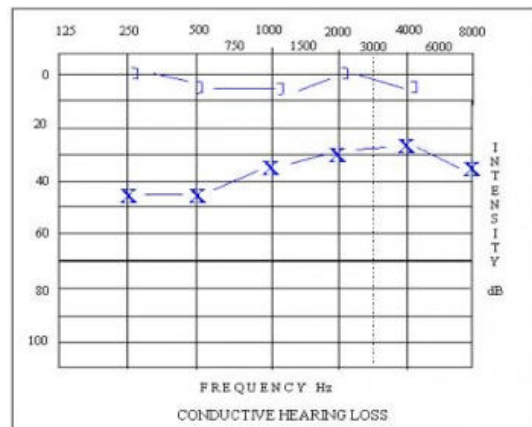
Figure 2.13. Audiogram of a patient with conductive hearing loss. A significant difference between air conduction (crosses, X) and bone conduction (brackets,]) is called an air-bone gap (ABG) and can indicate middle ear damage [47].

It has long been suspected that the specific circumferential and radial arrangement of collagen fiber bundles in the lamina propria of the TM is crucial for its function. The Italian scientists Leonardelli [48], Fumagalli [49], and Filogamo [50] were the first to identify and demonstrate the mechanical importance of these fibers in as early as 1948. Fumagalli noticed that these radial and parabolic collagen fiber bundles originated from the short process of the malleus and called this system the "paraboliccrescentic system" [49]. Mechanically, he noticed that when the malleus moves medially, the radial fibers stretch, and the parabolic fibers relax. As such, the overall tension of the TM remains constant during bending motions. A later study by Secondi in 1951 compared the fibrous structure of the TM between animals including a guinea pig, rabbit, dog, cat, ox, sheep, pig, and horse [51]. He found that in all species, the radial fibers originate

from the handle of the malleus; however, their arrangements differ. In the guinea pig TM, these fibers run uniformly, isolated from the annulus. For the rabbit TM, these fibers are grouped in thin, independent bundles with a similar "parabolic-crescentic system" seen in humans, as seen in scanning electron microscopy images by Lim *et al.* [18]. In all other species, Secondi found that these fibers are woven together into a dense plexus, whereby individual collagen fiber bundles cannot be easily distinguished.

In recent years, the fibrous structure of the collagen bundles has been related to the TM's sound-induced motion across the range of hearing. O'Connor *et al.* were the first to experimentally investigate this importance to high-frequency sound conduction in 2008 [6]. In this study, the authors created a series of slits in human TMs in cadaveric temporal bones in three groups: (1) circumferentially orientated slits to disrupt radial fibers in the superior-anterior, inferior-anterior, inferior-posterior, and superior-posterior directions (2) circumferentially orientated slits to disrupt radial fibers in the reverse anterior-superior, anterior-inferior, posterior-inferior, and posterior-superior directions, or (3) radially-orientated slits from the umbo to annulus to disrupt circumferentially oriented fibers. The authors then patched the TM after slits were made, keeping the overall structure intact and isolating changes to the fiber structure alone (**Figure 2.14**). Closing the resultant perforation is an important step, as otherwise, the pressure differential across the TM will be modified due to the presence of a perforation, causing additional hearing loss.
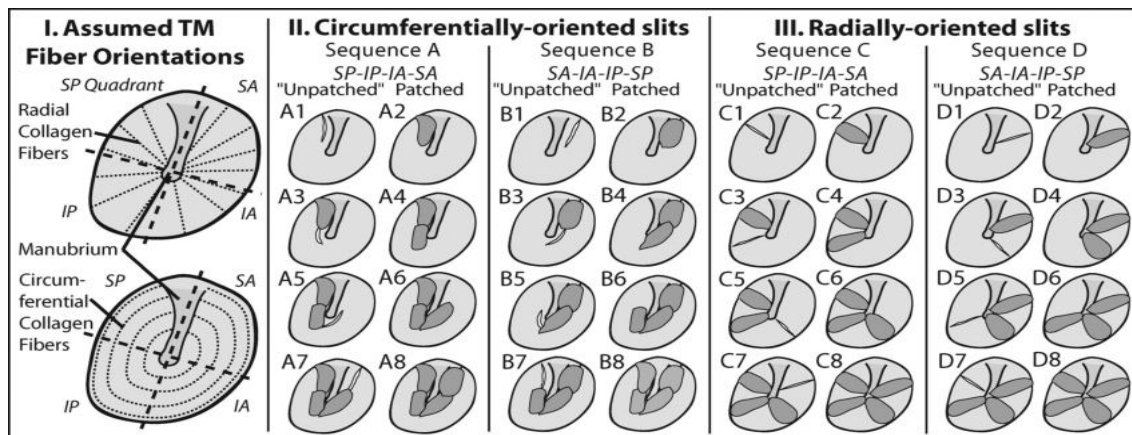
Figure 2.14. Assumed collagen fiber orientations on the tympanic membrane (TM) (panel I), and depictions of all four experimental sequences of TM slits and patches (panels II and III). Sequences A and B (panel II) involve a total of four slits and patches made circumferentially around the manubrium (depicted as eight distinct steps in A1–A8 and B1–B8). Sequences C and D (panel III) involve the same number of slits and patches made radially from the outer edge of the TM to the manubrium (steps C1–C8 and D1–D8). The location of each slit and patch pair is specified by one of four two-letter abbreviations (SP, IP, SA, and IA) which denote each of the four quadrants on the TM surface in terms of superior (S), inferior (I), posterior (P), and anterior (A) notation (see panel I) [6].

In each group of disrupted fibers, the ear canal pressure, middle ear cavity pressure, and stapes velocity were measured to compare relative amounts of sound energy transferred from the ear canal to the inner ear. The results were given as the velocity of the stapes (V_{st}) as measured by laser Doppler vibrometry normalized by the pressure differential between the middle ear and ear canal (P_{TM}) (**Figure 2.15**). The researchers found that slits that disrupted the radially oriented collagen fibers had a greater impact on sound-induced velocity than those that disrupted the circumferentially oriented collagen fibers. Importantly, they found that regardless of the order in which the slits that disrupted the radially-oriented collagen fibers were imparted, there was a consistent decrease in stapes velocity at an average of 11 dB at frequencies above 4 kHz. These results demonstrate the strong importance of the intact TM collagen architecture for sound conduction, in particular the significance of the radial fibers at high frequencies.
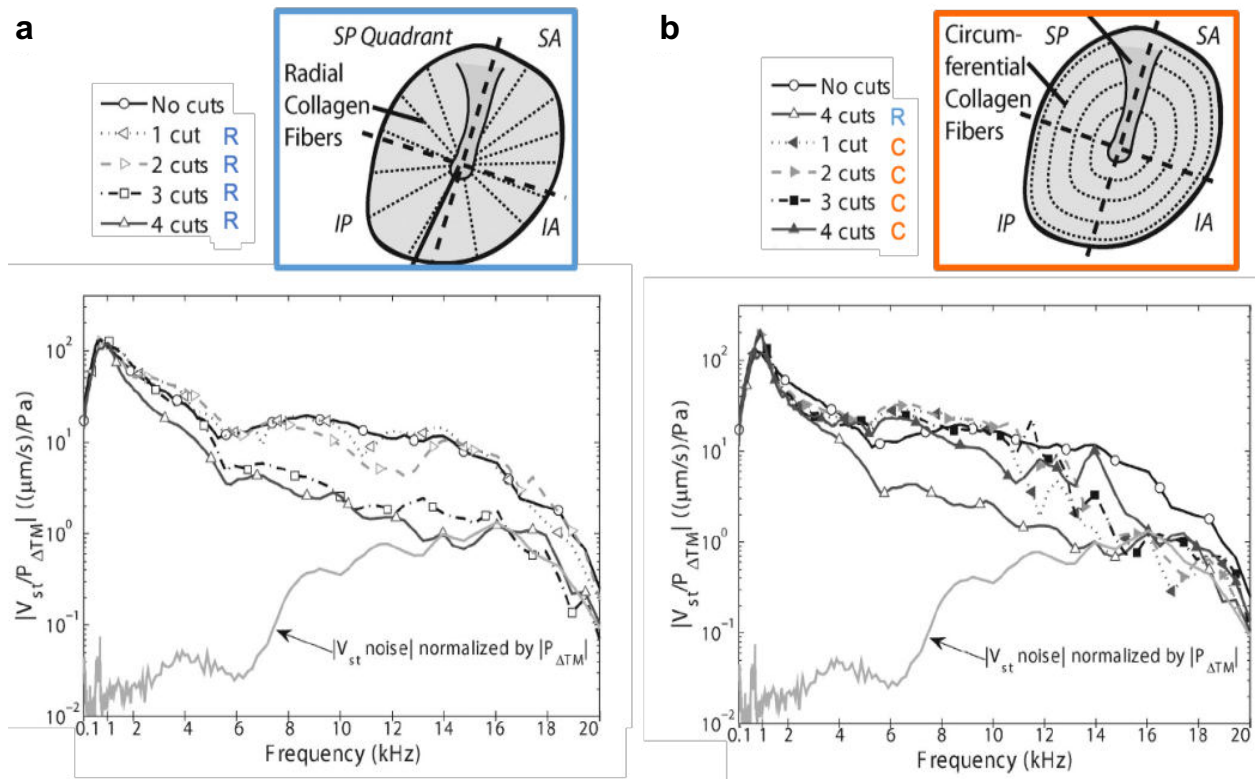
Figure 2.15. Modified figure demonstrating the acoustic impact of slits made in human cadaveric TMs to investigate the impact of different fiber orientations. Insets show the direction of fibers that are slit, with radial fibers cut in blue on the left and circumferential fibers cut in orange on the right. (a) Cutting radial fibers (open points) causes a significant decrease in sound-induced motion at frequencies about 4 kHz as compared to the normal, intact TM (circular points). (b) Comparing the response of 4 cuts through radial fibers with various numbers of circular cuts, it appears as though the reduction in sound-induced motion caused by radial cuts is greater than the impact of circular cuts [6].

The role of the radial collagen fibers in the TM to sound-induced motion has been further explored through modeling of the middle ear. In 2006, researchers created a mathematical model of the discordant motion of the TM to determine the properties that impact this motion [5]. Specifically, they noticed that above 3000 Hz, the TM vibrates chaotically with complex modes of motion, unlike its single resonance motion at low frequencies. It was suspected that multiple resonances across the TM are what enable it to transmit a broad range of frequencies by working through discord. They investigated the impact of features including shape, position, and mechanical properties on the ratio between the pressure in the vestibule of the cochlea (P_V) and the pressure in the ear canal (P_{EC}), also referred to as the middle ear gain (MEG). Importantly, to investigate the impact of the fibrous architecture on the TM, they modeled the TM with different isotropic and orthotropic mechanical properties by altering the Young's Modulus values (E) (**Figure 2.16a**). For the isotropic cases, the TM was modeled as either a "soft" tissue, E = 30 MPa, or a "stiff" tissue, E = 100 MPa. As an anisotropic soft tissue, the TM's Young's modulus has been measured at between 10 to 100 megapascals (MPa), depending upon the method and direction upon which the membrane is tested [34-38].
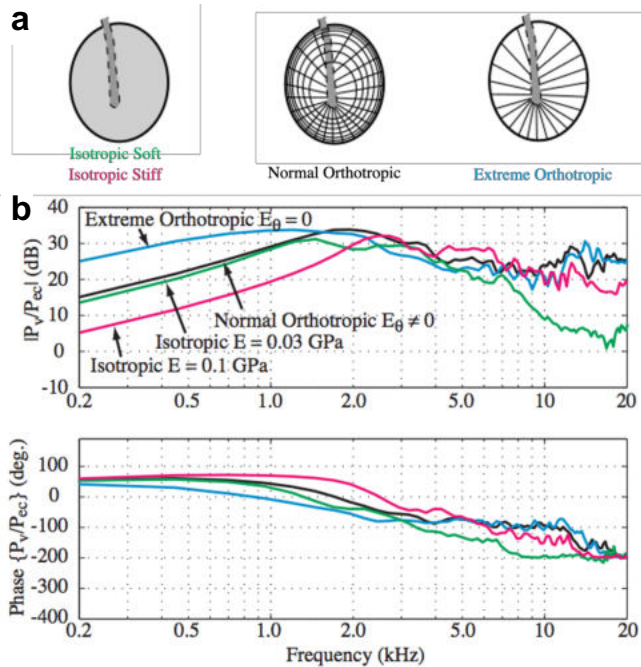
Figure 2.16. Microstructure effects of TM via modeling. (a) An isotropic eardrum (Left). Both circumferential and radial fiber layers are treated as isotropic sheets. The anatomically normal model (Center). All circumferential fibers have been eliminated (Right). (b) Effect of microstructure on the middle ear pressure transfer function. Compared with the normal, the isotropic eardrum shows significant loss, both for low frequency when the reference modulus near the tympanic annulus E = 0.1 GPa, and for the high frequency when E = 0.03 GPa. When all of the circumferential fibers are removed, E = 0 GPa, the transmission is increased for the low frequencies while being maintained at high frequencies [5].

For the orthotropic cases, the TM stiffness was varied in the circumferential (E_θ) and radial (E_r) directions. For the "normal orthotropic" TM, near the edge of the TM, these stiffnesses were assumed to be almost equal, whereas the radial stiffness was increased moving inward toward the umbo from 30 – 100

MPa, increasing as these radial fibers converge. The stiffness in the "normal orthotropic" TM mimicked that of the human TM as so to best approximate the actual response of the TM. In the "extreme orthotropic" TM, this assumes that $E_0 = 0$ MPa everywhere to approximate removing the circumferential fibers. The researchers found that the orthotropic nature of the TM allows it to conduct sound well at both low and high frequencies [5] (**Figure 2.16b**). At low frequencies, it is able to vibrate as one sheet, behaving as more of a soft material, and at higher frequencies, it creates multiple mistuned resonance modes of motion to drive the ossicles, behaving as more of a stiff material. The "isotropic soft" or "isotropic stiff" TM can match the "normal orthotropic" case in either the low frequencies or high frequencies; however, neither can achieve both. The "isotropic soft" TM could achieve similar pressure transfer at low frequencies to the "normal orthotropic" TM; however, at high frequencies above 8000 Hz, its single resonance mode means that it cannot vibrate enough to drive the umbo, causing an approximately 20 dB loss. Conversely, the "isotropic stiff" TM could achieve a similar response at high frequencies to the "normal orthotropic" TM. However, at low frequencies, the impedance mismatch between the air and the stiff TM tissue means that the TM cannot effectively vibrate, causing up to a 10 dB decrease in pressure transfer. Thus, the body has engineered this orthotropic architecture to efficiently transfer sound pressure at frequencies above approximately 3000 Hz. Interestingly, the authors found that the "extreme orthotropic" had superior vibration at low frequencies (<1500 Hz) compared to the "normal orthotropic" TM while maintaining similar levels of pressure transfer at higher frequencies. The authors hypothesized that while there are clear advantages to having dominant radial fibers, the presence of circumferential fibers is required to maintain structural integrity of the TM. Thus, while additional radial fibers may be beneficial, a TM composed solely of radial fibers may not be practically attainable.

The mathematical model from Fay *et al.* also examined the effect of the conical structure of the TM on sound-induced motion by modeling the TM as a "shallow" flat surface, a "normal" cone with depth of 1 mm, and a "deep" cone with depth of 2.5 mm [5] (**Figure 2.17a**). For comparison, the human TM has been measured to have conical height at around 2.42 mm [52]. They determined that the "shallow" TM had approximately a 25 dB loss at high frequencies compared to that of the "normal" conical architecture [38] (**Figure 2.17b**), demonstrating the importance of the previously mentioned pars tensa displacement to umbo displacement ratio of 2:1. However, they found that increasing the depth of the TM further had little

impact on sound-induced motion. The "deep" TM had a similar response to that of the "normal" TM. The authors explained this result by describing that the outer section of the TM is very flexible and has a large surface area, providing flexibility and low impedance needed to match that of air. The inner part of the cone with converging radial fibers toward the umbo has a larger impedance. The TM is able to transition between these regions to create in-plane modes of vibration in the conical region, creating in-plane wave speeds that are slower than air speed. In a "shallow" TM, the impedance matches the air but cannot easily make this transition to the umbo, particularly at high frequencies. Increasing conical depth further to the "deep" TM provides poor impedance matching to air.
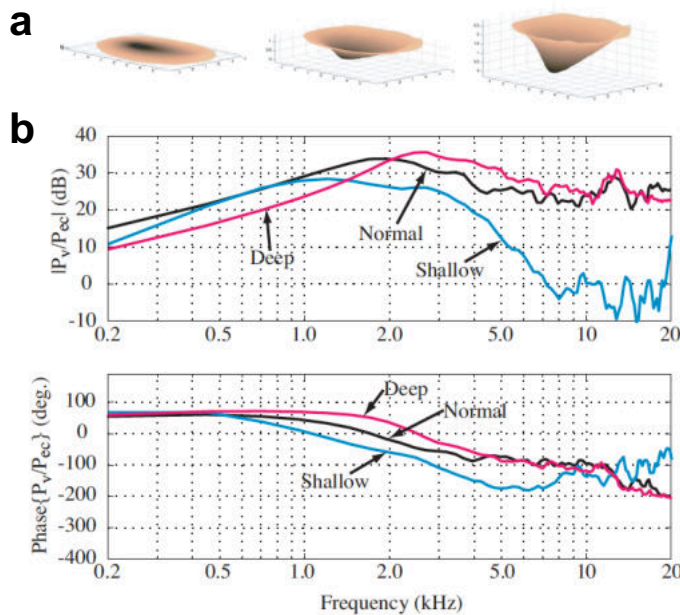
Figure 2.17. Modification of the eardrum depth. (a) The anatomically normal eardrum. (Center) The z coordinate of all of the points is divided by a factor of 10 to obtain the shallow eardrum (Left), and multiplied by a factor of 2 to obtain the steep eardrum (Right). (b) Effect of eardrum depth on the middle ear pressure transfer function. The deep eardrum is nearly the same as the normal, but the shallow eardrum has a 20 dB loss at higher frequencies [5].

By exhibiting multiple resonances (**Figure 2.18**), the TM is able to sensitively transmit a wide bandwidth of frequencies. The discordant wave motion on the surface of the TM has been confirmed via stroboscopic holography measurement techniques. Coupled with sound-pressure measurements to normalize by "loudness" of the sound, this technique allows one to visualize sound-induced displacement patterns at high spatial resolution across the surface of the TM. The authors studied the sound-induced motions at frequencies between 200 Hz – 18 kHz on cadaveric human temporal bones [53]. They were able to visualize both large standing-wave-like modal displacement as well as smaller traveling-wave-like displacement across the TM surface. By plotting the normalized displacement across radial line sections of the TM (**Figure 2.19**), they found at below approximately 8 kHz, there are multiple local displacement modal

magnitudes that are larger than those of the traveling waves, separated by deep minima. Phase angle is constant on the TM surface at these lower frequencies. At middle-range frequencies between 8 – 10 kHz, the umbo moves with a smaller displacement than the rest of the TM, and there are oscillations in phase angle in some displacements. At frequencies of 12 kHz and higher, it appears that the umbo moves out-of-phase from the rest of the TM, consistent with a combination of lower-order modal motions and higher-order traveling-wave-like displacements.
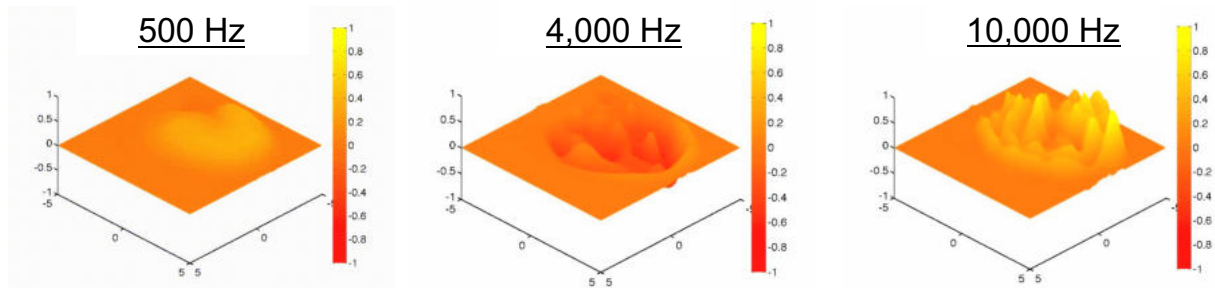
Figure 2.18. Representation of TM motion at different frequencies. At low frequencies, such as 500 Hz, the TM moves in a single modal motion. At higher frequencies, a complex combination of resonance modes allows the TM to move the umbo, transmitting sound through the ossicles and to the cochlea. (image credit: Jeffrey Tao Cheng).
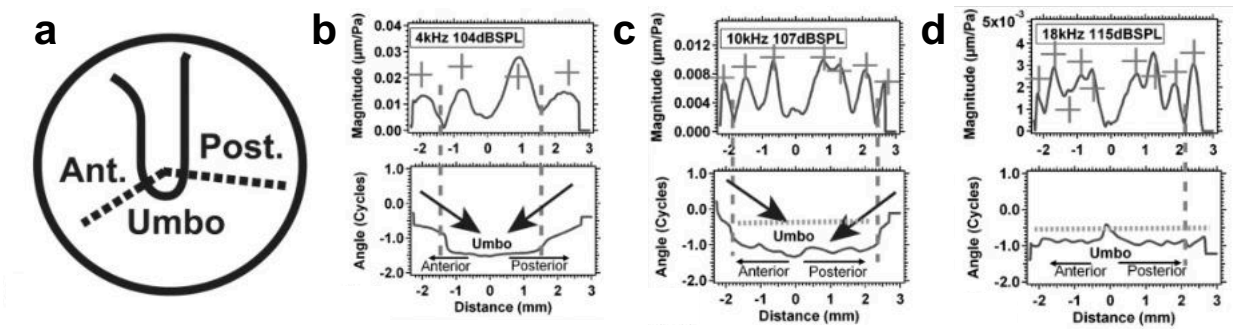
Figure 2.19. The normalized displacement magnitude and phase angle of the TM as a function of the distance from the umbo along two radial lines. (a) Direction of the radial lines. In each plot from (b) to (d), the x-axis represents the distance along two radial lines from the umbo (where x = 0), with x < 0 along the anterior radial line and x > 0 along the posterior radial line; the y-axis represents normalized displacement magnitude in μm/Pa and phase angle in cycles. Multiple local displacement magnitude maxima are marked by + signs [53].

The Puria group created a mathematical model of the TM in 2006, then subsequently created an anatomically based 3D COMSOL finite element model in 2017 [7]. Similarly, they used MEG, the ratio between P_V and P_{EC}, to quantitatively compare the impact of various mechanical properties of the model

on sound transmission (**Figure 2.20**). Baseline stiffness values used are in the radial direction $E_{TM}(R)$ = 140 MPa, in the circumferential direction $E_{TM}(\theta)$ = 20 MPa, and in the transverse direction $E_{TM}(\Phi)$ = 75 MPa. Firstly, they found that decreasing the overall mass of the TM increases the sound-induced motion at mid-to-high frequencies, while increasing the mass of the TM attenuates these frequencies (**Figure 2.21a**). This supports the theory that the mass, or thickness of the TM is crucial to its motion. Secondly, they varied the anisotropic properties of the TM in one direction at a time from 3 to 1000 MPa while leaving the other two directions constant at 3 MPa. They found that the impact of radial stiffness of the TM was more significant for sound transmission than either the transverse or circumferential stiffness (**Figure 2.21b-d**). For both $E_{TM}(\Phi)$ and $E_{TM}(\theta)$, there is very little variability.

P$_{EC}$: the pressure averaged over this plane

P$_V$: the average surface traction on the medial footplate surface, projected onto this direction
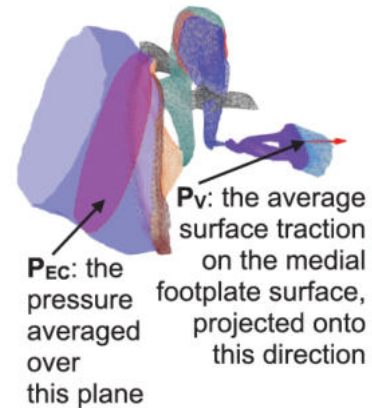
Figure 2.20. Anatomical features of the middle ear used in the model. The areas at which the pressure of the ear canal (P$_{EC}$) and the pressure at the vestibule of the cochlea (P$_V$) are measured are shown by black arrows [7].

However, when increasing $E_{TM}(R)$ from 3 up to 1000 MPa, the MEG in the region of 6 – 20 kHz is significantly affected, at a level of approximately 10 – 20 dB. Specifically, the authors found that when $E_{TM}(R)$ was increased, the gap between the baseline TM value is bridged up to about 6 kHz but only partially bridged between 6 – 12 kHz. When the $E_{TM}(R)$ values approach 1000 MPa, the effect compensates for this attenuation, which does not happen with the $E_{TM}(\Phi)$ or $E_{TM}(\theta)$ cases. By analyzing deviations of these MEG values from the baseline TM MEG (**Figure 2.21e**), the low-frequency region from 100 – 750 Hz shows little difference from the baseline for all three directions. In the mid-frequency region from 750 Hz – 5 kHz, the $E_{TM}(R)$ variation becomes more apparent going from 3 – 20 MPa. However, the greatest effect is seen at high frequencies 5 – 20 kHz, wherein the MEG increases by about 15 dB going from 3 up to 1000 MPa.

In summary, both experiments and modeling have suggested that the TM's complex circumferential and radial collagen fiber structure allows it to vibrate in harmonious modes of motion, allowing one to experience a wide range of sound frequencies as low as 200 Hz and as high as 20,000 Hz. At low frequencies, the TM vibrates as a single sheet with primarily lower-order modal motions. At high frequencies, higher-order traveling-wave-like displacements across the surface of the TM play a bigger role

to drive the umbo. Therefore, the anisotropic, radially stiff nature of the TM appears crucial for optimal sound conduction and normal conductive hearing.
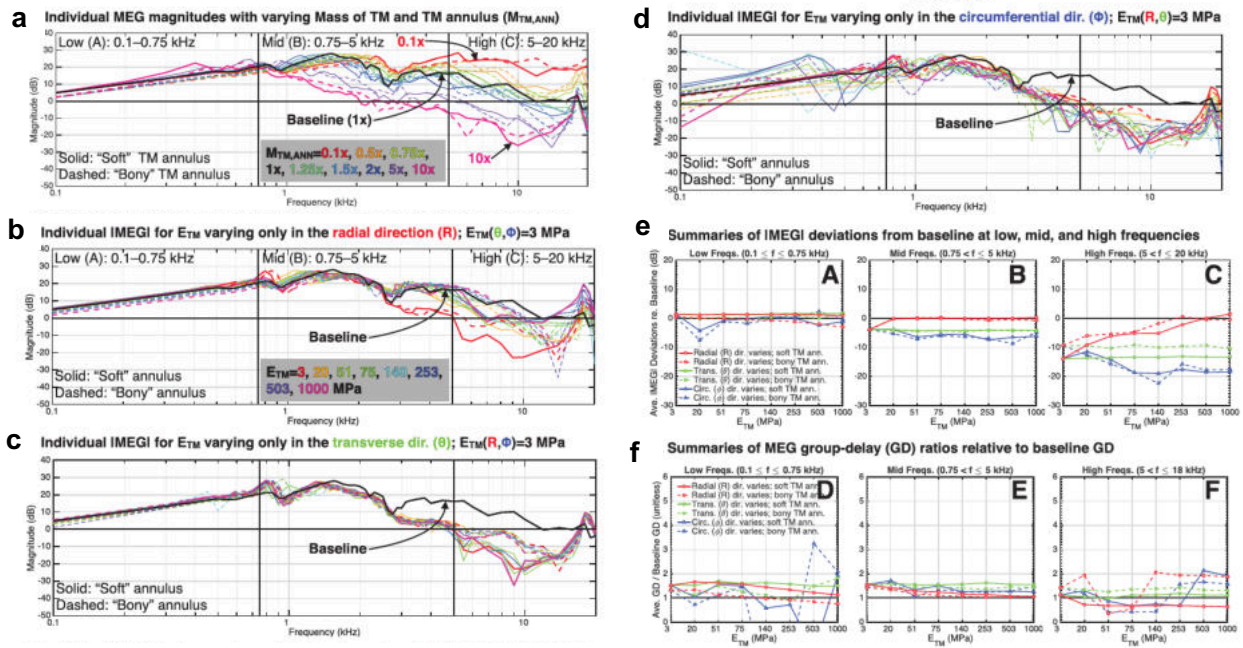
Figure 2.21. Investigating the importance of radial, transverse, and circumferential stiffness to the TM using COMSOL. Solid lines indicate a soft TM annulus and dashed lines indicate a bony TM annulus. (a) Individual middle ear gain (MEG) magnitude as the mass of the TM and TM annulus varies from 0.1 to 10 times the original value. (b-d) Individual MEG responses as E_{TM} increases in one direction at a time, from 3 to 1000 MPa. (a) Impact of changing radial stiffness, $E_{TM}(R)$. (c) Impact of changing transverse stiffness, $E_{TM}(\Phi)$. (d) Impact of changing circumferential stiffness, $E_{TM}(\theta)$. (e) Deviations in MEG from baseline for all 3 stiffness direction changes. (f) Deviations in MEG group-delay from baseline for all 3 stiffness direction changes [7].

2.4   Tympanic Membrane Damage and Repair

2.4.1   Tympanic Membrane Perforations

The TM can become damaged by several mechanisms. There are an estimated 30 million TM perforations worldwide each year, with approximately 3.86 million of these patients diagnosed in the US. TM perforations can range in size from a small hole (less than 2 mm) to total loss of the TM tissue (8 – 10 mm). A comparison between a healthy and perforated TM is shown in **Figure 2.22**. TM perforations are generally classified by size, and a grading scale has been introduced to help standardize clinical assessment and measure outcomes following surgery: Grade 1 (0 – 25%), Grade II (26 – 50%), Grade III (51 – 75%), and Grade III (76 – 100%) [54].
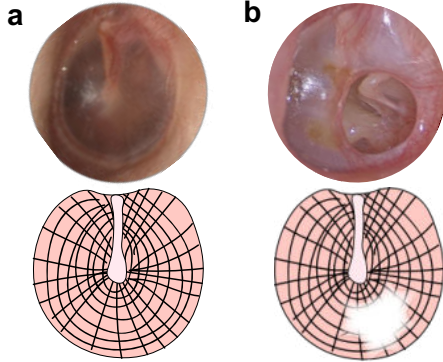
Figure 2.22. Structure of the normal and perforated TM. (a) An endoscopic image of an intact human TM and representation of its circumferential and radial collagen architecture. (b) An endoscopic image of a perforated human TM and representation of its damaged circumferential and radial collagen architecture.

The impact of TM perforations on proper sound conduction is vital. Hence, the U.S. military prohibits people whose TMs were perforated within the past 120 days from enlisting [55,56]. In addition to hearing loss, TM perforations create an opening to the middle ear space, through which environmental water, pollutants, and pathogens can enter. Infections can spread to surrounding tissues, resulting in complications such as otitis media, sensorineural hearing loss, vestibular dysfunction, acute mastoiditis, subperiosteal abscess, intracranial abscess, meningitis, and facial nerve palsy [57]. These complications lead to a significant healthcare burden each year.

Reasons for TM perforations include both pathological conditions and traumatic events. The most common reason for TM perforations is otitis media (OM), also known as middle ear infections (**Figure 2.23**). OM is a group of inflammatory diseases of the middle ear caused by viruses or bacteria. Two major types are acute otitis media (AOM) and otitis media with effusion (OME). AOM has a rapid onset, causing acute, unilateral ear pain and ipsilateral hearing loss. OME is a longer-term, persistent infection that is often affiliated with Eustachian tube dysfunction. Fluid accumulates within
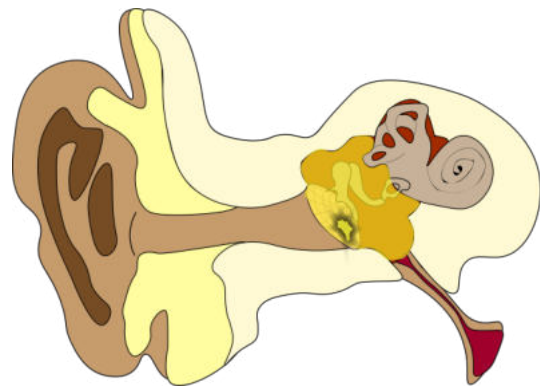
Figure 2.23. Otitis media with effusion causes a buildup of fluid in the middle ear space, as shown in yellow. TM perforations can form when this fluid pressure builds up significantly to exit via the TM, particularly in cases of eustachian tube dysfunction.

the middle ear space increasing the impedance of the middle ear and resulting in a moderate conductive hearing loss. In OME, a dysfunctional Eustachian tube results in persistent middle ear flud. This condition

can lead to a thickening of the middle ear mucosa, causing hearing loss and mucosal polyps. In chronic suppurative otitis media (CSOM), increased static pressure behind the TM from infection results in an acute TM ruptures to relieve this pressure, leading to a TM perforation with otorrhea. The WHO estimates that between 65 and 330 million individuals suffer from CSOM, and approximately 50% of these patients suffer from moderate to severe hearing impairment [58]. In 2020, CSOM is estimated to result in more than 25,000 deaths worldwide each year due to complications [58].

Many patients, particularly children, are treated for recurrent AOM or OME via the insertion of tympanostomy tubes (TTs), or ear tubes (**Figure 2.24**). TTs are placed across the TM by making a myringotomy (surgically created perforation in the TM) and placing a tube across the TM to 'ventilate' the middle ear into the ear canal. Such a procedures bypasses a dysfunctional Eustachian tube and is an important method of treating recurrent AOM and OME in children and adults. TT placement is such a prevalent procedure, with over 667,000 children under age 15 receiving tubes annually in the US alone and
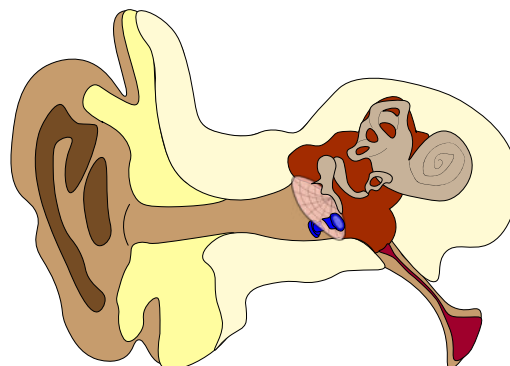
Figure 2.24. Tympanostomy tube (TT) placement in the TM. TTs, frequently made from silicone and fluoroplastics, are placed in the TM to ventilate the middle ear space. These often large and bulky tubes can cause chronic perforation following natural extrusion or removal.

accounting for more than 20% of ambulatory surgery in this age group [59]. These tubes are intended primarily for pressure equalization between the middle ear and the environment. However, many of these are made from materials, e.g. silicone and fluoroplastic, that present as a foreign body in the TM, causing gradual extrusion via the growth of keratincoytes on the lateral, epidermal side of the TM. Additionally, biofilms may coat the TT resulting in otorrhea. Approximately 21.4% of patients with TT experience otorrhea at least once [60,61]. While TTs typically fall out and the myringotomy heals, a significant subset of patients who have received TT will experience persistent tympanic membrane perforation. A study of 2,604 ears with tympanostomy tube insertion found that permanent TM perforations occurred in 3.06% of the ears, with a greater incidence in children younger than 5 years [62]. Thus, the high prevalence of TT placement makes the procedure a major contributor to chronic TM perforations.

A final major pathological cause for TM perforations is the development of cholesteatoma - a noncancerous benign growth of keratinizing squamous epithelial cells (**Figure 2.25**). Patients with prior TM perforations that are not repaired may develop cholesteatoma when skin cells from the lateral surface of the TM or the ear canal transverse the perforation. As keratinizing epithelium desquamates constantly, the buildup of desquamated skin within the middle ear results in pressure necrosis of bone, including the ossicles. Cholesteatoma may also result from
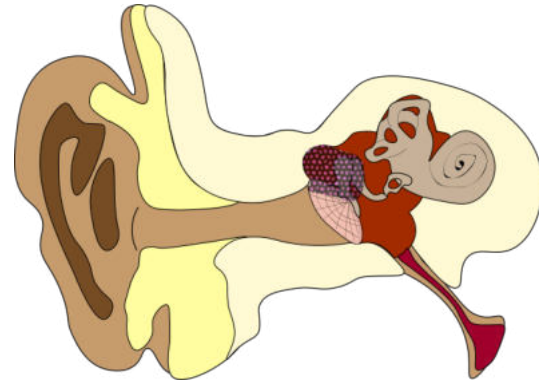
Figure 2.25. Cholesteatoma growth on the TM. A noncancerous benign growth of keratinizing squamous epithelial cells growing on the TM surface requires removal of the affected tissue via mastoidectomy followed by reconstruction of the TM via tympanoplasty.

retractions of the TM due to eustachian tube dysfunction. Regardless, cholesteatoma results from defects within a diseased or previously perforated TM. In terms of symptoms, pain and hearing loss is common, as the mass of the TM is drastically increased and the motion of the ossicles can be prohibited [63]. Otorrhea, dizziness and facial paresis are also possible complications of cholesteatoma. There are approximately 9.2 new cases of cholesteatoma each year per 100,000 people, as determined by a study of patients in northern Europe [64]. Often, the only treatment for cholesteatoma is surgical intervention. This usually involves a mastoidectomy to remove the diseased tissue from the bone, followed by reconstruction of the TM.

Traumautic injury is another major cause of TM perforations. Trauma can include blast injuries, barotrauma, and other injuries, such as head trauma and foreign objects being inserted into the EAC. Blasts are explosive detonations that produce transient shock waves that travel faster than the speed of sound [65]. Often, blasts produce a high-amplitude pressure wave, which can cause a sudden and large pressure gradient between the environment and the middle ear (**Figure 2.26**). Thus, the auditory system is highly sensitive to these pressures and is therefore frequently damaged by blast exposure [66]. The hearing loss affiliated with blast exposure is especially relevant to warfighters, who must remain fully aware of their environments and able to effectively to communicate. TM perforations are one of the most common primary blast injuries, with researchers reporting it as the second highest blast-related ear injury among 3,981 warfighters injuried while deployed for Operation Iraqi Freedom between 2004 and 2008 [67]. Additionally,

29

the researchers found that TM perforation was the strongest predictor of hearing loss and tinnitus one year from the blast injury. Ritenour *et al.* determined that of 436 blast-injured patients admitted to the USAIR Burn Center or Brooke Army Medical Center following injury in Afghanistan or Iraq, 16% had TM rupture [68]. They found that 40% of the TM perforations encompassed 50% or more of the TM (Grade III and IV perforations) [68].

Civilians can also suffer from TM perforations. One of the advisors for this thesis, Aaron Remenschneider, MD, MPH, cared for patients following the 2013 Boston Marathon Bombing. Inspired by this experience, he continued to study and monitor these patients. He found that 90% of patients hospitalized with blast injury symptoms sustained a TM perforation, making it the most common injury sustained as a result of this event [69]. In these patients, spontaneous healing was only observed in 38% of

Figure 2.26. Effect of blast waves on the TM. A high-amplitude pressure wave causes a large pressure gradient between the environment and middle ear space, often rupturing the TM.

cases [69]. For civilians, blast exposure is not limited to active combat zones and terrorist events; blast pressure waves can also occur from workplace and recreational accidents, such as fireworks.

Traumatic TM perforations can also form from sudden pressure changes, in which the middle ear does not have time to equalize pressure via the Eustachian tubes. Barotrauma (**Figure 2.27**) may result from activities including flying, skydiving, and diving can result in a high pressure differential between the environment and middle ear space. There is no agreed-upon pressure required to rupture the TM; however, many otolaryngolists believe that 14.7 psi, or 1 ATM of hydrostatic pressure is generally required, although TM perforations have occurred at lower

Figure 2.27. Effect of barotrauma on the TM. A large pressure gradient between the environment and middle ear space, such as by diving, can rupture the TM.

pressure changes [70]. When entering environments of lower atmostphereic pressure, such as during an

airplane flight, a vacuum forms in the middle ear space, and there is an increase in blood flow through the vasculature of the TM and surrounding tissues. These enlarged blood vessels can secrete serum, causing effusion. Further decreases in pressure can also cause rupture and bleeding from the TM or middle ear space. When entering environments of higher pressure, such as diving, excess pressure is transmitted to the round window and perilymph fluid in the cochlea. Thus, round window injury and perilymph fistula are often also affiliated with middle ear barotrauma and TM rupture [70]. In this serious conduction, perilymph can drain into the middle ear space, causing hearing loss, tinnituts, and vertigo. Thus, easily-observed TM perforations following these activities can indicate less-obvious inner ear damage.

The final major cause of TM perforations is through other traumatic events, such as foreign objects being inserted in the EAC (**Figure 2.28**). This commonly includes cotton swabs and other instruments used for cerumen removal. A study using NHS England hospital data showed that 85.9% of the 17,325 foreign bodies removed from the auditory canal between 2010 and 2016 were in children, with those aged 1 to 4 at the greatest risk [71]. Fortunately, a study
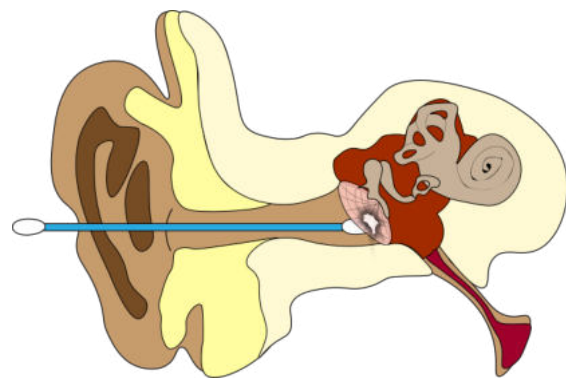
Figure 2.28. Effect of trauma on the TM. Foreign objects, such as cotton swabs, can rupture the TM.

of 54 patients with cotton swab induced TM perforations found that only 4 patients required surgical repair, while a majority had spontaneous healing over an average time of 1.75 months to perforation closure [72]. Workplace injuries have also been reported to cause TM perforations, including slag injuries in welders. In one case, a metalworker was exposed to slag entering his ear canal which burned the skin of his external auditory meatus, perforated his TM, and implanted around the ossicles [73]. Other traumatic injuries that do not cause direct contact to the TM can also cause perforations. A study of 53 patients aged 8 to 71 with traumatic perforations demonstrated that a majority of TM perforations were caused by domestic assault, such as slap injuries, (28.3%), self-inflicted/accidental injuries (20.8%), and road traffic accidents (18.9%) [74]. Of these patients, the median perforation size was 33.0% of the surface area of the TM, with only 34.4% caused by injuries where the TM was directly penetrated. Thus, any sudden change in air pressure in the ear canal can result in TM perforation. Often, TM perforations resulting from traumatic injuries are

associated with other injuries, particularly those related to the cochlea and vestibular system. However, a component of hearing loss resulting from traumatic injuries and blast injuries can often be attributed to a perforation. Audiometric measures looking at ABG, or the difference in air conduction and bone conduction thresholds as described previously, can be used as a measure of conductive hearing loss to decouple any sensorineural hearing loss effects to the cochlea.

2.4.2 Tympanic Membrane Perforation Effects on Hearing

TM perforations affect hearing because they disrupt the harmonic motion of the TM. Sound waves that normally would displace the TM due to the pressure difference across an intact TM, instead pass through the perforation and do not set the TM into motion. This reduction in sound pressure to mechanical vibration affects the amplitude of vibration of the ossicles and reduces the intensity of sound pressure that reaches the cochlea. Voss *et al.* investigated sound transmssion through perforated human cadaveric ears at low frequencies [75]. They showed that the dominant mechanism for hearing loss due to TM perforations is reduction in pressure differential across the TM. They also demonstrated a positive relationship between perforation size and degree of transmission loss. The losses in middle ear gain at low frequencies are primarily a function of the loss of pressure differential across the TM. Thus, the effects of TM perforations can be largely represented by the path for a volume of air to flow from the EAC to the middle ear cavity.

The extent of hearing loss suffered by those with TM perforations depends upon many factors, Overall, the single most important factor in hearing loss imparted by a TM perforation is the size of the perforation. Voss *et al.* were able to show in cadaveric specimens that TM perforations show frequency-dependent losses, whereby losses are largest at low frequencies, and this loss increases as perforation size increases from 0.5 – 5.0 mm in diameter. Location of perforation within the TM was not found to affect the degree of transimssion loss. Additionally, in human subjects Mehta *et al.* showed the larger the perforation surface area, the greater the air-bone gap is on average [76] (**Figure 2.29**). As previously described, this gap represents the difference in hearing between air conduction through the middle ear and bone conduction through the skull. Thus, conductive hearing loss caused by damage to the TM can be decoupled from any sensorineural hearing loss caused by damage to the inner ear. Similarly, a human subject study by Pannu *et al.* in 2011 categorized 100 patients by surface area of their TM perforation [77]. Patients in group I, consisting of those with the smallest perforations (0 – 9 mm^2), experienced a mean

hearing loss of only 31.43 ± 11.59 dB at 250 Hz and 19.91 ± 11.54 dB at 4000 Hz. Meanwhile, in group II with medium-sized perforations (9 – 30 mm^2), mean hearing loss increased to 39.88 ± 11.43 dB at 250 Hz and 28.05 ± 10.50 dB at 4000 Hz. Finally, those with large perforations in group III (>30 mm^2) experienced the highest extent of hearing loss at both high and low frequencies. These patients experienced a mean hearing loss of 55.22 ± 7.15 dB at 250 Hz and 32.61 ± 6.01 dB at 4000 Hz (p < 0.001 between all groups). A study by Lerut *et al.* in 2012 found a similar correlation between TM perforation size and hearing loss [78]. As the TM perforation size increases, the mean ABG across frequencies increases linearly. The authors also studied the impact of perforation sizes on specific frequencies. Specifically, they compared the impact of perforations on ABG at 500, 1000, 2000, and 4000 Hz [78] (**Figure 2.30**). 2000 Hz was the least affected frequency across all perforation sizes studied. Above and below 2000 Hz, they observed a consistent inverted V-shape in audiograms, with worse hearing at lower and higher frequencies.
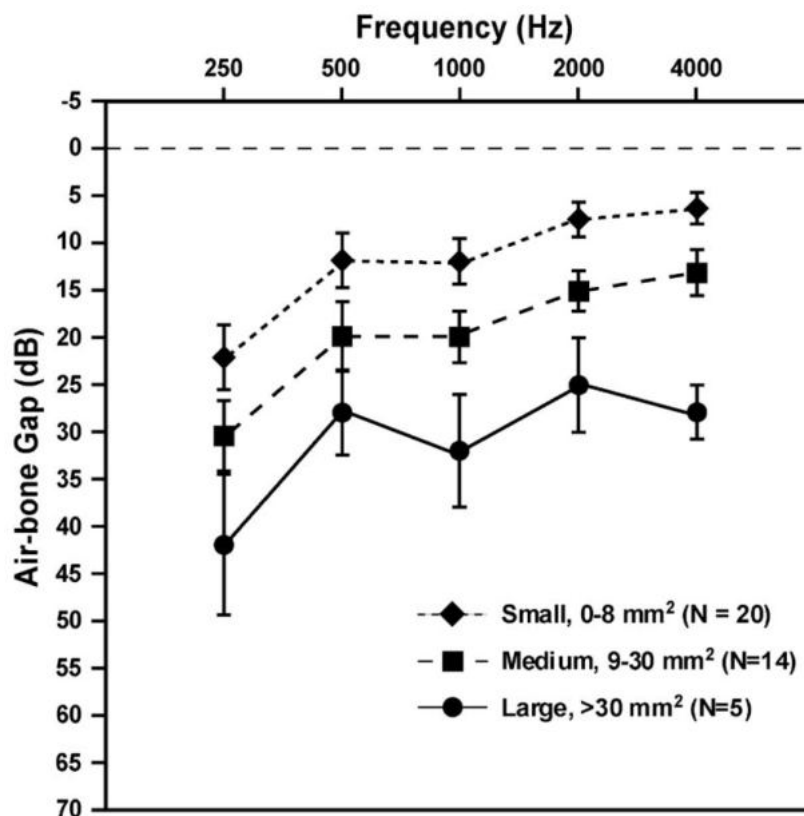
Figure 2.29. TM perforations lead to conductive hearing loss. Effects of area of perforation in patients with a large middle ear volume. Areas of perforations are in square millimeters. Error bars indicate standard error of the mean [76].
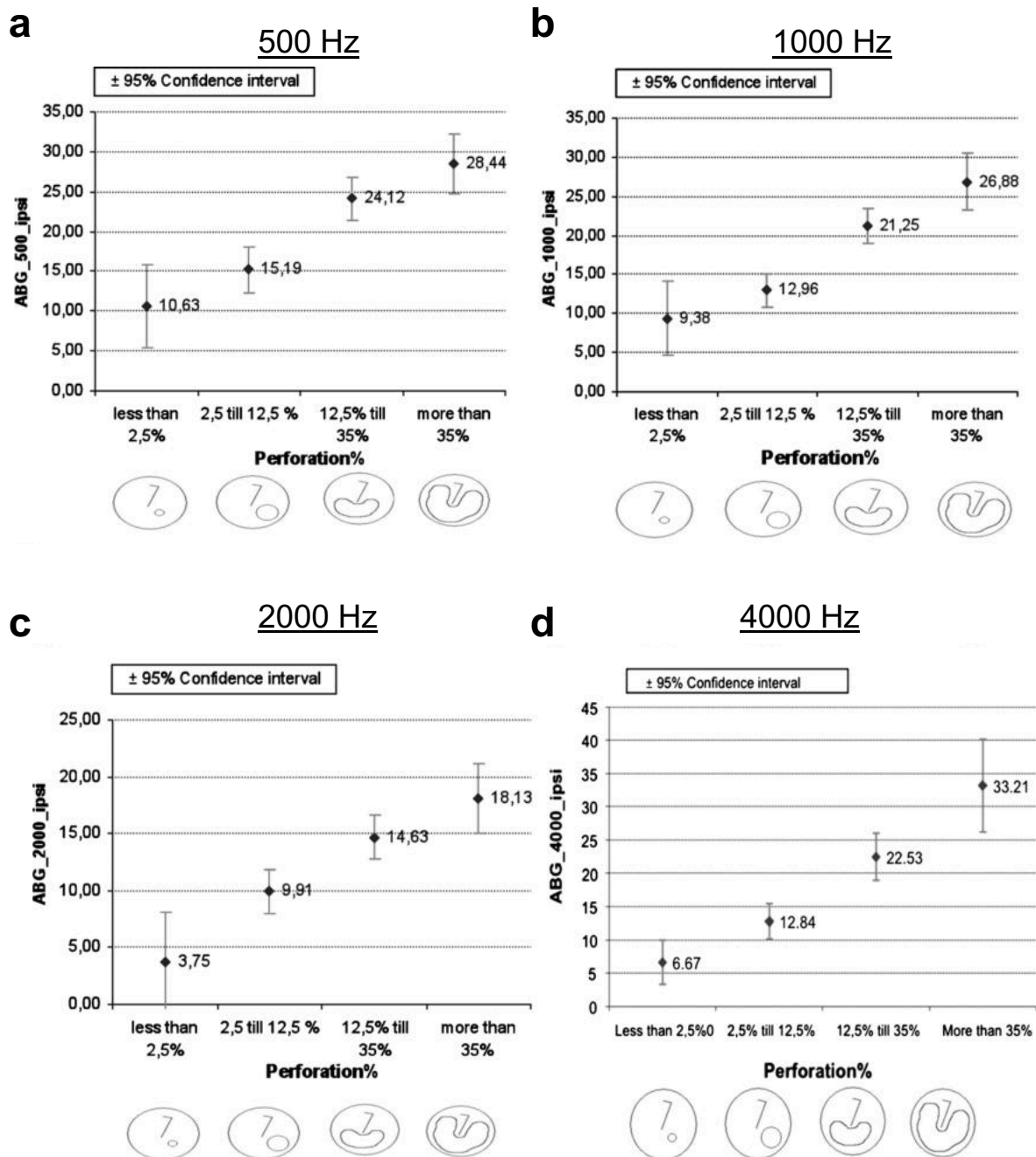
Figure 2.30. Relationship between TM perforation size and hearing loss for each frequency. (a) The ABG in decibels for 500 Hz for every size category, with a 95% CI. (b) ABG for 1000 Hz for every size category, with a 95% CI. (c) ABG for 2000 Hz for every size category, with a 95% CI. (d) ABG for 4000 Hz for every size category, with a 95% CI [78].

A potential reason for conductive hearing at 2000 Hz being most unaffected by TM perforation is that 2000 Hz is the dominant resonant frequency of the middle ear, causing maximal lever ratio and the ossicles. Guo *et al.* found that the lever ratio of the ossicular chain, determined using laser Doppler

vibrometry is maximized at around 2200 Hz [79], and Stasche *et al.* found that the highest degree of umbo displacement occurs at 2000 Hz [80]. Thus, the ability of the middle ear to transmit sound at this frequency is enhanced by the resonance of the ossicles, rather than relying exclusively on TM vibration. Interestingly, this frequency range is also important for speech perception. Hornsby & Ricketts studied the effect of hearing loss at various frequencies (250, 500, 1000, 1500, 2000, 3000, 4000, 6000, and 8000 Hz) on speech understanding by selectively filtering these frequencies [81]. The authors assessed sentence recognition using the connected speech test (CST), which uses everyday connected speech passages whereby higher scores indicate better recognition of 100 key words. They found that speech understanding scores were most affected by filters applied at frequencies at around 2000 Hz [81] (**Figure 2.31**). Thus, it is plausible that speech has evolved to be focused on producing frequencies around 2000 Hz for best transmission through the middle ear.
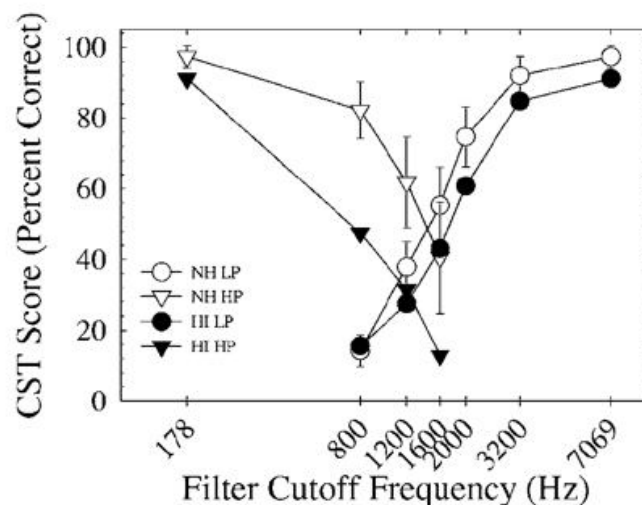
Figure 2.31. Average CST scores for NH and HI participants as a function of low- and high-pass filter cutoff frequency. The filled and unfilled symbols show scores for the hearing impairment (HI) and normal hearing (NH) participants, respectively, for low-pass (LP) and high-pass (HP) filtered sentences. The circles and triangles represent scores for low- and high-pass filtering, respectively. Error bars show 1 standard deviation around the NH means [81].

One anatomical influence on hearing loss observed by both Pannu *et al.* and Leirut *et al.* is the involvement of the malleus during TM rupture. Pannu *et al.* found that patients with the malleolar damage during TM rupture had statistically significant higher hearing loss at an average of 43.02 ± 9.70 dB across all measured frequencies, in contrast to those without any malleolar damage at an average of 28.25 ± 10.90 dB [77]. Leirut *et al.* also showed that malleolar involvement creates a worsening of hearing by approximately

5 – 6 dB (p < 0.0001) [78]. In addition to decreasing the efficiency of sound transfer between the TM and the cochlea, damage to the ossicular chain could affect the resonant frequency of the middle ear.

In the studies from both Pannu *et al.* and Leirut *et al.*, the location of the TM perforation on the TM surface (anterior vs. posterior) did not cause a significant difference in hearing outcomes [77, 78]. Pannu *et al.* found that perforations located exclusively in the anterior region caused a mean ABG at 250 Hz of 31.56 ± 13.77 dB, while perforations located exclusively in the posterior region caused a mean ABG of 36.29 ± 10.17 dB, with no statistically significant difference between the two groups [77]. Similarly, Leirut *et al.* separated perforations into anterior superior, posterior superior, anterior inferior, and posterior inferior quadrants. They found no statistically significant difference between mean ABG in perforations depending on the quadrant of the TM perforated, with the mean ABG ranging from 19 – 23 dB in all regions [78] (**Figure 2.32**). Therefore, while perforation size plays a role in the amount of hearing loss encountered following TM perforation, all areas of the TM appear to be equally affected.

Anterior Superior Perforation

Incidence: 61.1 %
Mean ABG 20.67dB

Posterior Superior Perforation

Incidence: 51.2 %
Mean ABG 19.4dB

Anterior Inferior Perforation

Incidence: 88.5 %
Mean ABG 19.2dB

Posterior Inferior Perforation

Incidence: 81.5 %
Mean ABG 22.1dB
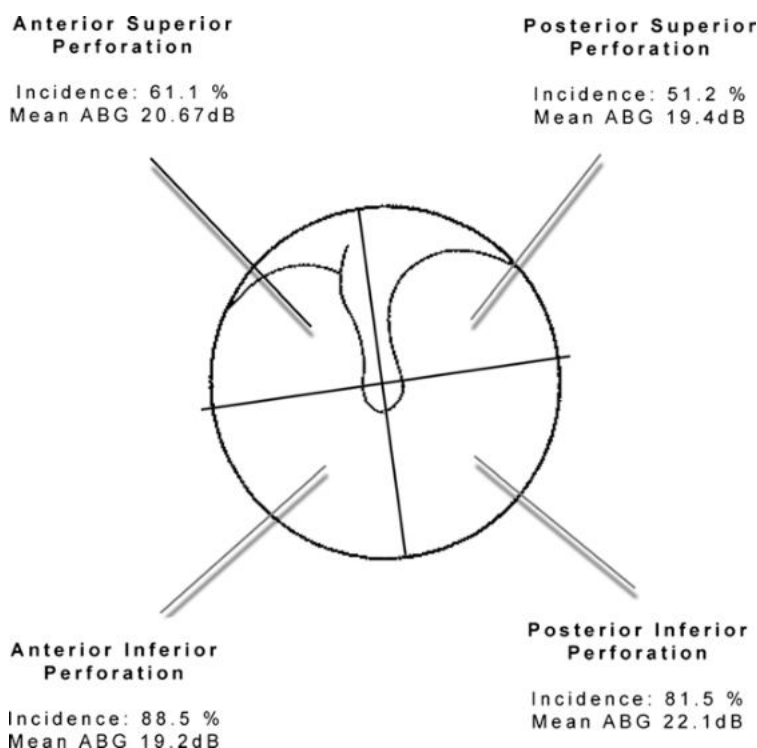
Figure 2.32. Statistical analysis revealing no significant difference between the conductive hearing loss at different locations of the perforation. The diagram shows the incidence of a certain quadrant being involved, whenever the tympanic membrane in general is perforated. This can be restricted to one quadrant or involve several quadrants [78].

Although the location of a TM perforation has not been found to affect hearing loss, the duration of time through which a patient has a TM perforation was found to affect hearing loss resulting from TM perforation, with patients having a persistent TM perforation for > 5 years experiencing significantly greater hearing loss than those who have had a TM perforation for < 1 year or 1 – 5 years [77]. This could be explained by larger perforations persisting longer without treatment, as this was not controlled for in the comparison. Additionally, the longer a perforation exists, there can be mucosal changes to the middle ear, leading to tympanosclerosis, and eventually, conductive hearing loss [82]. Prolonged exposure of the middle ear space to the environment can also lead to pathogen exposure, leading to otitis media. Otitis media has been shown to contribute to cochlear losses and therefore sensorineural hearing loss [83,84,85]. Thus, the longer that a TM perforation is left open and untreated, the risk for further hearing loss is increased. Hence, it is crucial to for TM perforations to close as soon as possible to prevent additional hearing loss.

2.4.3   Spontaneous Healing of the Tympanic Membrane

Restoration of the intact TM is crucial for sound conduction and maintaining a robust barrier between the middle ear space and environment. Indeed, permanent perforations can be detrimental to quality of life and can result in other morbidities. Fortunately, the TM does undergo a natural healing process following perforation. TM perforation repair is a multi-stage process involving a variety of cell types over approximately 7 – 10 days. Importantly, as the TM is located at an air-air interface, cells involved in repairing TM perforations must bridge an air gap with no underlying substrate on which to migrate [86]. Additionally, unlike other epithelial tissues located at fluid interfaces, the influx of nutrients and growth factors such as basic fibroblast growth factor (bFGF) [87] and platelet-derived growth factor (PDGF) [88] is lower in the TM. Clymer *et al.* found that epidermal growth factor (EGF) and fibroblast growth factor (FGF) both stimulate the migration of fibroblasts and thus wound healing, whereas keratinocyte growth factor (KGF) does not affect the rate of wound healing but does result in a more organized wound repair process [89]. The remodeling process in the pars tensa is generally conducted in three stages, as demonstrated below: (1) inflammatory stage, (2) proliferative stage, and (3) remodeling stage [90] (**Figure 2.33**). Overall, TM repair occurs in a similar manner to other wound sites, with first an accumulation of vascularized connective tissue followed by epithelial proliferation and migration [91].
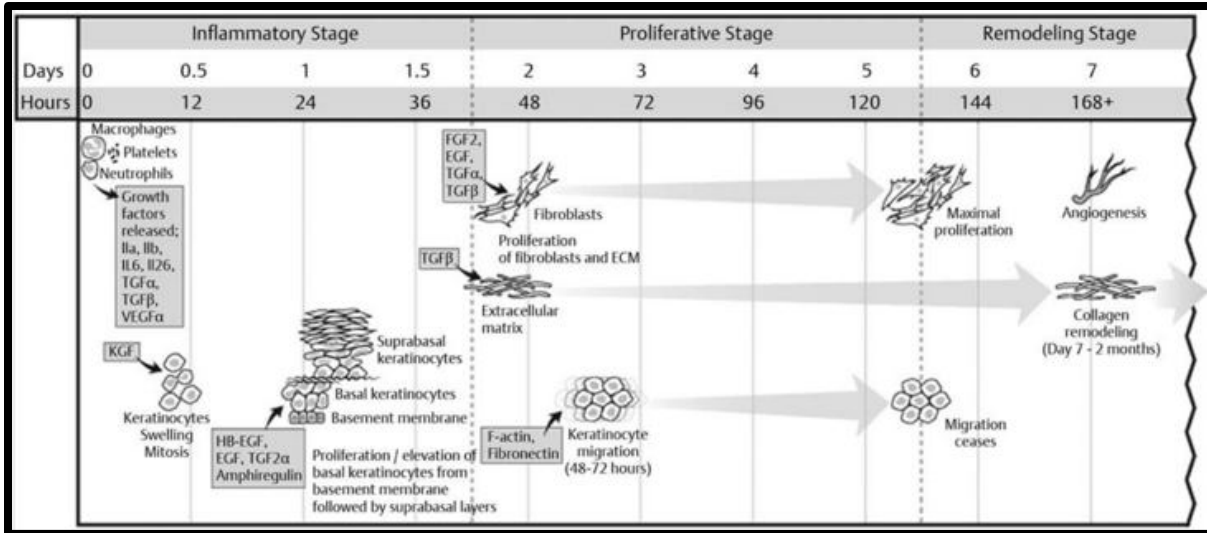
Figure 2.33. Summary of the major events leading to perforation closure in the TM. Wound healing in the tympanic membrane is divided into three stages, with keratinocyte migration beginning as early as 48 hours following perforation [90].

During the first 48 h after a TM is ruptured, an acute inflammatory response occurs, termed the "inflammatory stage." A combination of interstitial fluid, lymph fluid, and blood accumulates at the edges of the perforation from the vascular network within the TM, while increased vascularity of the TM can be observed, particularly along the malleus and annulus [90]. A crust layer forms temporary support for ingrowing cells, and mitotic activity can be histologically observed as cells begin to proliferate [92].

The second stage, termed the "proliferative stage", occurs from approximately day 2 up to day 4 – 7 following TM injury. In this stage, the epithelial tissue begins to migrate, elevating from the lamina propria containing connective tissue and causing the wound edge to advance together. The epidermal layer begins to proliferate, particularly at the umbo where the TM connects to the malleus [93]. This process begins with the migration of basal keratinocytes, followed by the migration of suprabasal keratinocytes [94]. Then, granulation tissue begins to form under the keratinizing squamous epithelium. This granulation tissue is important for perforation closure. Without it, there is no support for the proliferating squamous epithelium, and the epithelium shows hyperplasia (enlargement by cell proliferation) and resultant thickening up to 3 – 4 times thicker than the normal TM [90]; however, it does not close the perforation. After between 4 – 7 days, the perforation is closed at a superficial level [95,96], often without any connective tissue in the lamina propria layer [97], completing this stage of remodeling.

38

The third stage of TM perforation closure, termed the "remodeling stage" occurs after the perforation has closed, as the tissue begins to reform its trilaminar structure. Over the next 7 days, the thickness of the epithelium decreases, as an ingrowth of fibroblasts and deposition of connective tissue from the lamina propria layer occurs. This process of a fibrous connective tissue layer forming after the epidermis is in contrast to most wound healing processes, whereby epidermal cells migrate across a connective tissue substrate [90]. Spandow *et al.* found during a structural study of TM remodeling that the lamina propria layer also becomes thicker than normal, containing a disorganized, fibrous collagen network with sclerotic plaques [98]. In approximately half of specimens studied, the epithelial junction ended at the perforation border, and at this junction, keratinocytes were covered by a thick layer of keratin protruding centripetally to bridge the perforation. Unlike the inner mucosal epithelium of the normal TM that contains unciliated mucosal cells, that of remodeled TM regions contain abundant ciliae, similar to the mucosal epithelium lining the middle ear space and supporting the theory that these mucosal cells can differentiate into ciliated cells in inflammatory conditions. It may take up to 2 months for the TM to return to its normal thickness, and there is visible scar tissue for up to 6 months following TM perforation [95]. Although a perforation may close, the fibrous lamina layer may not always reform, as has been seen in rat TMs [99,100]. Importantly, de Araújo *et al.* showed that the mean thickness of the lamina propria layer of the TM in rats decreased from 46.1 µm for normal, healthy TMs down to 12.5 µm following 14 days of spontaneous healing and complete perforation closure [100]. Additionally, they noted a lower presence of fibroblasts in this layer [100]. Thin neomembranes may easily reperforate or retract, creating a new perforation. Additionally, the mechanical properties of this remodeled tissue will not have the same properties as the original TM due to the lack of arranged collagen fibers. Thus, even if spontaneous healing occurs, outcomes may not be ideal.

Perforations to the pars flaccida of the TM are similar to that of the pars tensa; however, they generally result in a greater amount of bleeding and exudation of interstitial fluid and lymph fluid. Proliferation of the fibrous lamina propria occurs as soon as the first day. Additionally, proliferation of the epithelial is not seen, except near the annulus [101]. Perforations in the pars flaccida often cause epidermal hyperplasia in the pars tensa [101], which refers to an increase in the number of cells in the epidermis, often within the stratum spinosum layer.

Clinical studies conducted across the world have determined that the spontaneous TM closure rate in humans is between 80% and 97% overall, depending upon etiology [102-108]. One study examining TM perforations in 760 perforation cases covering more than 500 texts found a spontaneous healing rate of 78.7% of those TM perforations diagnosed within 14 days of injury [109]. However, the rate of TM perforation closure without intervention varies widely based on the size of the perforation, the location of the perforation, the mechanism through which the TM is injured, and other underlying patient conditions.

Perforation size is a major indication of whether or not the perforation will heal, as ingrowing tissue has a larger gap to bridge. Orji and Agu found that comparing "small" perforations (< 50% of the TM) with "large" perforations (≥ 50% of the TM), while healing rates of the 44 "small" perforations were around 86% by 8 weeks, healing rates of the 9 "large" perforations were significantly lower, with only 56% healing by 8 weeks [103] (**Figure 2.34**).
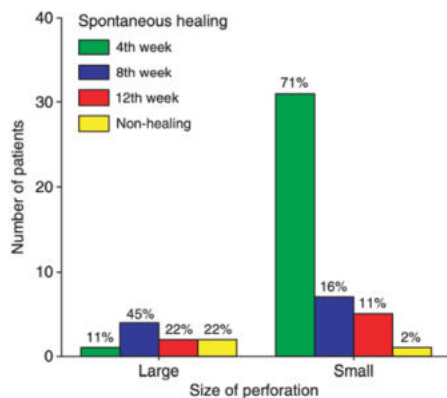
Figure 2.34. Spontaneous healing outcome at the follow-up re-evaluation for large versus small sized perforations. The first three columns indicate the number of perforated TM that healed at 4th, 8th and 12th week of injury respectively. The last column indicates the non-healed perforations by 12th week of injury [103].

Similarly, Lou *et al.* found that among 114 patients, those with small perforations (<12.5% of the pars tensa) healed at the highest rate, at 91%. Meanwhile, healing rates were only at 84% for medium perforations (12.5% – 25% of the pars tensa) and at 80% for large perforations (> 25% of the pars tensa) [104]. In the study, "small" and "medium" classifications cover Grade 1, while the "large" classification covers Grade 2, 3, and 4 perforations. Otoendoscopic images of the TM following healing show the differences in healing between TM perforation size classifications [104] (**Figure 2.35**). In 2012, Lou looked at larger Grade 3 and 4 perforations, determining that natural healing rates in 94 patients with large (>50% TM) are as low as 55% [110]. Jellinge *et al.* found that the time to perforation closure was also significantly different between perforation sizes, where TMs with Grade 1 and 2 perforations had significantly shorter closure times (median of 22.5 and 24 days) when compared to TMs with Grade 3 or larger perforations (median of 28.3

days) [108]. Orji and Agu found no significant difference in the rate of the spontaneous healing between the anterior and posterior TM perforations [103].

Small TM Perforation   **Large TM Perforation**
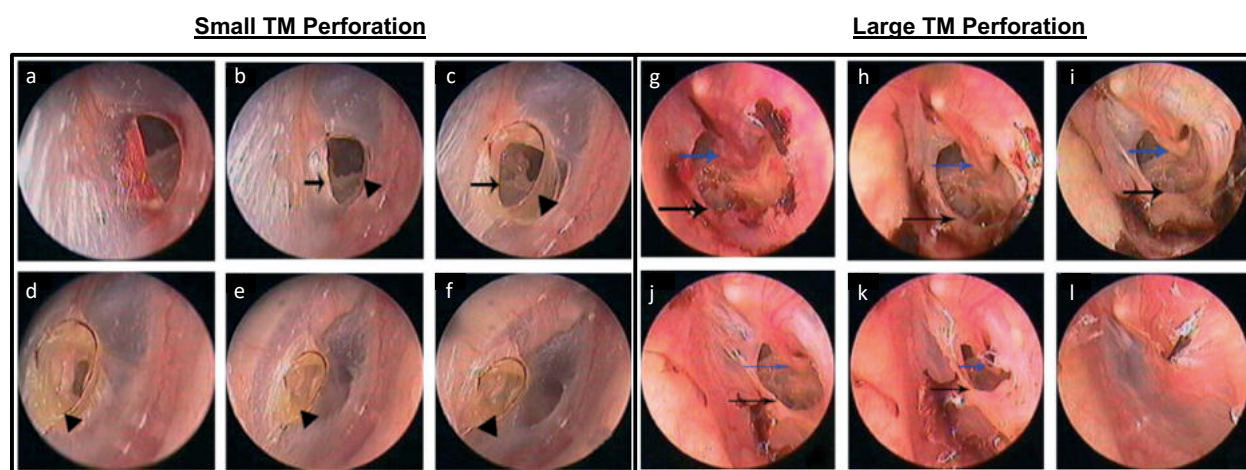
Figure 2.35. Otoendoscopic images of representative (a-f) small and (g-l) large-sized dry traumatically perforated TMs during the course of spontaneous healing. Small perforation at (a) 1 day, (b) 1 week, (c) 3 weeks, (d) 6 weeks, (e) 7 weeks, and (f) 8 weeks. Large perforation at (g) 1 day, (h) 1 week, (i) 2 weeks, (j) 3 weeks, (k) 4 weeks, and (l) 6 weeks [104].

In addition to perforation size, the condition of the perforation is important to healing outcomes. Lou *et al.* found that healing rates of "wet" TM perforations with discharge healed at a higher rate than "dry" perforations (95% vs. 85%) and had a shorter average healing time (16 days vs. 28 days) [106]. They found that granulation tissue formation and epithelial migration were different between these two groups. For "dry" perforations, the healing process began with the growth of a thin epithelial layer inward from the perforation edge followed by fibroplasia from the lamina propria layer, creating a yellow-brown crust comprising cell debris, keratin, and clotted fluids. By contrast, the closure of "wet" perforations began with the formation of granulation tissue from the perforation edge, which is then overlaid by epithelium without the formation of a yellow-brown crust. The morphology of the perforation was also seen to be important to healing outcomes. They found that while TM perforations with inverted edges healed at a greater extent and at a faster closure rate than those with everted edges (95% vs. 82% healed, 24 days vs. 27 days closure time), this difference was not statistically significant. However, TM perforations with everted skin edges can be at risk of cholesteatoma following spontaneous healing due to enhanced epithelial ingrowth, as has been seen in patients with TM perforations following OM and TT placement [111-114]. This phenomenon was first observed in 1889 by Habermann, whereby an ingrowth of stratified squamous epithelium was observed to ingrow

from the EAC into the middle ear following OM in children [115]. Thus, even acute TM perforations that spontaneously heal may eventually require tympanoplasty to replace the pathological TM tissue.

The cause of a TM perforation may affect the size and condition of the perforation, thus indirectly affecting closure rates. Larger perforations tend to be caused by traumatic and blast injuries than those from other aetiologies. However, controlling for these factors, perforation cause does not appear to significantly affect healing rates. Lou *et al.* found that complete perforation closure occurred in 88% of the 95 total patients with slap- or blow-related perforations, 75% of the 12 total patients with blast-related perforations, and 86% of the 7 patients with ball injury perforations [104]. Additionally, penetrating injuries wherein the TM contains shrapnel or other foreign debris have been found to lower TM perforation healing rates [74,103]. For example, among 2013 Boston Marathon bombing patients, spontaneous healing was only observed in 38% of cases [69].

The age of the patient is also shown to be correlated with healing rates of TM perforations, with younger patients faring better in terms of healing outcomes. TM perforations appear to be most prevalent in populations aged 10 – 30 years [77,108], representing active individuals who are at higher risk for infectious and traumatic TM perforations. The patients from Orji and Agu's contained an age range from 2 – 86 years [103]. The authors found a significant correlation between age and spontaneous healing rate, with TM perforations in younger patients aged 0-20 healing significantly faster than those in older patients >40 (61% vs. 20% perforation closure rate at 4 weeks) [103]. Other researchers have also demonstrated better healing ratio for patients under the age of 30 than for those above the age of 30 [116,117].

Growth factors are thought to play an important role in TM healing and remodeling. As a consequence, research groups have investigated the application of topical growth factors for the regeneration of the TM in animal models. These growth factors include EGF [118-122], bFGF/FGF-2 [123-127], KGF/FGF-7 [89], TGF-ß1 [128], and PDGF [88]. In particular, bFGF has been studied due to its importance in stimulating the proliferation and differential of endothelial cells, fibroblasts, and keratinocytes [129,130]. While some of these studies did demonstrate significantly improved perforation closure rates, many were based in animals with small TMs, such as rats [87,88,118,127,130] and guinea pigs [123-125], where perforations nearly always heal on their own due to the small overall size of the TM. Importantly, Mondain *et al.* and Vrabec *et al.* both found that the topical application of bFGF in rat models led to increased connective tissue and

lamina propria remodeling [123-125]; however, due to the small size of the rat TM at around 3 – 3.5 mm in diameter [131], it is challenging to create a chronic perforation that does not spontaneously heal, and as a result, it is hard to know if the remodeled TM was due to growth factor effect or spontaneous effect. Chinchillas are ideal animal models for studying TM perforation healing, as their TM is approximately 8.32 – 8.53 mm in diameter, corresponding to about 90% of the size of the human TM [132]. Unfortunately, the topical application of EGF in chinchilla models was not found to have a significant effect on TM healing, and in some cases promoted reperforation and cholesteatoma formation [120,122]. EGF is not used today in humans because of these critical findings.

Studies of topical growth factor application in humans are limited, and the results to date have not been in favor of the utility of topical growth factors. A study by Hakuba *et al.* in 2003 looked at the application of bFGF for closing TM perforations in 14 adult patients [133]. They used a piece of atelocollagen/silicone infused with either 0.1% bFGF solution (9 patients) or saline as a control (5 patients). The authors found complete closure of the TM perforations in both bFGF and control groups within 3.7 weeks. While trimming of the perforation edges prior to placement is to enable better growth factor absorption, excising the edges of a TM perforation, termed "rimming," creates a fresh, bleeding edge by removing a small part of the epithelium, allowing for reactivation of cells involved in TM remodeling [134]. Additionally, the added moisture imparted by the atelocollagen/silicone graft at the perforation edges likely improved healing rates. To further investigate the impact of bFGF on TM healing, a comprehensive, randomized phase 2 clinical trial on 54 patients sustaining chronic TM perforations for 3 or more months was conducted at Massachusetts Eye & Ear hospital by Santos *et al.* in 2020 [135]. Patients had their TM perforated rimmed and then received either bFGF (40 patients) or sterile water (14 patients) saturated into a gelatin sponge held in place by fibrin glue. Interestingly, there was a higher rate of TM perforation healing in the placebo group as compared to the experimental group with bFGF (71.4% vs. 57.5% healed), with no statistically significant difference in hearing outcomes. A human clinical study by Lee *et al.* in 1994 in investigating the impact of EGF found that EGF-healed TMs were histologically similar to normal TMs [121]. Additionally, Röösli *et al.* found that PDGF applied to the TM caused no significant change in healing rates compared to a placebo [136]. Thus, due to the lack of promising alternatives, many patients with chronic TM perforations must seek surgical intervention to restore the middle ear barrier and restore efficient sound conduction.

2.5   Repair of Chronic Tympanic Membrane Perforations

2.5.1   Surgical Procedures to Repair Chronic Tympanic Membrane Perforations

If a TM perforation has existed for more than 3 months without infection or drainage, it is unlikely to close by itself and is termed a chronic perforation [137,138]. Approximately 10 – 20% of TM perforations become chronic [139]. A surgical procedure, either tympanoplasty or myringoplasty, can be performed to graft TM perforations. These procedures recreate a robust barrier between the ear canal and middle ear and reestablishes sound transmission to the ossicular chain. The procedure involves placing a graft to repair the perforation and then stabilizing the graft with packing materials. Over time, native cell types proliferate and migrate onto the edges of the graft, enabling the graft to integrate with the remnant TM tissue and close the hole. In the current standard of care, an autologous (from the patient) tissue is harvested at the time of the procedure, typically temporalis fascia, skin, or cartilage. Fascia is most often used because it is a robust, collagenous tissue, similar to the TM. Harvesting of temporalis fascia requires the creation of an incision behind the ear to access the temporalis muscle (**Figure 2.36**). After harvesting, this tissue is laid flat and dessicated to enable better handling and placement of the graft [140].
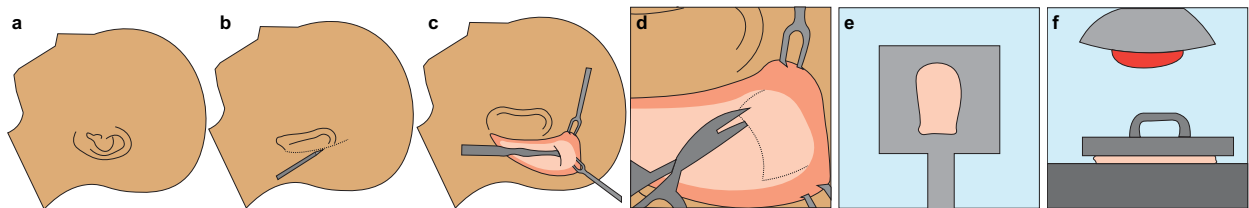
Figure 2.36. Harvesting of autologous tissue for TM graft material. (a) An incision is made behind the ear. (b) The temporalis muscle is exposed, and (c,d) a piece of fascia is excised from the surface. (e,f) The fascia is dried and pressed to obtain workable tissue. (image credit: Cindy Liu, Aaron Remenschneider, and Nicole Black).

Generally, myringoplasty refers to repair of the TM itself, while tympanoplasty addresses the TM along with other middle ear pathologies, such as cholesteatoma or ossicular chain damage. Tympanoplasty is classified into five major types: Type 1 involves repair of the TM alone, Type 2 involves repair of the TM and slight defects in the ossicles, Type 3 involves removal of the ossicles and replacing with a prosthesis, Type 4 involves a technique whereby the stapes footplate is exposed to sound and the round window is shielded with a cavum minor graft, and Type 5 involves grafting directly into the inner ear [141,142].

In a patch myringoplasty, the TM perforation is patched by a graft inserted through the ear canal. The perforation becomes temporarily plugged by the material. Since this procedure is frequently conducted in awake patients in the clinic, the graft used is often a piece of paper or gelatin rather than autologous tissue, which is quite invasive to harvest in an awake patient. Placed in an overlay approach, the graft sits against the lateral, keratinocyte epidermal layer of the TM. As this procedure can be performed in an awake patient in a clinic setting, it takes 5 – 10 minutes using an otoscope or endoscope. However, since migration of the mucosal epithelium on the medial side of the TM plays a large role in remodeling, the cells on this layer cannot access the lateral graft material to use as a scaffold for migration. Additionally, the currently available non-autologous materials generally do not integrate into the TM as well as harvested fascia, skin, or cartilage. Thus, perforation closure following patch myringoplasty is only useful in small perforations and maintains a high rate of failure.

For larger perforations, it is advantageous to harvest autologous tissue grafts and to access the medial surface of the TM for an underlay approach, such that the graft sits against the mucosal epithelium. As the surface of the TM is challenging to access, a tympanoplasty procedure is typically performed under general anesthesia with the aid of a microscope and/or an endoscope. Thus, an endaural incision (made through the ear canal to significantly widen it) or a postauricular incision (through the area behind the ear) are used. Both procedures lead to similar results for patients; however, the location and prevalence of scar tissue differs [143]. In an endaural incision, the ear canal skin is sectioned from the periosteum, and the auricle and conchal cartilage are pulled posteriorly to enable better access to the TM. Then, the TM is often cut and raised via a posterior tympanomeatal flap that is raised to enter the middle ear space (**Figure 2.37**). This approach generally gives a limited view of the middle ear. Thus, when a postauricular incision has already been made to harvest temporalis fascia, this approach is more common than endaural incision. In this technique, the same incision made behind the ear to harvest fascia can be used to access the middle ear space (**Figure 2.38**). Incisions in the ear canal from the posterior aspect of the auricle permit an improved anterior view of the TM and ossicular chain. This permits better visualization of the eustachian tube orifice, but limited view of the ossicular chain. Typically bony drilling is necessary to widen the ear canal to enable placement of the graft. In both approaches, the graft is supported by packing material placed inside the middle ear space, typically GelFoam® (Pfizer), which slowly dissolves in 2 – 3 months. Packing

material is also placed in the ear canal to hold the graft in place during healing for 1 – 2 weeks, upon whence it is removed. By 4 weeks post-operative, it can then be determined whether the graft has integrated and the tympanoplasty was successful.

Tympanoplasty is a relatively common surgical procedure. Each year, the number of tympanoplasty procedures performed is approximately 150,000 in the US, 424,400 in the EU, and 17,000 in Canada [144]. A study of 1000 adults by Kaftan *et al.* in Germany found that only 1 in 9 patients found to have chronic TM perforations decided to proceed with tympanoplasty [145]. This is partially due to the invasiveness of the procedure, which requires general anesthetic, a trip to the operating room (OR), and external incisions. In addition, the cost of the procedure may be a barrier for some patients. Tympanoplasty surgeries are not only inconvenient for patients but are also costly, at around $3,000-8,000 with surgeon, anesthesia, and facilities costs. As the procedure is often considered to be elective, out-of-pocket costs can be prohibitive. Thus, the current standard of care that consists of harvesting autologous tissue and placing via endaural or postauricular incisions under general anesthetic are not ideal. The availability of non-autologous grafts that can be placed in an underlay fashion without additional incisions would substantially increase access to tympanoplasty, healing TM perforations to prevent infection-related complications and allowing for restoration of sound conduction.
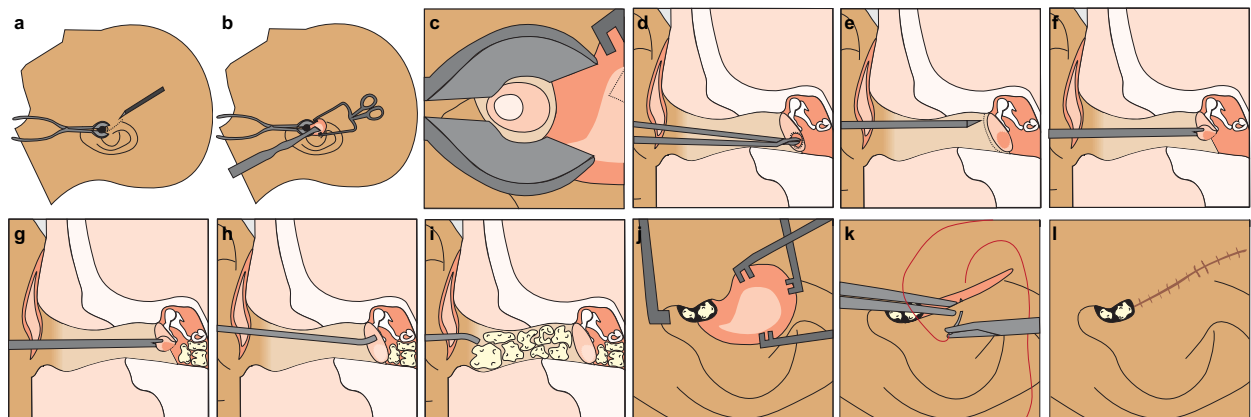
Figure 2.37. Endaural tympanoplasty approach. (a-c) Approaching the TM through an endaural incision, whereby the auricle and conchal cartilage are pulled posteriorly, and the helical and tragal cartilage are incised. (d-f) Elevation of the tympanomeatal flap. The perforation is prepared and the TM is lifted. (g-i) The graft is placed under the perforation and the TM is packed with Gelfoam® on the medial and lateral surfaces to keep it in place. (j-l) The incision is closed and sutured to heal. (image credit: Cindy Liu, Aaron Remenschneider, and Nicole Black).
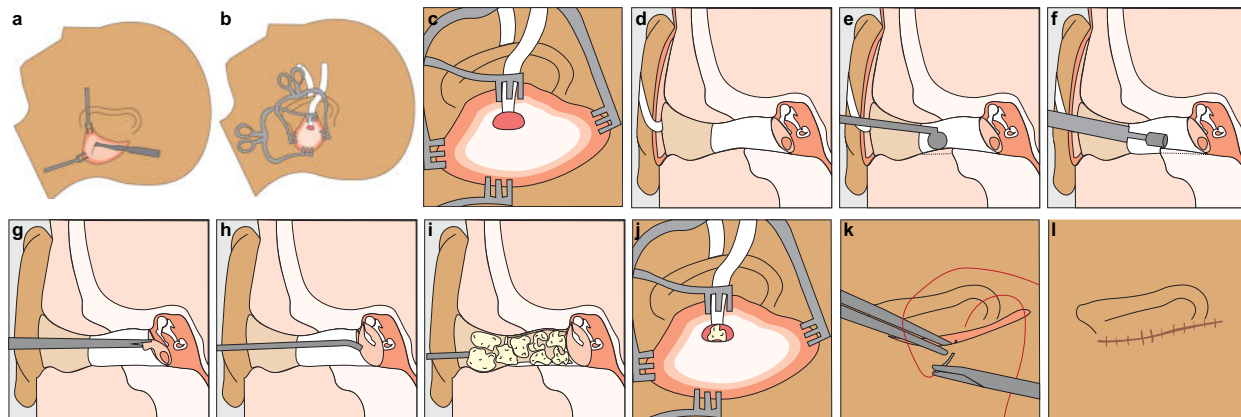
Figure 2.38. Postauricular tympanoplasty approach. (a-c) Approaching the TM through an postauricular incision, whereby the area behind the ear is incised to allow direct exposure of the anterior TM. (d-f) Cartilage and bone are removed from the external auditory canal (EAC) to increase visibility. (g-h) The tympanic membrane is removed, and the fascia graft is wrapped around the malleus. (i) The EAC skin is then replaced. (j) The EAC is packed with Gelfoam® and other packing materials on the lateral surface to keep it in place. (k-l) The incision is closed and sutured to heal. (image credit: Cindy Liu, Aaron Remenschneider, and Nicole Black).

The emerging field of endoscopic ear surgery could provide a means for the repair of chronic TM perforations. First described in 1990 by Thomassin *et al.* [146], endoscopic ear surgery allows ENT surgeons to view the TM through the EAC, enabling rapid access to intricate and precise structures [147]. Thus, endoscopic ear surgery, as compared to microscopic surgery enabled the avoidance of endaural vertical and postauricular incisions [148]. Thus, a transcanal approach is possible by elevating a tympanomeatal flap, providing views of the middle ear space. A retrospective study of 73 patients who underwent Type I tympanoplasty via conventional microscopic tympanoplasty (n = 48) or endoscopic tympanoplasty (n = 25) revealed that not only was the mean operating of microscopic tympanoplasty (88.9 ± 28.5 minutes) significantly longer than endoscopic tympanoplasty (68.2 ± 22.1 minutes), self-reported pain 1 day following surgery was significantly less in the group that underwent endoscopic tympanoplasty [148]. Furthermore, audiometric results including bone and air conduction thresholds and air-bone gap were not significantly different between the two groups [148]. Despite promising results from endoscopic ear surgery, the need to harvest autologous tissue via an incision typically requires the patient to undergo general anesthesia regardless. Thus, the development of non-autologous grafts may shift the field toward minimally invasive clinic-based procedures with only local anesthesia. Ultimately, this could expand access to tympanoplasty.

2.5.2 Outcomes from Autologous Tympanic Membrane Grafts

In addition to harvesting and placement challenges, autologous materials used as tympanoplasty grafts also lead to nonideal healing and hearing outcomes for patients. The success of any tympanoplasty procedure can be assessed in anatomical as well as functional terms. Anatomical success (healing outcomes) is defined as an intact graft with a dry ear, and functional success (hearing outcomes) is defined as an air-bone gap ≤20 dB after the procedure [149]. Healing success rates are reported to be between 78 – 93% [150-152], with high variability due to differences in healthcare settings. For hearing success rates, Faramarzi *et al.* reported that among 116 patients studied, the percentage of air-bone gap on audiometry ≤20 dB was 83.8% and 76% in the primary tympanoplasty and revision groups, respectively [150]. Often, poor healing and hearing outcomes lead to additional revision surgeries.

The quality of the graft is dependent upon the donor site tissue and skill of the surgeon, contributing to inconsistently harvested graft tissues and poor healing outcomes (**Figure 2.39a**). Graft defects and inconsistent mechanical properties can cause additional perforations in the material and retraction from the remnant TM tissue, requiring revision surgeries. Specifically, the lack of dimensional stability of fascia as it becomes repeatedly moistened and dried during the healing process may lead to residual perforations, especially in cases of large perforations [153]. Follow-up studies conducted on tympanoplasty patients of the Boston Marathon Bombings determined that 14% of patients required revision surgery at 1 year [69] and 44% required at least one additional revision surgery after 5 years [154]. As blast patients tended to have larger TM perforations, revision surgery can be more common among these patients than among those with TM perforations from other etiologies. In addition to differences in surgeon skill and the size and morphology of perforations, closure success rates are associated with a variety of demographic and clinical factors, including age, gender, the status of the middle ear mucosa, and the presence of other ear morbidities, such as tympanosclerosis (TM scar tissue) or chronic otitis media [155-157]. The material used can also affect healing outcomes. Cartilage grafts have been used to increase graft strength and stability [158]. They often offer a better ability to resist infection and pressure changes. Cabra *et al.* reported a tympanoplasty success rate of 82% in using cartilage grafts compared to a success rate of 64% using fascia grafts [159]. Overall, healing outcomes with current tympanoplasty graft materials are inadequate.

Hearing outcomes can be nonideal even in cases where the TM perforation has been successfully closed (**Figure 2.39b**). Autologous graft materials are often substantially thicker than the approximately 100 µm thin native TM, which adds significant mass to the healed TM, further affecting sound transmission [7]. Additionally, as previously discussed, the anisotropic circumferential and radial collagenous structure in the lamina propria is critical for the ability of the TM to conduct sound across a wide range of frequencies [5-7]. Trakimas *et al.* investigated the thickness and microstructure of autologous fascia tissue grafts in human TMs [16]. Temporal bone specimens from patients who underwent successful subtotal or total TM replacement were identified. The thickness and structure were compared to surgically prepared temporalis fascia as well as normal TMs. While the normal human TM specimens had an average thickness of 83.7 ± 42.4 µm, the fascia remodeled TMs were significantly thicker at 162.9 ± 71.9 µm, with no significant difference between the pre-implanted and post-implanted fascia thickness. Additionally, the fascia-reconstructed TMs in all 3 cases studied contained a thick, longitudinal fiber structure within the lamina propria [16] (**Figure 2.40a**) that was qualitatively similar to pre-implanted fascia and unlike the fibers arranged in a circumferential and radial structure that can be seen in the TM, as previously shown [16] (**Figure 2.3a**). This suggests that while native cells grow on the medial side of the graft to reform a mucosal epithelial layer, and keratinocytes grow in on the lateral side of the graft to reform an epidermal layer, autologous grafts do not undergo any remodeling to reform the anisotropic middle lamina propria layer.
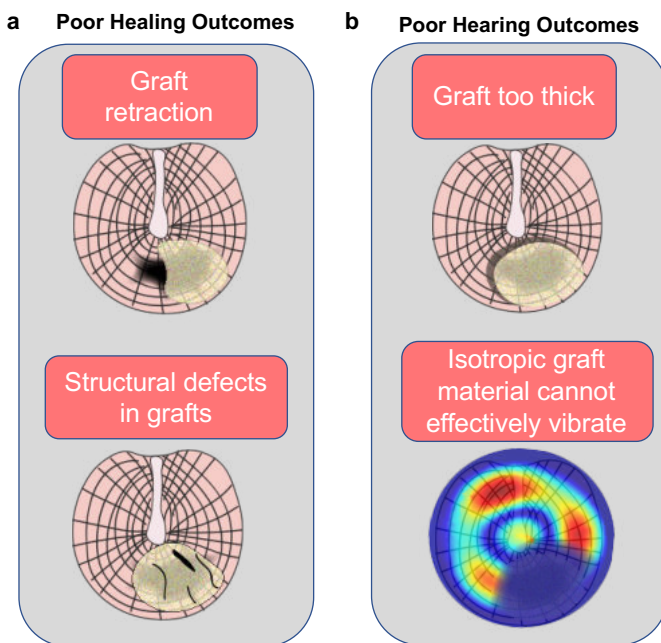
Figure 2.39. Autologous TM grafts can lead to poor healing and hearing outcomes following tympanoplasty. (a) Graft retraction from the remnant TM tissue along with structural defects can require revision surgery can lead to poor healing outcomes. (b) Inconsistent graft thickness and the lack of a circumferential and radial collagen network within autologous tissues can lead to poor hearing outcomes.
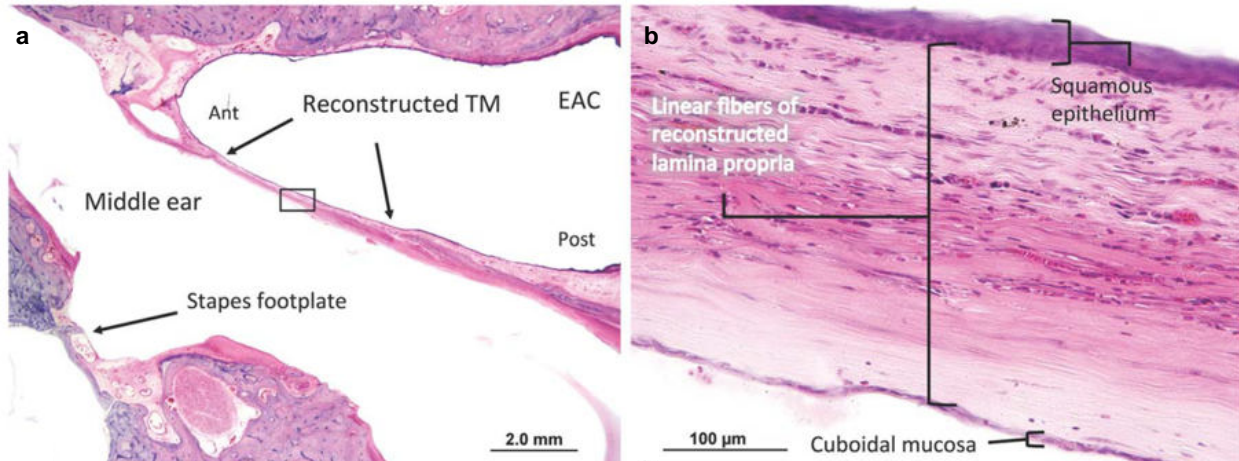
Figure 2.40. Reconstructed autologous fascia graft of a 62-year-old patient underwent a right total drum replacement with temporalis fascia with cartilage ossiculoplasty. (a) The TM does not demonstrate blunting but is uniformly thickened anteriorly and posteriorly. (b) A high-power view of the reconstructed TM clearly demonstrates thick linear fibers. Ant=anterior; EAC=external auditory canal; Post=posterior; TM=tympanic membrane [16].

Since autologous materials do not degrade or remodel to restore native TM fibrous microstructure or thickness, poor hearing outcomes can result. This means that the choice of TM graft material can highly affect hearing outcomes of the patient. In addition to thickness differences between tissues, the stiffness of the materials can highly differ. As described previously in the mathematical model developed by Fay *et al.*, modeling the TM as an isotropic tissue, the Young's Modulus has a large impact on sound conduction, whereby "soft" tissues such as temporalis fascia can vibrate well at low frequencies but cannot drive the umbo at higher frequencies, and "stiff" tissues such as cartilage can vibrate well at high frequencies but cannot match the impedance of air to move the TM at low frequencies [5]. Polanik *et al.* analyzed the audiograms of 23 patients who underwent type I tympanoplasty following trauma (14 patients) or chronic otitis media (9 patients) using a lateral temporalis fascia graft between August 2016 and February 2019 [160]. Hearing outcomes were assessed by ABG at low frequencies (250, 500, and 1000 Hz) as well as a high frequency (4000 Hz). At low frequencies, the average ABG improved substantially from 27.8 ± 12.6 dB before the TM was repaired to 12.3 ± 10.9 dB after healing. However, at the high frequency tested, there was not a substantial improvement in ABG. High frequency ABGs started at an average of 21.5 ± 15.1 dB but only decreased to 18.9 ± 12.4 dB, which was determined to be insignificant. The audiograms of two patients preoperatively and postoperatively demonstrate this lack of high frequency hearing restoration [160] (**Figure 2.41**). The ability to hear frequencies above 5 kHz has been shown to be important to speech

comprehension [161-164], particularly in multi-speaker environments [165]. Additionally, it is believed that a lack of stimuli at certain frequencies reaching the cochlea may contribute to tinnitus [166-168], as the brain may produce auditory input to compensate for the lack of stimuli.

Figure 2.41. Representative pre and post-operative audiograms of a patient demonstrating near closure of the low-frequency ABG but worsening high-frequency ABG. (a) Preoperative and (b) postoperative audiograms of the left ear in a patient who underwent lateral tympanoplasty with a temporalis fascia graft [160].
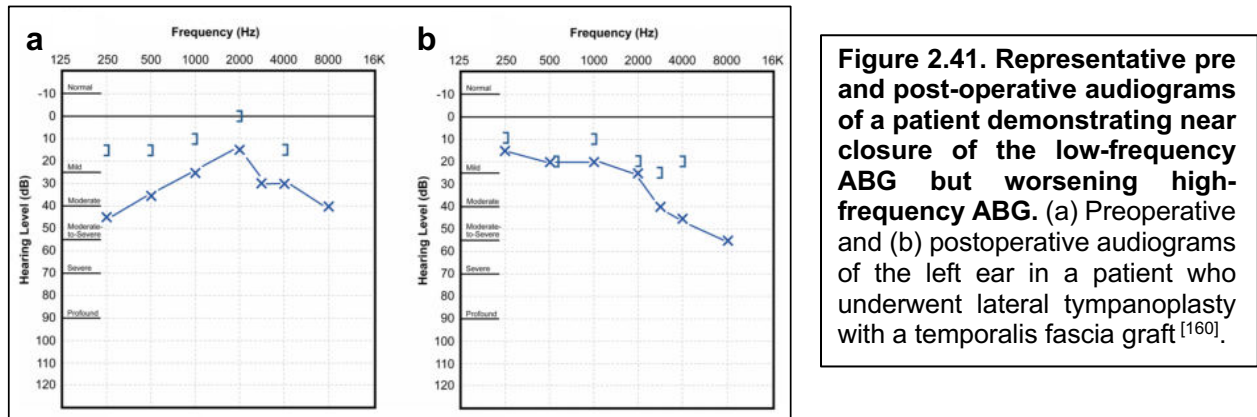
Although healing outcomes of cartilage grafts may be slightly better than of fascia grafts, hearing outcomes can suffer, particularly due to the inability of stiff cartilage to match the impedance of air across most frequencies tested in an audiogram. Yung *et al.* studied tympanoplasty with temporalis fascia (n = 20 patients) or cartilage (n = 18 patients) in TM perforations comprising 50% or more of the TM [169]. The authors found that the average postoperative ABGs were better in those patients who received temporalis fascia grafts as compared to cartilage grafts (16.97 dB vs. 20.63 dB) [169]. Unfortunately, standard audiograms are only conducted up to 8000 Hz, while the normal human can typically hear frequencies up to 20 kHz. In addition, ABG can only be assessed up to 4000 Hz as standard bone conduction transducers are unable to reliably measure high frequencies.

In addition to the material, other factors such as placement technique and original size of the perforation can affect hearing outcomes following tympanoplasty. In a study of 115 patients, hearing outcomes were better in patients who underwent an underlay graft placement, as compared those who underwent overlay graft placement [170]. Additionally, larger perforation size causes poorer hearing outcomes following tympanoplasty. Röösli *et al.* investigated hearing restoration in temporal bone models as a function of TM perforation size [171]. They found that although the pressure difference across the TM was almost fully recovered, stapes motion was highly limited at frequencies above 4.5 kHz for larger perforations. Intuitively, this makes sense, as larger perforations have a greater surface area of structural

damage that must patched by a graft. Thus, more of the TM will be composed of the isotropic and thick graft material, rather than the thin, highly organized original TM microstructure.

2.6 Non-Autologous Tympanic Membrane Grafts

2.6.1 Outcomes from Non-autologous Tympanic Membrane Grafts in Humans

The use of non-autologous materials may be advantageous in solving many of the currently existing challenges with autologous TM grafts. Firstly, graft tissue does not need to be harvested from the patient at the time of the procedure, saving surgeon time and reducing scarring and the risk of post-operative infections. Secondly, graft placement ability may be improved through resilient materials, potentially enabling placement in a clinic setting and eliminating the need for general anesthesia. Thirdly, unique material properties of the grafts may enable better integration and remodeling into TM tissue, particularly through the use of biodegradable materials. Finally, the use of non-autologous materials can allow for consistency in graft thickness and mechanical properties for more predictable outcomes.

The use of non-autologous grafts in human patients has been limited due to regulatory processes required for new devices and materials. The only FDA-approved device marketed for TM repair in the US is Biodesign® Otologic Repair Graft (acellular porcine small intestinal submucosa, Cook Medical®, USA) [172-175]. Thus, most non-autologous materials studied in humans are readily available materials, such as paper [143,176,177], silk fibroin [178], and bacterial cellulose [179,180]. Medical materials in other markets have also been investigated, such as Terudermis® (protease-solubilized atelocollagen, Olympus Terumo Biomaterials Corp, Japan) [181-183], Steri-Strip™ tape (3M, USA) [184,185], Gelfoam® or Gelfilm® (gelatin, Pfizer, USA) [104,186,187], EpiFilm®/EpiDisc® (hyaluronic acid, Medtronic, USA) [188-195], and AlloDerm® Regenerative Tissue Matrix (acellular human skin, BioHorizons, USA) [196].

As Biodesign® has received 510(k) clearance for TM repair, it is the most well-characterized in clinical settings. A comprehensive study by D'Eredità looked at outcomes of 404 patients with TM repairs performed by the same surgeon, where 217 underwent TM repair with Biodesign® and 215 with temporalis fascia [172]. Stable TM perforation closures were seen in 97.2% of patients who had their TM grafted with Biodesign® and 94.8% of patients who had their TM grafted with temporalis fascia. They also found no difference in procedural times or mean ABG values between the two groups. One major benefit of non-

autologous graft materials is the ability to use them for TM repair in a clinic setting for minimal invasiveness. In 2017, Yawn *et al.* performed endoscopic tympanoplasty with Biodesign® in 37 patients, 70% of whom underwent endoscopic placement through the ear canal and 30% underwent microscopic placement through a postauricular incision [173]. They found average success rates of 86.5% and mean ABG improvement of 7.6 dB in patients, with no statistically significant differences between the endoscopic and microscopic placement groups. To enable better endoscopic placement of Biodesign® grafts, Kozin *et al.* designed a novel bilayer approach in 2019 [175] (**Figure 2.42**). In this method, the graft material is cut into two sections, and slits are used to interdigitate the sections and hold the graft in place, sandwiching the TM from both the medial and lateral surfaces and reducing procedure time down to 25 minutes. The authors found that all 5 patients had healed perforations with evidence of vascular ingrowth. ABG improved from 12.2 ± 4.1 dB preoperatively to 4.2 ± 2.1 dB postoperatively [175]. While this study is promising, the perforations were all between 2 – 4mm in diameter. Thus, using this approach with larger perforations would be insightful as to its potential for treating larger perforations in a noninvasive manner.
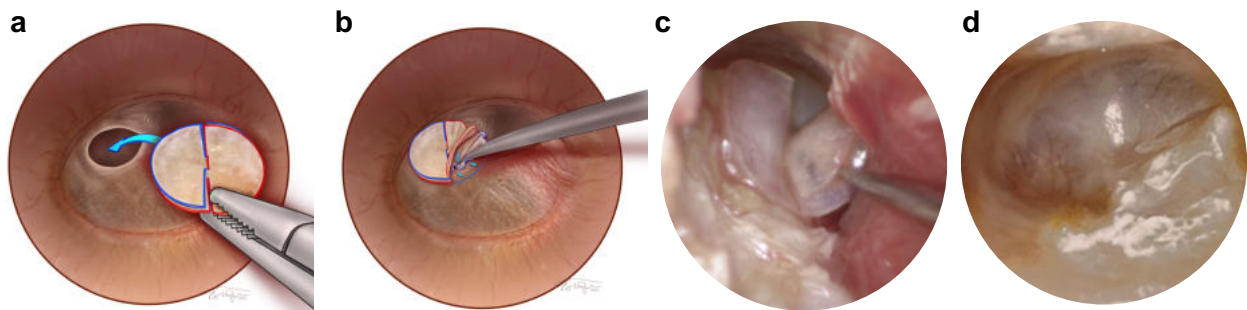
Figure 2.42. Transcanal endoscopic tympanoplasty surgical approach using Biodesign®. (a) Illustration shows graft placement with an alligator forceps (b,c) A curved needle is used to tuck medial grafts beneath the TM. (d) Healed TM with robust vascular ingrowth at 3 months [175].

A systematic review of TMs repaired with non-autologous graft materials previously mentioned was conducted by Ghanad *et al.* in 2020 of 53 manuscripts, including 2794 ears [197]. Traumatic injuries accounted for 56.8% of TMs repaired, while otitis media related perforations accounted for 36.9% and failure of tympanostomy tube perforation closure accounted for 2.9%. Overall closure rate was 82.8% using these materials, with higher closure rates in acute perforations compared to chronic perforations. Steri-Strip^TM Tape by 3M and Biodesign® porcine small intestinal submucosa (SIS) grafts achieved the highest overall closure rates, at 96.8% and 96.4%, respectively [197] (**Table 1**). Silk fibroin, gelatin, hyaluronic acid,

growth factor application, and bacterial cellulose also had healing rates above 80%. Unfortunately, many of these studies were limited to small, Grade I perforations. Additionally, graft remodeling and hearing outcomes were not extensively studied. For the 21% of studies that reported hearing outcomes, a median postoperative ABG was determined to be 8.5 dB. Thus, while the use of non-autologous graft materials is promising from the perspective of non-invasive placement and healing outcomes, hearing outcomes need to be further investigated. None of these grafts mimic the native TM's circumferential and radial microstructure. Thus, a lack of remodeling into this architecture could lead to nonideal hearing outcomes.

Table 1. Comparison of closure rates in 53 clinical studies with non-autologous TM graft materials.
* Statistically significant (p<0.05) †. SIS = small intestinal submucosa. Statistics performed using Chi-squared test [197].

	No. of Studies	No. of Ears	Overall	Acute	Chronic	Acute vs. Chronic
Paper Patch	19	723	66.8%	87.7%	45.3%	p<0.0001*
Silk Fibroin	2	46	82.6%	92.3%	70.0%	p=0.47
Steri Strip	3	158	96.8%	96.8%	-	-
Gelatin	8	423	85.3%	85.5%	82.4%	p=0.58
Hyaluronic Acid	3	88	89.8%	95.2%	0%	p<0.001*
Growth Factors	15	1039	87.6%	98.1%	73.6%	p<0.001*
Bacterial Cellulose	3	76	88.2%	-	88.2%	-
Atelocollagen	1	19	42.1%	-	42.1%	-
Porcine SIS	2	222	96.4%	-	96.4%	-
All Materials	53†	2794	82.8%	92.3%	64.9%	p<0.01*

2.6.2   Outcomes from Non-autologous Tympanic Membrane Grafts in Animal Models

In animal models, both natural and synthetic non-autologous graft materials have been investigated for use as TM grafts, including alginate [198,199], silk fibroin [200,201], paper [166,168,202], acellular porcine collagen [168], gelatin [168], synthetic polymers [203-205], urinary bladder matrix [206], and Biodesign® [207]. While these animal models include rats, guinea pigs, and chinchillas, the small TM size of the former two animals are poor models for TM regeneration. Thus, the use of these animal models have limited relevance of outcomes for chronic TM repair. Chinchillas are ideal as animal models in tympanoplasty due to their large TM size (8.32 − 8.53 mm in diameter), corresponding to approximately 90% of the size of the human TM [208]. Perforations can be created in chinchilla TMs that do not spontaneously heal after at least 4 weeks, akin to

chronic perforations in humans [209-213]. Chinchillas also have a similar hearing frequency range (50 Hz – 33 kHz on average) and sound sensitivity as humans (**Figure 2.43**) [214,215].
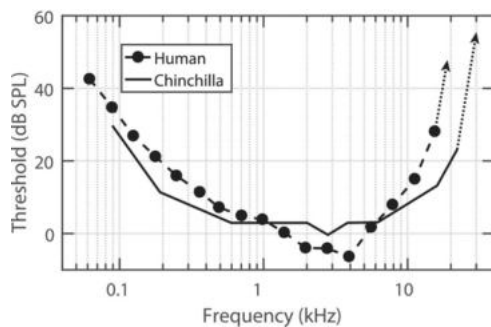
Figure 2.43. The hearing frequency range and sensitivity of chinchillas overlap significantly with that of human hearing. This similar hearing range is one of the main advantages of chinchillas as an animal model of hearing. Behavioral audiograms are compared between chinchillas and humans. Copyright 1970, Acoustic Society of America [214].

Underlay tympanoplasty has been successfully performed in chinchillas by other research groups, using packing materials such as Gelfoam® to hold the grafts in place [213,216-218]. While postauricular incisions have been made for successful tympanoplasty in chinchillas, the inability to raise a tympanomeatal flap limits access to the TM via the ear canal. To overcome this limitation, a transbullar incision can also be made to directly access the middle ear space and medial side of the TM in chinchillas, and permit underlay tympanoplasty.

Although traditional audiometry is not possible for assessing hearing outcomes, a neurological technique to measure auditory brainstem response (ABR) audiometry can be used to look at hearing thresholds at specific frequencies. During ABR, an evoked potential is generated by a click or tone pip through an earphone. The waveform response is measured by surface electrodes placed at the junction of the scalp and ear lobes. As the sound pressure stimulus level is increased (the sound becomes louder), the peaks of the waveforms become pronounced, and thresholds can be determined. Lower ABR threshold values correspond to better hearing, as a lower sound pressure level is required for a detectable peak.

In 2006, Weber *et al.* looked at calcium alginate and paper patches in a chinchilla model of chronic TM perforations ranging from 2 – 5 mm in diameter [198]. At 10 weeks post-implantation, healing was observed in 9 out of 13 chinchillas with alginate patches, in contrast to only 2 out of 9 in the paper patch group and 1 out of 11 in the control group without a graft. Endoscopic imaging and histologic processing after 10 weeks of remodeling show the calcium alginate graft being shed into the middle ear, with a keratinizing epithelium resurfacing the lateral side of the TM and a mucosal epithelium resurfacing the medial side of the TM [166]. Bilateral ABR measurements of hearing thresholds were conducted after perforation creation and at 6 weeks post-implantation. Control ears exhibited hearing thresholds from 25 –

40 dB across frequencies tested, while those with calcium alginate grafts exhibited hearing thresholds from 30 – 45 dB. According to the authors, the lack of significant differences between these groups demonstrated a lack of ototoxicity from the material placement. However, one would expect perforation closure to improve hearing thresholds compared to ungrafted ears. While calcium alginate grafts may promote closure of the TM perforations, the lamina propria may not be restructured.

Evaluation of inner ear health in chinchillas may be performed using cochlear histopathology. There are several materials that have been used for embedding temporal bones to assess TM remodeling and cochlear histopathology, including paraffin embedding and celloidin embedding [219]. Paraffin is a translucent, waxy solid consisting of a mixture of saturated hydrocarbons. This option is inexpensive and readily available, yet cochlear sections fixed with paraffin often show poor morphological preservation and can lead the disruptions of the vestibular and cochlear labyrinths. In contrast, celloidin is a semisolid solution of pyroxylin in ether and alcohol. While it is more expensive than paraffin, it exhibits superior preservation of the bony and membranous labyrinths, enabling more accurate determination of cochlear damage [220].

In 2009, Parekh *et al.* studied repair of chinchilla TM with urinary bladder matrix [206]. Subtotal perforations were created in chinchilla TMs that persisted over an 8-week period. Left TMs were left untreated, while right TMs were implanted with urinary bladder matrix grafts. The authors found that both control and patched TMs were thicker than native tissue, with urinary bladder matrix grafts being readily degraded and replaced with native tissue that recapitulated the trilaminar TM structure [206] (**Figure 2.44**). The authors found that TMs treated with urinary bladder matric grafts were thicker and exhibited more organized collagen. Despite promising healing and histological results with regard to reformation of the TM structure, the authors did not measure hearing outcomes in the chinchillas. Finally, Wieland *et al.* investigated the use of poly(glycerol sebacate) (PGS) grafts to repair chronic TM perforations in chinchilla models [203]. PGS is a biodegradable thermosetting elastomer that can be cast into desired geometries. After 12 weeks, the ears repaired with PGS grafts were endoscopically and histologically examined. The authors found that 10 out of the 11 TMs repaired with PGS and 6 of the 8 TMs repaired with Gelfilm® had healed at this timepoint. Additionally, endoscopic imaging suggested incorporation of both the lateral epithelial surface and the medical mucosal surface of the PGS grafts, along with neovascularization [203]. These results demonstrate the potential for native cells to grow onto synthetic polymeric graft materials.
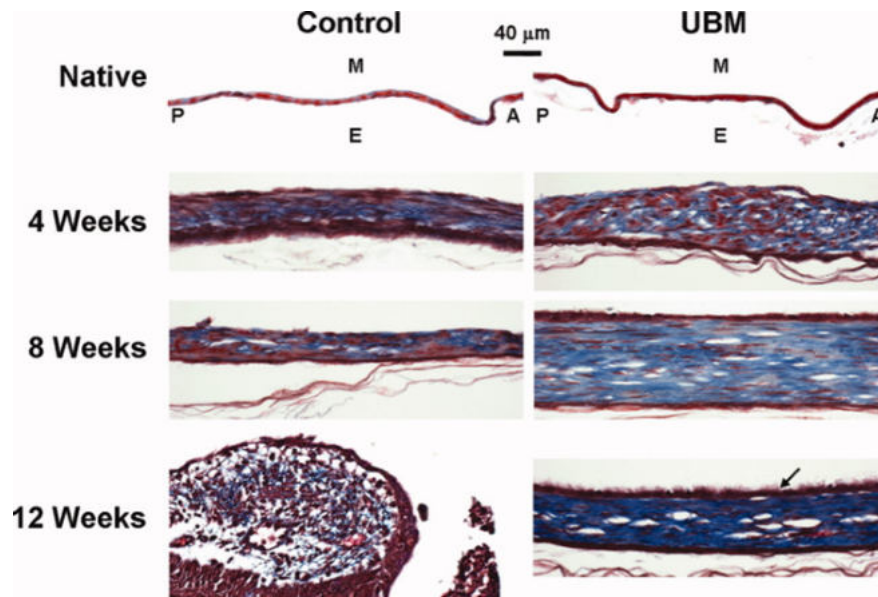
Figure 2.44. Representative histological sections stained with Masson's trichrome of control TMs (left) and TMs treated with urinary bladder matrix (UBM) patches (right) at 4 weeks, 8 weeks, and 12 weeks. M ¼ mucosal side, E ¼ squamous epithelial side, P ¼ posterior region, and A ¼ anterior region of the TMs. Scale bar represents 40 μm [206].

Non-autologous tissue grafts from both natural and synthetic sources have led to successful perforation closure in chinchilla models for chronic perforations. However, most studies did not assess hearing outcomes. Therefore, while promising for remodeling, the mechanical properties of the remodeled tissue as the materials integrate with the tissue and the graft potentially degrades may have a significant impact on hearing outcomes, particularly as none of these grafts demonstrated anisotropic tissue remodeling into an architecture that matches the circumferential and radial collagen in the native TM.

2.7   Ideal Properties and Manufacturing Methods for Tympanic Membrane Grafts

Designing the ideal TM graft is a significant undertaking that enables an understanding of both ear, nose, and throat (ENT) surgeons who perform the procedures alongside patient problems and priorities. Through literature review, conversations with ear surgeons, and feedback from patients, several important properties for the ideal tympanic membrane graft have been identified (**Figure 2.45** and **Table 2**). Some of these properties relate to the choice of material itself, such as surgical feasibility, adhesion to the TM, and biodegradation. Other properties relate to both the material and the manufacturing method, such as acoustic properties, customization, and the potential for cellular alignment.
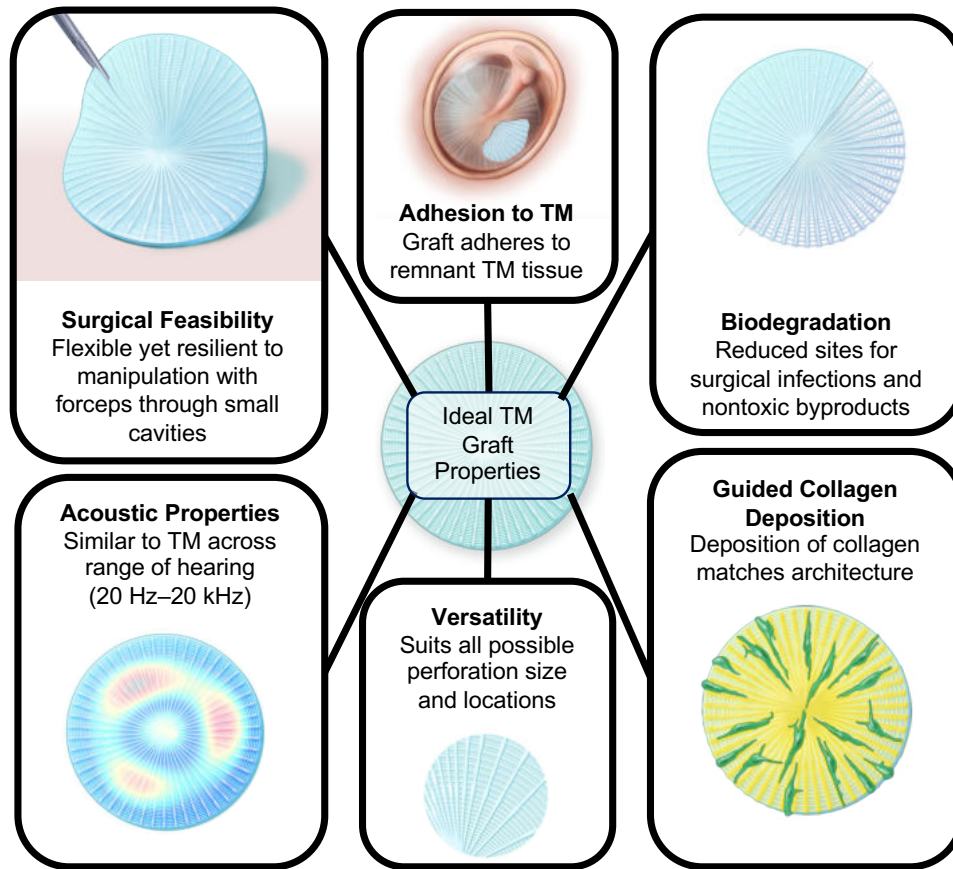
Figure 2.45. Design parameters for ideal TM grafts. Ideal properties include surgical feasibility, acoustic properties, customization, adhesion to the TM, biodegradation, and cellular alignment. (image credit: Shawna R Snyder).

Table 2. Criteria determined for "ideal TM grafts" alongside design goals for each criterion.

Criteria		Design Goals
Material Design	**Surgical Feasibility**	Graft thickness from 80 – 120 μm Ability to retain its shape after flexing
	Adhesion to the TM	Young's Modulus between 10 – 100 MPa Failure of grafts (i.e. graft retraction) is lower than fascia
	Biodegradation	Complete graft degradation achieved in 2 – 6 months *in vivo*
Material and Manufacturing Design	**Acoustic Properties**	Ability to conduct sound to the ossicular chain from 20 Hz – 20 kHz
	Versatility	Grafts can be altered to match the perforation size and location
	Guided Collagen Deposition	Ingrowing cells remodel the graft into an anisotropic collagen structure

When determining the ideal TM graft material, the first major category of optimization is mechanical properties for graft placement by ENT surgeons. As previously described, the TM is approximately 80 – 120 μm in thickness across the pars tensa region, which is the most frequently damaged [7]. Thus, the ideal TM graft should be in this range of thickness. Autologous grafts, such as temporalis fascia, have a wide range of thickness. Even those harvested from the same surgical using the same technique have been shown to range from 234.9 ± 144.9 μm in thickness [16]. 52 ENT surgeons were surveyed in 8 countries to determine pain points around tympanoplasty and outcomes of patients. Most surgeons interviewed had performed tympanoplasties for between 5 to 20 years, performing at least more than 50 tympanoplasties per year. The main indications were traumatic perforations, chronic otitis media, tympanostomy tube placement, and cholesteatoma. The major reasons these surgeons would choose not to perform the procedure were associated costs and invasiveness. An average of 1.37 hours is taken for a procedure, starting from when the patient arrives at the surgery room and ending when the patient gets to the recovery room. Autologous tissues, such as fascia and cartilage, are the most commonly used graft material. The most common pain point from the surgical procedure, mentioned by 42% of ENT surgeons, is placement and manipulation of the graft material (**Figure 2.46a**). Harvesting the graft material was another major struggle, with 11% of surgeons identifying it as a top pain point. Autologous graft materials are challenging to manipulate when wet, a graft from an autologous material can bunch in on itself, rendering re-flatting and placement challenging. Thus, designing a non-autologous graft material that does not require time to be harvested, allows for bending through small ear cavities without fracturing or breaking, and then is able to quickly return to its original flattened structure to lay flush against the TM perforation would greatly improve surgeon experience. **Chapter 3** and **Chapter 4** give an overview of the mechanical properties of novel biomimetic TM grafts to ensure feasibility, while **Chapter 6** discusses potential strategies for further improvement of graft placement through bilayer architectures.

As previously mentioned, lack of graft integration with the remnant TM tissue can lead to re-perforation and poor healing outcomes. Revision surgeries can become necessary after the packing material is removed at 2 weeks if the graft is noticed to not be integrated. Additionally, re-perforation of the graft can occur; this is most commonly noticed at the 2-month follow up visit, but it can also occur several months or years after surgery. Indeed, the same group of ENT surgeons noted re-perforation was the most

common reason for a patient to undergo a revision surgery, at 84% (**Figure 2.46b**). Poor graft integration

can be due to the mechanical properties of the material and the material's inability to encourage native

cellular ingrowth. Ideally, the graft should be hydrophilic and porous. TM grafts should be able to absorb

fluids and growth factors, enabling a suitable environment for native cells to grow onto the graft and

incorporate with the remnant TM tissue on the medial and lateral surfaces. Thus, autologous tissues and

natural hydrogel materials have been extensively used due to their capability to support ongrowing cells.

Autologous tissue grafts can have rapidly changing mechanical properties after implantation, particularly

as they undergo constant drying and moistening. Mismatch of mechanical properties can cause graft

retraction. As an anisotropic soft tissue, the TM's Young's modulus has been measured at between 10 –

100 MPa depending upon the direction in which the membrane is tested [34-38]. The ideal TM graft would

match this modulus range, with little change in shape and morphology during drying and remoistening.

Thus, designing a material that integrates with host TM tissue and matches its mechanical properties can

prevent a lack of graft integration or re-perforation that leads to revision surgeries. **Chapter 4** and **Chapter

5** address a novel synthetic material approach to ensuring that grafts become integrated with host tissue,

while mitigating potential graft rejection or retraction.
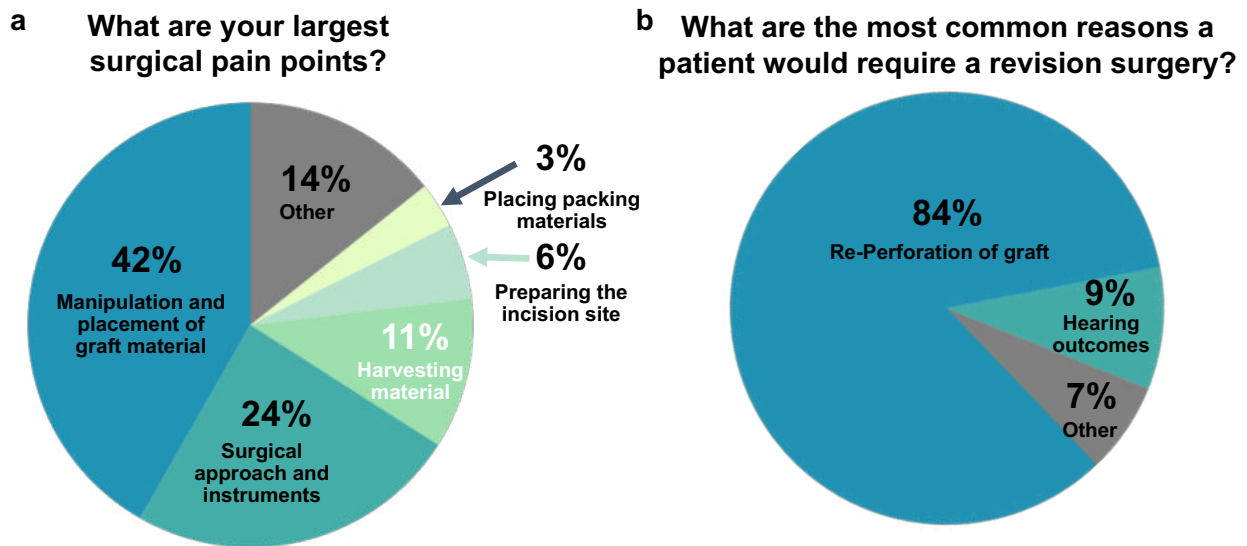
Figure 2.46. Summary of survey responses from 52 ENT surgeons in 8 countries. (a) Large pain points encountered by ENT surgeons during tympanoplasty include challenges with manipulating the graft material, surgical approaches, and harvesting the graft material. (b) Re-perforation of graft material is the most common reason for a tympanoplasty revision surgery, with poor hearing outcomes second.

A third material-specific property of the ideal TM graft material is biodegradation. As described previously, autologous tissue grafts and many non-autologous tissue grafts such as Biodesign® do not degrade or remodel. Thus, while native cells may grow onto and form the lateral-facing epidermal layer comprising keratinocytes or the medial-facing musical epithelial layer containing cuboidal epithelial cells, if the bulk of the tissue graft does not degrade, it cannot fully integrate into the remnant TM tissue or return the TM to its original thickness or structure. Additionally, it is challenging for host vasculature and lymphatic networks to grow onto non-degradable tissues. The presence of foreign tissues and materials in the ear has been shown to cause post-operative infections, leading to conditions such as biofilm formation and otorrhea, or drainage of the ear [221,222]. Bacteria and viruses can readily proliferate on the surface of non-biodegradable grafts, and without integration into the host vascular and lymphatic network, it can be challenging for immune cells to reach these pathogens. It is challenging to define an ideal range over which biodegradation should occur, as this is largely due to the size of the perforation. The TM healing environment is unique, being located at an air-air interface that enables tissue ingrowth exclusively from the outer circumference of the perforation. Thus, larger TM perforations will require longer healing times than smaller TM perforations.

If a graft degrades too quickly, the patient will be left with a new perforation or without adequate support for tissue ingrowth. If a graft degrades too slowly, there is a longer period of time over which biofilms can form or the graft material can retract from the remnant TM. The natural healing process of the TM in spontaneous closure of small perforations takes approximately 6 – 8 weeks, with a majority occurring during the remodeling phase [95,103]. Therefore, a minimum of 2 months up to a maximum of 6 months for total graft degradation is a feasible range for balancing both aspects. Thus, **Chapter 4** explores the biodegradation of a novel biodegradable polymer through *in vitro* approaches, and **Chapter 5** examines the *in vivo* implications of a biodegradable material on the TM and the resultant integration with host tissue. The degradation byproducts of the graft should also be systemically nontoxic. Additionally, ototoxic efforts of small molecule byproducts of the graft must be avoided. Ototoxic effects have been observed for small molecule therapeutics, such as aminoglycoside antibiotics [223-225], cardiac glycosides [226-228], and chemotherapeutic molecules [229-232]. as the adjacent inner ear contains sensitive hair cells and spiral ganglion neurons that frequently become damaged, creating irreversible sensorineural hearing loss [233-235].

Thus, when designing the biodegradable material, it must be considered that the ear is a unique and sensitive environment beyond other organs in the body, indicating a need for additional toxicity testing. Thus, monomers that can be commonly found in the body or can be easily metabolized or excreted will likely be the safest with regards to systemic toxicity and ototoxicity.

Other ideal features of TM graft also relate to the material but can also be enabled by unique manufacturing mechanisms, such as 3D printing. As previously described, the hearing outcomes of patients across the standard range of human hearing, 20 Hz – 20 kHz, are heavily reliant upon the structure of graft placed. While maintaining a graft with Young's Modulus (E) in the 10 – 100 MPa range of the normal human TM [34-38] will help, those in the lower range (e.g. E = 30 MPa "soft" material) will have an improved ability to match impedance of air at low frequencies but not vibrate well at high frequencies, while those materials in the upper range (e.g. E = 100 MPa "soft" material) will be able to drive the umbo but will struggle to vibrate at low frequencies, as shown by Fay *et al.* [5]. Thus, it is necessary to develop a TM graft that will perform well at both low and high frequencies. One method to do so is to mimic the native TM structure through the inclusion of a circular and radial fibrous architecture. This may enable its vibration as one sheet of a "soft" material at lower frequencies, with the radial fibers enabling more complex modes of motion for the graft to behave as a "stiff" material at higher frequencies. While Mota *et al.* described a 3D printing technique to recapitulate this fibrous architecture in 2015 [289], they did not explore the acoustic properties of their grafts, nor their effect on hearing outcomes *in vivo*. 3D printing may be a suitable technique for recreating this microstructure in a TM graft; however, the limited experimental exploration of the impact of these fibers in sound conduction must be explored, as is done through *in vitro* characterization methods for sound-induced motion in **Chapter 3** and **Chapter 5**.

TM perforations occur in multiple locations and in multiple sizes, as described previously. Thus, the macroscale size and microscale fiber arrangement of the missing TM region vary widely between patients. Thus, there are two important aspects of TM grafts to ensure versatility. The first is in the macroscale size and shape of the graft. While grafts do not necessarily need to be tuned for a specific patient, as was conducted by endoscopic imaging and measurement for chinchillas by Kuo *et al.* [288], they should be able to be tuned to match a range of sizes of the perforations. If a 3D printing approach is taken, rapid customization is indeed feasible. However, most TM perforations are in a standard set of sizes and

locations: Grade 1 (0 – 25% of the TM, 0 – 2.5 mm in diameter), Grade II (26 – 50% of the TM, 2.5 – 5 mm in diamater), Grade III (51 – 75%, 5 – 7.5 mm in diameter), and Grade III (76 – 100% 7.5 – 10 mm in diameter). Thus, either creating a kit of various graft sizes to suit most perforations or having the ability to readily cut a graft material into the desired size would also likely enable perforation closure. Similarly, the second major aspect, which is matching the fiber arrangement of the missing location, could also be enabled either by subtracting material from a larger graft and orienting the graft during placement. While TM graft customization is important, TM grafts do not necessarily need to be 3D printed for a specific patient, as long as the chosen graft suits the perforation size and fiber arrangement.

As a TM graft containing a circumferential and radial structure becomes integrated with the host tissue, if the material is biodegradable, it is important that the tissue that forms retains this architecture. As the lamina propria is comprised mainly of collagen fibers deposited by fibroblasts, it is important that these cells grow onto the graft and lay down their own collagen, in a manner that mimics the original TM. Otherwise, after the graft is degraded in the desire 2 – 6 months, the patient will be left with an isotropic arrangement of extracellular matrix (ECM) proteins and a lamina propria layer that does not enable sound conduction across a wide range of frequencies. Even following spontaneous TM perforation closure, the lamina propria usually does not reform in the original architecture; rather, there may be a neomembrane of only mucosal and epithelial layers, or, the collagen network that is deposited may not match the original architecture, particularly in larger perforations [26]. Additionally, it is not enough to simply implant a biodegradable graft material and assume that once the graft has degraded, the remodeled tissue will match native tissue. Among biodegradable grafts studied previously in animal models, none of the histological sections of these grafts demonstrated an organized, bilayered lamina propria with circumferential and radial layers. Thus, for ideal ENT experience in placement, healing outcomes, and hearing outcomes, the ideal TM graft would consist of a biodegradable, elastomeric material with easy handling properties and matched circumferential and radial architecture of the native TM with potential to remodel into this architecture. The ability for novel materials to induce cellular alignment is optimized *in vitro* in **Chapter 4**, and the implications of this anisotropic remodeling to hearing threshold changes are seen *in vivo* in **Chapter 5**.

Alongside the material, the manufacturing method by which TM grafts are produced could be critical to their function. There are several techniques to encourage anisotropy in engineered tissue, including

mechanical stimulation [236-240], electrical stimulation [241-245], micropatterning [246-249], cellular confinement between topographical features [250-257], electrospinning, and rotary jet spinning. Many of these methods have limited complexity or can be challenging to apply during an *in vivo* environment. Cellular alignment and migration correspond highly to the alignment of extracellular matrix proteins that contribute to the mechanical functions of the tissue. Fibrillar collagen (type I, II, and II collagen) is formed when procollagen is secreted into the extracellular space parallel to the direction of highest spreading [258] (**Figure 2.47a**). These procollagen molecules are cleaved together to form a triple-helical collagen molecule [259] (**Figure 2.47b**). If a cell is elongated, collagen fibers will be formed in the direction of spreading. Thus, controlling the cell alignment will in turn control collagen fiber alignment in the tissue. By utilizing mechanotransduction, cells can sense the mechanical properties of their environment. Inside a cell, integrin-based adhesion complexes couple the actin cytoskeleton of a cell to its substrate. Cells generate larger cytoskeletal forces on stiff substrates than on soft substrates, as demonstrated by the Hill Curve [260] (**Figure 2.48a**). Thus, cells on stiffer substrates spread out more than those on soft substrates, which have a rounded morphology [261] (**Figure 2.48b**).
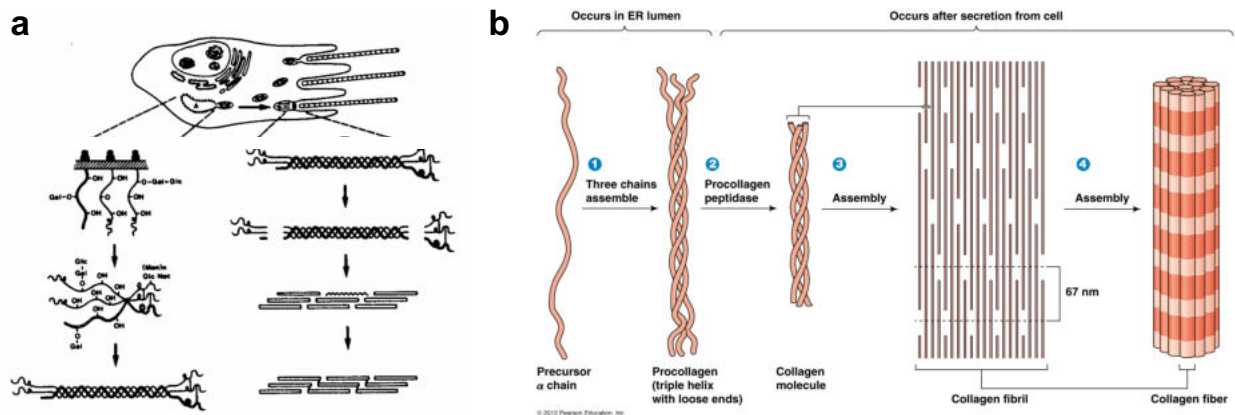
Figure 2.47. Collagen fibers are formed in the direction of fibroblast elongation. (a) Fibroblast assembly of collagen I fibrils parallel to the elongation direction of the cell [258]. (b) the self-assembly of collagen fibrils into collagen fibers [259].
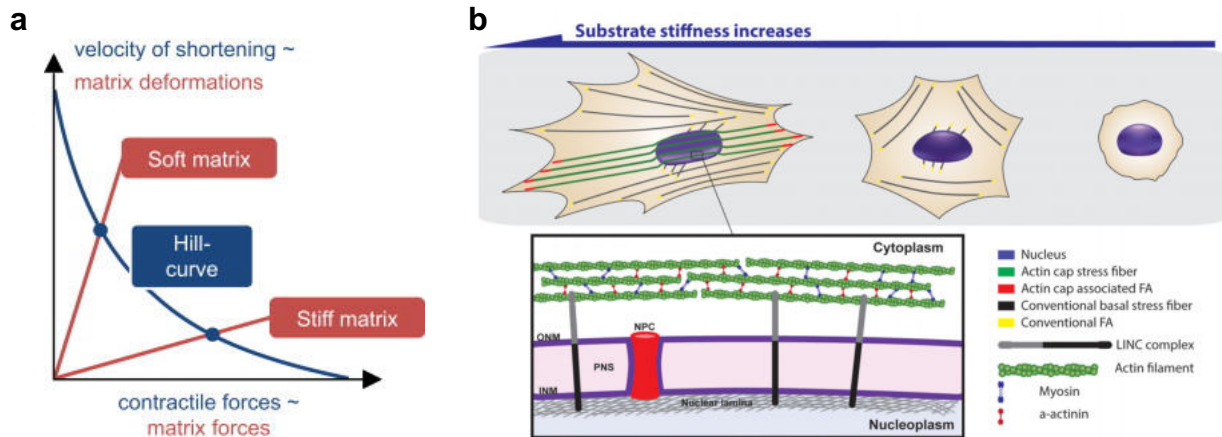
Figure 2.48. Mechanotransduction as a method of cell alignment. (a) Different spreading and migration behavior of cells attached to soft versus stiff substrates is a consequence of the inverse relationship between the maximum shortening velocity and force generation due to the internal resistance and reaction kinetics of force-bearing cytoskeletal structures [260]. (b) Cellular mechanosensing in response to substrate compliance. Well-organized actin cap fibers (green) on top of the nucleus are terminated by ACAFAs (red) at the periphery of the adherent cell, and the nucleus (blue) is elongated in the same direction as actin cap fibers (left) [261].

2.7.1 Three-Dimensional (3D) Printing of Tympanic Membrane Grafts

3D printing techniques have been widely used to create medical devices [262-270], scaffolds [271-276], and even human tissues [277-282]. Unlike subtractive manufacturing in which materials is selectively removed to generate the desired object of interest, 3D printing relies on additively depositing material in a layerwise manner [283] (**Figure 2.49**). Additive manufacturing relies on the three primary components:

(1)   **Computer-aided design** to guide the deposition of material in x-y-z dimensions

(2)   **Material** building blocks that bond, fuse, or sinter together

(3)   **3D printers** that can deposit materials in a controlled manner in x-y-z dimensions

There are four primary benefits to 3D printing medical devices, scaffolds, and engineered tissues. First, there is less waste is generated during the fabrication process, which is particularly relevant for expensive biologic materials. Second, higher shape complexity is possible when materials are printed in a layerwise fashion. Third, higher compositional complexity is possible by simultaneously printing multiple materials, e.g., multiple cell types and extracellular matrix (ECM) materials [277-279]. Finally, 3D printing enables mass customization, e.g., patient-specific devices and tissues can be constructed on demand. To date, both light- and ink-based 3D printing methods have been developed. Direct ink writing (DIW), a

filamentary-based 3D printing method, is of particular interest for this Ph.D. research [271-274,277-280,284]. In DIW, a material, termed an "ink," is held within a reservoir in a printhead. Pneumatic pressure, piston-driven, and screw-driven systems can be used to extrude the ink out of the nozzle and onto the substrate. Most inks developed to date for DIW exhibit a viscoelastic response, i.e., the ink flows readily when the extrusion pressure exceeds its shear yield stress, but rapidly solidifies upon exiting the nozzle (where it returns to a quiescent state). Inks can be printed under ambient conditions or at elevated temperatures, using a variant known as HOT-DIW [285-287].
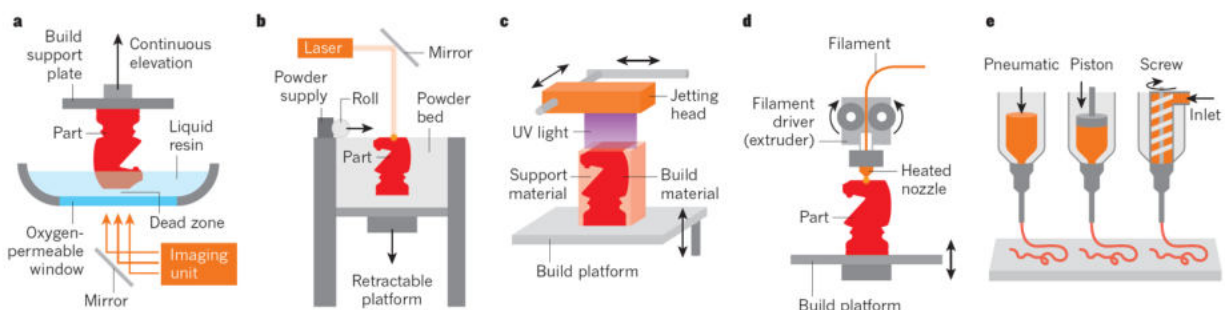
Figure 2.49. Common light- and ink-based 3D printing methods. (a) The light-based 3D printing method known as continuous liquid interface production. (b) Light-based selective laser sintering of powders. (c) Light- and ink-based photocurable inkjet printing of photopolymerizable resins. (d) Ink-based fused deposition modelling [283].

A potential method of enabling mechanotransduction is through the creation of anisotropic stiffness within a 3D printed filament. Importantly, the high shear forces experienced by materials in nozzle cause structures to align along the filament (**Figure 2.50**). Gladman *et al.* has demonstrated the ability for cellulose fibers to align along a programmed architecture, enabling shape-changing architectures [284]. Additionally, Kotikian *et al.* utilized high operating temperature-direct ink writing (HOT-DIW) to induce molecular alignment of LCE polymer chains prior to crosslinking, thus enabling programmed actuation [285]. Thus, filamentary extrusion allows materials to be patterned with a degree of anisotropy within the printed filament and therefore the final object. Filamentary extrusion 3D printing may allow for anisotropic mechanical properties to be patterned into a tissue graft in a custom direction. Thus, mimicking the circumferential and radial organization of the TM using this method would enable exploration of the impact of this architecture on sound conduction.
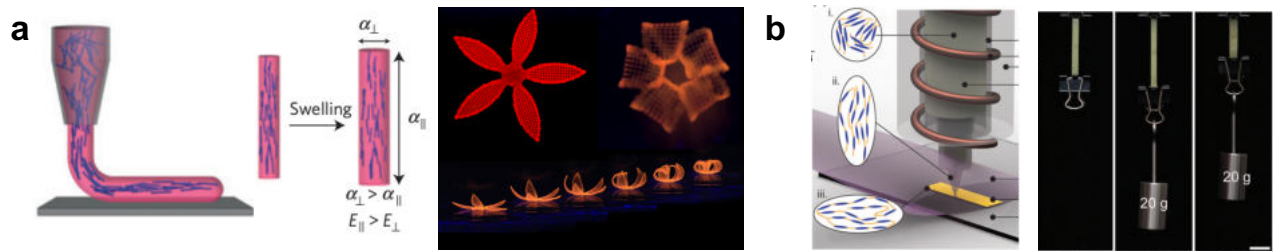
Figure 2.50. Two examples where filamentary extrusion imparts unique properties on the extruded filaments. (a) A hydrogel-based ink containing cellulose fibrils is extruded through a nozzle, aligning the cellulose fibrils in the direction of the print path. Differential swelling of the material causes the objects to morph shapes when submerged in water [284]. (b) In liquid crystal elastomer inks, hot melt extrusion causes polymer chains to align along the filament, allowing the material to contract and expand upon exposure to elevated temperatures [285].

Given the potential for non-autologous materials to reduce the invasiveness of tympanoplasty, researchers have recently created TM grafts by 3D printing these materials. By creating architectures that can bridge TM perforations [288], the placement of TM grafts through an endoscopic transcanal graft approach becomes feasible. 3D printing also offers the potential to recapitulate the microarchitecture of the native TM [289,290]. Ultimately, we aim to have program cellular ingrowth and collagen fibril deposition along a circumferential and radial architecture, potentially, leading to enhanced healing and hearing outcomes.

2.7.2   Biomimetic Tympanic Membrane Grafts via 3D printing

Recently, Kuo *et al.* explored the use of 3D printing for the macroscale design and fabrication of TM grafts from gelatin methacrylate (GelMA) containing EGF [288]. The motivation for their work was the wide variability in successful tympanoplasty procedures, which rely heavily on surgeon skill to shape the graft. Thus, they hypothesized that patient-specific grafts that are bioprinted to match the perforation size would be useful in enabling placement. Design and fabrication of the grafts, termed EarGraft, were conducted in a multi-stage process (**Figure 2.51**). The video recordings from perforation creation were used to generate computer aided design (CAD) models of the surface dimensions of the perforations using a commercial 3D-Bioplotter™ by EnvisionTEC®.

For *in vivo* implantation into the chinchilla perforations, customized grafts were bioprinted and implanted on day 7 following TM perforation. Micro computed tomography (micro-CT) and histological analysis showed that the TMs were well-healed; however, healed TMs were thicker than control TMs without perforations. Overall, this study was an interesting exploration of the use of new materials for TM perforation repair alongside 3D printing for a customized bilayer architecture. However, the authors did not

assess hearing outcomes in the chinchillas. Thus, the impact of thickened TMs and presence of cartilage growth was not adequately assessed in its relationship to functional outcomes. Additionally, placement time and stability of the graft in the perforation were not analyzed, which seemed to be the driving factors in the patient-specific geometry. Thus, the overall utility of the 3D printing process for the grafts was not immediately obvious. Additionally, a major limitation of this study is the short follow-up time of 21 days, considering the TM can undergo remodeling processes for several months following tympanoplasty.
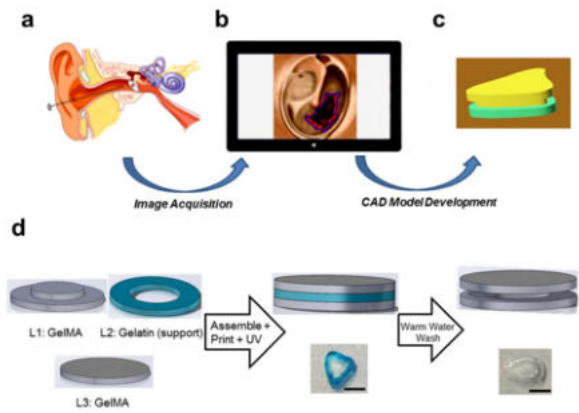
Figure 2.51. Concept of Automated Bioprinting of Tissue Engineered Grafts for Tympanic Membrane Repair (EarGraft). The four steps in the process are (a) capture the image of the perforation and (b) outline the defect on a computer and (c) develop a CAD model based on the outline and (d) design and printing of ear graft. Scale bars in panel D = 5 mm [288].

3D printing allows the circumferential and radial architecture of the TM to be recapitulated, which is important for enabling sound conduction at both low and high frequencies. In 2015, Mota *et al.* explored the creation of biomimetic, 3D-printed and electrospun TM grafts from synthetic polymers [289]. First, a radial arrangement of poly(lactic-co-glycolic acid) fibers were electrospun onto a substrate. Then, a poly(ethylene oxide terephthalate)/poly(butylene terephthalate) (PEOT/PBT) block copolymer was 3D printed into a biomimetic structure, designed with Rhinoceros® for use in the 3D-Bioplotter™ by EnvisionTEC®. Electrospun and 3D-printed TM scaffolds were combined in either a dual or triple layered arrangement (**Figure 2.52**). The authors cultured human mesenchymal stromal cells (MSCs) onto the grafts, demonstrating that they were metabolically active and organized themselves on top of the scaffolds [289] (**Figure 2.53**) While cells grew between the voids, it is not clear if the structure would be remodeled in this architecture. The authors did not characterize the mechanical or acoustic properties of these grafts *in vitro*, nor did they perform *in vivo* implantation of the grafts. Thus, while this study represents a step forward in creative manufacturing approaches to mimic this architecture, the functional benefits of having a biomimetic architecture in a TM graft are not explored.
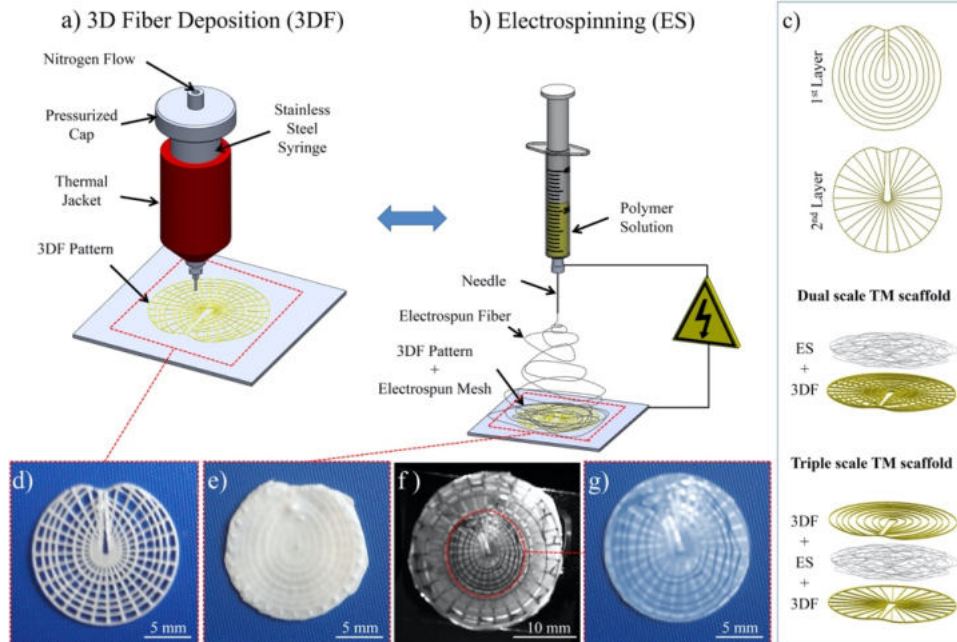
Figure 2.52. Strategy for the production of dual and triple scale scaffolds for TM scaffolds. (a,b) The first step comprises the production of the pattern via 3D fiber deposition technique and subsequent coating of the pattern with an electrospun mesh. (c) Simplified patterns with circular concentric microfibers and radial microfibers. (d) and (e) photographs of one-piece grid layer before and after coating with the electrospun membrane (dual scale TM scaffold). (f) and (g) photographs of a triple scale TM scaffold [289].
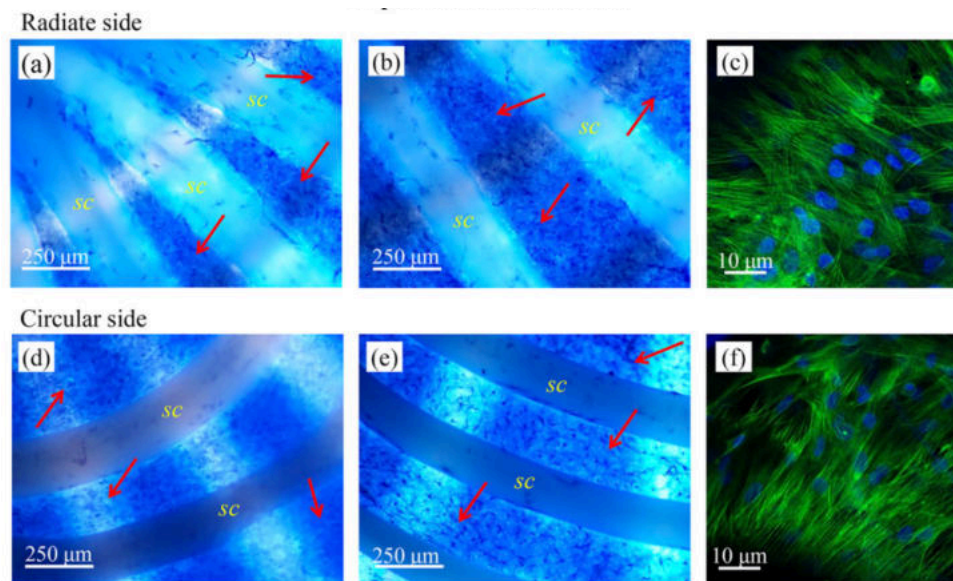
Figure 2.53. Imaging of triple scale TM scaffold/human MSC constructs at the endpoint scaffolds. (a-c) Radially patterned side; (d–f) circumferentially patterned side: (d) and (e) light microscopy images of methylene blue staining showing cells in blue; (c,f) CLSM micrographs showing f-actin filaments in green and nuclei in blue. Arrows indicate cells, and 'sc' indicates the scaffold biomaterial [289].

A third study investigating the creation of TM grafts by 3D printing was published by Ihan *et al.* in 2020 [290]. The authors prepared inks of polylactic acid (PLA) and chitosan in various ratios, and they 3D printed these using an extrusion-based printer, Hyrel 3D, alongside an SDS-5 Extruder. However, these grafts were not created in a biomimetic circumferential and radial architecture, but rather in a orthogonal lattice structure into square patches. Scaffolds containing 3 wt% chitosan exhibited favorable features in printing quality. The scaffolds were analyzed for physical, chemical, morphological, and mechanical properties, in addition to biocompatibility with MSCs. However, the only structural similarities to the TM was the overall size of the 3D printed grafts and the thickness of the grafts, and 3D printing appears to be mainly used to create "pores" on the order of 100 – 200 µm on the grafts. Thus, it is unclear whether these scaffolds would be functionally useful as TM grafts. Overall, these studies are limited in feasibly tackling the major challenges in TM graft placement, hearing outcomes, and healing outcomes.

2.7.3 Material Design for Tympanic Membrane Grafts

As described in **Chapter 2**, a biodegradable material would be ideal for TM grafts, due to their ability to be readily flexed while retaining their shape for placement, and their ability to degrade into nontoxic byproducts. While the studies conducted in **Chapter 3** demonstrate the importance of architecture of sound conduction, they utilized off-the-shelf biocompatible polymers that did not promote anisotropic remodeling. Additionally, although polydimethylsilioxane (PDMS) demonstrates resilient elastomeric properties, it does not biodegrade, leaving potential sites for infections on the foreign material. However, the Young's modulus of many commonly used biodegradable polymers are at least an order of magnitude higher than that of most commonly used biodegradable polymers, including poly(l-lactic acid) (PLLA, E = 2.7 GPa) [291], poly (d,l-lactic acid) (PDLLA, E = 1.19 GPa) [292], poly(glycolic acid) (PGA, E = 7.0 GPa) [292], poly(lactic-co-glycolic acid) (PLGA, E = 2.0 GPa) [292], and poly(3-hydroxybutyrate) (PHB, E = 1.95 GPa) [293]. Thus, for the duration the healing process while the material degrades, hearing outcomes may not be ideal because the grafts does not initially match the mechanical properties of the human TM.

Two major categories of soft biodegradable elastomers have been previously developed: dicarboxylic acid-based polymers and polyurethanes. The synthesis of biodegradable dicarboxylic acid-based elastomers involves the synthesis of a biodegradable polyol, such as glycerol or 1,8-octanediol, with a dicarboxylic acid monomer, such as sebacic acid or citric acid. The resultant prepolymer is cured under

heat and vacuumed to produce a covalently crosslinked thermoset elastomeric structure. These polymers and co-polymers have been studied for use in a variety of tissue engineering applications with success, such as nerve guides [294], myocardial patches [295-298], smooth muscle tissue [299], cartilage tissue [300-302], and vascular grafts [303,304]. Additionally, as described Wieland *et al.* used PGS, one of these polymers, as a TM graft material with success [203]. Unfortunately, the thermosetting process to cure these polymers makes them challenging for use with many manufacturing technologies. Firstly, their viscosities lower drastically during curing; thus, without supporting molds or materials, the structure loses its architecture as bubbles are formed from released water. Secondly, the degradation byproducts of these polymers can be acidic [305], causing tissue damage.

Given the processing limitations of dicarboxylic acid-based elastomers, they are most frequently used in the production of simple, molded parts, whereby a mold provides support as the viscosity is lowered and vaporized water leaves the part. However, another class of biodegradable elastomers—polyurethanes – can provide better processing as well as biocompatibility. Polyurethanes are block copolymers containing urethane bonds formed by reacting a polyol "soft segment" with a diisocyanate "hard segment" (**Figure 2.54a**) [306]. The diisocyanates tend to hydrogen bond and crystallize with other diisocyanates in nearby polymer chains (**Figure 2.54b**) [307]. These pseudo-crosslinked hard segments connecting between the soft segments are what gives polyurethane its elastomer-like properties. Thus, polyurethanes have Young's modulus values much closer to the range of human soft tissues, with Young's moduli typically measured at between 10 – 1000 MPa [308,309].
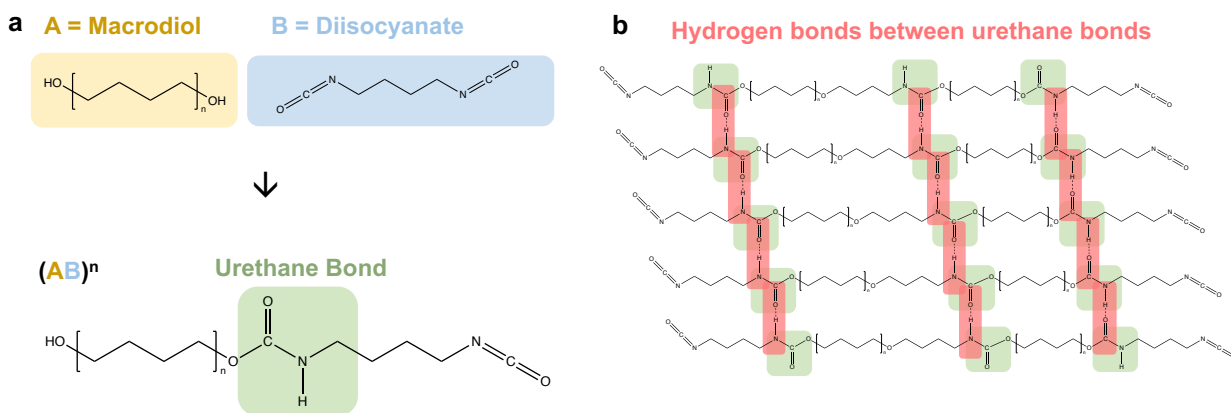
Figure 2.54. Synthesis and structure of biodegradable polyurethanes. (a) Monomers of a macrodiol and diisocyanate combine to form a urethane bond in a repeating manner. (b) Hydrogen bonds form between the covalent urethane bonds, creating a pseudo-crosslinked structure.

Many groups have successfully synthesized biodegradable polyurethanes dating back as early as 1987 using a variety of soft segments, hard segments, and chain extenders to alter the degradation rate, mechanical properties, and other features of the polyurethane. Specifically, biodegradable polyurethanes also have been used extensively in recent tissue engineering applications, showing good biocompatibility and support of a wide range of cell types including chondrocytes [310-312], fibroblasts [313-315], smooth muscle cells [316-319] cardiac muscle cells [320], endothelial cells [321,322], mesenchymal stem cells [323], adipose-derived stem cells [324], bone marrow stromal cells [325], osteoblasts [326], keratinocytes [327], and epithelial cells [328].

In addition to their use in academic research contexts, there are multiple medical devices on the market made from biodegradable polyurethanes. These include Degrapol®, a porous foam for nerve and bone regeneration (AB Medica Spa, Italy), Lacthane™, a foam for wound and nasal dressing (Polyganics, Netherlands), Epidel® for catheter cuffs (Interface Biologics, Canada), NovoSorb™ for orthopedic applications (PolyNovo Biomaterials, Australia), SynBioSys® stent coatings (Octoplus, Netherlands), Artelon® for ligament fixation and bone scaffolds (Artimplant, Sweden), and Actifit® for meniscal repair (Orteq, Netherlands). In particular, Actifit® has shown success in several clinical studies [329,330,331]. While these clinical papers do not discuss the reasons for using biodegradable polyurethanes in the medical products, overall, the success of biodegradable polyurethanes in medical implant locations can be attributed to their unique mechanical properties which are easily handled during complex surgical procedures and can mimic that of soft tissue, in contrast to other stiffer, more crystalline biodegradable polymers.

The pseudo-crosslinked nature of polyurethanes can enable interesting mechanical properties when these materials are stretched. One potential way in which biodegradable polyurethanes could be utilized for cellular alignment through mechanotransduction is by "stretching" the polymer within a nozzle. In contrast to conventional elastomers, as mechanical forces are applied to polyurethanes, the hydrogen bonds are broken, and more energetically favorable bonds are formed from the densification of the hard domains [332]. This results in a polymer with hard segments densified orthogonal to the tensile direction and therefore polymer chains oriented parallel to the tensile direction. This new structure leads to a behavior known as "densification hardening" or "strain hardening", where the polymer becomes progressively stiffer as it begins to be stretched, as there begin to be stronger covalent bonds in tensile direction and weaker hydrogen bonds in the direction orthogonal to the applied force [333]. This lamellar-like formation of hard

segments transverse to the extension direction in polyurethanes and orientation of soft segments with the tensile direction have been confirmed using X-ray diffraction [334]. This structure holds true for strain levels up to about 500%, after which the hard domains become disrupted [335].

Densification of hard segments in electrospun nanofibers can also be visualized using tapping-mode atomic force microscopy (AFM), where hard segments appear stiffer than soft segments. Through a combination of AFM and traditional tension testing, researchers investigated the nanomechanical properties and morphology of 500 mm thick polyurethane films subjected to normal loads in the range of 3 – 35 nN and longitudinal strains up to 150%. They found that at 10% elongation, the bulk elastic modulus and roughness increased, but the surface elastic modulus decreased. In contrast, at 150% elongation, the roughness decreased while both surface and bulk modulus increased [336] (**Figure 2.55**). Sakamoto *et al.* found that by stretching electrospun nanofibers, tapping-mode AFM showed densification of the hard segment domains within the fibers, although the electrospinning process on its own appears to be insufficient for inducing this densification to occur [337]. Therefore, this mechanical property might be utilized to induce anisotropy and preferential stiffening behavior within stretched fibers.
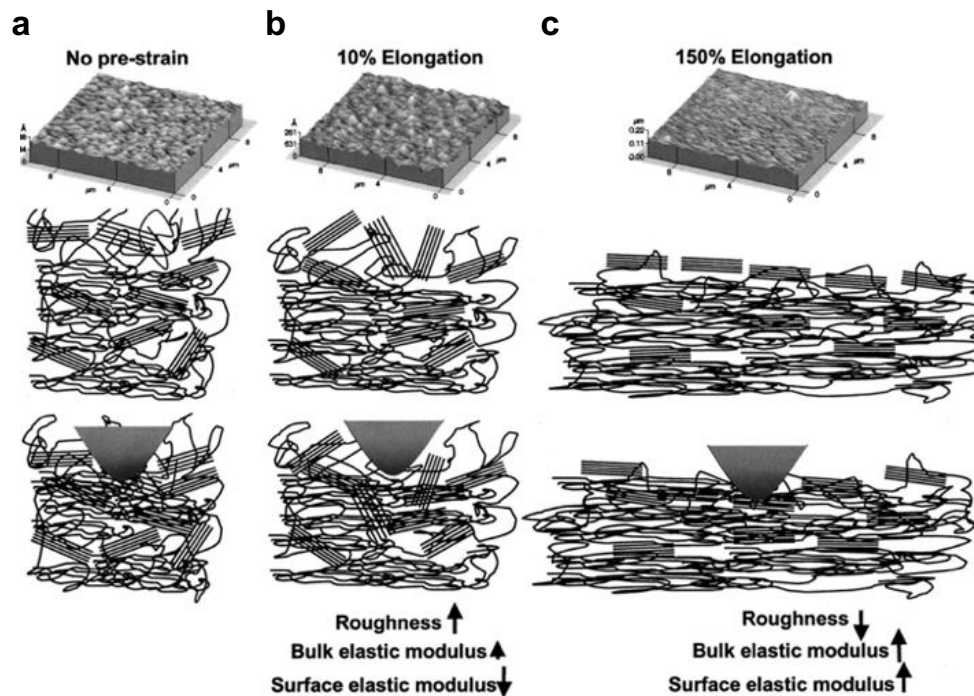
Figure 2.55. Alignment of polymer chains during extension of a polyurethane. AFM images of polyurethane films for (a) zero, (b) 10%, and (c) 150% elongation, accompanied by illustrations showing the mechanisms responsible for the morphology evolution due to stretching and compression [336].

However, despite the vast body of literature on biodegradable polyurethanes for tissue engineering, very few people have used this material in 3D printing applications, and to date no groups have used it in filamentary extrusion 3D printing techniques that could enable cell alignment. Chen *et al.* used fused deposition modeling 3D printing to melt extrude a composite thermoplastic polyurethane (TPU) / poly(lactic acid) (PLA) / graphene oxide material with 3T3 fibroblasts, and with graphene oxide loading at different amounts throughout the polymer matrix [338] (**Figure 2.56**). As a second 3D printing approach, Hung *et al.* developed a method to incorporate biodegradable polyurethane nanoparticles into a water-based ink that was seeded with chondrocytes [339]. However, since these methods relied on cooling from high temperatures and water evaporations for the structures to solidify, the polyurethane polymer chains themselves were not significantly extended during either of these printing processes. Indeed, there is no mention or demonstration of cell elongation in any figures that show cell behavior on the surface of the constructs.
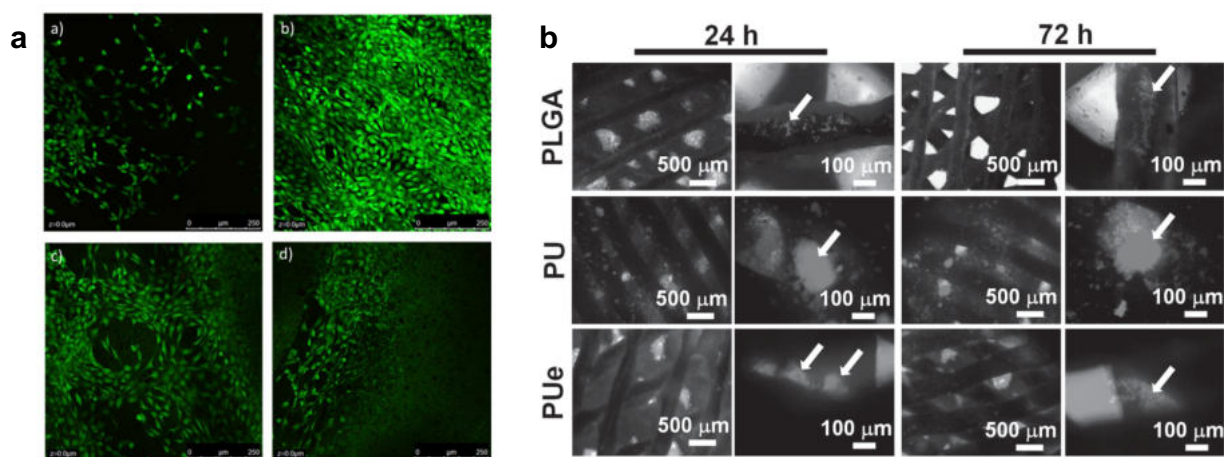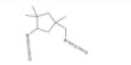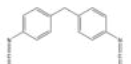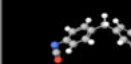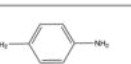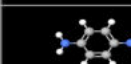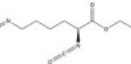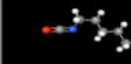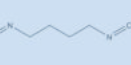
Figure 2.56. No obvious cell elongation or alignment is seen prior research approaches involving 3D printing of biodegradable polyurethane materials. (a) Fused deposition modeling heat deposition method. 96-hour cell culture results of 3T3 cells on 3D printed polyurethanes with different graphene oxide loading [338]. (b) Extrusion of polyurethane nanoparticles within a water-based ink. The morphology and proliferation of chondrocytes in 3D-printed scaffolds do not show cell alignment [339].

To optimize the potential for densification hardening, the diisocyanate hard segments can be analyzed for their ability to hydrogen bond with one another. Linear and ring-containing diisocyanates exhibit a higher degree of hydrogen bonding with neighboring hard segments due to their propensity to closely stack together [340-344]. However, ring-containing hard segments also tend to degrade or metabolize into toxic benzene ring-containing molecules, as with toluene diisocyanate, which has had several public health concerns to their carcinogenic potential [345,346]. Thus, several commonly-used diisocyanate hard

segments for tissue engineering applications were compared for (1) their propensity for hydrogen bonding based on their molecular structure and (2) their biocompatibility by analyzing toxicity information (**Table 3).** Butane diisocyanate **(**BDI) is determined to be the ideal diisocyanate hard segment for biodegradable, biomimetic TM grafts, as its short, linear structure enables close packing of hard segments, and it degrades into putrescine, a molecule found naturally in the body, and therefore has been shown to have high biocompatibility [347-356,322]. Additionally, three of the current medical devices– Lacthane[TM] wound and nasal dressing, Actifit[TM] for meniscal repair, and SynBioSys[TM] for stent coatings are known to contain BDI as their hard segment [357]. Therefore, BDI appears to be a suitable hard segment choice for creating biodegradable polyurethanes due to its propensity to hydrogen bond and its likely safe degradation byproducts.

Table 3. Comparison of possible hard segments for use in biodegradable polyurethanes.

	2D Structure	3D Structure	Hydrogen Bonding	Biocompatibility
IPDI isophorone diisocyanate			Low	Intermediate
MDI 1,4-methylene diphenyl diisocyanate			Intermediate	Low
PPDI 1,4-phenylene diisocyanate			High	Low
LDI lysine diisocyanate			Intermediate	High
HDI hexamethylene diisocyanate			High	Intermediate
BDI 1,4-butane diisocyanate			High	High

In addition to the hard segment which creates the urethane bonds, various chain extenders can be used to impart other bonds into the polymer backbone. Additionally, these chain extenders can increase the molecular weight of the final polymer, providing additional mechanical robustness. These chain extenders typically are a dihydroxy (creating additional urethane bonds) or a diamine (creating urea bonds) between the hard segment free ends. One popular chain extender is 1,4-butanediamine (BDA), commonly known as putrescine, which is also the byproduct of BDI as well and found normally in the body, playing an important role in the regulation of division, differentiation, and maturation of cells [358]. Numerous research groups have used BDA with success in polyurethane formulations [313,317,318,322,359-361]. Thus, BDA provides

the potential to increase the molecular weight of a polyurethane without introducing additional potentially toxic byproducts following degradation.

Importantly, many of these previously designed biodegradable polyurethanes are thermosets. Thermoset polyurethanes require solvation in an organic solvent, such as acetone, HFIP, or toluene to enable sufficiently low viscosity for 3D printing. However, these solvents often take hours or days to evaporate from the polymer, inhibiting the formation of hydrogen bonds between hard segments and creating a longer period of time over which polymer chains can relax to a random configuration [362]. Thus, synthesizing a version of polyurethane that is able to exhibit rheological properties for 3D printing while eliminating the need for solvent evaporation is a promising direction. Furthermore, it may be ideal to extrude the biodegradable polyurethane inks at lower temperatures, as processing temperatures have been shown to have a strong influence on the morphology and properties of thermoplastic polyurethanes, with samples processed at higher temperatures exhibiting a lack of large hard segment agglomerates and a smaller strength for strains up to 250% [363]. Additionally, high processing temperatures could cause premature degradation of the polymer and a resultant lower molecular weight and mechanical properties [364,365,366].

To create a biodegradable polyurethane, the polyol segment usually contains hydrolysable bonds, such as esters, ethers, or carbonates. Commonly, chain extenders are also used to increase the molecular weight of the polyurethane or add additional bonds, such as urea bonds. These bonds undergo hydrolysis in the presence of water to break the polymer backbone (**Figure 2.57**).
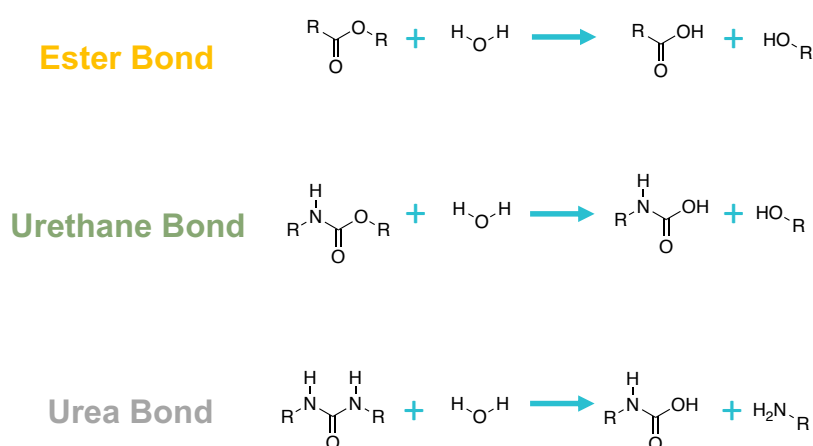
Figure 2.57. Hydrolysis of bonds commonly found in biodegradable polyurethanes. Ester, urethane, and urea bonds enable biodegradation.

Thus, most *in vitro* polyurethane degradation studies have been conducted in saline solutions, including phosphate buffered saline (PBS). Guan *et al.* observed 10 – 50% mass loss in PBS after 56 days depending on the soft segments used [318], whereas Guelcher *et al.* observed 15 – 27% mass loss in PBS after 8 months [367]. However, the enzymatic and inflammatory cell environment in the body makes it difficult to predict the *in vivo* behavior of an implant in an *in vitro* setting. The phospholipase A_2 pathway is one of the primary cell signaling events in inflammation and has been shown to be associated with macrophage-mediated polyurethane biodegradation [368]. Monocyte-derived macrophages (MDM) have emerged as the predominant cell type that is orchestrating the damage in biodegradation processes. However, neutrophils, or polymorphonuclear cells (PMN), are the first phagocytic cells to respond to an implanted device, while MDMs are the most abundant phagocytic cells at the time of explant [369]. MDMs and PMNs secrete a cocktail of oxidative and hydrolytic enzymes, including serine protease and cholesterol esterase. Although MDMs appear to be the primary cell line responsible for the hydrolytic degradation of biodegradable polyurethanes, primary harvesting from blood does not allow for continuous and homogenous culture, leading to inconsistencies and irreproducibility. The U937 cell line was originally derived from a patient with diffuse histiocytic lymphoma. Once differentiated, U937 cells develop the characteristics of mature MDMs, including an increase in size, lobed nuclei, and adhesion to a material surface. Thus, groups have been culturing biodegradable polyurethane samples alongside MDMs [370,371], PMN cells [371], or U937 cells [368,372] and observing the degradation rate. Labow *et al.* found that their MDM cell system had 5 – 10 times the degradative potential towards PEUU when compared to those cultured in a PMN cell system, as determined by the release of radiolabeled components [371]. Additionally, Matheson *et al.* found that both U937 cells and MDMs elicited comparable radiolabel release and esterase activity, secreting both monocyte-specific esterase and cholesterol esterase enzymes [372].

However, due to challenges to culture these cells *in vitro* and unclear relevant to the precise biologic environment of the tissue, many research groups have attempted to mimic the enzymatic conditions found in the body through the addition of enzymes including thiol protease [373,374], serine protease [375], urease [254,376], esterase [377,378], and lipase [360,379-381]. These enzymes have a substantial impact on degradation; for example, Ma *et al.* observed 80 – 90% mass loss of polyurethanes comprising ester-diol soft segment, BDI hard segment, and BDA chain extender after 3 weeks in 100 U/mL lipase [381]. Additionally, Nelson *et*

al. used 100 U/mL lipase to investigate growth factor release from polyurethanes from ester-diol soft segment and BDI hard segment [380]. Thus, it is clear that a wide range of *in vitro* degradation rates can be determined based on the testing conditions used. While lipases pose a suitable solution to mimicking *in vivo* conditions, it must be noted that the TM is located at an air-air interface, unlike most other tissues in the body which are surrounded by fluid and enzymes. Thus, these approximately *in vitro* environments may widely differ from the actual *in vivo* degradation rate of the material once implanted in the TM.

Encouragingly, implants created from biodegradable polyurethanes have been successfully implanted *in vivo* by other research groups with little toxic effects observed. Multiple groups studied material degradation *in vivo* by implanting the material subcutaneously [356,361,382-389]. Many of these studies showed good incorporation with native tissue along with angiogenesis. Shen *et al.* synthesized a biodegradable polyurethane that was implanted subcutaneously in rats [385]. After 7 days, they found the grafts enclosed in the skin hypodermis. By day 49, the blood swelling was comparatively reduced, inflammatory cells filled the circumference of the material, and angiogenesis was observed (**Figure 2.58**). Additionally, van Minnen *et al.* studied the *in vivo* degradation of a porous polyurethane based on a hard segment of BDI and a soft segment of DL-lactide-co-caprolactone [356]. After 1 week of subcutaneous implantation in rats, the authors observed macrophages, and after 4 weeks, they saw macrophages containing polyurethane pieces, suggesting phagocytosis. At 26 weeks, the polyurethane samples had completely resorbed, with few macrophages noticed in the lymph nodes. Similarly, Asplund *et al.* studied the *in vivo* subcutaneous degradation of a polyurethane in rats [313]. After 1 week, there was an infiltration of ED1 positive macrophages close to the implant surface, an outside layer of fibroblasts, and some collagen formation. After 6 weeks, the foreign body capsule had matured, displaying lower numbers of interfacial macrophages and increased collagen in the fibrotic capsule. The authors found that degradation rate was dependent on the soft segment structure, with a higher rate of degradation for polyester-dominating polyurethanes. Overall, the *in vivo* results from previous research suggest good integration and vascularization of polyurethanes, making them a promising material for TM grafts. However, to date, no researchers have investigated ototoxicity of biodegradable polyurethanes. Thus, our findings will provide novel information on the utility of these materials for applications in the ear.
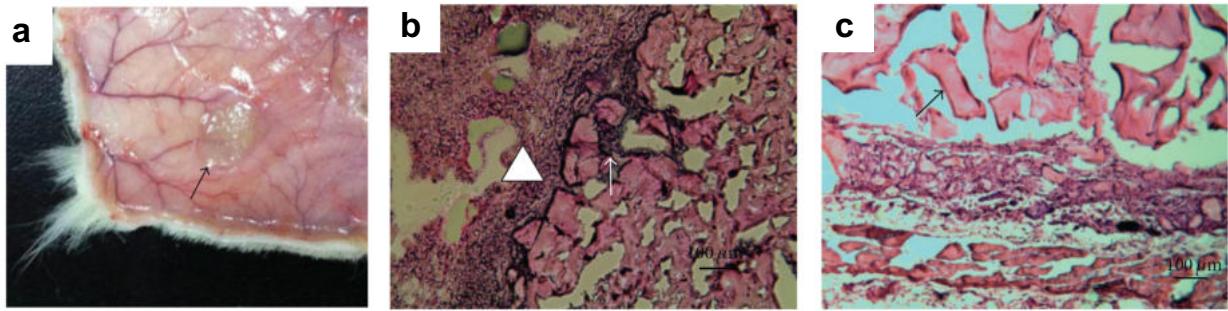
Figure 2.58. Degradation and integration of subcutaneously implanted biodegradable polyurethane. (a) Appearance of subcutaneously implanted membrane in the back of SD rats for 70 d; arrow indicates the location of the material. (b) H&E staining of microtome section after 21 d implantation; white triangle and arrow indicate the site filled with inflammatory cells. (c) H&E staining of microtome section after 70 d implantation. Arrow indicates the biodegraded fragment [313].

In addition to looking at subcutaneous degradation, several research groups have utilized biodegradable polyurethanes to create tuned grafts and devices for *in vivo* use in specific applications, including vascular grafts [390,391], abdominal defect grafts [392], and myocardial patches [393]. Hashizume *et al.* created myocardial onlay support patches from poly(ester urethane) urea (PEUU), poly(ester carbonate urethane)urea (PECUU), and poly(carbonate urethane) urea (PCUU) for a rat model of ischemic cardiomyopathy [393]. Besides material degradation and integration, they looked at functional outcomes via echocardiography. They found that the end-diastolic area for the PEUU group was significantly larger than for the PECUU or PCUU groups, and histological analysis showed the greatest vascular density in the infarct region for PECUU [393]. As PECUU is slower in degrading, the authors noted that the degradation rate influences the function, with a moderately slow degrading PECUU patch providing improved outcomes. Thus, when designing TM grafts, functional implications of degradation rate on acoustic performance should also be considered. Another relevant application was the creation of a composite PEUU with extracellular matrix (ECM) gel for the repair of abdominal wall defects by Hong *et al.* [392]. The composites and control scaffolds of solely PEUU were implanted into full-thickness abdominal wall defects of rats. After 4 weeks, histological staining demonstrated cellular infiltration into the composite scaffold, while there was limited infiltration to the PEUU scaffold. The composite scaffolds adopted similar mechanical properties to the native abdominal wall. This paper showed the potential of PEUU composite materials to enable soft tissue repair. Thus, when designing a material for TM grafts, a similar composite approach can be taken to enhance tissue ingrowth.

To enhance the degradation rate of the polyurethane, one can alter the backbone chemistry in the hard segment to include the incorporation of ester, ether, or carbonate bonds. Additionally, one can also look to enhance the overall surface area exposed to enzymatic fluids in the body. By incorporating a fugitive porogen-like material into the polymer that can be leached from the composite material via water, heat, or another method, an interconnected network of pores can be formed within the polymeric structure that enables fluid absorption throughout the structure. Thus, a bulk degradation process can be encouraged, rather than limiting the degradation process to surface degradation at the beginning [394-397]. Other researchers have utilized porogens including salt [398-400], sucrose [398,401], wax [402], gelatin [403,404], and polyacrylate microspheres [405,406] for both increasing degradation rate and cellular ingrowth into the material. However, none of these compounds are easily miscible with polyurethanes. Additionally, the large particle size of salt, sucrose, and microspheres is challenging to incorporate with high-resolution extrusion-based 3D printing technologies. Therefore, a material that can be easily incorporated into the polyurethane inks without significant impact on the 3D printing resolution must be identified.

Short-chain water soluble polymers including polyethylene glycol (PEG) have been utilized in the formation of interconnected nanoporous networks within structures due to its biocompatibility and solubility in water. Columbus *et al.* investigated the incorporation of PEG at 50 wt% in various molecular weights into PCL scaffolds with high success [407]. The resultant scaffolds had an inner diameter of 4 mm with a wall thickness of 80 μm (**Figure 2.59**). They found that a narrower pore size was observed when PEG with a smaller molecular weight (MW = 3400 Da) was used as compared to a larger molecular weight (MW = 8000 Da). Microcomputed tomography (micro-CT) studies demonstrated that 78% of pores fell within the 12 – 24 μm diameter range for those scaffolds created using the smaller molecular weight PEG, resulting in better retention of morphological and mechanical properties during degradation. Similarly, Courtois *et al.* investigated the effect of PEG loaded at 20 wt% in acrylate polymer scaffolds at PEG molecular weights including 1500, 4000, 10,000, and 20,000 Da [408]. Similarly, they found that smaller molecular weight PEG led to smaller average pore sizes and a greater overall surface area exposed (**Figure 2.60**). Therefore, smaller molecular weight PEG, such as 1500 Da, can lead to scaffolds containing interconnected pores with greater overall surface area exposed than those created with larger molecular weight PEG following leaching from the grafts. While these pores are not large enough for cell infiltration, they can promote

absorption of growth factors and nutrients, indirectly enhancing cell proliferation and tissue ingrowth. PEG has been used successfully in various drug delivery applications for the ear [409-411]; thus, we predict that any residual amounts of PEG in the grafts following leaching will not cause ototoxic effects to the cochlea, which will be described in **Chapter 5.**
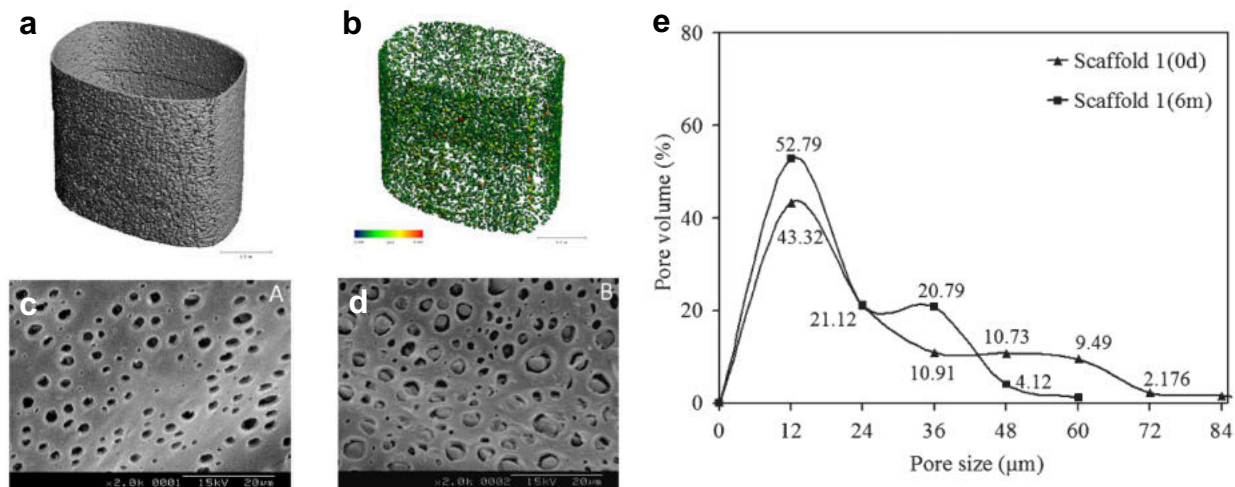
Figure 2.59 Porosity in PCL scaffolds induced by 50 wt% incorporation of PEG in MW = 8000 Da. (a) Micro-CT analysis and (b) 3D reconstruction showing the porosity distribution within the scaffold after leaching. SEM images of scaffolds (c) before and (d) 6 months after degradation. (e) Histogram showing the porosity distribution of scaffold before and after 6 months degradation [407].
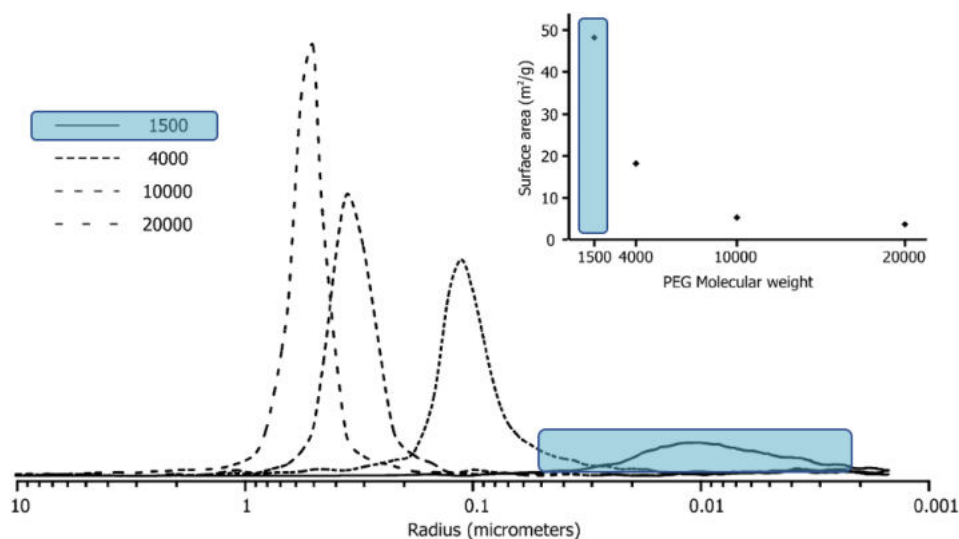
Figure 2.60 Median pore diameter of the monoliths synthesized using PEGs of different molecular weight. The insert in the top-right corner shows surface area exposed vs. molecular weight of the PEG in the porogen. Blue indicates data for PEG with a molecular weight of 1500 Da [408].

2.8 Conclusions

TM perforations represent a significant healthcare burden around the world by impacting hearing and by creating an opening to the middle ear space for pathogens to enter. As the TM plays a crucial role in transducing sound pressure waves into mechanical motion of the ossicles, its structure highly correlates to its function. In particular, the anisotropic circumferential and radial collagen architecture in the lamina propria of the TM have been shown to be crucial for allowing proper vibration, and therefore, sound conduction across the 20 – 20000 Hz frequency range of human hearing. Thus, tympanoplasty procedures are necessary to close the perforation and to restore normal hearing and barrier functions. The most commonly used graft materials are autologous tissues, such as fascia, cartilage, fat, and dermis, harvested from the patient. Unfortunately, these autologous tissues do not degrade or remodel into native TM tissue. The implications of this are twofold: (1) poor healing rates due to the lack of true integration of the graft material, and (2) poor hearing outcomes due non-ideal acoustic properties of the reconstructed TM.

Multiple research groups have investigated the use of non-autologous graft materials in humans and in animal models for chronic TM perforations, including Biodesign® Otologic Repair Graft. However, none of these materials have been able to recapitulate the circumferential and radial architecture of the TM, nor have they been able to demonstrate restoration of sound conduction across the range of human hearing. Additionally, relatively few biodegradable materials have been explored. Such materials may ultimately improve healing by allowing for graft integration and the gradual disappearance of foreign sites. 3D printing represents a promising manufacturing method for biomimetic TM grafts from custom materials. The creation of biomimetic grafts can allow for both the investigation of the acoustic implications of this circular and radial architecture. Thus, advancements in the design and production of biomimetic TM grafts will further the scientific understanding of the TM's structural role in middle ear mechanics. Additionally, designing biodegradable and biocompatible input materials for use in architecturally biomimetic TM grafts will hopefully improve healing and hearing outcomes for all treated patients. Such grafts may also minimize patient morbidity through enabling minimally invasive tympanic membrane repair.

Chapter 3

Materials Composition and Architecture Effects on Sound-Induced Motion
of 3D Printed Tympanic Membrane Grafts

This chapter has been adapted from the following publication:

Kozin, E. D., Black, N. L., Cheng, J. T., Cotler, M. J., McKenna, M. J., Lee, D. J., Lewis, J.A, Rosowski, J.J, & Remenschneider, A. K. (2016). Design, fabrication, and in vitro testing of novel three-dimensionally printed tympanic membrane grafts. *Hearing Research*, *340*, 191-203.[412]

3.1   Introduction

The tympanic membrane (TM) is an exquisitely tuned structure that captures and transmits sound from the environment to the ossicular chain of the middle ear, enabling conversion of sound pressure waves into mechanical motion. The size and structure of the TM enables impedance matching to the cochlea and permits effective transmission of mechanical energy through the ossicles to the inner ear where movement of perilymph results in stimulation of the hair cells, which convert mechanical energy into neuronal impulses. The conversion of environmental sound to mechanical motion is the critical function of the TM, which possesses a host of vital structural elements including a conical shape, arranged collagen fiber architecture, and three-layered architecture (**Figure 2.3**). These structural features work in concert to enable the effective transmission of sound across a wide range of amplitudes and frequencies (humans: 20 Hz – 20 kHz) and result in complex movements that vary in magnitude from picometers to microns [413,414] The dynamic functional properties of the TM are contained in a structure that is approximately 100 μm thick.

Damage to the tympanic membrane, such as from chronic otitis media (COM) or traumatic perforation, results in hearing loss due to ineffective sound transmission [415,416] Suppurative COM affects over 30 million individuals worldwide each year, leading to a significant health care burden [3] The most common long-term complication in patients with COM is persistent tympanic membrane (TM) perforation and conductive hearing loss. Damage to the TM is surgically correctable via a procedure called tympanoplasty and is performed tens of thousands of times each year in the United States [417]. Successful tympanoplasty re-establishes efficient sound transmission from the environment to the ossicular chain, as well as recreates a robust barrier between the ear canal and middle ear.

Historically, cadaveric tympanic membranes [418,419], bovine pericardium [420], and synthetic matrices [421,422] are used as TM grafts with moderate success in tympanoplasty. Today, autologous temporalis fascia

and cartilage are commonly harvested from the patient at the time of surgery for use as graft materials. However, these materials are far from perfect. Temporalis fascia and cartilage may have intrinsic defects rendering them susceptible to the effects of ongoing COM [423,424] Such defects may not be perceptible at the time of surgery, leading to unpredictable outcomes. Patients who undergo tympanoplasty for COM are at significant risk for re-retraction and re-perforation of their grafts, necessitating revision surgery. Large published series document revision tympanoplasty rates for patients with COM around 28% [425]. Revision procedures often leave the surgeon without adequate graft materials for TM reconstruction. Collectively, current autologous graft materials stand to benefit from refinement in order to improve patient outcomes and decrease surgery-related morbidity.

Here, we build on recent advances in multi-material, 3D printing of biocompatible polymers and hydrogels [271-280] to fabricate biomimetic TM grafts with superior acoustic and mechanical properties compared to current graft materials, e.g. temporalis fascia, used for surgical repair of the TM. Specifically, we explore the use of bioresorbable (polylactic acid [PLA] and polycaprolactone [PCL]) and non-resorbable (polydimethylsiloxane [PDMS]) polymers as candidate materials, given their successful use in other implantable applications, particularly in the auditory space [426-433].

Using 3D printing, we created biomimetic TM grafts of varying circumferential and radial fiber count, which is subsequently infilled with a fibrin-collagen composite. We then characterized their acoustic and mechanical properties, which strongly depend on both the polymer composition and printed geometry. Akin to the human TM, these biomimetic TM grafts exhibit simple surface motion patterns at lower frequencies (400 Hz) with a limited number of displacement maxima. At higher frequencies (>1000 Hz), the displacement patterns are highly organized with multiple areas of maximal displacements separated by regions of minimal displacement. By contrast, temporalis fascia and planar polynitrile sheets (controls) exhibit either asymmetric or less regular holographic patterns. We also find that biomimetic TM grafts display a consistent sound induced point velocity across specimens and frequencies, while the velocity of human fascia varies widely between specimens and across frequencies. Biomimetic TM grafts are also more mechanical resilient than temporalis fascia. Our 3D printing platform offers the ability to both customize biomimetic TM grafts from both bioresorbable and non-resorbable materials and to systematically probe the effects of their complex architecture on key performance properties.

3.2 Experimental Methods

3.2.1 Ink Formulation and Rheology

Inks for 3D printing for the three biocompatible materials are formulated and characterized. PLA inks are created by dissolving PLA-Flex filament (Orbitech, Germany) at 20 wt% in hexafluoroisopropanol (HFIP, 99%, Strem Chemicals Inc., USA). PCL inks are created by dissolving PCL (MW = 43 kDa, Polysciences, USA) at 50 wt% in toluene (ACS Reagent Grade, Ricca Chemical Company, USA). PDMS inks are created from a 10:1 ratio of base to catalyst by weight of SE1700 (Dow Corning, USA). A speedmixer (AE-310, Thinky Corp, Japan) is used to efficient mix each of these ink formulations.

The ink rheology is measured using a controlled-stress rheometer (Discovery HR-3 Hybrid Rheometer; TA Instruments, USA) equipped with a 40 mm, 2.005° steel cone plate geometry. All tests are performed at room temperature. Viscometry measurements are carried out on each ink by sweeping the shear rate from $0.01 - 100$ s^{-1} at 1 Hz. While oscillatory measurements are carried out on each ink by performing stress sweeps from 0.0001 Pa to 10000 Pa at 1 Hz.

3.2.2 3D Printing of Biomimetic Grafts

The design of biomimetic TM grafts is based on direct observations of the ultrastructure of the normal human TM [4,434,435]. Patterns of radial, circumferential, and parabolic fibers are qualitatively analyzed from scanning and transmission electron microscropy images to determine the fibrous connections attaching the TM graft to the fibrous/bony annulus. Specifically, our biomimetic TM graft design (15 mm in diameter), which consists of a series of circumferential and radial fibers and an outer border region for clamping the grafts (**Figure 3.1b**). The outer region adds an additional 5 mm circumferentially, resulting in a TM graft with an overall diameter of 25 mm. Using a software package, AeroBasic G-code (Aerotech, USA), we generate the x-y-z printpath required to pattern the circumferential and radial fibers along with an inner (open) region of prescribed diameter and the border region.

The biomimetic TM grafts are printed using a custom-designed 3D printer with an overall build volume of 725 mm × 650 mm × 150 mm (ABG 10000, Aerotech Inc., USA) (**Figure 3.1a**). It is equipped with four independent, z-axis-controlled ink reservoirs, allowing for multi-material printing through filamentary extrusion with features as small as 1 μm in diameter. The inks are loaded into syringes with plungers (EFD Inc., USA). PLA and PCL-based grafts are printed through a straight steel nozzle (inner

diameter, ID = 100 μm, Nordson EFD, USA) (**Figure 3.1c**), while PDMS-based grafts are printed using tapered steel nozzle (ID = 100 μm, GDP Global, USA). During 3D printing, a second set of inks of the same composition are co-printed using a larger tapered plastic nozzle (ID = 610 μm, GDP Global, USA) to generate the desired border region (**Figure 3.1d**).

Following printing, the biomimetic TM grafts are either dried or thermally cured to drive solidification. Both the PLA and PCL grafts solidify upon solvent evaporation inside of fume hood. PDMS grafts contain a platinum catalyst, which is activated at high temperatures to induce crosslinking. The printed PDMS grafts are cured in an oven (Fisher Scientific, USA) at 100ºC for 2 h. Graft architectures are visualized using a Keyence digital microscope (VHX2000, Keyence, Japan). Fiber widths are measured using ImageJ software (National Institutes of Health, USA) for on TMs produced from the same ink (n = 5 each 8C/8R and 16R/16R). Fiber thicknesses are measured using a digital micrometer (Mitutoyo, Japan).
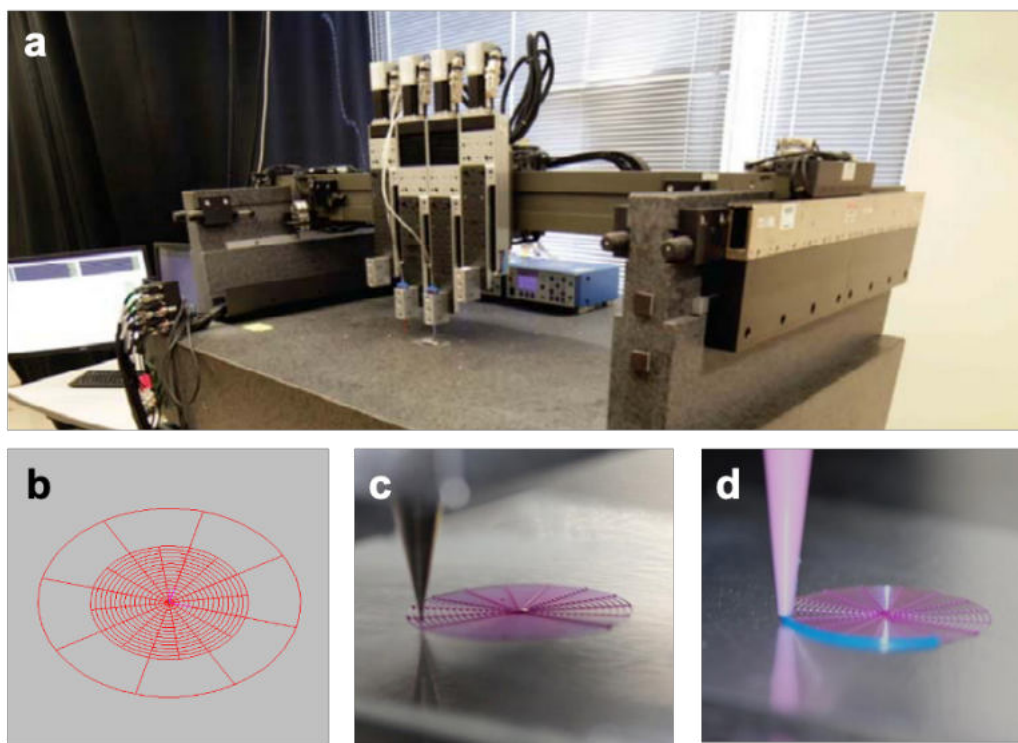
Figure 3.1. 3D printing process for fabricating TM composite grafts with an inner diameter of 15 mm and an outer border diameter of 25 mm. (a) The multi-material 3D printing apparatus composed of an X-Y air bearing gantry on a granite slab with independent print heads. Total build area is 750 mm x 650 mm. (b) A biomimetic circular and radial architecture is designed in Aerobasic G-code, along with a surrounding region for clamping. (c) The inner circumferential and radial fibers are printed first using a 100 μm steel nozzle at a 15 mm diameter. (d) Printer switches to another nozzle containing the same material (with added blue colorant) with a plastic nozzle to print the outer border at a 25 mm diameter. Graft shown is from the PDMS ink, with pigment added for improved visualization.

Both biomimetic flat grafts with 8 circular and 8 radial print lines (8C/8R) or 16 circular and 16 radial print lines (16C/16R) are 3D printed from PDMS ink to investigate the impact of conical height on sound conduction. Conical substrates with an inner diameter of 15 mm and a center height of 0, 1, 2, and 3 mm are 3D printed using stereolithography (HTM 140, Aureus, EnvisionTEC, USA). A layer of Pluronic F127 (Sigma-Aldrich, USA) at 40 wt% in water is used to coat the surface of the substrates to enable easy removal post-curing. For creating conical 8C/8R TM grafts, the G-code program is modified to incorporate z-height changes imposed by the conical substrate, while retaining the border region with an outer diameter of 25 mm (**Figure 3.2**). As the changing z-height on the substrates creates less contact with the printing nozzle, both the inner diameter and border region are printer from tapered tip 410 µm plastic nozzles (GDP Global, USA) at a layer height of 200 µm. The conical PDMS TM grafts are placed in an oven (Fisher Scientific, USA) at 100ºC for 2 h. They are then placed in water to dissolve the Pluronic F127 coating and thereby release the grafts from the underlying substrates.
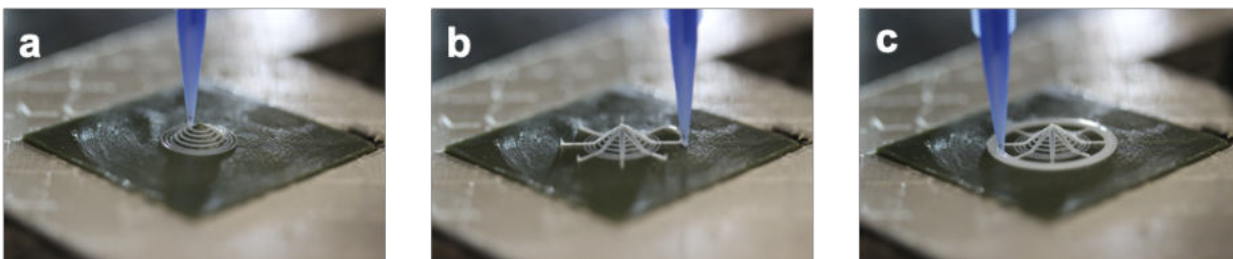
Figure 3.2. 3D printing of biomimetic TM composite grafts. Grafts have an inner diameter of 15 mm and an outer border diameter of 25 mm with a conical height. A conical substrate 3D printed using stereolithography is coated in 40 wy% Pluronic F-127 prior to printing. (a) A custom G-code program is used to 3D print a series of 8 circular lines on the conical surface. (b) A series of 8 radial lines are 3D printed down the height of the cone that extend to the outer diameter edges. (c) A border region of 25 mm is 3D printed for clamping grafts during testing.

3.2.3 Infilling Grafts with Composite Hydrogel

Using plasma treatment (Femto PCCE plasma cleaner, Diener Electronic, Germany), the PDMS grafts are transformed from their initially hydrophobic state to a hydrophilic state. Each graft (PLA, PCL, and PDMS) are then infilled with a biodegradable hydrogel to create an environment that mimics the natural extracellular matrix (ECM) of the human TM [436,437]. The infill is prepared by first creating a solution of 80 mg/mL fibrinogen (Calbiochem, USA) from bovine plasma in Dulbecco's Phosphate-Buffered Saline (DPBS).

This solution is allowed to sit on the hotplate at 37ºC for 1 h to allow for complete solubilization of the protein. Next, a solution of 3 mg/mL rat collagen I (Cultrex, Trevigen, USA) is neutralized with a buffer containing N-2-hydroxyethylpiperazine-N'-2-ethanesulfonic acid (HEPES) and DPBS. The two solutions are mixed to obtain a final infill concentration of 40 mg/mL fibrinogen and 1 mg/mL collagen. From this bulk mixture, 100 μL is pipetted into 2 μL of human high activity thrombin enzyme at 1000 U (Calbiochem, USA) ($V = \pi r^2 h$ with 100 μl volume infill over 7.5 mm radius). The resultant aliquot is evenly deposited over the top of each biomimetic TM graft via a pipette to obtain a uniform infill between the fibers (**Figure 3.3**). The slides are covered to prevent evaporation during the enzymatic conversion process. The TM grafts are placed on Bytac® (Saint-Gobain, France) coated glass slides to be easily removed following curing. These slides are placed on top of a hotplate held at 37ºC. Final TM composite grafts, consisting of the 3D printed polymeric skeleton and hydrogel composite infill, are removed from the slide and placed in DI water. The infilled composite grafts are left in an incubator at 37ºC until testing is performed. The uniform infill creates a confluent membrane structure for sound transmission and acoustic testing.
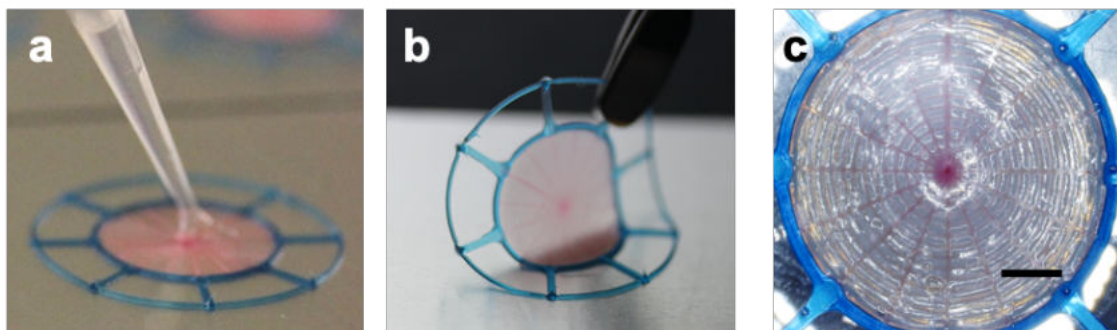
Figure 3.3. Infilling biomimetic TM grafts with fibrin/collagen solution. (a) A pipette is used to infill the inner circular and radial 3D printed and cured graft with 100 μL of a fibrinogen/thrombin/collagen solution. (b) TM grafts are easily removed from the Bytac® slide coating. (c) Digital microscopic image showing the infill surrounding the fibers. Graft shown is from the PDMS ink, with pigment added for improved visualization. Scale bar is 2 mm.

3.2.4 Controls for Mechanical and Acoustic Measurements

For control experiments, human temporalis fascia and planar polynitrile sheets (Kimberly Clarke, USA) are used to compare with TM composite grafts in mechanical and acoustic studies. Human temporalis fascia is harvested in standard surgical fashion from fresh, unfixed cadaveric specimens for research use. Briefly, a vertical temporal scalp incision is made with a scalpel and the true temporalis fascia is exposed after clearing the temporoparietal fascia. The true temporalis fascia is incised and separated from the

underlying temporalis muscle. A circular piece, approximately 30 mm x 30 mm, is harvested from the superior, thin region of the temporalis fascia. Once harvested, any soft tissue including any attached muscle or fat, is removed. The fascia is then washed in sterile saline, cut to 25 mm x 25 mm, and mounted for acoustic testing using the same techniques as described above. Polynitrile sheets are obtained from standard surgical gloves.

3.2.5   Customized TM Graft Holders for Acoustic Measurements

Customized TM graft holders are designed and fabricated to facilitate *in vitro* acoustic testing (**Figure 3.4**). These holders ensure secure placement and peripheral clamping of TM composite graft, temporalis fascia, or polynitrile sheet during testing. The holders consist of a base with an inner hole diameter of 9 mm, well diameter of 25.5 mm, outer diameter of 35 mm, inner well depth of 3 mm, and total length of 30 mm. The cap had the same inner and outer radii as the base with an extruded portion diameter of 25 mm, extruded portion length of 2.5 mm, and total length of 5.5 mm. The cap is designed to completely cover the border region, ensuring that only the inner graft region filled with collagen/fibrin is subjected to acoustic testing. Each holder is fabricated using an Objet Connex 500 printer with VeroBlue RGD840 rigid opaque material (Stratasys, USA). The holders have four vertical pegs with a diameter of 2.6 mm that secure the border region thereby restricting it in-plane (x-y axis) motion. They also have side pegs, which secure the cap onto the base with rubber bands to restrict any out-of-plane (z-axis) motion outside of the inner hole. Prior to testing, the grafts are placed in the top region of the holder, exposing the inner 9 mm of the graft, similar to the diameter of the human TM.

Figure 3.4. Custom-built holders for digital opto-electronic holography (DOEH) and laser Doppler vibrometry (LDV). (a) Customized 3D printed holder is designed for use in DPOE and LDV experiments. (b) 3D printed holder open, without a graft. (c) 3D printed holder containing a graft clamped and held together by rubber bands.

3.2.6 Digital Opto-Electronic Holography

Digital Opto-Electronic Holography (DOEH) interferometer records motion-induced holograms in real-time through two interfering laser beams, providing qualitative and quantitative full-field information on the sound induced motion of a membrane. The magnitude and phase angle of displacement of more than 400,000 points on the surface of the membrane can be acquired simultaneously. DOEH hardware and data acquisition techniques have been previously described by our research group [53,438,439] Briefly, each membrane is held in the customized holder placed against a sound coupler integrated into the interferometer camera head and oriented such that the surface of the membrane is orthogonal to the object beam of the laser. The sound coupler is connected to a sound source (CF1, Tuker-Davis Technologies, USA) to deliver continuous single tones at selected frequencies and at appropriate stimulus levels to the membrane surface. A calibrated ER-7C probe microphone (Etymotic Research, USA) measured sound pressure near the edge of the membrane. DOEH is operated in stroboscopic mode in which nine stroboscopic holograms of the membrane, phase-locked to stimulus phase of 0, $\pi/4$, … 2π, are used to derive a displacement vs time waveform for each point on the membrane surface, and Fourier transformation is used to compute displacement magnitude and phase at each point [438] (**Figure 3.5**).

Biomimetic TM grafts are mounted onto the customer holder: PDMS (n = 6), PLA (n = 6), and PCL (n = 6), temporalis fascia specimens (n = 2), and polynitrile planar sheets (n = 2). To increase the amount of reflected light from the TM composite graft surface, the graft is lightly painted with a solution of ZnO_2 powder and saline (Acros Organics, USA). This application of creating a reflective surface has previously been shown to not significantly change the acoustical/mechanical properties of the painted material [440]. The grafts are then subjected to continuous tones at four different frequencies across the human range of sound perception: 400 Hz, 1000 Hz, 3000 Hz and 6000 Hz. Sound intensity varied from 80-110 dB sound pressure level (SPL) at different frequencies to produce DOEH measurable fringes on the membrane surface. The displacement sensitivity of DOEH is 10-30 nm. The sound stimulus levels used in this study are within the linear response range of the human TM and middle ear [441,442]. Displacement of the membrane at each stimulus frequency is normalized by the stimulus sound pressure, monitored near the membrane surface. Displacement magnitude and phase are independently color mapped and compared between TM composite grafts and the two controls: fascia and polynitrile sheets.
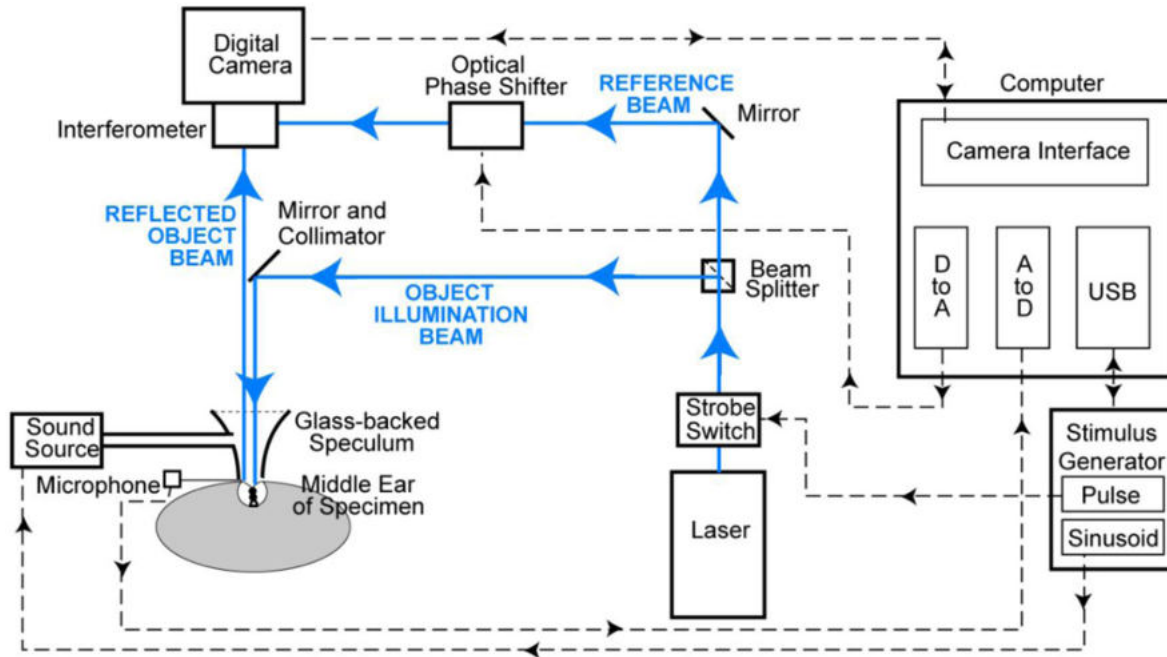
Figure 3.5. Setup for digital opto-electronic holography (DOEH). Experimental setup and schematic of opto-electronic holographic (OEH) interferometry system. The sinusoid acoustic stimuli are generated by a computer-controlled stimulus generator that drives an earphone. The sound pressure near the TM surface is monitored by a probe-microphone and recorded in the computer via an analog-to digital (A/D) converter. In stroboscopic holographic measurement mode, the laser beam (473 nm wavelength) is controlled by the 'strobe switch' (an opto-acoustic modulator capable of high-frequency switching) which generates a series of stimulus-phase-locked strobed laser pulses with a duration of 10% of the tonal stimulus cycle. The laser pulses are split into a reference beam and an object beam with a beam splitter. The reference beam is subjected to an optical phase shift that changes the optical path length by 0, 1/4, 1/2 or 3/4 of the optical wavelength, and the object beam is sent to illuminate the specimen through a mirror and collimator. The reflected object beam interferes with the reference beam producing interferograms that are recorded by the digital camera of the OEH system. The time varying displacement of the TM is measured by the computer as a series of stroboscopic holograms at different time instants and processed by computer to provide quantitative measurements of the deformations of the TM between two different time instants [438].

3.2.7 Laser Doppler Vibrometry

Laser Doppler vibrometry (LDV) hardware and data acquisition techniques have been previously described by our group [443,444]. In brief, measurements of the sound-induced velocity of the TM composite grafts, fascia and polynitrile sheets at the membrane's center point are made with a two dimensional LDV setup (Polytec OFV 501 fiber interferometer and OFV 2600 vibrometer controller; Polytec Inc., USA) focused on 2-3 50nm diameter polystyrene micro-beads placed at the graft's center. The sound stimulus for LDV measurements is broadband chirps containing frequencies of 200 Hz to 10 kHz. The stimulus signals are delivered to the CF1 sound source to produce sound levels between 80 – 120 dB SPL near the

membrane surface. The ER-7C probe microphone is used to monitor SPL near the membrane surface. At each measurement, the LDV and ER-7C microphone response signals to a series of repeated chirps are recorded through an A/D acquisition board running on a PXI system (National Instruments, USA) and averaged (n = 200). The membrane velocity measured by LDV is normalized by the sound pressure monitored by the ER-7C microphone. The sound-induced velocity of the surface of the graft holder is used to define a 'noise and artifact' level, which described the smallest discriminable velocity.

3.2.8 Mechanical Properties of Biomimetic TM Grafts

Biomimetic TM composite grafts along with both controls, fresh human temporalis fascia and polynitrile sheets, are subjected to repeated loading in tensile mode (Electroforce® 3200, TA Instruments, USA) to assess their mechanical strength and hysteresis. TM composite grafts are mounted at the inner border region of the grafts using tensile grips at a jaw gap of 1.2 cm. Temporalis fascia and polynitrile sheets measuring 25 mm x 25 mm are similarly mounted at a jaw gap of 1.2 cm. For DMA studies, in plane loading force (N) required to cycle the bottom motor through constant sinusoidal displacements of 2 mm in amplitude at a frequency of 20 Hz are recorded. Measurements are conducted over 60 sec to obtain sufficient data to observe any change in mechanical integrity over time. In plane load is compared between the beginning of the experiment and the end of the experiment to assess for evidence of hysteresis. Additionally, in plane loading is measured over a controlled displacement ramp up to 6.5 mm at a rate of 0.2 mm/sec to examine the relationship between load and strain for each material and fiber arrangement. TM composite grafts made of the same 3D printing material are compared to identify any mechanical differences in load between the fiber arrangements. All studies are conducted at a temperature of 25°C. To replicate the conditions in the operating room where fascia is directly harvested and subsequently implanted without any pre-stress, no materials are preconditioned.

To determine the robustness of the 3D printed fiber network, a connector loop is 3D printed in the center of 8C/8R (n = 3) and 16C/16R (n = 3) PDMS grafts prior to curing and infill. Custom holders are 3D printed that circumferentially clamp the grafts. The design of the holder from acoustic testing is modified to allow for clamping into tensile grips with a 10 mm bottom flat region while maintaining an inner clamping diameter of 9 mm. Extension is performed at a rate of 0.1 mm/sec until fiber fracture is observed. The spring constant of the grafts is calculated as the stress over strain up until fiber fracture.

3.2.9   Cellular Ingrowth onto Biomimetic TM Grafts

To determine the cellular ingrowth and remodeling potential of these biomimetic TM grafts *in vitro,* a custom setup is designed to investigate ingrowth from the circumference. PDMS molds are 3D printed to mimic the external auditory canal overlap of the TM grafts. The molds are designed with an inner diameter of 8.6 mm, outer diameter of 17.0 mm, inner well height of 0.86 mm, and an outer wall height of 1.15 mm. PDMS inks are created from a 10:1 ratio of base to catalyst by weight of SE1700 (Dow Corning, USA) and loaded into a syringe (EFD Inc., USA) with 610 µm plastic nozzles (GDP Global, USA). Following 3D printing, the molds are placed in an oven (Fisher Scientific, USA) at 100ºC for 2 h. Plasma treatment (Femto PCCE plasma cleaner, Diener Electronic, Germany). A cellular hydrogel solution is created by mixing 50,000 Human neonatal dermal fibroblasts (HNDFs), modified with enhanced green fluorescent protein (EGFP, λex = 488 nm), (Angio-Proteomie, USA) into a 40 mg/mL fibrin hydrogel solution. The outer ring of each molds is filled with the solution to create a cellularized ECM region.

The impact of material composition is investigated by creating 3D printed TM grafts of varying geometry (8C/8R and 16C/16R) from PDMS, PLA, and PCL inks (n = 3 of each group). PDMS, PLA, and PCL-based TM grafts are infilled with the hydrogel solution with and without 10 µg/mL bFGF (ab191756, Abcam, USA) (n = 3 of each group). Grafts are overlayed onto the molds **(Figure 3.6**), placed in 6-well plates, and cultured in Dulbecco's modified eagle medium supplemented with 862 mg·L-1 L-alanyl-glutamine (Gibco, USA) and 10% fetal bovine serum (FBS, ATCC, USA) in an incubator at 37°C with 5% CO_2 atmosphere. Cell medium is pre-warmed and replaced every 2 days.

To determine HNDF ingrowth, cellular proliferation is quantified at Day 31 after graft placement. The grafts are removed from the wells and placed into 6-well plates containing MTS tetrazolium colorimetric assay (ab197010, Abcam, UK). A volume corresponding to 10% of the culture volume of sterile MTS in phosphate buffer solution is added to each culture well an incubated for 1 h at 37°C with 5% CO_2 atmosphere. The solutions are then transferred to a 96-well microwell plate and measured used absorbance at 490 nm on a plate reader (Synergy HT, BioTek Instruments, USA). Absorbance readings show relative cell proliferation on each graft material type. Statistical significance is attributed to values of $p < 0.05$, as determined by an unpaired t-test.

To visualize cell ingrowth into the TM graft, PDMS grafts are fixed at day 92 or 134. On day 92, actin is visualized via ActinRed™ (555 ReadyProbes™, Thermo Fisher Scientific, USA) and collagen deposition is visualized via immunostaining for collagen I (1:500, rabbit monoclonal, ab138492, Abcam, USA). An upright confocal microscope (LSM710, Zeiss, Germany) is used in conjunction with objectives ranging from 5x to 20x and spectral lasers at wavelengths of 488 nm (GFP) and 647 nm (collagen I). For both actin and collagen I visualization, 3D projections and z-stacks are generated using manual and automated processes in Imaris (Imaris 7.6.4, Bitplane Scientific Software, Switzerland). At day 134, histological staining with Masson's Trichrome (Polysciences, USA) is performed on PDMS 8C/8R grafts per manufacturer's instructions. Masson's Trichrome is a three-color staining protocol whereby collagen is stained in blue, cytoplasm is stained in pink, and cell nuclei are stained dark brown. A Keyence digital microscope (VHX2000, Keyence, Japan) is used to visualize the histological staining.
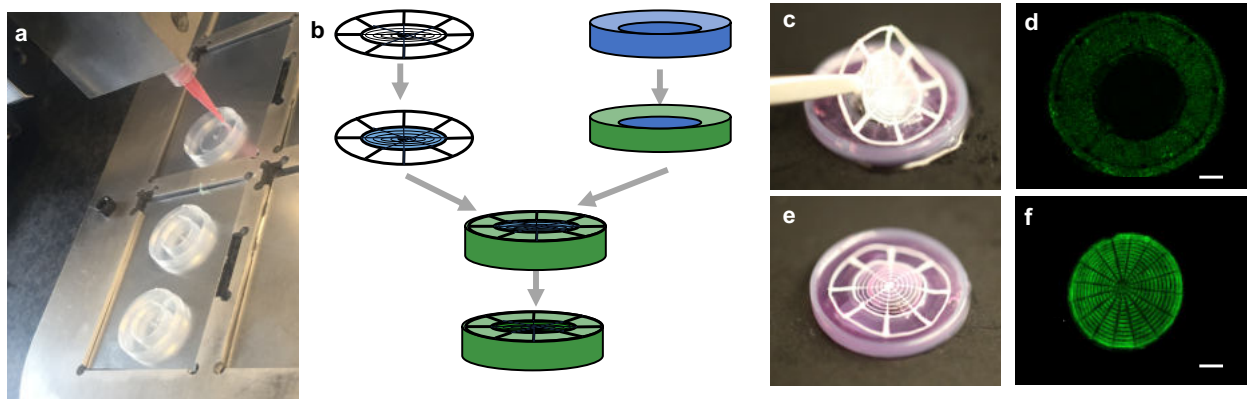
Figure 3.6. Cell ingrowth from EAC-mimicking molds. (a) Molds are 3D printed from a PDMS ink in a donut-like geometry. (b) Schematic showing the outer ring of the molds filled with a hydrogel solution. (c-d) TM grafts are laid onto molds containing GFP-expressing HNDFs, visualized by confocal microscopy. (e-f) Over time, the GFP-HNDFs begin to migrate into the grafts. Scale bars are 3 mm.

3.3   Results and Discussion

We first created viscoelastic inks composed of PDMS, PLA, and PCL for direct writing of biomimetic TM grafts. The PDMS ink exhibited shear thinning rheology and a shear elastic modulus of ~6000 Pa at low strains (**Figure 3.7a-b**). Additionally, the PDMS ink exhibits a yield stress behavior, which facilitates direct writing of filamentary features upon extrusion from a nozzle. By contrast, both the PLA and PCL inks exhibit Newtonian behavior with viscosity of ~20 Pa.s and far lower shear storage moduli of 10 Pa and 1

Pa, respectively (**Figure 3.7c-d**). While these inks are dominated by their loss modulus and do not have a yield stress across decades of strain shown, they rely upon solvent evaporation for solidification upon extrusion from the nozzle. This rheological behavior is less ideal for direct writing, as could lead to wetting and spreading as the ink exits the nozzle. However, the organic solvent components have a high vapor pressure ($P°_{HFIP}$ = 21.2 kPa at 25°C, $P°_{toluene}$ = 3.8 kPa at 25°C) [445,446], enabling rapid evaporation.
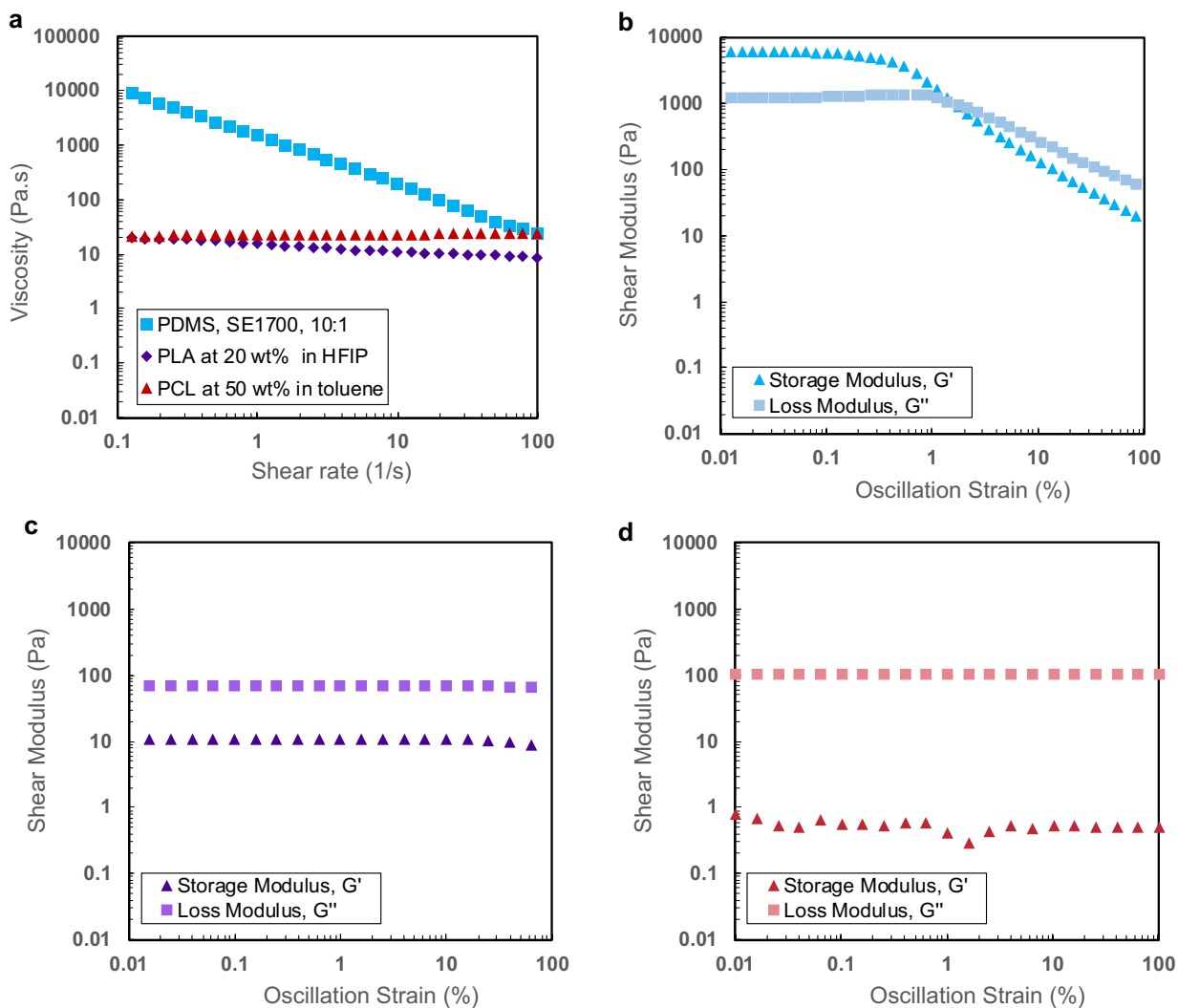
Figure 3.7. Rheological properties of three biocompatible polymer inks. (a) Apparent viscosity as a function of shear rate for PDMS, PLA, and PCL inks. Shear storage modulus (triangle markers) and shear loss modulus (square markers) of (b) PDMS, (c) PLA, and (d) PCL inks as a function of oscillation strain. Storage modulus (G') is shown using triangular markers, while loss modulus (G") is shown using square markers.

Next, we fabricated biomimetic TM grafts by direct writing of PDMS, PLA and PCL inks in two fiber geometries: 8R/8C or 16R/16C fibers (**Figure 3.8**). These graft designs mimic the basic circumferential and radial fiber arrangement of the human TM. The fiber diameters are determined in part by the nozzle diameter, extrusion pressure, and print speed. Given the differences in ink rheology described above, the printed fiber widths for the inner TM region are 209 ± 9 µm for PDMS, 215 ± 8 µm for PLA, and 246 ± 15 µm for PCL. TM graft thicknesses (z-axis) prior to infill are 56 ± 12 µm for PDMS, 32 ± 6 µm for PLA, and 48 ± 10 µm for PCL (**Figure 3.9**). Following TM graft printing and curing, they are infilled with a uniform collagen / fibrin solutions to yield composite grafts whose thickness varies between 592 – 616 µm for the different graft materials. Moist temporalis fascia and polynitrile sheets (controls) have an average thickness of 750 µm and 60 µm in thickness, respectively.
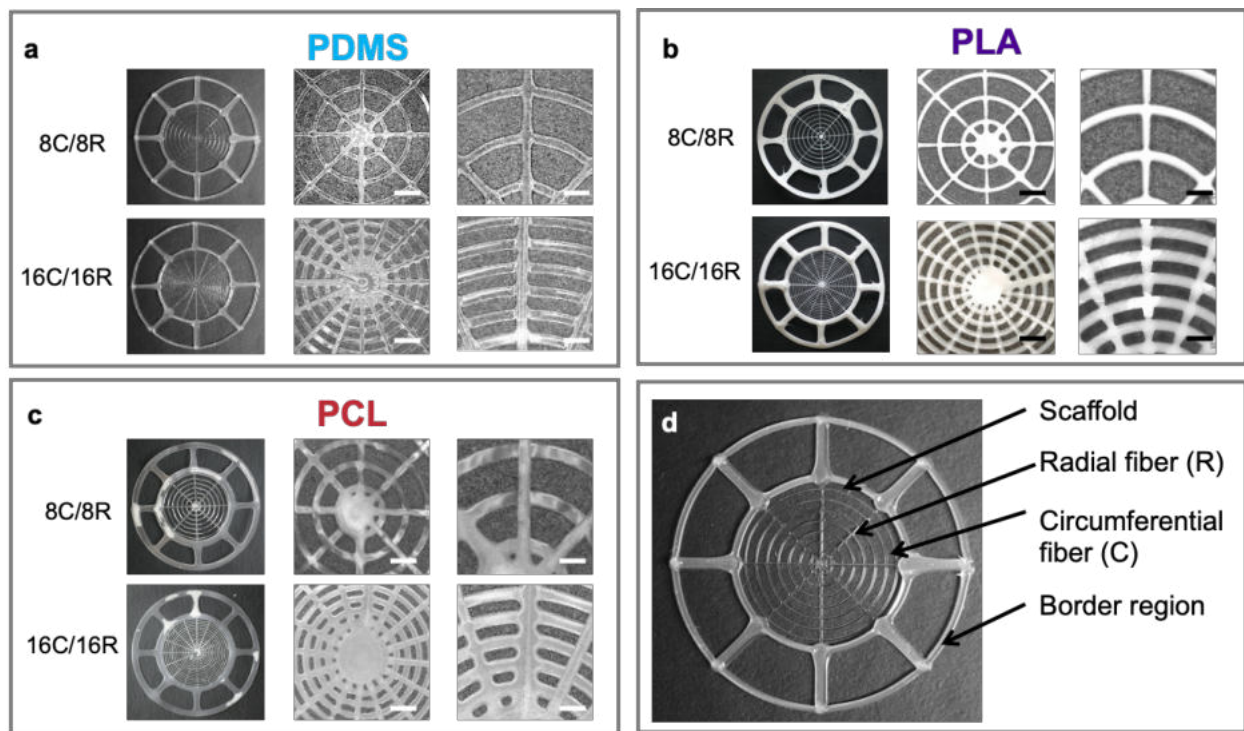
Figure 3.8. Biomimetic TM grafts with different materials and fiber geometries. Images of biomimetic TM grafts (25 mm in diameter) with increasingly higher magnification images are shown in left, middle, and right columns for (a) PDMS, (b) PLA, and (c) PCL-based grafts. [Note: Scale bars of 1 mm and 500 µm are shown in images in the middle and right columns.] (d) Labeled features of the printed TM grafts.
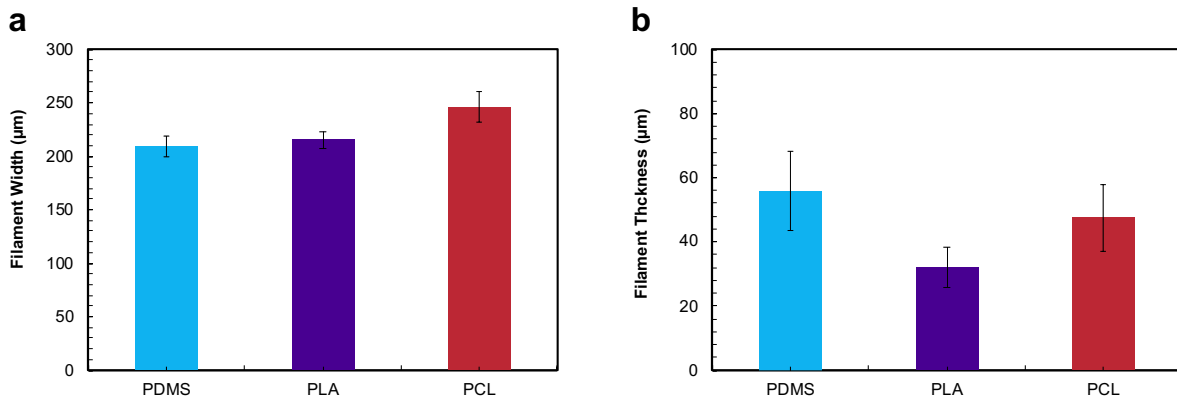
Figure 3.9. Fiber width and thickness of biomimetic TM grafts with different materials. Measurements are taken from n = 5 each 8C/8R and 16C/16R grafts (n = 10 total). Figure shows the mean ± SD for each 3D printed material group of PDMS, PLA, and PCL inks. (a) Filament width across various circular and radial filaments. (b) Filament thickness as measured by digital micrometers.

We then carried out DOEH to determine the acoustic properties of both biomimetic TM grafts and two controls (human temporalis fascia and polynitrile sheets). Representative DOEH maps of the magnitude of displacement at over 400,000 points on the surface of two representative PDMS grafts, temporalis fascia and polynitrile sheet are illustrated (**Figure 3.10**). The normalized displacement magnitudes (dB re 1 µm/Pa) are coded with progressive colors and standardized by frequency (color bar to the right of each plot). The 8C/8R and 16C/18R composite grafts resulted in similar patterns at each tested frequency; however, displacement magnitude varied by frequency. DOEH findings illustrated simple modal motion patterns at 400Hz, with one to three displacement maxima distributed over the entire membrane surface for all three TM composite grafts, the temporalis fascia and the polynitrile sheets. There is a clear increase in complexity of displacement patterns from low to high frequency; however, the locations of the displacement maxima and minima (nodes) are largely similar irrespective of fiber count. Temporalis fascia showed a similar increase in complex modal pattern with increasing frequency, but also demonstrated a greater degree of spatial asymmetry in fringe patterns. The polynitrile sheets had highly irregular and asymmetric displacement patterns at frequencies above 1000 Hz.
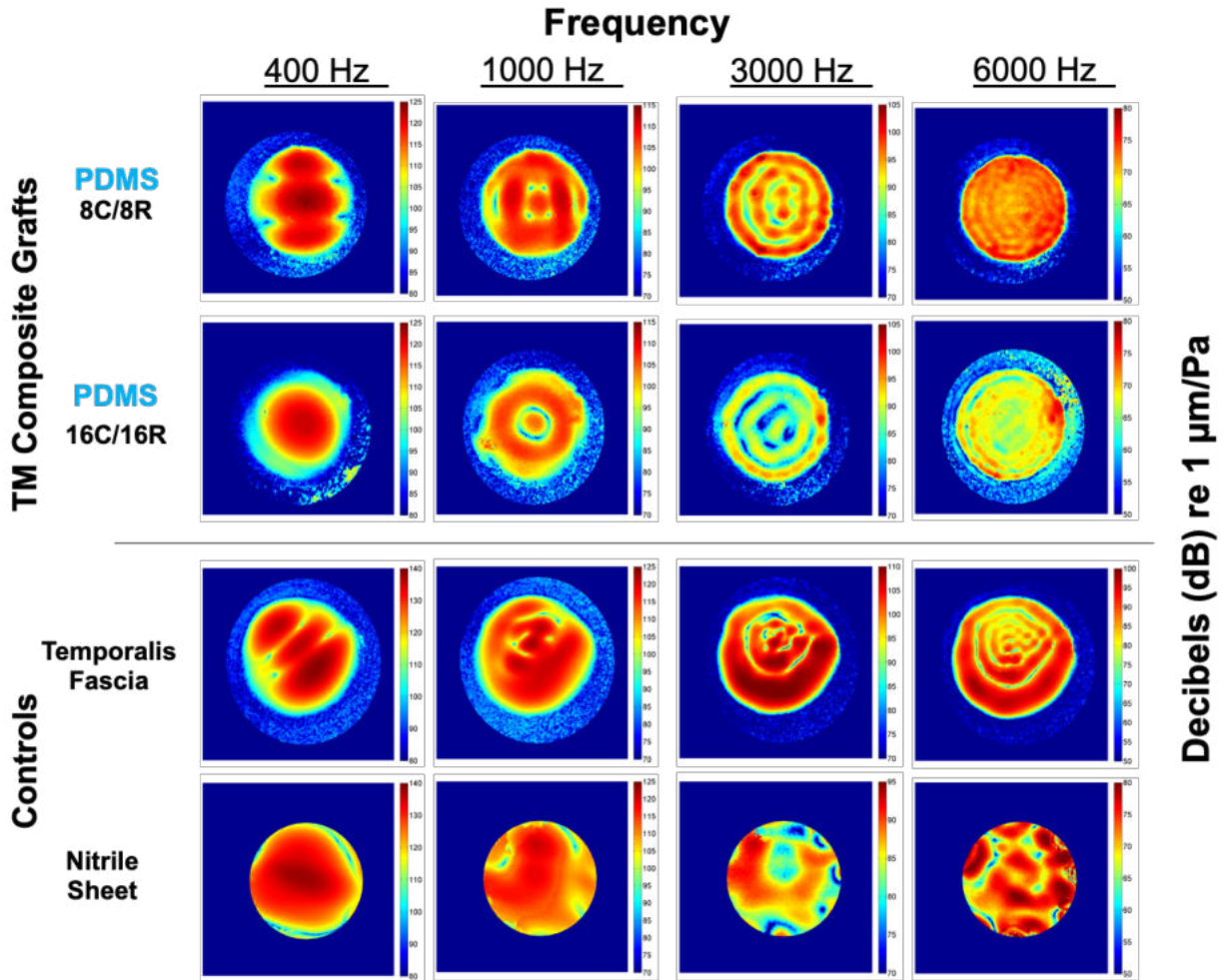
Figure 3.10. Representative DOEH fringe patterns of biomimetic TM grafts (PDMS) and control materials. Top row demonstrates the displacement patterns of an 8C/8R arrangement. Displacement is normalized by sound pressure and units are decibels (dB) re 1µm/Pa. Second row demonstrates 16C/16R arrangement.

At higher frequencies (1000 Hz and greater), motions of all three print materials: PCL, PDMS and PLA, became more complex with multiple areas of maximal displacement separated by regions of reduced displacement (**Figure 3.11**). The locations of the maximal displacement magnitudes varied among the three TM composite grafts and temporalis fascia, suggesting the choice of print material affects motion patterns. At 3000 and 6000 Hz, all three TM composite grafts and the temporalis fascia showed 'ordered' motion patterns, with many local displacement maxima and minima arranged alternatively like 'concentric rings' over the membrane surface. The number of 'rings' increased from 3 at 3000 Hz to more than 5 at 6000 Hz. These motion patterns are reproducible and appear similar between 8C/8R and 16C/16R fiber counts for

all materials. While the human temporalis fascia also exhibited increasingly complex modal pattern, similar to the biomimetic grafts at higher frequencies, the fringe patterns are less symmetric. The polynitrile sheet showed irregular patterns of displacement maxima at the tested frequencies. Surface motion pattern suggests similar progression of simple low frequency patterns to more complex, organized motion patterns at high frequencies. There are clear differences in magnitude of displacement among three printed grafts. Maximum displacement observed for the biomimetic TM grafts also depended on their composition and also the fiber arrangement (**Table 4**). Maximum average displacement for the PDMS, PLA, and PCL-based grafts is highest at low frequencies (Max: PLA, 16C/16R, 6.4 µm/Pa) and reached a minimum at higher frequencies (Min: PDMS, 16C/16R, 0.01 µm/Pa). By contrast, their fiber arrangement had little effect on the maximum displacement. However, when looking at displacement patterns (**Figure 3.10**), lower fibers lead to greater overall displacement across the graft, while higher fiber counts lead to lower displacement, implying that higher fiber counts lead to 'stiffer' grafts.

Compared to the biomimetic TM composite grafts, the human temporalis fascia and polynitrile sheet exhibited higher maximum displacements of 8.8 and 8.08 µm/Pa respectively at the lowest frequency of 400 Hz. However, they are surpassed by PCL grafts in both the 8C/8R and 16C/16R fiber arrangement at both 1000 Hz and 3000 Hz. PCL grafts exhibit the highest maximal displacement at all frequencies, except at 400 Hz where human temporalis fascia grafts better match the impedance of air at these frequencies due to their lower stiffness. At the highest tested frequency of 8000 Hz, the average fascia control displacement amount is surpassed in maximum displacement by the 16C/16R PCL grafts.

Table 4. Maximum displacement (µm/Pa) as measured by DOEH in biomimetic TM grafts fabricated with PCL, PLA and PDMS, as well as control materials.

	Frequency tested							
	400 Hz		1000 Hz		3000 Hz		6000 Hz	
Scaffold (circumferential x radial)	8x8	16x16	8x8	16x16	8x8	16x16	8x8	16x16
PDMS (n=3)	1.88	1.30	0.44	0.37	0.14	0.11	0.01	<0.01
PLA (n=3)	5.66	6.40	1.25	1.64	0.27	0.40	0.03	0.06
PCL (n=3)	4.05	4.08	1.41	3.11	0.41	0.38	0.03	0.13
Temporalis Fascia (n=1)	8.8		1.3		0.33		0.08	
Nitrile Sheet (n=1)	8.08		1.02		0.05		0.05	

*All values are in µm / Pa
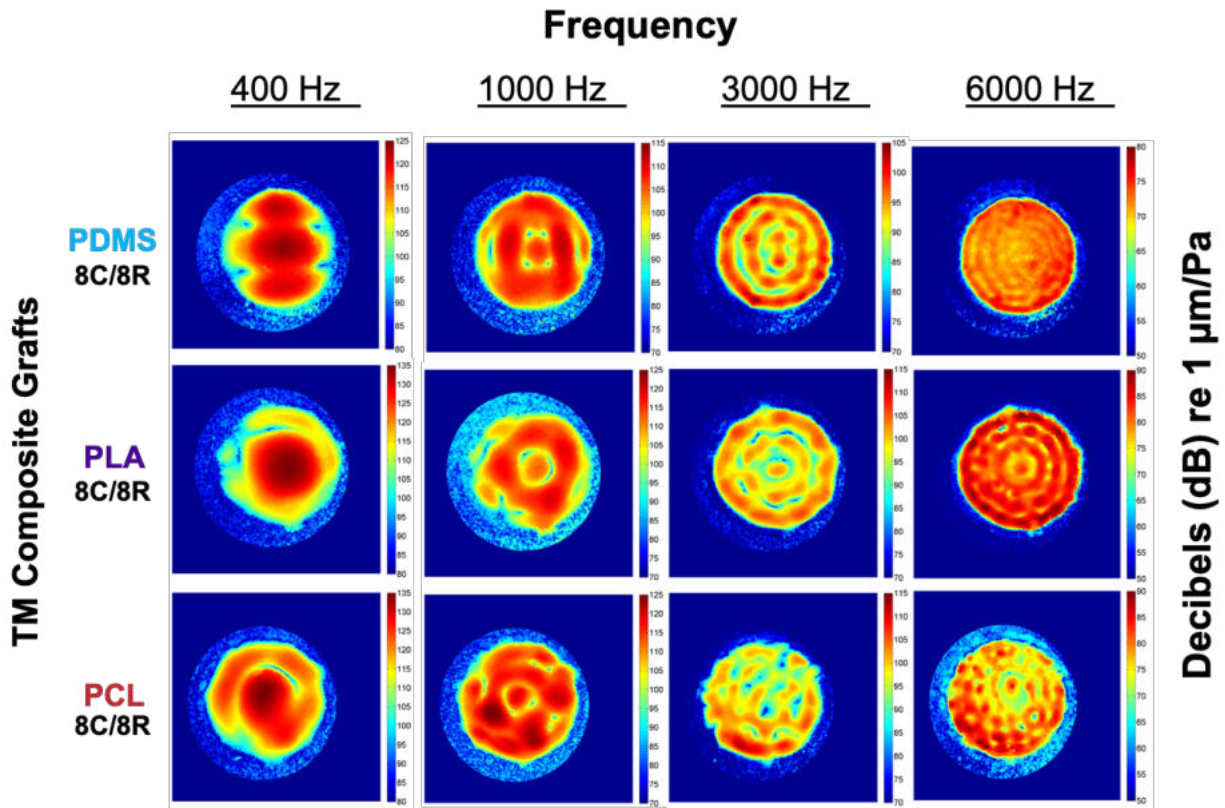
Figure 3.11. Representative DOEH fringe patterns of representative 8C/8R biomimetic TM grafts fabricated with PCL, PLA and PDMS. Biomimetic TM grafts consisting of PCL, PLA and PDMS (all 8 circumferential and 8 radial fibers) are imaged by DOEH. Displacement is normalized by sound pressure, and color bars were standardized across print materials at each frequency. Displacement is recorded in decibels (dB) re 1μm/Pa.

The phase angle between the displacement and stimulus sound pressure, an indication of the relative timing and directionality of membrane motion, is also measured by DOEH (**Figure 3.12**) Similar to magnitude, the phase angle varied by frequency and print material. At 400 and 1000 Hz, the biomimetic TM grafts exhibited several adjacent areas of opposite phase (light blue with phase ~0 radians and dark blue and dark red with phases of ~ π radians), which is also similar to human temporalis fascia and the polynitrile sheet. At higher frequencies, the spatial arrangement of the phase angle variations matches the complexity of the measured magnitudes. The fascia and polynitrile sheet show +/- half-cycle phase angle changes between adjacent regions, with the polynitrile sheet showing greater variability in angle of motion without apparent symmetry as in the magnitudes**.** The 8C/8R PDMS graft showed smaller cyclical variations in phase over the TM surface (orange to yellow, or dark blue to dark red).
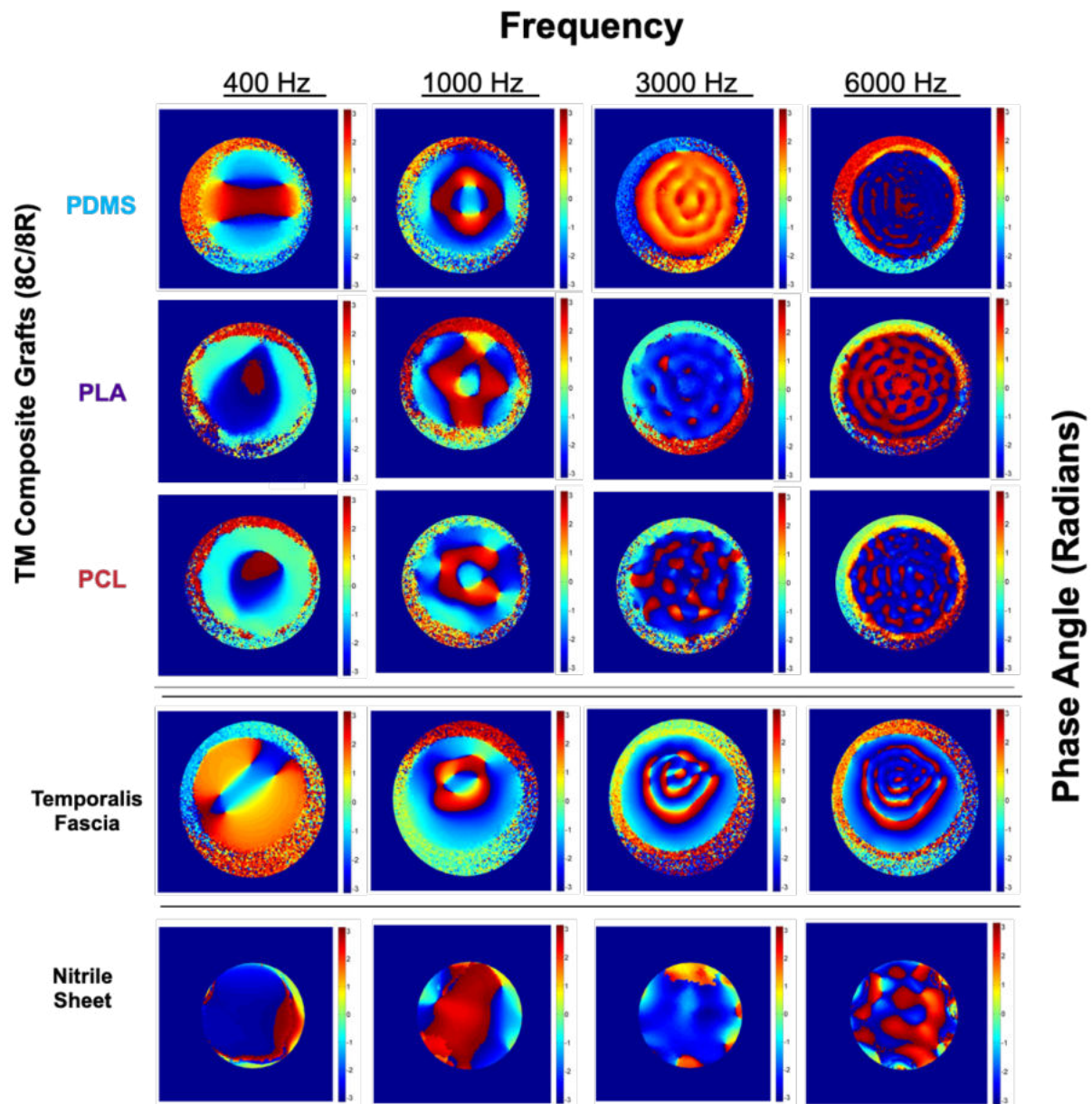
Figure 3.12. Phase angle of 8C/8R biomimetic TM grafts composed of PCL, PLA and PDMS versus fascia and polynitrile planar sheet. Representative DOEH images demonstrating the phase angle of the displacement relative to sound pressure in radians. Red represents a phase angle of ~ π radians, dark blue represents a phase angle of ~ π radians, and light blue represents a phase angle of ~0 radians).

DOEH provides a high spatial resolution image across the entire surface of the membrane, but it is limited in its frequency resolution. To determine the acoustic properties of TM composite grafts at a finer frequency resolution, LDV is used to measure sound induced velocity of the center of the membrane across more than 400 frequencies ranging from 0.01 kHz to 10kHz. Mean normalized velocity of the membrane to sound pressure of different tested materials is displayed in **Figure 3.13**. PDMS, PLA, and PCL-based grafts exhibit similar velocities within the tested frequency range. Velocity is highest at lower frequencies and peaks around 400 Hz at 0.08 m/s•Pa. Mid frequency (0.5 – 4 kHz) velocity is more consistent between grafts. Human fascia exhibit similar LDV velocity to the biomimetic TM grafts, but noticeably greater motion at frequencies above 4 kHz. The polynitrile control did not display clear velocity peaks.
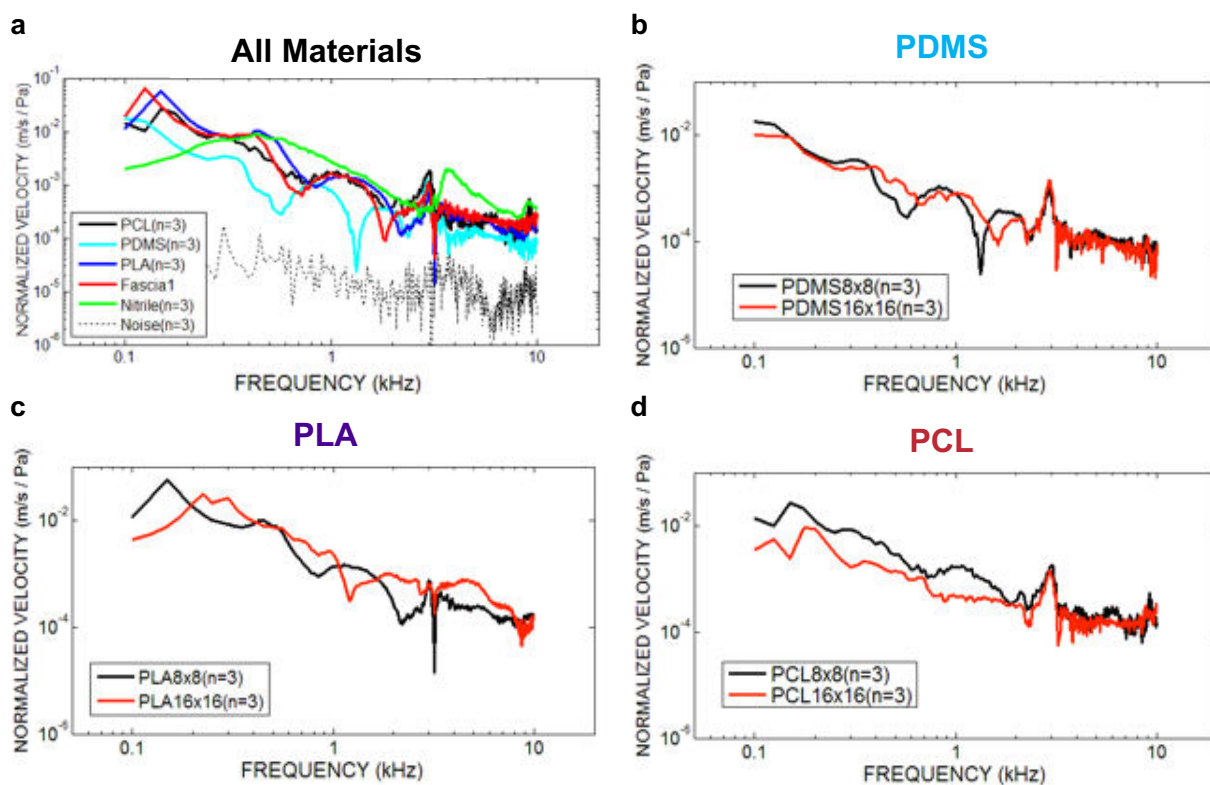
Figure 3.13. Velocity normalized by stimulus sound pressure of biomimetic TM grafts and controls across human frequency range. (a) Comparison of PCL, PDMS, PLA, fascia and polynitrile for normalized velocity (n = 3). Comparisons are shown of 8R/8C and 16R/16C (b) PDMS, (c) PLA, and (d) PCL TM grafts. Normalized velocity is similar among graft designs. [Note: Noise-artifact level indicates background movement of the graft support. Velocities at least a factor of 3 above the noise-artifact level are considered significant.]

When comparing TM composite grafts of 8C/8R fiber count to 16C/16R fiber count, there is slightly less motion at low frequencies for the higher fiber count 16C/16R grafts, although this difference is not observed at mid and high frequencies. Notably, TM composite graft motion for three representative samples (PLA 8C/8R) are highly reproducible (**Figure 3.14**). The patterns and location of local peaks in velocity is consistent across the entire frequency range in the three specimens. By contrast, the motion of three human temporalis fascia grafts harvested and prepared in identical fashion varies widely between grafts.
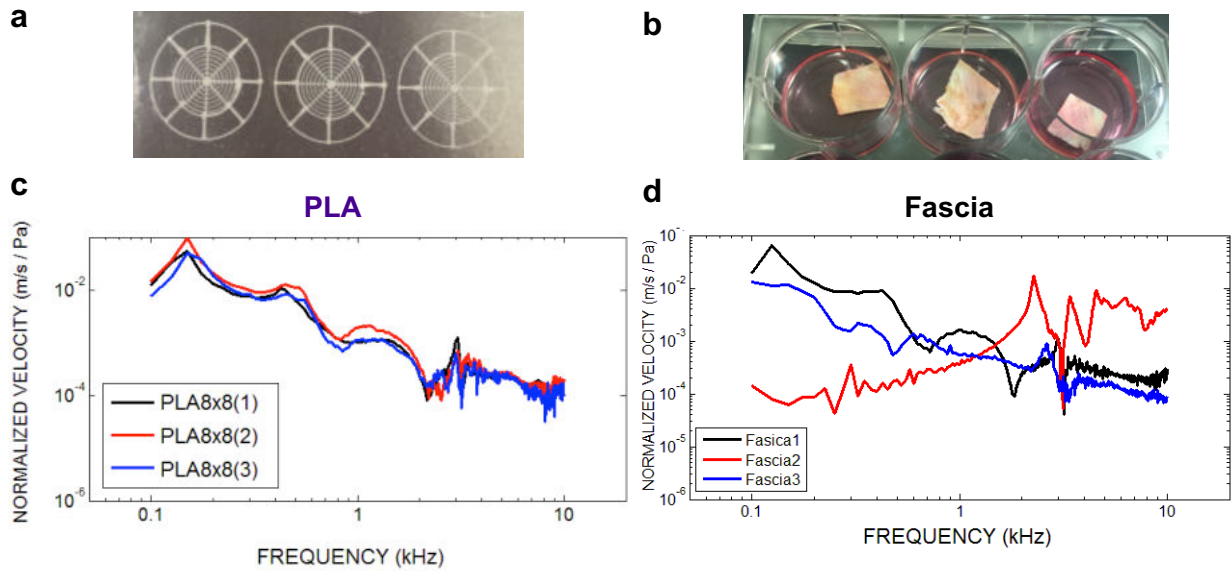
Figure 3.14. Differences in stimulus normalized velocity of biomimetic TM grafts and human temporalis fascia. (a-b) Optical images of the printed PLA-based grafts and the human fascia (controls), respectively. (c-d) Normalized velocities as a function of frequency for three PLA-based grafts and three human fascia controls, respectively. [Note: Both PDMS and PCL-based graft exhibited consistent normalized velocities over this frequency rate, data not shown.]

As discussed previously in **Chapter 2**, the adult human TM has a conical geometry with a depth of ~2.4 mm [52]. Fay et al. demonstrated that increasing the TM depth from 0 mm, i.e, a "shallow" flat surface, to a height of 2.5 mm, i.e., a "deep" conical surface, causes an upward shift in the amount of pressure transferred from the ear canal to vestibule of the cochlea, particularly at high frequencies [5]. To investigate these effects, we created conical TM grafts (PDMS, 8C/8R) with heights of 0, 1, 2, and 3 mm (**Figure 3.15a**) that are subsequently infilled with the composite hydrogel. LDV measurements reveal that their graft motion (**Figure 3.15b**), i.e., the velocity of center point of the printed grafts, consistently decreases as the conical depth increases at low frequencies. These findings suggest that the graft stiffness increases with increasing conical depth, which is consistent with a shift in the first resonant frequency (first velocity peak) of the grafts

to higher frequency with increasing conical depth. However, unlike the model predictions of Fay et al., we observe less difference in velocity at higher frequencies among TM grafts of conical shape. This discrepancy may arise due to the lack of ossicular loading on the grafts at the apex of the conical geometry, which provides increased input impedance to the TM and therefore increased stiffness at the center, which we did not have in these isolated grafts.
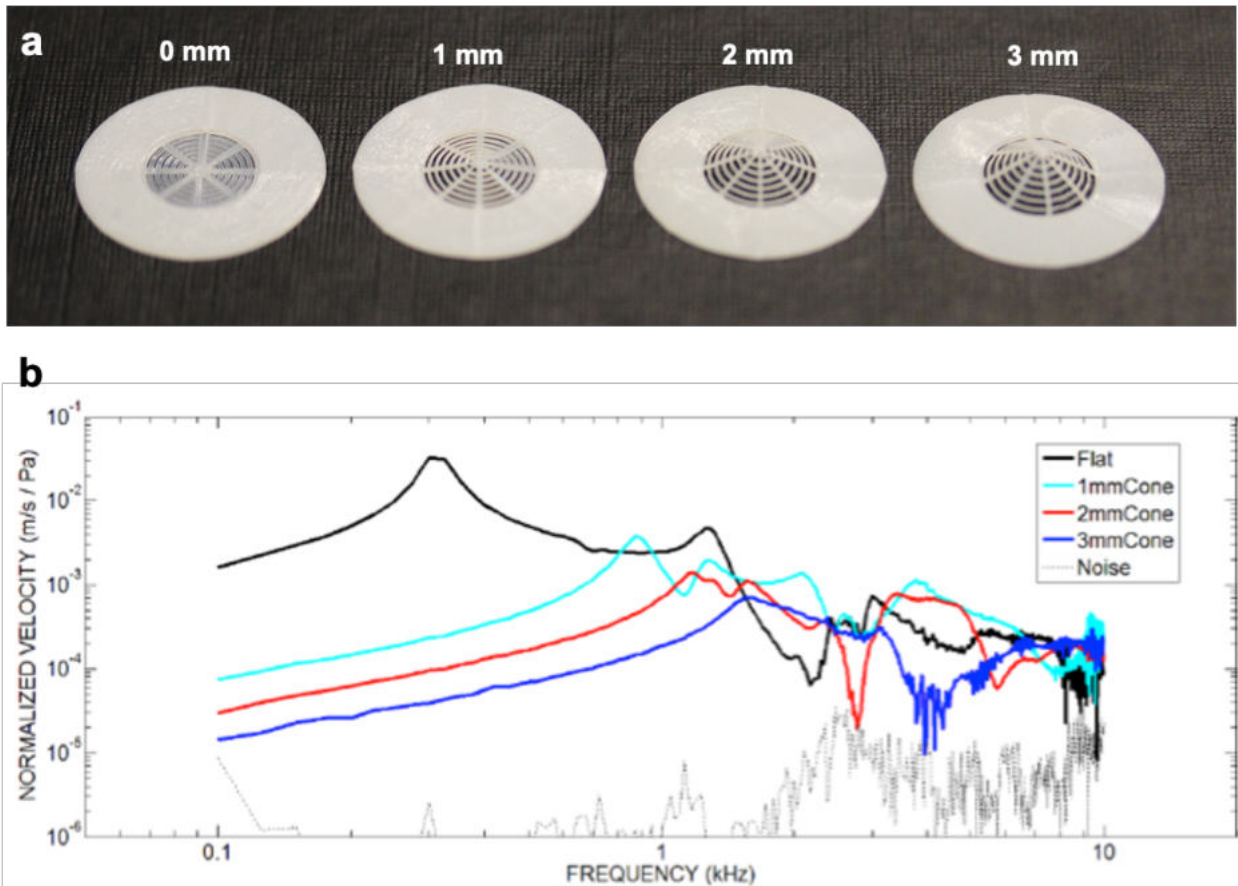
Figure 3.15. Sound induced velocity of conical TM grafts. (a) Optical images of conical PDMS-based TM grafts (8C/8R) of varying maximum depths (0, 1, 2, and 3 mm) printed using a tapered nozzle (ID = 410 µm). (b) Normalized velocity as a function of frequency for PDMS-based TM grafts (8C/8R) of varying maximum depths. [Note: Signal is above the noise floor from 100 Hz to 8000 Hz.]

DOEH data obtained for conical TM grafts exhibit simple, modal motion at low frequencies (400 Hz, 1000 Hz) with more complex modes of motion at higher frequencies (3000 Hz, 6000 Hz) for all conical depths tested (**Figure 3.16**). Biomimetic TM grafts (PDMS, 8C/8R) exhibit frequency dependent motion patterns in experimental DOEH testing. Overall, grafts with larger TM depths exhibit a smaller displacement at low frequencies, consistent with LDV motion of these grafts. The magnitude of their displacement is

significantly less for 3 mm conical TM grafts, compared to those with 1 mm and 2 mm depths. At high frequencies, there is no consistent pattern observed in maximal displacement. Akin to LDV measurements, while the resonant frequency shifted to the right for higher conical heights, the overall velocity curve is lowered. Hence, these values could either be lower or higher depending upon minor resonant peaks. There is a directional irregularity in motion in conical grafts, likely related to slight non-uniformity of TM grafts printed onto the conical substrates. We note, however, that the impact of macroscale conical architecture on sound conduction *in vitro* is difficult to assess in the absence of ossicular loading.
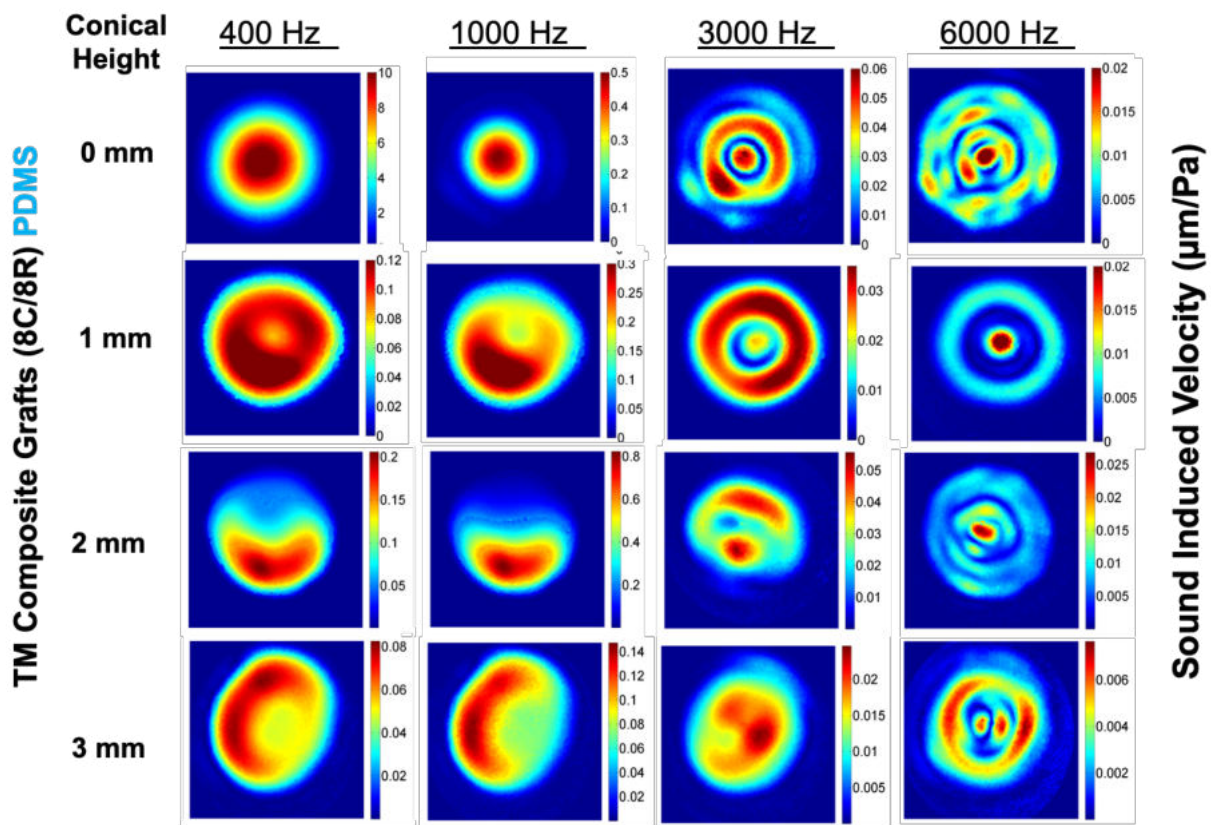
Figure 3.16. Representative DOEH fringe patterns of biomimetic TM grafts printed on conical substrates of varying height. Biomimetic PDMS-based TM grafts (8C/8R) with conical depths of 0, 1, 2, and 3 mm are imaged by DOEH. Displacement is normalized by sound pressure, and color bars were standardized across print materials at each frequency. Displacement is recorded in decibels (dB) re 1 µm/Pa.

We also carried out repeated mechanical in plane loading measurements on biomimetic TM grafts in 8C/8R and 16C/16R architectures (flat, 0 mm depth) of PDMS, PCL, and PLA-based grafts. Repeated

loading at 20 Hz for 60 sec (1200 total cycles) demonstrated variable strength and degree of deformity among the tested materials, as determined by force required to deform the grafts. Comparing the first and last 0.05 sec cycle of loading between grafts of varying material among 16C/16R grafts (**Figure 3.17a-b**), PCL-based grafts had the highest load required for deformation in both the first and last cycle (2.49 N vs. 2.14 N, 14% decrease). While temporalis fascia grafts had the second highest force required for displacement in the first cycle, by the last cycle of loading this significantly decreased (1.62 N vs. 0.45 N, 73% decrease). PLA-based grafts exhibited lower initial force required for displacement but maintained their mechanical properties better than fascia by the last cycle (1.41 N vs. 1.23 N, 13% decrease). Meanwhile, PDMS-based grafts exhibited the lower force required for displacement during both the first and last cycles, consistent with the trend in overall Young's Modulus of the bulk polymers (0.25 N vs. 0.19 N, 14% decrease). In addition to the 3D printed materials, the specific biomimetic TM graft fiber arrangement resulted in differential load by fiber count. For PLA grafts, the 16C/16R fiber arrangement recorded a higher load at the same displacement magnitude than did the 8C/8R arrangement, requiring a 1.43x higher loading during the first cycle and a 1.49x higher loading for the last cycle (**Figure 3.17c-d**).

Little hysteresis (decrease in stiffness) is observed in the deformation of the 16C/16R biomimetic grafts, even when displaced over 60 seconds (**Figure 3.17e-g**). In contrast, the force required to maintain a constant deformation of fascia degraded over the testing period and is particularly noticeable after the first several seconds of constant displacement, resulting in the 73% decrease in load required for displacement between the first and last cycles of loading (**Figure 3.17h**). Such hysteresis is common in viscoelastic biological tissues [447,448]. Therefore, 3D printed TM grafts from biocompatible materials are feasible at maintaining their mechanical properties after stress and deformation. From a surgical context, this suggests that manipulation and placement of these grafts should not result in a substantial alteration in their preimplantation acoustomechanical properties. These mechanical findings are notable as: (1) hysteresis of human temporalis fascia provides a potential explanation for how surgically placed temporalis fascia thins and retracts over time, and (2) biomimetic TM grafts may provide mechanical advantages over current graft materials.
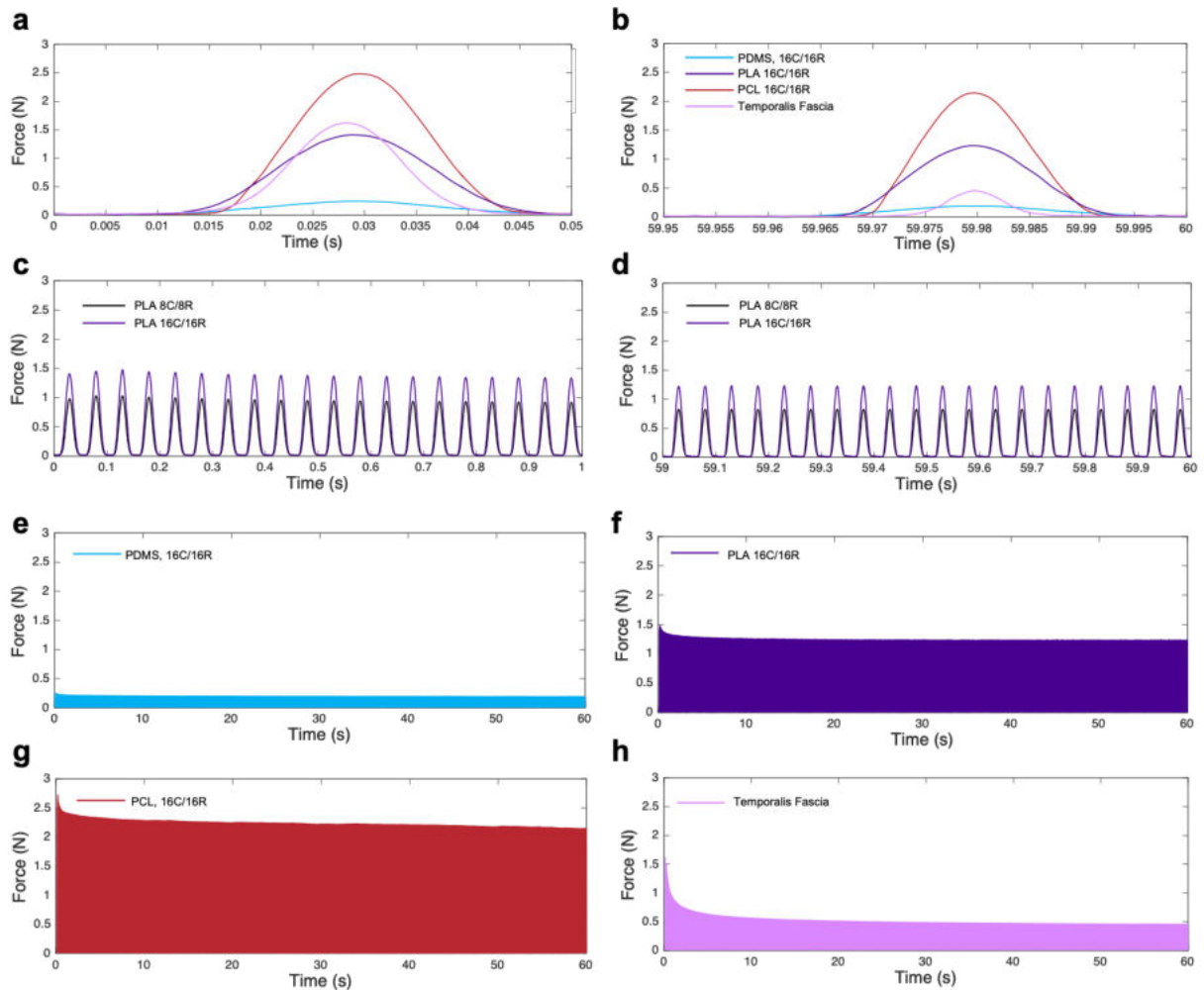
Figure 3.17. Repeated mechanical testing of biomimetic TM grafts and human temporalis fascia. All grafts similarly mounted at a jaw gap of 1.2 cm. Loading force (N) required to cycle the bottom motor through constant sinusoidal displacements of 2 mm in amplitude at a frequency of 20 Hz are recorded for 60 sec for 1200 total cycles. (a,b) Comparison of the first and last 0.05 sec of testing for 16C/16R PDMS, PLA, and PCL-based biomimetic grafts. (c,d) Comparison of the first and last 1 sec of testing for 8C/8R and 16C/16R PLA-based biomimetic grafts. Loading forces over the full 60 sec of loading are shown for (e) 16C/16R PDMS-based biomimetic grafts, (f) 16C/16R PLA-based biomimetic grafts, (g) 16C/16R PCL-based biomimetic grafts, and (h) temporalis fascia grafts.

Biomimetic TM grafts are printed in varying architectures [PDMS, 8C/8R (n = 3) and 16C/16C (n = 3)] with a connector region. Similar to those utilized in acoustic testing and those subjected to repeated mechanical loading, the biomimetic TM grafts are cured and infilled with the composite hydrogel. Circumferential clamping and out of plane deformation from the center of these grafts demonstrate a stable, elastomeric behavior (**Figure 3.18**). The spring constants are defined as the force required to out of plane deform the grafts at a displacement up to their fracture. 8C/8R TM grafts fractured sooner and exhibited a

lower average spring constant (k = 54.3 ± 4.8 N/m) than the 16C/16R grafts (k = 64.2 ± 6.7 N/m). This observation is not surprising, since a higher fiber count should enhance graft stability during deformation from the center point. Since the human TM normally undergoes microscopic deformations, these grafts are not expected to exhibit permanent deformation or fiber fracture during normal acoustic stimulation.
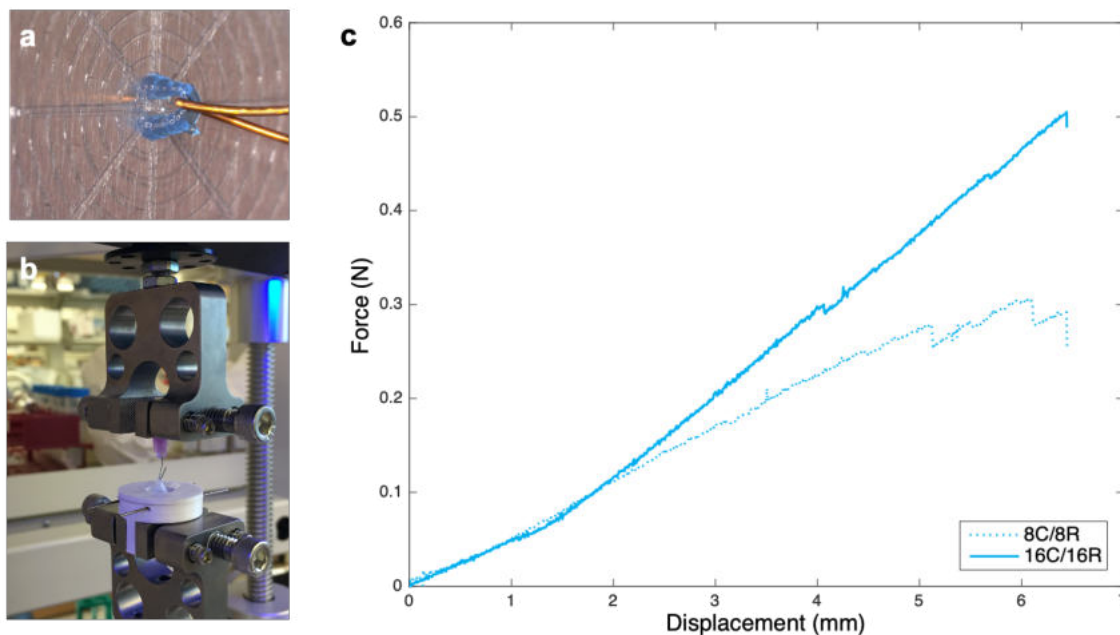
Figure 3.18. Mechanical loading of biomimetic TM grafts. (a) Optical image of the connector printed in the center of the TM graft. (b) Image of mechanical testing apparatus equipped with a custom holder that applies a force to center of the graft, exposing a 9 mm inner region. (c) Plot of force as a function of displacement for biomimetic TM grafts (PDMS) of different geometry (8C/8R and 16C/16R).

Beyond optimizing their *in vitro* acousto-mechanical properties, it is critical to assure that biomimetic TM grafts are both biocompatible and capable of being remodeled by cell ingrowth after implantation. Hence, we studied the migration and proliferation of GFP-HNDFs from the periphery to the center of the TM grafts (8C/8R) composed of PDMS, PLA, and PCL. PCL grafts exhibiting the greatest degree of fibroblast cell proliferation, as determined by the MTS assay (**Figure 3.19a**). However, the inward migration of GFP-HNDFs and subsequent deposition of native ECM by these cells occurs primarily within the infilled composite hydrogel matrix. Since the cells do not align along the printed radial and circumferential fibers within each TM graft (**Figure 3.19b**), their native collagen ECM is deposited in a random configuration (**Figure 3.19c-d**). To overcome this limitation, we explore new TM graft designs (in **Chapter 4**) that facilitate preferential deposition of collagen in a directed architecture.
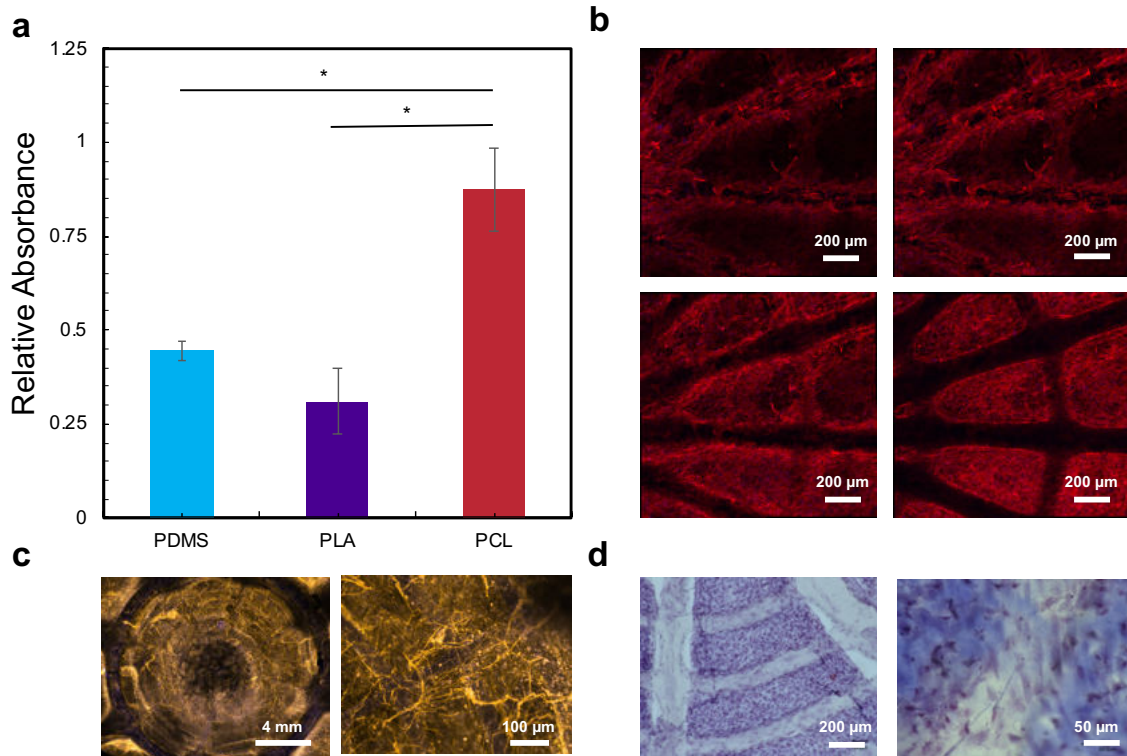
Figure 3.19. Ingrowth of GFP-HNDFs onto biomimetic TM grafts. (a) Proliferation as quantified by an MTS assay at day 31 (n = 3, * p < 0.05). (b) Ingrowth of cells visualized by actin (red) at day 92 under confocal microscopy. (c) Collagen I deposition visualized by collage I immunostaining (orange) at day 92 under confocal microscopy. (d) Masson's Trichrome stain at day 134 shows deposition of collagen (blue) and ECM proteins (pink) surrounding cell nuclei (brown).

Finally, the human TM possesses a significantly more complex ultrastructural design than what has been generated and described through additive manufacturing in this chapter. Going forward, new designs could be explored for these TM grafts (**Figure 3.20**).
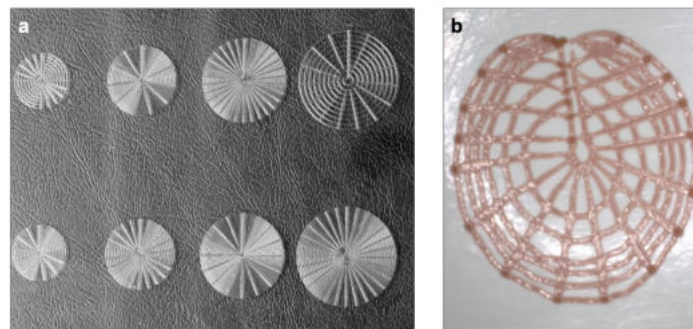
Figure 3.20. Customized geometries of biomimetic 3D printed TM grafts. (a) Customized size and fiber architecture can be rapidly tuned in G-code. (b) Custom fiber arrangements more closely mimicking those found in the native TM can be further explored.

3.4   Conclusions

This study is the first to demonstrate the design, manufacture, and characterization of the acoustic and mechanical properties of a biomimetic TM graft. 3D printing enables the fabrication of biomimetic TM grafts composed of FDA-approved materials with customizable radial and circumferential fiber arrangements. We showed that the magnitude of displacement and point velocity of these printed grafts (*in vitro*) are similar to that of human temporalis fascia over the frequency range of human hearing. Importantly, biomimetic TM grafts exhibited a more symmetric and regularly varying spatial displacement pattern compared to either human fascia or polynitrile sheets, similar to patterns observed in human and animal TMs [438-440,449]. The printed graft composition had a greater effect on their spatial displacement pattern compared differences in graft geometry. While increased conical depth increased the resonant frequency of the grafts, the overall impact of this parameter on sound conduction was difficult to assess without biomimetic ossicular loading to mimic middle and inner ear input impedance.

Beyond the potential for use as graft material in human tympanoplasty procedures, the ability to control the design of a TM-like structure has implications for the study of middle ear mechanics. There are still many unanswered questions regarding the function of the TM and its role in the regulation of sound transmission to the middle ear. In particular, there are a host of biophysical models, such as modal and traveling wave models, that attempt to explain the motion of the TM at high and low frequencies [449]. The ability to fine-tune the microarchitecture and microarchitecture of TM grafts to control for specific properties of the TM may enable further experimental understanding of the nuances of TM motion and provide experimental designs to test the findings of finite element and mathematical models.

Chapter 4

Biodegradable Elastomeric Inks for 3D Printing of Biomimetic TM Grafts

4.1   Introduction

The tympanic membrane (TM) has a complex trilaminar structure, comprising a lateral-facing epidermal epithelium, middle lamina propria, and a medial-facing mucosa. As discussed in **Chapter 2**, there are two major cell types in the human TM responsible for remodeling. The first type, keratinocytes, are located in the lateral-facing epidermal epithelium layer [450]. These cells are responsible for migration during the "Proliferative Stage" from days 2 up to days 4 – 7 following TM damage, forming scar-like tissue on the TM surface. The second major cell type are fibroblasts [451], which begin re-forming the lamina propria layer, where the circumferential and radial collagen architecture is located. The viability of both cell types on biomimetic TM grafts is crucial. Additionally, fibroblasts should ideally deposit collagen along the filament direction within these printed architectures. As the graft material degrades, it would ideally be replaced by collagen fibers that adopt the underlying graft geometry yielding an anisotropic tissue.

In this chapter, we created biodegradable, elastomeric inks that can be printed and remodeled for repairing perforated TMs via tympanoplasty. Specifically, we synthesized a poly(ester urethane urea) (PEUU), a class of polymers described in **Chapter 2,** which can be blended with poly(ethylene glycol) (PEG), which serves as a porogen as described in **Chapter 2**, to create porous graft materials. The printed TM grafts must meet several requirements: (1) biodegradable elastomeric material must be mechanically robust for surgical handling, integrate with the surrounding TM tissue to reduce graft retraction, re-perforation, and infection, (2) the printed biomimetic TM graft architecture should enable sound conduction across a wide range of frequencies upon implantation, and (3) the grafts should be slowly reabsorbed and remodeled yielding an anisotropic tissue that recapitulates the native TM tissue with an oriented lamina propria. We demonstrate a route for creating biodegradable elastomeric inks that yield mechanically anisotropic responses across printed TM grafts with prescribed circular and radial features. We further show that these graft materials exhibit a propensity for remodeling into anisotropic tissue via *in vitro* fibroblast alignment and biodegradation.

4.2   Experimental Methods

4.2.1   Biodegradable Elastomer Synthesis

A thermoplastic biodegradable polyurethane is synthesized composed of soft and hard segments and different chain extender ratios, whose composition was optimized over several iterations by assessing its ability to be extruded by high operating temperature-direct ink writing (HOT-DIW) at a temperature of 115°C or less (**Table 5**). The optimal poly(ester urethane urea) (PEUU) is then produced using a two-step reaction, comprising a soft segment of polycaprolactone diol (PCL, M_n=2000, Sigma-Aldrich, USA) containing hydrolysable ester bonds, a hard segment of butane diisocyanate (BDI, Sigma-Aldrich, USA), and a chain extender of 1,4-butanediamine (BDA, Sigma-Aldrich, USA) (**Figure 4.1**). These are combined in a molar ratio of 1:1.5:0.75 of soft segment-to-hard segment-to-chain extender. The PCL is first dried in a vacuum oven at 100°C overnight to remove residual water before synthesis. The dried PCL is added to a 3-neck flask along with 30 wt% anhydrous dimethyl sulfoxide (DMSO, Sigma-Aldrich, USA) under the flow of nitrogen at 80°C. BDI is then added to the flask along with 0.01 wt% stannous octoate catalyst (Spectrum Chemical, USA). During this step, urethane bonds form in the polymer. After 2 h, BDA is mixed with additional DMSO and added to the flask to achieve a 20 wt% in DMSO polymer solution. The reaction is then continued for 1 h under nitrogen during which chains extend with urea bonds. This results in a stiffer and more biocompatible polymer, as the urea bonds are amide bonds [452] that resemble peptide bonds to cells. After the reaction is complete, PEUU is precipitated in water to remove DMSO and then dried in a vacuum oven at 100°C overnight to remove residual water and DMSO and to obtain the final polymer.

Table 5. Synthesis protocols showing molar ratios trialed between soft segment (PCL-diol), hard segment (BDI), and chain extender (BDA) to achieve melt-processable polymer.

Soft Segment PCL-diol	Hard Segment BDI	Chain Extender BDA	Notes
1	2	1	Inaccessible T_m
1	1.75	1	Inaccessible T_m
1	1.7	1	Inaccessible T_m
1	1.6	1	Inaccessible T_m
1	1.6	0.8	Inaccessible T_m
1	1.5	1	Thermoplastic, $T_m \approx 190°C$
1	1.5	0.75	Thermoplastic, $T_m \approx 40°C$
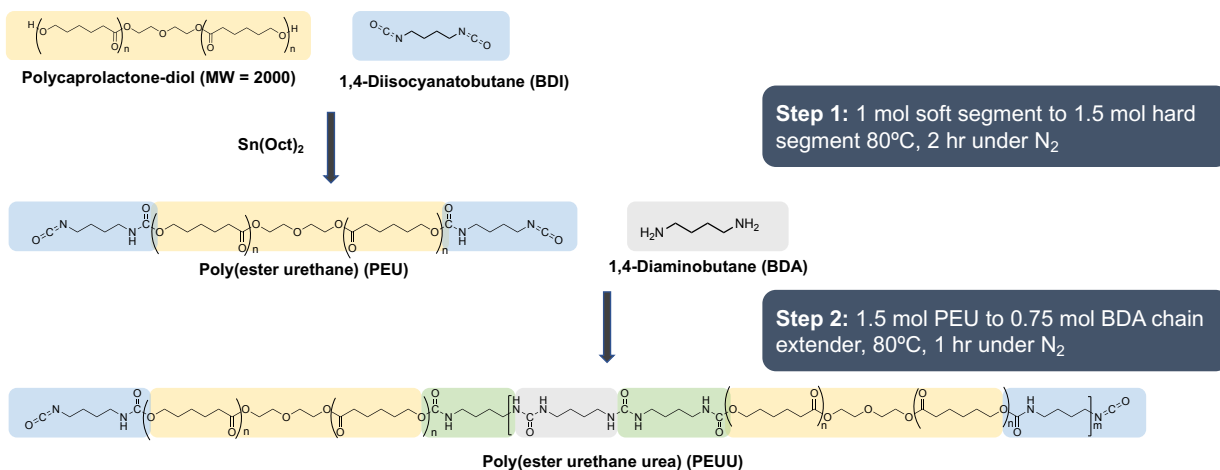
Figure 4.1. Two-step synthesis of biodegradable poly(ester urethane urea) (PEUU). In the first step, a polycaprolactone (PCL) soft segment is reacted with a 1,4-diisocyanatobutane (BDI) hard segment to create poly(ester urethane). Then, in the second step, 1,4-diaminobutane (BDA) is used to extend the chains and to impart urea bonds in the final polymer.

4.2.2 Gel Permeation Chromatography

To confirm polymer synthesis from the 2000 Da PCL-diol soft segment monomers, 140.14 Da BDI hard segment monomers, and 88.15 Da BDA chain extender, gel permeation chromatography (GPC) (DVD1260, PSS SECcurity 1260, Agilent, USA) is carried out by our collaborators at Triton Systems (Chelmsford, MA). In addition to as-synthesized PEUU, samples held at either 4°C, room temperature (RT), or 40°C for 3 months are tested to determine if any changes in molecular weight occur under storage. PEUU samples are dissolved in chloroform at concentrations of 2 – 3 mg/mL. The sample solutions and eluent are shaken at 40°C for 24 h and then filtered through a polytetrafluoroethylene syringe filter with a nominal porosity of 1.0 μm prior to injection. A flow rate of 1.0 mL/min is used with an injection volume of 100 μl at a temperature of 30°C. Polystyrene standards are used for normalization (Agilent, USA).

4.2.3 Printable Inks

To create composite inks with a fugitive component, PEUU and PCL (control) (M_n = 50,000, Sigma-Aldrich, USA) are combined with 25 wt% PEG (M_n = 1500, Sigma-Aldrich, USA). To facilitate mixing, PEUU is dissolved in acetone at 75 wt/vol% (VWR International, USA) and PCL is dissolved toluene at 75 wt/vol% (Reagent Grade, Ricca Chemical, USA). The solutions are heated at 50°C for PEUU/PEG/acetone inks and 100°C for PCL/PEG/toluene inks for 1 h before blending in a high-speed mixer (FlackTek, USA) at 2000 rpm for 5 min. Following complete mixing, the solvents are evaporated in a vacuum oven at 60°C for

PEUU/PEG/acetone inks and 120°C for PCL/PEG/toluene inks for 24 h. PEUU and PCL inks are also produced without PEG (porogen) following the same solution and evaporation processes. Four inks are therefore generated for characterization: PCL, P-PCL (PCL + 25 wt% PEG1500), PEUU, and P-PEUU (PEUU + 25 wt% PEG1500) (**Figure 4.2**) and, ultimately, printing biomimetic TM grants.
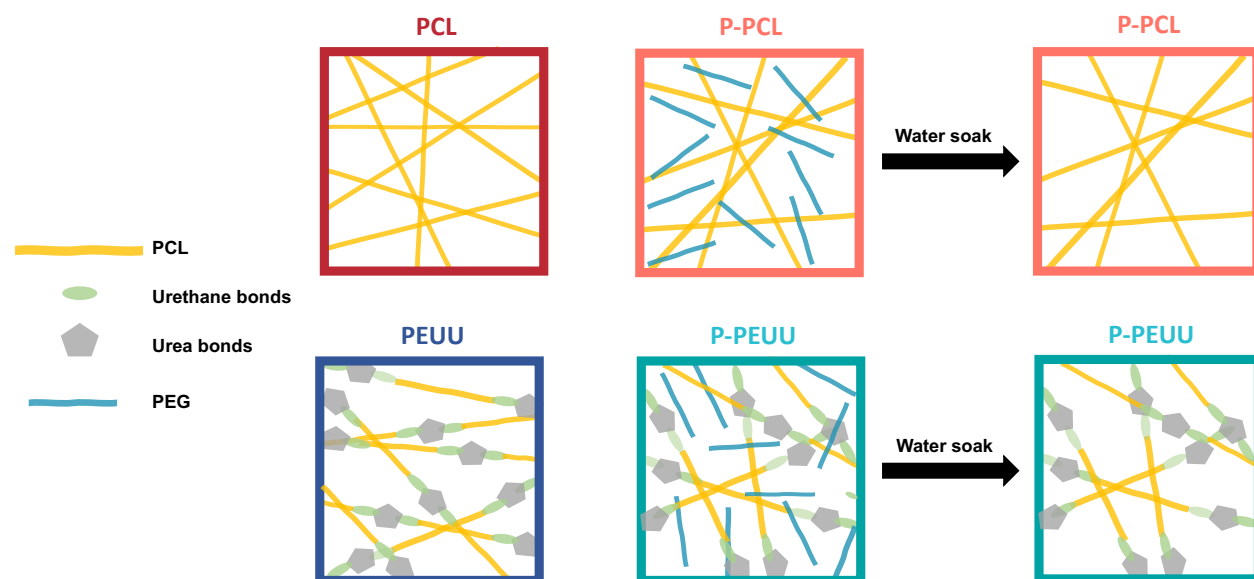
Figure 4.2. Inks created for 3D printing of biomimetic TM grafts. (Top row) Schematic views of pure PCL and porous P-PCL inks and (bottom row) Schematic views of pure PEUU and porous P-PEUU inks blended with 25 wt% PEG. PEG is removed by immersing the 3D-printed grafts in water.

4.2.4   Differential Scanning Calorimetry

The melting behavior of PEUU and P-PEUU inks is measured by differential scanning calorimetry (DSC) (Q200 calorimeter, TA Instruments, USA). Samples of PEUU and P-PEUU (prior to PEG leaching) are hermetically sealing inside aluminum pans (TZero, TA Instruments, USA). Samples are analyzed via a heat-cool-heat cycle between −50° and 200°C at a rate of 10°C/min to clear the thermal history of the material. The melting temperature, T_m, is determined from the summit of the melting peak.

4.2.5   Rheological Characterization

The rheological properties of each ink are measured using a controlled-stress rheometer (Discovery HR-3 Hybrid Rheometer; TA Instruments, USA) equipped with a 20 mm peltier plate geometry. To simulate printing conditions during HOT-DIW, a temperature sweep is performed at a temperature of 90°C for P-PCL and P-PEUU inks and at 115°C for PCL and PEUU inks, after holding for 5 min to equilibrate at the desired temperature. Viscometry measurements are carried out by subjecting the inks to an

increasing shear rate swept from 0.01 – 100 s^{-1} at 1 Hz. All 4 inks (PCL, P-PCL, PEUU, and P-PEUU) are analyzed for Newtonian or shear thinning rheological properties. Printing temperatures are chosen so that 100 µm filaments can be successfully extruded from 200 µm inner diameter (ID) nozzles, which was conducted because the inks cannot be extruded through smaller ID nozzles using the current HOT-DIW setup, and we aim to achieve small feature sizes more closely mimicking those of the native TM.

4.2.6   Biomimetic TM Graft Fabrication via 3D Printing

A custom 3D multi-material printer (Aerotech) with a ~1 µm resolution is equipped with a custom-designed hot printhead from which the ink is extruded pneumatically. A custom Aerobasic G-code program is used to control the print path, height, speed, and extrusion temperature. This method, known as HOT-DIW, is used to melt extrude the PEUU and PCL-based inks at elevated temperatures. The printhead contains a machined copper block containing a custom-machined steel 3 mL syringe coupled to a high-pressure adaptor (HPx High-Pressure Dispensing Tool, Nordson EFD, USA), with an enclosing fluoroplastic insulating block. Two 100-W 0.25" x 2" cartridge heaters (Omega Engineering, USA) are controlled via a resistance temperature detector sensor adjacent to the syringe. Feedback control is provided via a PID Controller (Platinum Series Versatile High Performance PID Controllers, Omega Engineering, USA).

To create consistent graft architecture from each ink, the print parameters are optimized such that extruded ink filaments (100 µm in width and 50 µm in height) are achieved. The inks are extruded through tapered-tip stainless steel nozzles (inner diameter = 200 µm, Tecdia Inc., Japan) held at 90°C for P-PCL and P-PEUU or 115°C for PCL and PEUU. A custom Aerobasic G-code program is designed to create a meandering path that changes extrusion pressure with each line. Four print speeds of 5, 10, 15, and 20 mm/s are tested at extrusion pressures ranging from 40 to 100 psi. For each combination of ink, print speed, and extrusion pressure, 6 lines of length of 5 mm are printed onto a glass slide substrate. The width of each fiber is measured using a Keyence digital microscope (VHX2000, Keyence, Japan) and recorded to determine print parameters required to obtain filaments with the desired width and height.

For *in vitro* cellular alignment studies, square grafts (8 mm x 8 mm) are printed using both PEUU- and PCL-based inks at a speed of 20 mm/s (**Figure 4.3a**). To investigate print speed effects on cellular alignment, additional grafts are fabricated at print speeds of 5, 10, and 15 mm/s using the same 200 µm nozzle. To create isotropic P-PEUU grafts, the printed grafts (200 µm nozzle diameter at 20 mm/s speed)

are melted to "erase" any anisotropy imparted by HOT-DIW. For *in vitro* degradation and cell proliferation studies, biomimetic TM grafts composed of PCL, P-PCL, PEUU, and P-PEUU with an overall diameter of 8 mm are printed in a circular and radial architecture (**Figure 4.3b**). A series of 50 concentric circles are printed first, spaced 80 µm apart at 20 mm/s. Next, a series of 50 radial lines from the center of the grafts are printed at 20 mm/s. The resultant biomimetic TM grafts are defined by their 50 circular (C) and 50 radial (R) (50C/50R) structure.
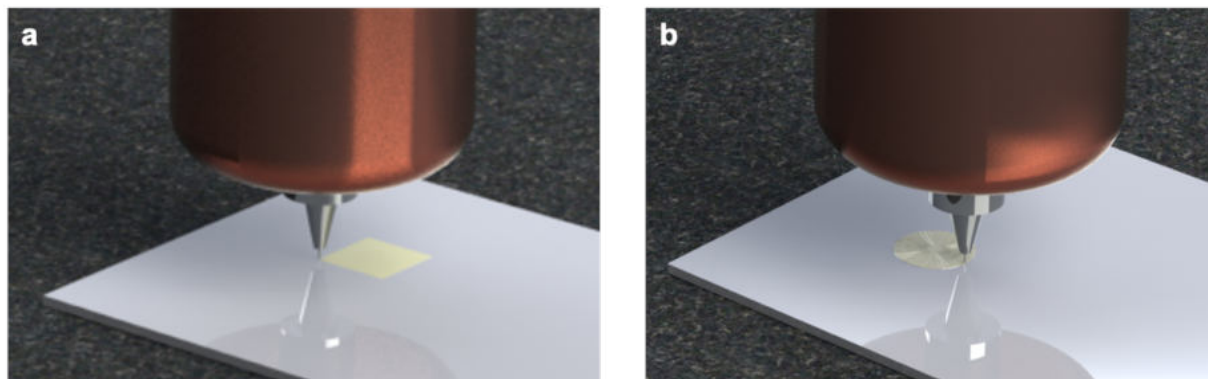
Figure 4.3. Schematic illustrations of TM graft fabrication via HOT-DIW. (a) Square grafts (8 mm x 8 mm) and (b) biomimetic TM grafts (50C/50R) patterned with an outer diameter of 8 mm and 50 concentric circles (C), followed by 50 radial (R) lines.

4.2.7   TM Graft Post-Processing and Sterilization

All printed grafts are placed in a plasma treatment system (Diener Femto PCCE, Germany) and exposed to oxygen plasma for 30 sec to both render their surfaces hydrophilic and to achieve sterilization. The grafts are then placed under UV germicidal irradiation in a biosafety cabinet for 5 minutes per top and bottom surface. To determine the impact of sterilization on molecular weight of the polymer, PEUU grafts sterilized via plasma and UV germicidal radiation also undergo standard ethylene oxide (EtO) processing at a temperature of 30°C. The total EtO exposure time was 16 h (4 h for injection + 12 h of holding), followed by 3 h purge and 1 h aeration.

To remove PEG, biomimetic TM grafts (50C/50R) are immersed in deionized (DI) water at 37°C thereby producing P-PCL and P-PEEU grafts. This process is also carried out on biomimetic TM grafts (50C/50R) printed using pure PCL and PEUU inks to determine if any mass loss arises that cannot be attributed to PEG leaching. The minimum time required for complete PEG leaching was determined by placing the grafts in DI water at 37°C and removing them at predetermined timepoints of 0.16, 0.5, 1, 2, 4,

8, 24, and 48 h (n = 3 for each graft per timepoint). Excess water is removed from the grafts using KimWipes (Kimberly-Clark, USA) following by drying in a vacuum oven at 37°C overnight (AT09.110.UL, Across International, USA). Grafts are weighed before and after soaking at each timepoint. Thermogravimetric analysis (TGA) (TA Instruments, USA) is used to weigh the grafts with accuracy of 0.0001 mg.

Upon leaching PEG from each TM graft, samples (n = 6 of each graft) are placed in 1X Dulbelco's phosphate buffered saline (PBS) without calcium and magnesium (Corning, USA) for 30 min. The grafts are weighed before and after this process to determine the amount of PBS absorbed by each graft (i.e., PCL, P-PCL, PEUU, and P-PEUU grafts).

4.2.8 Fourier-Transform Infrared Spectroscopy

To assess the presence of urethane and urea bonds in PEUU as well as PEG incorporation within these inks, Fourier-transform infrared spectroscopy (FTIR) in double-sided transmittance mode (Bruker Hyperion Vertex 70 FTIR Spectrometer, Bruker Corporation, USA) is performed on biomimetic 50C/50R P-PEUU and PEUU grafts after printing and post-leaching for varying immersion times. Their initial and final (post-leaching) IR spectra are compared to ensure complete removal of PEG.

4.2.9 Surface Profilometry

The height profile of the top and bottom graft surfaces is characterized using an optical profiler (CCI HD Optical Profiler, Taylor Hobson, UK), which relies on coherence correlation interferometry (CCI) to generate high-resolution sub-nanometer 3D surface measurements without contacting the substrate. Each printed graft is affixed to a glass slide with double-sided tape with either their top or bottom surface facing upward. Profiling is conducted in XY mode with a 20x objective for high data resolution. TallySurf (Taylor Hobson, UK) is used for data collection, while TallyMap is used to display 3D rendering of the surface profile and to provide the ISO 25178 "Geometric Product Specifications" height parameters of the surfaces. The root mean square (rms) heights of the top and bottom surfaces of each graft are compared.

4.2.10 *In Vitro* Graft Degradation Rates

In vitro degradation rates for printed biomimetic TM grafts (50C/50R) composed of each ink (PCL, P-PCL, PEUU, and P-PEUU) are measured. Prior to testing, each graft is weighed to obtain its initial mass (M_0). Prior studies used a lipase concentration of 100 U/mL to mimic biological conditions [380,381] However, given that the TM is located at the air-air interface with decreased access to biologic fluids, we also carried

out these tests at a lower lipase concentration (1 U/mL). The tests are performed in both phosphate buffered saline (PBS, Lonza, USA) and in PBS containing a lipase concentration of 1 U/mL or 100 U/mL (*Aspergillus Oryzae*, Sigma, USA). The grafts are placed in a 24-well plate with 1 mL of solution per well. The samples are then placed on a rocker (LSE Platform Rocker, Corning, USA) at 60 rpm in an incubator at 37°C with 5% CO_2 atmosphere. The grafts are removed from the solution at specific time points and rinsed using deionized water. The samples are dried at 37°C in a vacuum oven and then weighed (M_x). The remaining graft mass is calculated using:

$$Percent = \frac{M_x}{M_0} * 100$$ (4)

Following sample weighing, the samples are placed back in the well plates, which are replenished with fresh PBS or lipase solutions.

4.2.11 *In Vitro* Cell Proliferation on TM Grafts

The proliferation of human keratinocytes and fibroblasts on biomimetic TM grafts is studied, including an assessment of cell alignment and collagen deposition. Primary human epidermal keratinocytes (HEKs) (ATCC, USA) are cultured in dermal cell basal medium (ATCC, USA) supplemented with keratinocyte growth kit (ATCC, USA) according to the manufacturer's instructions. Cells are kept in an incubator (VWR International, USA) at 37°C with 5% CO_2 atmosphere up to passage 10. Cell medium is pre-warmed and replaced every 2 days. At 80% confluency, cells are passaged with 0.05% trypsin-0.53 mM EDTA (ATCC, USA), which is deactivated with trypsin neutralizing solution (ATCC, USA). Human neonatal dermal fibroblasts modified with enhanced green fluorescent protein (GFP, λ_{ex} = 488 nm), (GFP-HNDFs, Angio-Proteomie, USA) are cultured in Dulbecco's modified eagle medium supplemented with 862 mg·L^{-1} L-alanyl-glutamine (Gibco, USA) and 10% fetal bovine serum (FBS, ATCC, Manassas, VA) in an incubator at 37°C with 5% CO_2 atmosphere. Cell medium is pre-warmed and replaced every 2 days up to passage 20. At 80% confluency, cells are passaged with 0.05% trypsin-0.53 mM EDTA (Gibco, USA).

For cell proliferation assays, HEKs and GFP-HNDFs (100,000 cells per graft) are seeded onto the top surface of biomimetic TM grafts (8 mm 50C/50R grafts of PCL, P-PCL, PEUU, and P-PEUU) in a 48-well plate (n = 6 per graft material). After allowing 1 h for cell adhesion, additional media is placed in each well. At time points of 1, 3, 7, 14, 21, and 28 days, an MTS tetrazolium colorimetric assay (ab197010,

Abcam, Cambridge, UK) is performed to assess cell proliferation. Each graft is moved into a new well to ensure that only cells growing on the grafts are included and to exclude cells growing on cell culture plastic of the well plates. 10 mL of assay buffer is mixed with 10 µl of bis-AAF-R110 substrate and stored at -20°C between assays. A volume corresponding to 10% of the culture volume of sterile MTS in phosphate buffer solution is added to each culture well and incubated for 1 h at 37°C with 5% CO_2 atmosphere. The solutions are transferred to a 96-well microwell plate and measured using absorbance at 490 nm on a plate reader (Synergy HT, BioTek Instruments, USA) to assess the relative cell proliferation on each graft material. Media is aspirated and replaced for the corresponding cell type after each assay (every 2 – 3 days). The average and standard deviation of absorbance values are calculated. A Student's t-test (JMP Pro 15, USA) is conducted to determine statistical significance between groups.

4.2.12 Mechanical Characterization

The elastic properties of the biomimetic TM grafts are measured under ambient conditions using tensile testing. Tensile specimens (48.0 mm long, 3.52 mm wide, and 100 µm thick) of each material (PCL, P-PCL, PEUU, and P-PEUU) are printed with filamentary features that are aligned either parallel and orthogonal to the direction of applied stress (**Figure 4.4**). Note, two layers are printed on top of one another to mimic the ~100 µm thickness of the human TM in the pars tensa [15].

An Instron machine (Model 3342, Norwood, MA) with a load cell maximum of 50 N is used to apply unidirectional load on specimens. Tabs are fabricated at the ends of 3D printed specimens using double-sided tape to prevent slippage from the tensile grips, resulting in a gage length (L_0) of 25 mm and width of 3.52 mm. Specimens are tested at a strain rate of 5 mm/s in a tensile direction both parallel and orthogonal to the print path for all 4 inks (n = 6 each). Young's modulus (E) is calculated as the stress (σ) over strain (ε) at a displacement of 1 mm (4% of total gage length), as given by:

$$E = \frac{\sigma}{\varepsilon} = \frac{\frac{F_n}{A}}{\frac{\Delta L}{L_0}}$$

(5)

where F_n is normal force acting orthogonal to the cross-sectional area (A) and ΔL/L is the strain. The mean value and standard deviation (SD) of Young's modulus are calculated for each graft (n = 6 of each material for both print paths) and values parallel ($E_{\parallel}$) and orthogonal ($E_{\perp}$) to the uniaxial testing direction are reported.

A Student's t-test (JMP Pro 15, Cary, NC) is conducted to determine statistical significance between $E_{||}$ and $E_{\perp}$ of each of the 4 inks (PCL, P-PCL, PEUU, and P-PEUU).
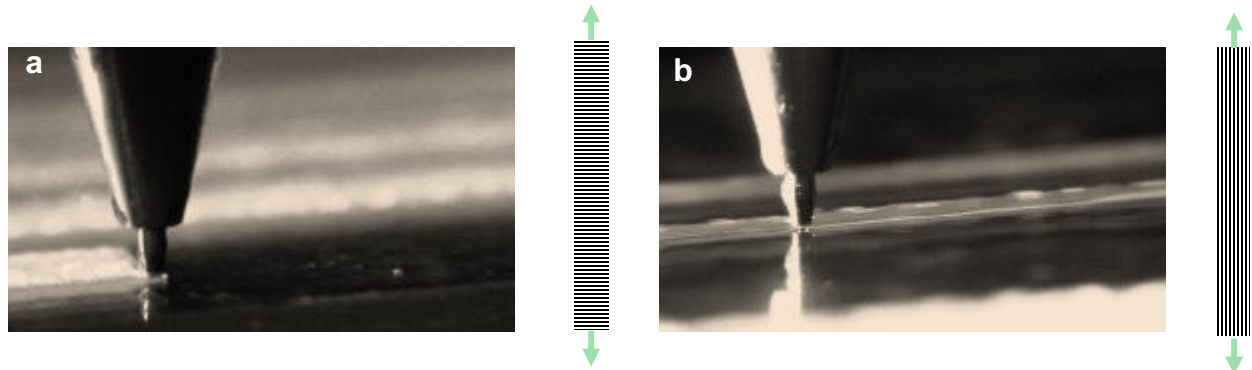
Figure 4.4. Tensile specimens are 3D printed from PCL, P-PCL, PEUU, and P-PEUU inks. The long axis and tensile direction is either (a) orthogonal to the print path or (b) parallel to the print path. All samples are printed utilizing a 200 µm inner diameter nozzle and a print speed of 20 mm/s. Green arrows indicate the direction of applied tension.

4.2.13 *In Vitro* Fibroblast Alignment on TM Grafts

To characterize fibroblast alignment, GFP-HNDFs (100,000 cells per graft) are seeded onto the top surface of P-PEUU 20 mm/s square grafts as well as the bottom surface of square grafts printed with varying materials composition at 20 mm/s print speed (PCL, P-PCL, PEUU, and P-PEUU) and varying print speed of P-PEUU ink (5, 10, 15, and 20 mm/s) as previously described (8 mm x 8 mm, n = 6 each). Each graft contained printed filaments (100 µm wide with a center-to-center spacing of 80 µm). Samples are fixed at day 7 (BD Cytofix™, BD Biosciences, US). Grafts undergo immunostaining for collagen I (1:500, rabbit monoclonal, ab138492, Abcam, USA). An upright confocal microscope (LSM710, Zeiss, Germany) equipped with a 5x objective is used for imaging. To eliminate edge effects, images are only acquired from the center-most 6 x 6 mm region. 3D projections and Z-stacks are generated using manual and automated processes in Imaris (Oxford Instruments, UK). The Directionality plugin through ImageJ (National Institutes of Health, US) is used to analyze the alignment of both GFP-fibroblasts and collagen I for each graft. Averages and standard deviations for found for each group from -90° to 90° across the graft, whereby 0° is the direction of the print path.

4.3   Results

PEUU was successfully synthesized from PCL-diol soft segment, BDI hard segment, and BDA chain extender monomers in a 1:1.5:0.75 molar ratio to achieve a thermoplastic for use in HOT-DIW. As expected, PEUU contained urethane/urea bonds along its backbone with a characteristic C=O stretching peak observed at 1722 cm^{-1} indicating the presence of ester and urethane bonds and another peak at 3330 – 3340 cm^{-1} corresponding to N-H stretching in urethane and urea bonds (**Figure 4.5a**). Additionally, the FTIR spectrum of P-PEUU prior to PEG leaching indicates successful incorporation of PEG into this material, as reflected by an increased peak at 2500 – 3000 cm^{-1} corresponding to O-H stretching and an increased peak at 1000 – 1200 cm^{-1} corresponding to C-O stretching (arising from ether bonds along the PEG backbone) [453]. While PEUU has a melting temperature, T_m of 38°C, the presence of PEG leads to a secondary melting temperature peak, $T_{m,}$ at 46°C (**Figure 4.5b**).
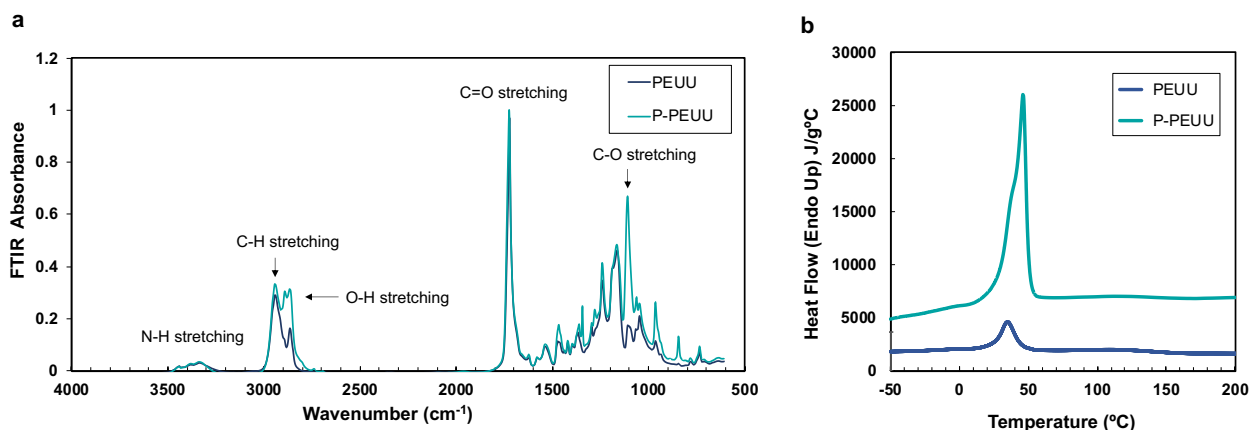
Figure 4.5. Characterization of PEUU and composite P-PEUU (PEUU + 25 wt% PEG) material. (a) FTIR spectra of PEUU and P-PEUU, with peaks for relevant bonds indicated by arrows. (b) Heat flow during final heat ramp of a heat-cool-heat cycle between -50°C and 200°C. Melting temperature, T_m, is defined as the maximal endothermic peak for each material.

GPC was used to determine the as-synthesized PEUU molecular weight distribution as well as any changes that may have occurred during sterilization and storage (**Figure 4.6** and **Table 6**).The final polymer has a number average molecular weight (M_n) of 16,200 Da, weight average molecular weight (M_n) of 56,800 Da, and a polydispersity index (PDI) of 3.51. Sterilization and storage of the PEUU grafts for 3 months at 4°C had a minimal impact on the molecular weight, which was found to be M_n = 16,900 Da, M_w = 57,900 Da, PDI = 3.41 (after sterilization) and M_n = 15,300 Da, M_w = 55,800 Da, PDI = 3.63 (after storage). However, storage at higher temperatures did lead to a decrease in PEUU molecular weight.
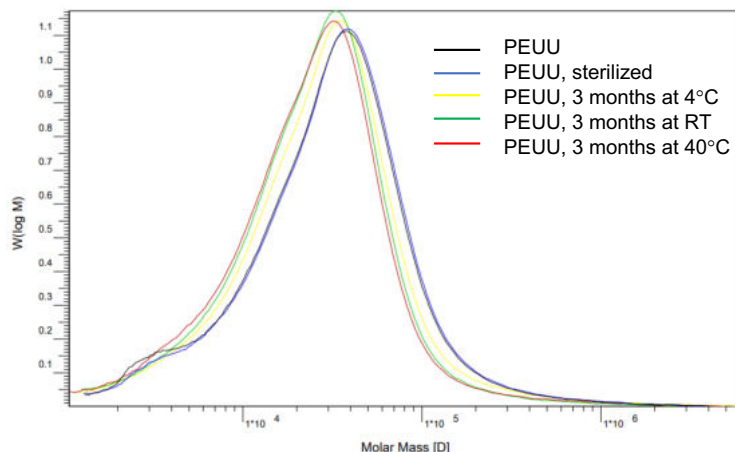
Figure 4.6. GPC results of newly synthesized, sterilized, and stored PEUU samples. The results of newly synthesized PEUU is shown alongside results of sterilized samples that underwent plasma treatment, UV irradiation, and ethylene oxide treatment. Additionally, the results of PEUU stored for 3 months under various temperature conditions is shown. RT = room temperature.

Table 6. Summarized GPC results of newly synthesized, sterilized, and stored PEUU samples. Number average (M_n) and weight average (M_w) molecular weights and the polydispersity index (PDI).

Sample	M_n	M_w	PDI
PEUU	16,200	56,800	3.51
PEUU, sterilized	16,900	57,900	3.42
PEUU, 3 months at 4°C	15,300	55,800	3.63
PEUU, 3 months at RT	14,600	42,400	2.90
PEUU, 3 months at 40°C	13,500	46,000	3.41

The apparent viscosity as a function of shear rate is reported for each ink used to produce biomimetic TM grafts via HOT-DIW (**Figure 4.7**). These measurements are carried out at 90°C for P-PCL and P-PEUU inks and 115°C for PCL and PEUU inks, respectively, as this was deemed to be the optimal temperatures for patterning 100 μm filaments. While each of these inks exhibits the desired shear thinning behavior, the low shear viscosity varies from 100 — 1000 Pa•s, and the onset of shear thinning varies from roughly 1 s^{-1} — 20 s^{-1} depending upon the ink composition and temperature. Next, we explored the effects of printing speed and pressure on the width of the patterned filaments for inks extruded through a 200 μm nozzle at a layer height of 50 μm (**Figure 4.8**). In all cases, a linear relationship between filament width and extrusion pressure, with increasing print speed and decreasing extrusion pressure resulting in filaments of smaller width. These information used to identify print parameters that result in 100 μm wide filaments.
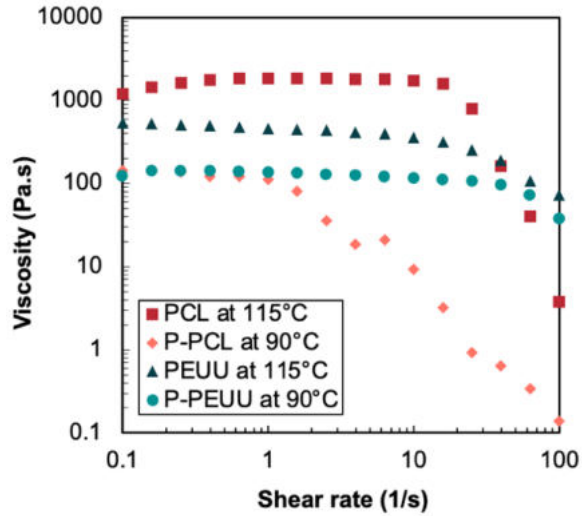
Figure 4.7. Apparent viscosity as a function of shear rate for thermoplastic biodegradable inks. Inks tested include PCL, P-PCL, PEUU, and P-PEUU. [Note: P-PEUU and P-PCL inks contain 25 wt% PEG1500].
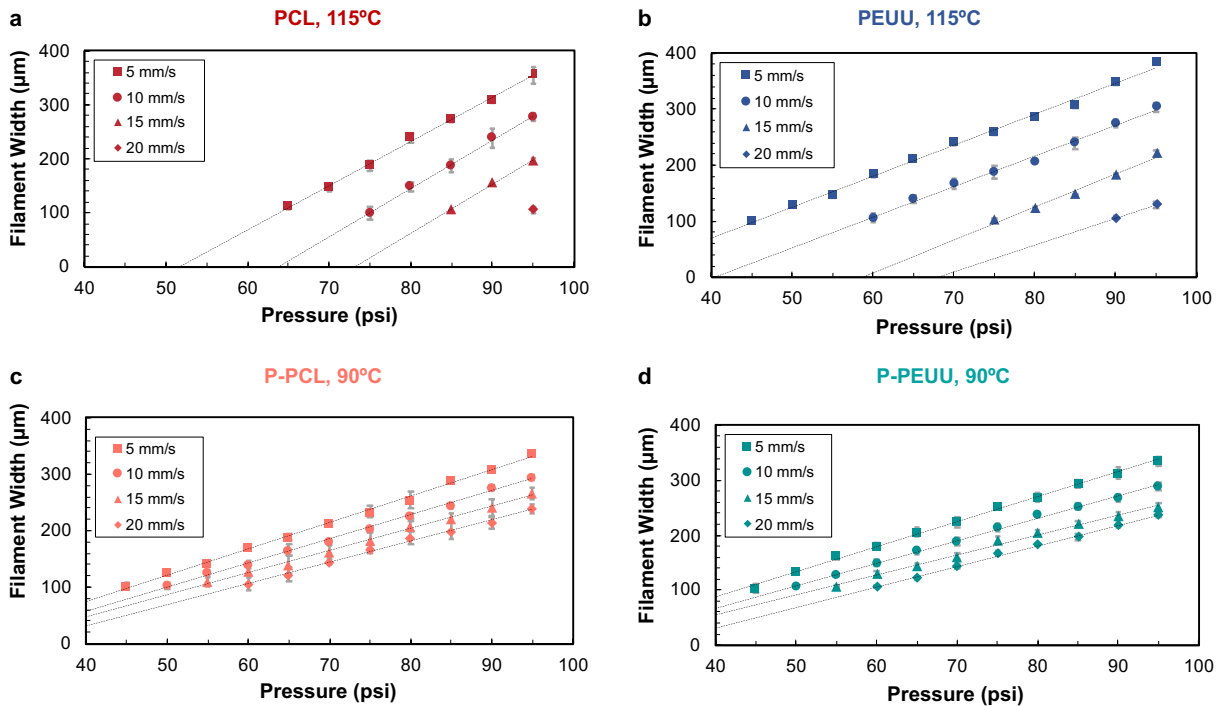
Figure 4.8. Filament width of 3D printed lines of 4 biodegradable inks from 200 μm inner diameter nozzles. (a) PCL inks extruded at 115°C, (b) PEUU inks extruded at 115°C, (c) P-PCL inks extruded at 90°C, and (d) P-PEUU inks extruded at 90°C. Measurements are taken from non-adjacent lines (n = 6). Error bars represent ± SD.

To demonstrate the suitability of each ink for HOT-DIW, we printed biomimetic TM grafts (50C/50R, 8 mm in diameter) from each ink (**Figure 4.9**). After immersion in DI water for 4 h, the P-PCL and P-PEUU grafts lost ~25% of their initial weight, which corresponds to their initial PEG content (**Figure 4.10b**). As expected, pure PCL and PEUU grafts lost minimal weight over this time period, likely due to the removal of trace amounts of unreacted monomer or residual solvent. Full-thickness FTIR demonstrates that composition of P-PEUU grafts is nearly identical to the pure PEUU grafts after leaching process is complete, as noted by a concomitant decrease of peaks at $2500 - 3000$ cm$^-$ and $1000 - 1200$ cm^{-1} (**Figure 4.10a**). The absorption of $20 - 25$ wt% PBS in **Figure 4.10c** is attributed to a nanoporous structure formed by PEG leaching in P-PCL and P-PEUU grafts.
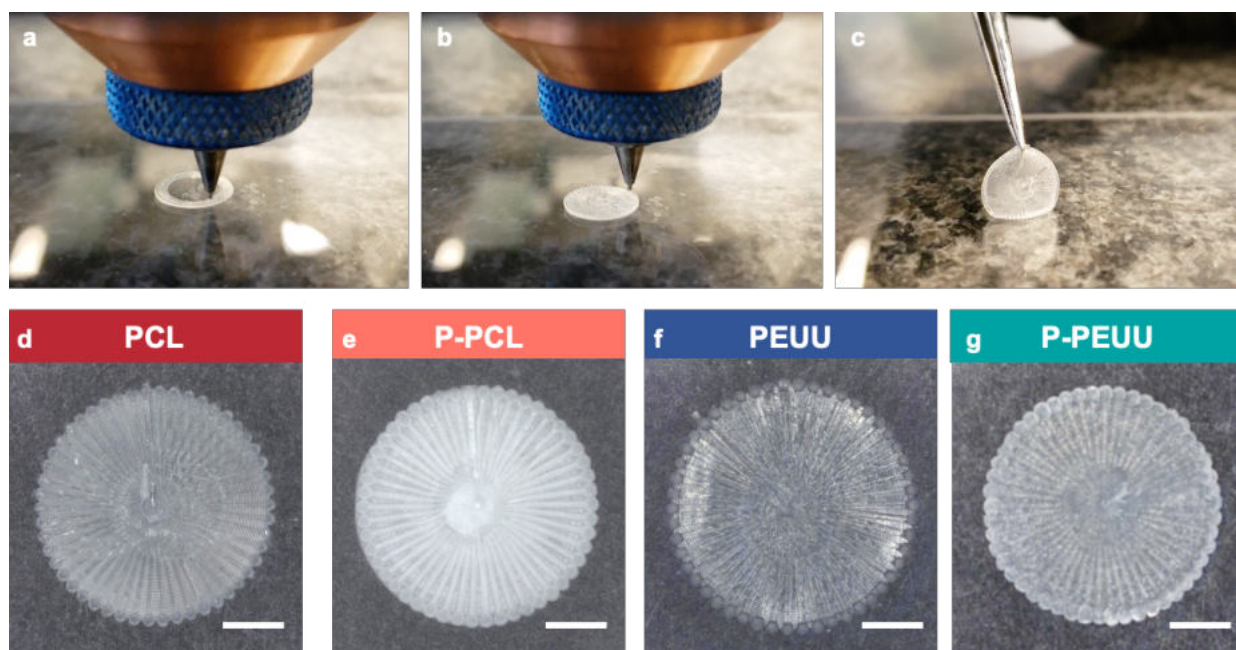
Figure 4.9. 3D printing of 8 mm biomimetic 50C/50R TM grafts by HOT-DIW. (a) 50 circular lines are 3D printed onto a glass substrate from the outer diameter inward. (b) 50 radial lines are 3D printed on top of the circular fibers from the center of the graft to the outer diameter. (c) Due to rapid solidification following melt extrusion, grafts can be readily removed from the substrate following printing. (d-g) Representative 50C/50R biomimetic TM grafts for the 4 biodegradable materials. All grafts are 3D printed utilizing a 200 μm inner diameter nozzle and a print speed of 20 mm/s. Scale bars: 2 mm.
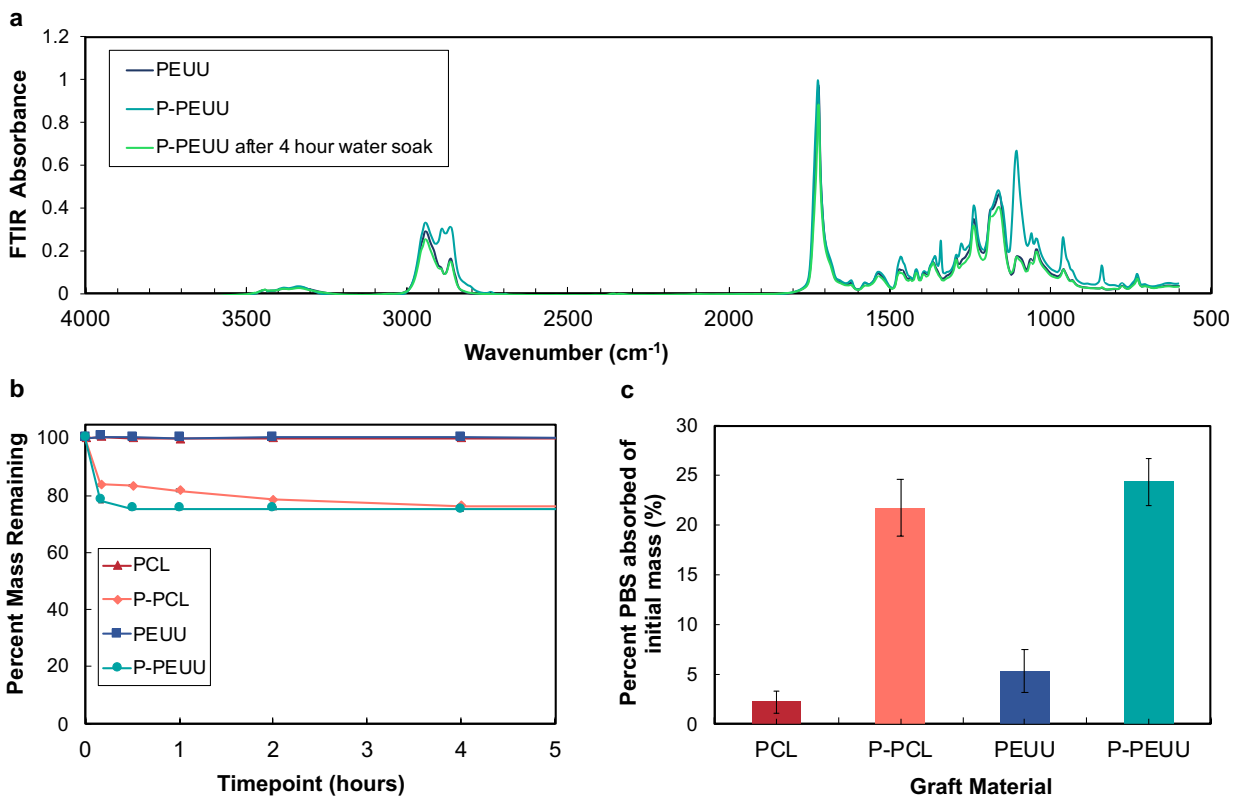
Figure 4.10. Validation of PEG leaching from 8 mm biomimetic 50C/50R TM grafts. (a) FTIR spectra of PEUU grafts, P-PEUU grafts, and P-PEUU grafts that have been leached for 4 h in DI water. (b) Change in mass of grafts after soaking in DI water at various timepoints (n = 6). (c) Absorbance of PBS by grafts after PEG has been leached from the grafts (n = 6). Error bars represent ± SD.

The biomimetic TM grafts (50C/50R) have a mass of 4 – 6 mg with the lower values associated with those subjected to PEG leaching (**Figure 4.11a**). Graft degradation as a function of time in PBS, 1 U/mL lipase, and 100 U/mL lipase solutions are shown in **Figure 4.11b-d**. When immersed in PBS, the maximal degradation occurs for P-PEUU grafts, which loses ~35 wt% of their initial mass after 30 days, followed by P-PCL grafts. The addition of lipase significantly enhances the degradation rate of all 4 grafts materials. For example, P-PEUU grafts lose ~25 wt% of their initial mass after 7 days in 1 U/mL lipase. At even higher lipase concentrations, all grafts completely degrade after 7 days in 100 U/mL lipase. However, P-PEUU grafts exhibit the fastest degradation rates under all conditions. This enhanced degradation could be enabled by a nanoporous structure via both higher absorption of PBS and lipase solutions and also enhanced diffusion of degradation byproducts from the grafts.
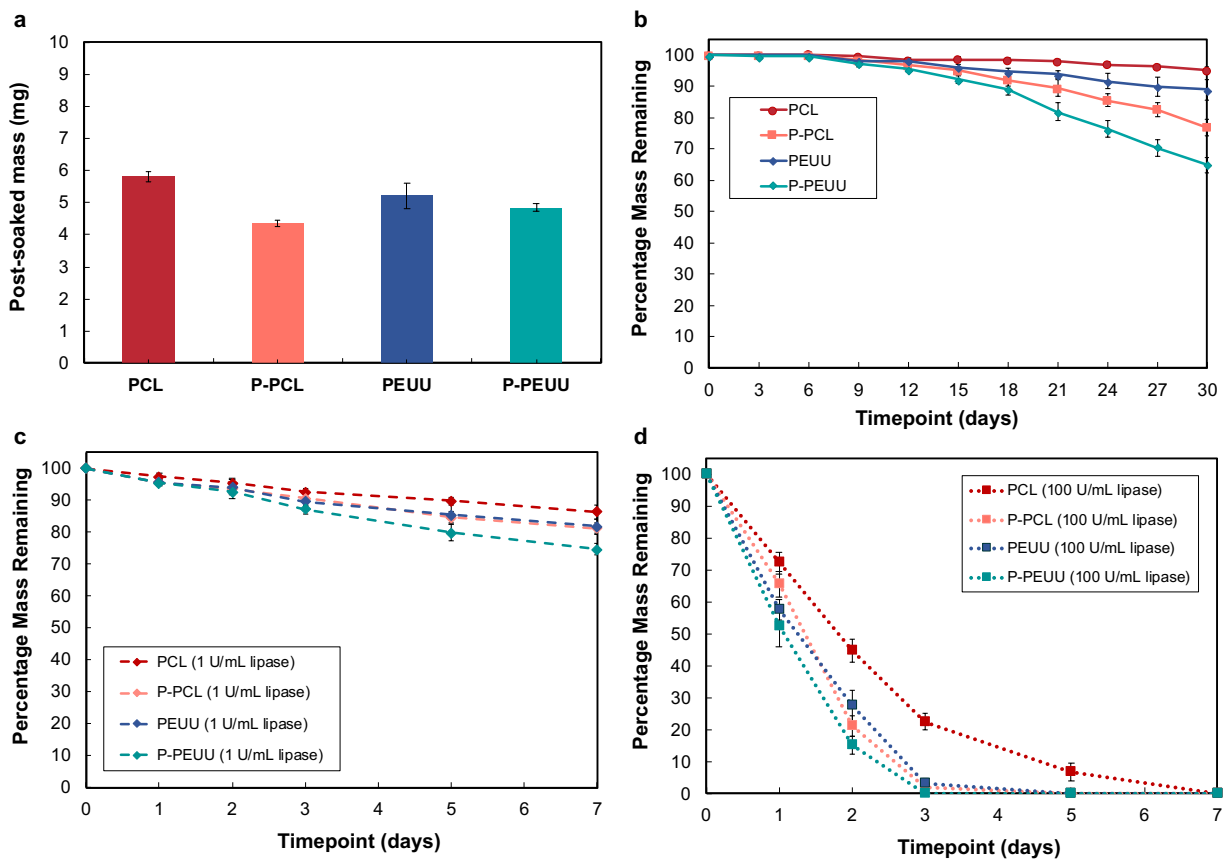
Figure 4.11. Mass and *in vitro* degradation profile of 8 mm biomimetic 50C/50R TM grafts (n = 6). (a) Initial mass of grafts from the 4 biodegradable materials. P-PCL and P-PEUU grafts have a lower starting mass due to the leaching of their PEG component prior to degradation studies. Degradation in (b) PBS, (c) 1 U/mL lipase, and (d) 100 U/mL lipase. All studies are conducted on a rocker at 60 rpm in an incubator at 37°C with 5% CO_2 atmosphere. Error bars represent ± SD.

Both HEKs and GFP-HNDFs proliferate on biomimetic TM grafts (50C/50R) produced from all 4 inks (**Figure 4.12**). There is no statistically significant difference between HEK proliferation on materials at most timepoints. At day 21, HEK proliferation is significantly higher ($p < 0.05$) on the P-PEUU grafts than on grafts printed from the other 3 inks. At day 7, GFP-HNDF proliferation is significantly lower ($p < 0.05$) on PCL grafts than P-PCL, PEUU, or P-PEUU grafts. At day 21, GFP-HNDF proliferation is significantly higher ($p < 0.05$) than both PCL and P-PCL grafts. By day 28, GFP-HNDF proliferation is significantly higher ($p < 0.05$) on the P-PEUU grafts than on grafts printed from the other 3 inks. Since PCL is widely used as a biocompatible polymer in medical implants, it is promising that grafts from novel P-PCL, PEUU, and P-PEUU inks promote cell proliferation at a similar rate. Additionally, as we observe P-PEUU grafts to have the highest proliferation at the most timepoints, this material is promising for *in vivo* applications.
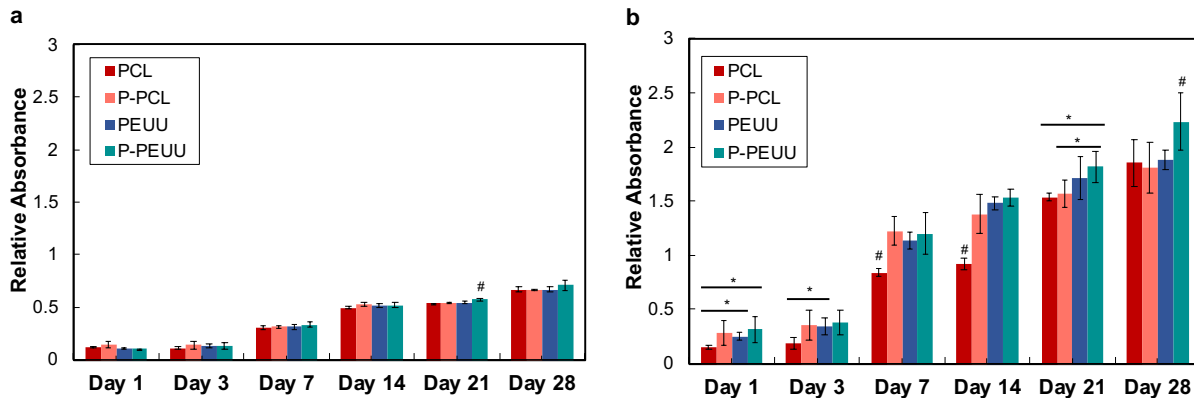
Figure 4.12. Proliferation of two common cell types responsible for TM remodeling on 8 mm biomimetic 50C/50R TM grafts (n = 6). (a) HEKs, a human keratinocyte cell line, proliferate on all graft materials, as determine by an MTS assay. (b) GFP-HNDFs, a human fibroblast cell line, proliferate on all graft materials, as determine by an MTS assay. All samples are initially seeded with 100,000 cells on the top surface. Error bars represent ± SD. * $p < 0.05$ from one specified group. # $p < 0.05$ from all other groups in timepoint.

Tensile testing was successfully performed on printed PEUU, P-PEUU, PCL, and P-PCL dogbone samples soaked in PBS (prior to testing), in which the tensile load was applied in directions parallel and orthogonal to the print path (**Figure 4.13**). There is a statistically significant difference ($p < 0.001$) between tensile specimens printed in a parallel versus an orthogonal orientation to the tension testing direction for both PEUU and P-PEUU. Specifically, the mean Young's modulus of PEUU specimens printed parallel to the testing direction is nearly 2x higher than the value measured orthogonal to this direction ($E_{||} = 72.6 \pm 4.9$ MPa, $E_{\perp} = 40.2 \pm 4.2$ MPa), while the mean Young's modulus of P-PEUU specimens printed parallel to the testing direction is nearly 1.5x higher than the value measured orthogonal to this direction ($E_{||} = 33.7 \pm 2.8$, $E_{\perp} = 23.8 \pm 1.5$ MPa). PCL specimens also exhibited a statistically significant difference as a function of their orientation, but to a far lesser extent ($p < 0.05$). The mean Young's modulus of PCL printed parallel to the testing direction is nearly 1.04x higher than the value measured orthogonal to this direction ($E_{||} = 164.9 \pm 4.2$ MPa, $E_{\perp} = 158.3 \pm 2.9$ MPa). There is not a statistically significant difference between P-PCL printed in parallel and orthogonal directions ($E_{||} = 125.2 \pm 9.4$ MPa, $E_{\perp} = 123.8 \pm 5.4$ MPa). PEG removal from the P-PCL grafts reduces their Young's modulus values by 21.2% in the parallel direction and 24.1% in the orthogonal direction, whereas the mean Young's modulus of P-PEUU grafts decreased by 41.0% in the parallel direction and 53.6% in the orthogonal direction. Finally, the stiffnesses of the printed PEUU and P-PEUU grafts in both the parallel and orthogonal directions are in the range of that of the human TM,

between 10 – 100 MPa [34-38]. For comparison, the two control materials used in tympanoplasty, cadaveric temporalis fascia and Biodesign® porcine small intestinal submucosa (pre-soaked in PBS), have Young's moduli of E_{fascia} = 6.46 ± 2.63 MPa and $E_{Biodesign®}$ = 20.6 ± 3.82 MPa.
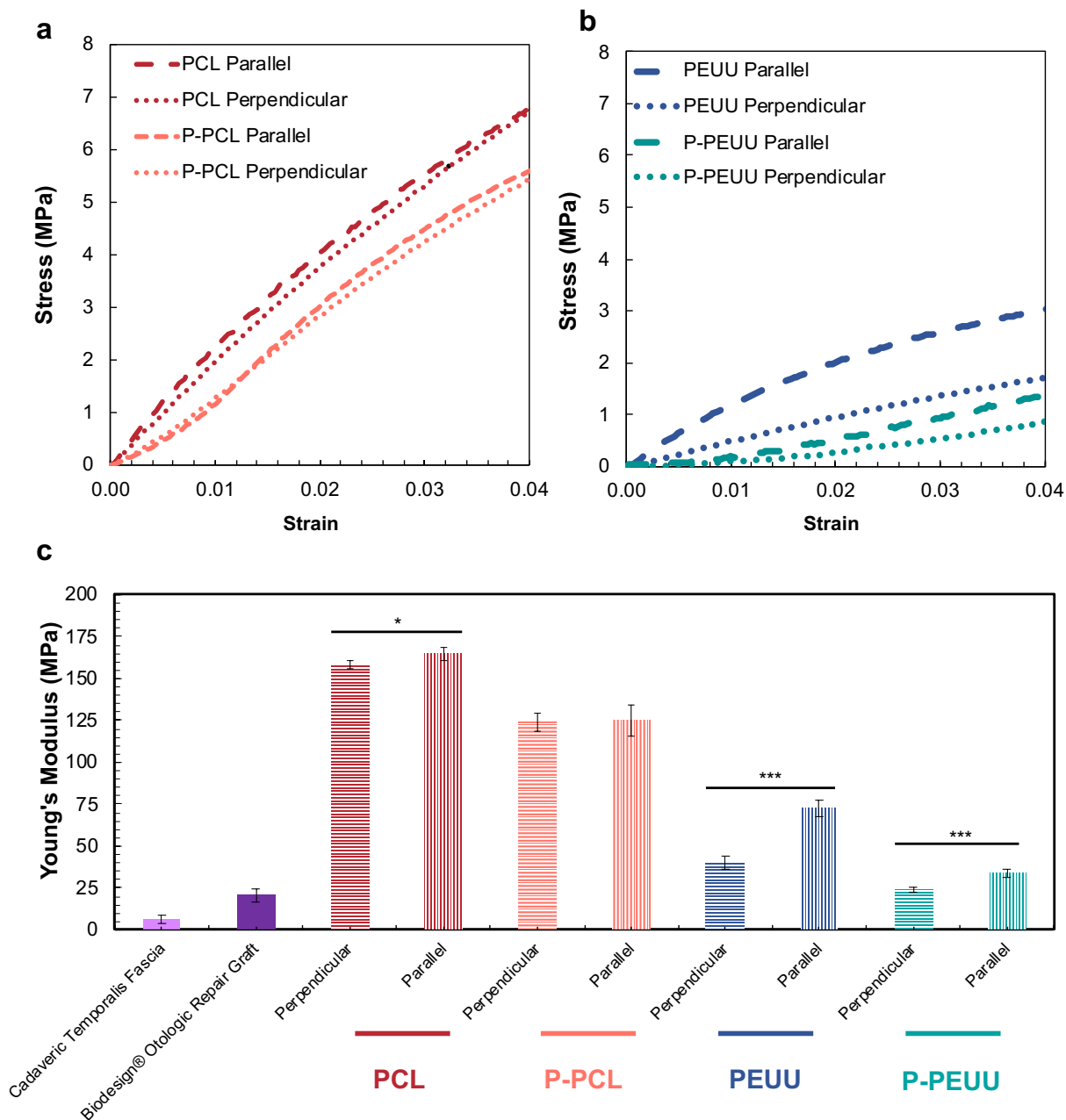
Figure 4.13. Mechanical properties of tensile specimens (n = 6). Representative stress-strain curves for (a) PCL and P-PCL and (b) PEUU and P-PEUU for specimens printed parallel and orthogonal to the print path. (c) Comparison of average Young's Moduli of control and printed specimens. Error bars represent ± SD. * p < 0.05. *** p < 0.001.

While the anisotropic mechanical properties of printed PEUU and P-PEUU grafts may induce the desired cellular alignment, their topography may also play an important role. To assess their height profile, we printed square grafts (8 mm x 8 mm) from each ink composed of 100 μm wide filaments printed at a height of 50 μm and speed of 20 mm/s (**Figure 4.14a,b**). Optical profilometry reveals the presence of filamentary features on their top surfaces, particularly for P-PCL and P-PEUU inks containing PEG (**Figure 4.14c**). The root mean square (RMS) heights of their top and bottom (in direct contact with the underlying glass substrate) surfaces are profoundly different for these grafts (**Figure 4.14d**).
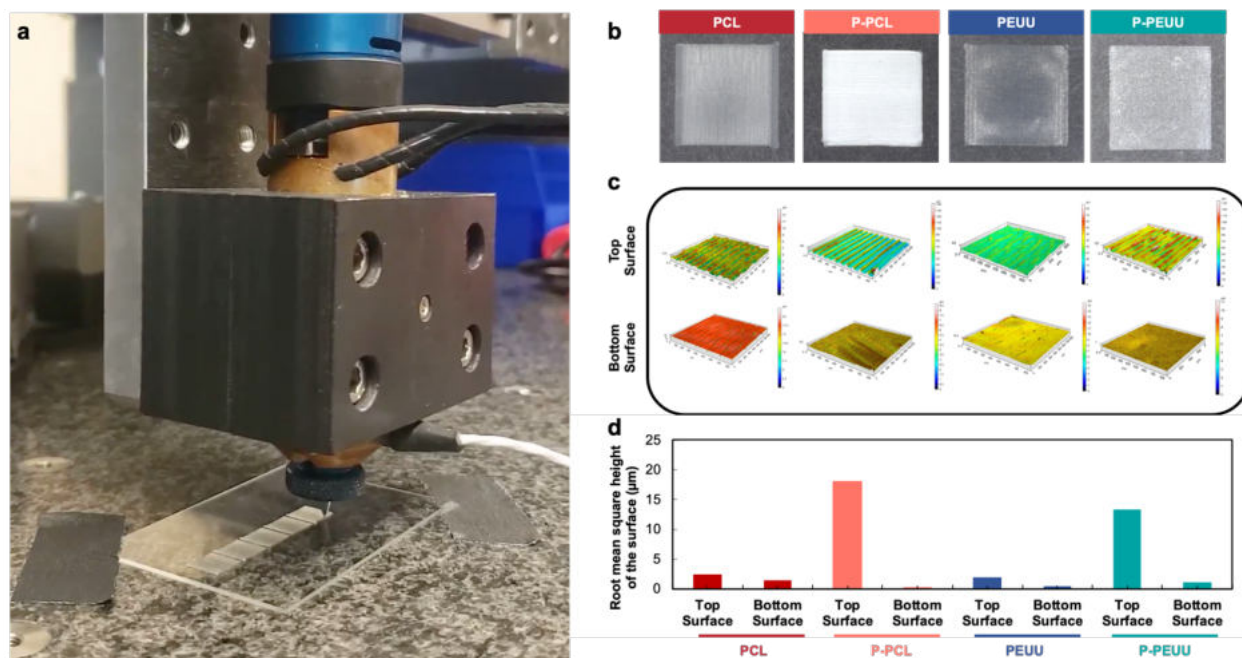
Figure 4.14. Topography of square grafts 3D printed from 4 biodegradable materials. (a) Representative 3D printing of 8 mm square grafts. (b) Square grafts printed from 4 biodegradable materials, all utilizing a 200 μm inner diameter nozzle and a print speed of 20 mm/s. (c) 3D renderings of surface topography of the top and bottom surfaces of grafts in 4 materials, where color shows the z-height across the surface of the grafts. (d) Root mean square (RMS) height of the top and bottom surfaces of grafts, with lower values corresponding to a flatter morphology on the bottom surface of grafts. Values represent averages over the profiled surface area (0.8 x 0.8 cm).

Next, we investigated the alignment of GFP-HNDFs and extracellular collagen I on biomimetic TM grafts printed from each ink via confocal imaging. Example confocal Z-stacks are shown wherein the channel indicating GFP-HNDF cellular alignment (**Figure 4.15a-c**) and the channel indicating extracellular collagen I alignment (**Figure 4.15d-f**) on P-PEUU grafts printed at a speed of 20 mm/s to varying extents depending upon the top surface of the grafts, bottom (topographically more flat) surface of the grafts, or the bottom surface of grafts that have been melted to "erase" any graft anisotropy.
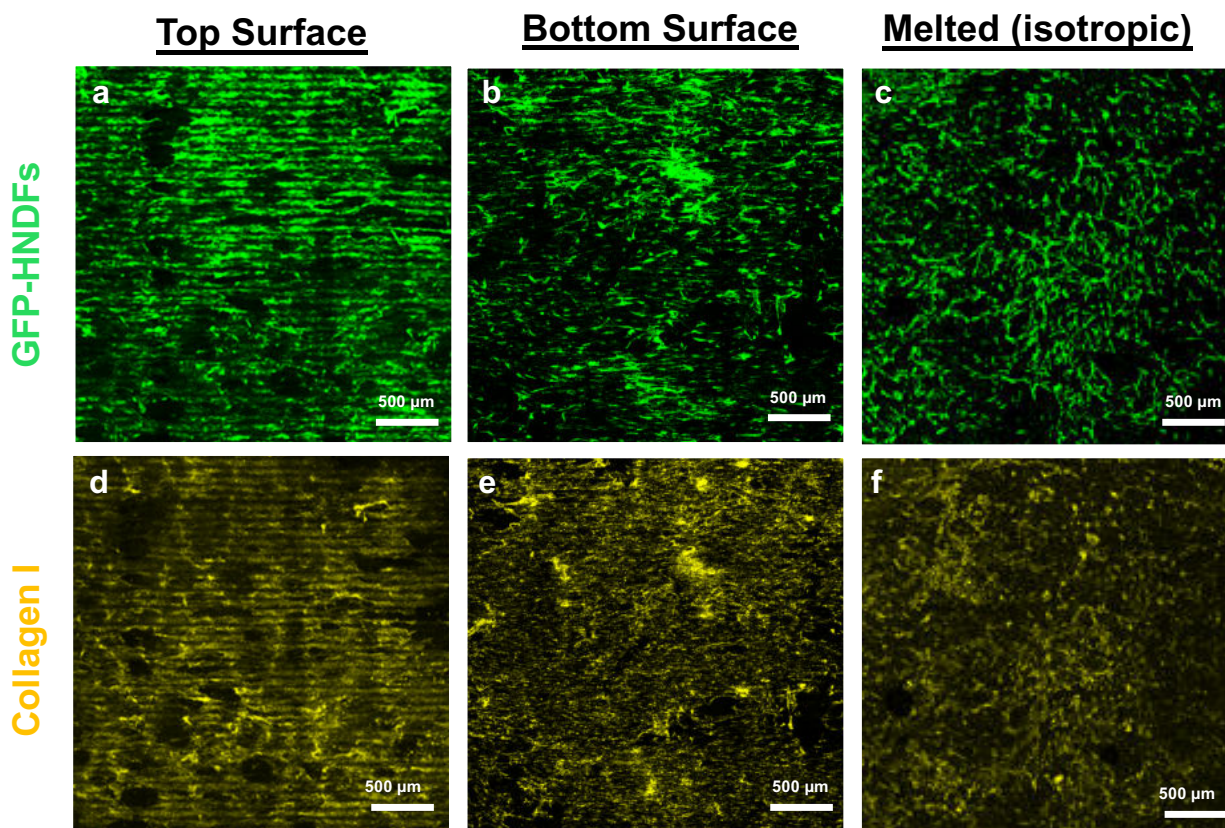
Figure 4.15. Alignment of GFP-HNDFs and collagen I deposition on P-PEUU grafts printed at a speed of 20 mm/s. GFP-HNDFs are seeded onto the top and bottom surface of grafts, as well as the bottom surface of melted grafts to "erase" anisotropy. Confocal images show channels corresponding to (a-c) intracellular GFP (green) and (d-f) collagen I (yellow) deposition. [Note: The center 6 x 6 mm region of each graft whose total size is 8 x 8 mm is used in ImageJ Directionality analysis, but only a 3 x 3 mm region is shown in this figure to more clearly demonstrate cell morphology in the images.]

GFP-HNDFs are successfully seeded onto a variety of 8 x 8 mm square grafts printed from 200 μm inner diameter nozzles while maintaining a layer height of 50 μm and a filament width of 100 μm (**Figure 4.16a**), as described previously. An assessment of these two channels separately with ImageJ Directionality analysis quantifies this cellular and extracellular matrix protein alignment, whereby the print path corresponds to a direction of 0°. The relative impacts of topography, material, and print speed on the cellular and extracellular collagen I alignment are quantified and compared between graft groups (n = 6 each).

The highest extent of GFP-HNDF and collagen I alignment is observed on the top surface of P-PEUU grafts printed at a speed of 20 mm/s, as compared to those seeded on the bottom (topographically flatter) surface of the grafts or the bottom surface of grafts that have been melted to "erase" any graft anisotropy. Alignment is highest for cells seeded on the top surface of these grafts, whereby filaments

produce distinct topographical features, reaching an average normalized intensity of 0.0841 at its peak for the GFP-HNDF channel (**Figure 4.16b**) and 0.0556 at its peak for the collagen I channel (**Figure 4.16c**). However, even on the bottom (topographically flatter) surface of the grafts, there is distinct GFP-HNDF and collagen I alignment. This directional alignment disappears for cells seeded on the bottom surface of grafts that have been melted to "erase" any anisotropy imparted into the grafts by the printing process.

To decouple the impact of macroscale filament topography on cellular and extracellular matrix protein alignment on the grafts, comparisons are made between grafts of different materials whereby cells are seeded only onto the bottom (topographically flatter) surface of grafts. When comparing the 4 biodegradable inks (PCL, P-PCL, PEUU, and P-PEUU) printed at a speed of 20 mm/s, we observe the highest extent of both GFP-HNDFs and collagen I alignment for fibroblasts seeded onto P-PEUU grafts, reaching a normalized intensity of 0.0306 at its peak for the GFP-HNDF channel (**Figure 4.16d**) and 0.0222 at its peak for the collagen I channel (**Figure 4.16e**). For PCL grafts printed at a speed of 20 mm/s, there is a very low extent of alignment in the GFP-HNDF channel observed, reaching a normalized intensity of 0.0118 at its peak, and almost no obvious direction of alignment observed in the collagen I channel.

For a similar comparison of the impact of print speed, P-PEUU grafts are successfully printed via HOT-DIW with varying print speeds, using the pneumatic expression pressures determined previously in **Figure 4.8**: 5 mm/s at 45 psi, 10 mm/s at 50 psi, 15 mm/s at 55 psi, and 20 mm/s at 60 psi. We observe that increasing the print speed of P-PEUU during HOT-DIW while maintaining the filament diameter by increasing extrusion pressure increases alignment of both the cells themselves via GFP-HNDF channel (**Figure 4.16f**) and the collagen deposition via the collagen I channel (**Figure 4.16g**). Overall, alignment of collagen I is lower than intracellular GFP alignment itself for all samples.

Extrusion processes through small diameter nozzles, such as HOT-DIW, cause high shear stress in the nozzle. This shear stress increases with increasing print speeds while maintaining filament diameter. This shear stress could potentially cause molecular alignment of the polymer along the print direction, which could then be maintained by physical bonding between hard segments (**Figure 4.17a**). We observe GFP-HNDF and extracellular collagen I alignment along the print path of biomimetic P-PEUU 50C/50R grafts printed at 20 mm/s on both the bottom, circular surface (**Figure 4.17b**) and the top, radial surface (**Figure 4.17c**). As the topography of the bottom surface of the grafts was relatively flat, cellular alignment in the P-

PEUU inks may be attributed to the anisotropic properties of the grafts. However, it is challenging to conclusively determine the relative impact of mechanical anisotropy and topography, as the feature sizes visualized via optical profilometry in **Figure 4.14c** do not assess nanoscale topography.
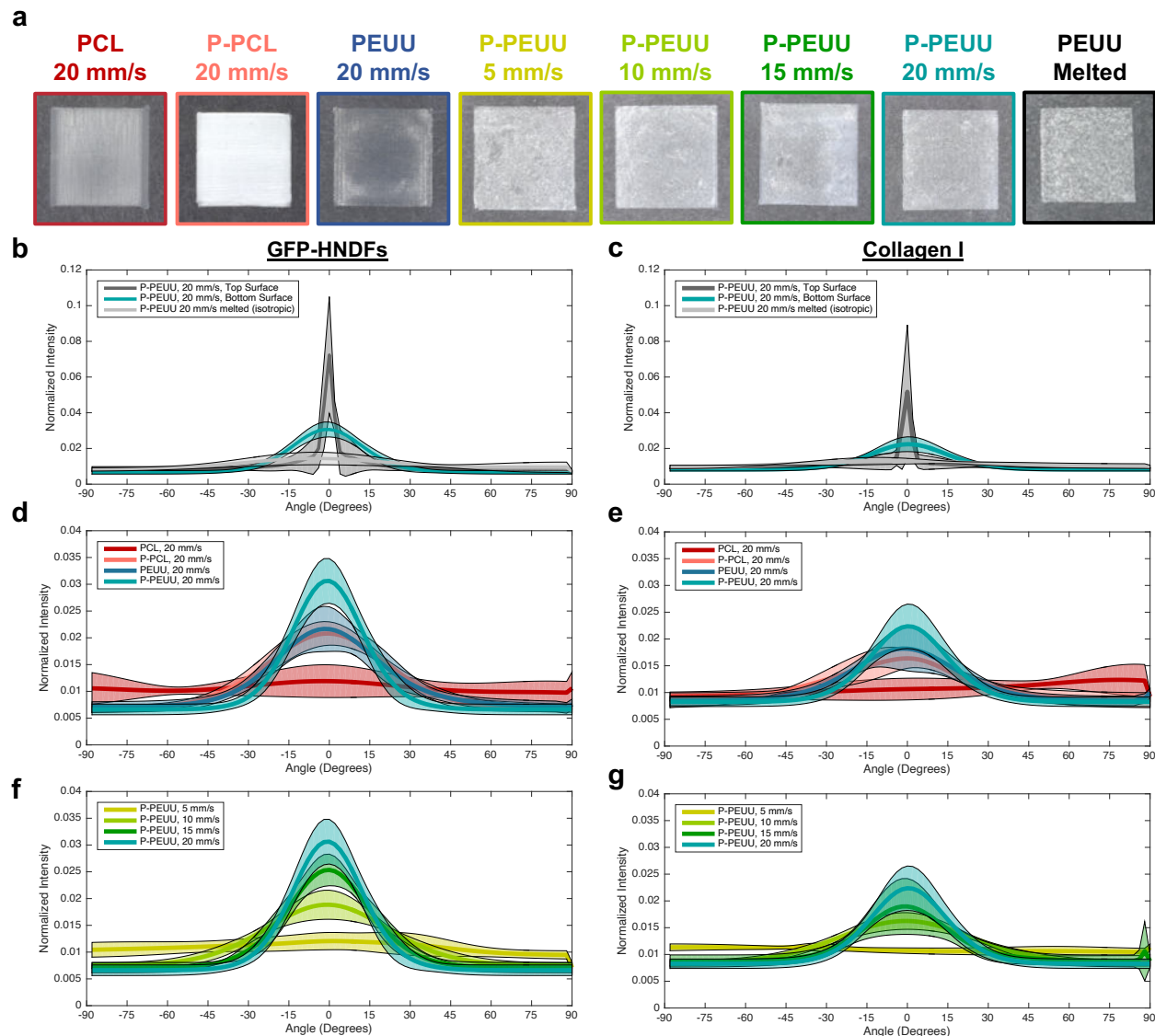
Figure 4.16. 3D printing of square grafts to determine the impact of material print speed, and nozzle diameter on cellular alignment after 7 days of GFP-HNDFs culture on the topographically flat surface of grafts (n = 6). (a) Optical microscopy images of 8 x 8 mm square grafts 3D printed from various materials and print speeds while maintaining a print height of 50 µm and filament width of 100 µm. Alignment on grafts of 4 materials all printed at 20 mm/s of (b) GFP-HNDFs and (c) collagen I. Alignment on P-PEUU grafts printed from 4 print speeds of (d) GFP-HNDFs and (e) collagen I. Alignment on the top and bottom surface of P-PEUU grafts printed at 20 mm/s compared to melted grafts for (f) GFP-HNDFs and (g) collagen I. [Note: angles of -90° and 90° correspond to the direction orthogonal to the print path, while an angle of 0° corresponds to the direction parallel to the print path. Narrower and taller distribution around 0 corresponds to a highest extent of alignment in the direction the print path.]
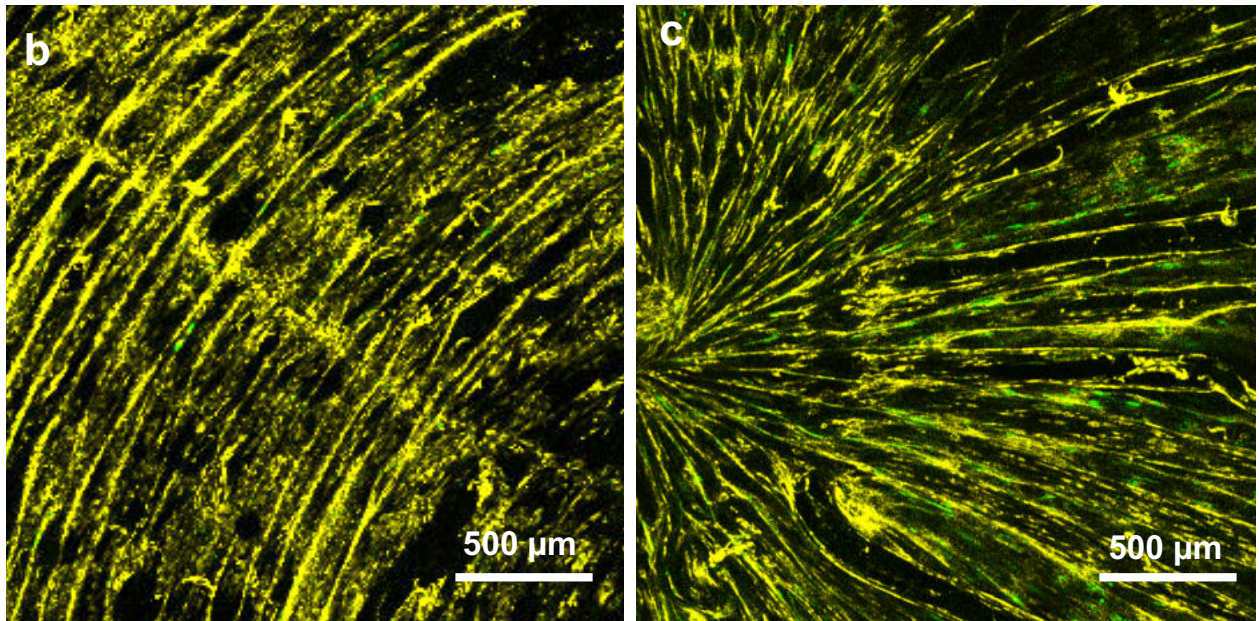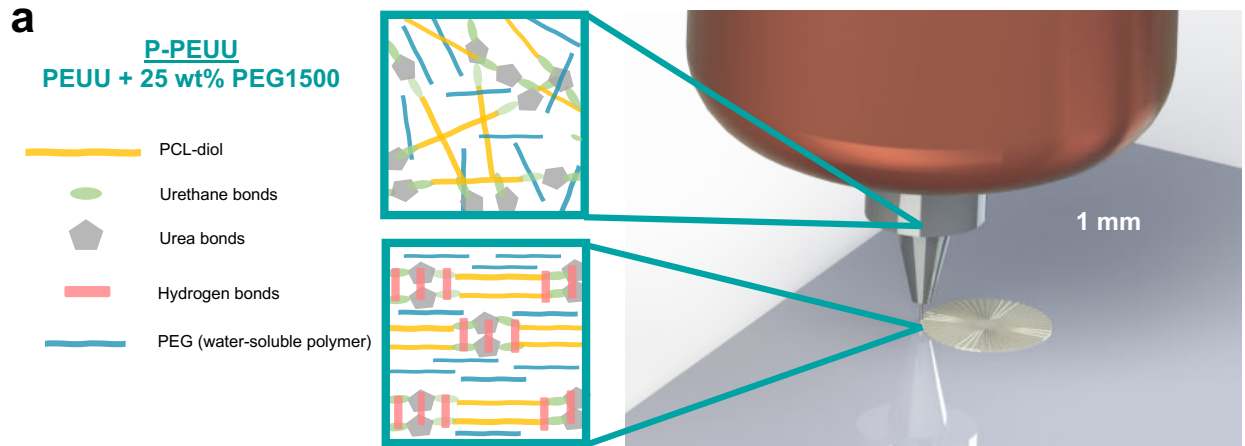
Figure 4.17. HOT-DIW of biomimetic circular/radial P-PEUU grafts results in alignment of collagen I along the print path. (a) Expected printing behavior of inks upon extrusion, whereby hydrogen bonding occurs between urethane and urea bonds. Fugitive PEG is shown in blue. Biomimetic P-PEUU grafts after 7 days of GFP-HNDF growth show intracellular GFP (green) and collagen I (yellow) along the direction of the print path along both the (b) bottom circular surface and (c) top radial surface.

4.4   Conclusions

We designed novel biodegradable inks based on PCL, which is widely used in tissue engineering, and based on a custom thermoplastic biodegradable polyurethane, PEUU. Both pure and porous PCL and PEUU inks were produced by selectively incorporating PEG as a porogen. We optimized the ink rheology and printing parameters for HOT-DIW of TM grafts in arbitrary designs. We demonstrated that both PEUU and P-PEUU grafts exhibit significant anisotropic stiffness when tested parallel and orthogonal to the print direction. Importantly, their stiffnesses are similar to that of the native human TM. While their mechanical properties of these grafts will evolve as they degrade *in vivo* and are replaced by ingrowing tissue, our ability to create synthetic TM grafts with tailored mechanical properties is expected to facilitate effective sound conduction to the ossicular chain immediately following implantation. Both GFP-HNDF alignment and extracellular collagen I alignment were maximized on grafts printed from P-PEUU ink at a print speed of 20 mm/s, supporting the use of this material and print speed in TM grafts that could potentially remodel in an anisotropic fashion.

Chapter 5

Healing and Hearing Outcomes of Biomimetic Tympanic Membrane Grafts

5.1   Introduction

The tympanic membrane (TM) is an important tissue that transduces acoustic waves into mechanical motion of the ossicles, as described in **Chapter 2**. When damaged, the primary outcomes of an effective tympanoplasty are (1) healing rate and (2) hearing improvement after repair of the TM. While *in vivo* studies can simultaneously assess both of these outcomes, *in vitro* studies are necessary initially to optimize graft design within this context. In this chapter, we create biomimetic TM grafts by HOT-DIW of the P-PEUU ink described in **Chapter 4**. We first characterize their acoustic response *in vitro* using the methods described in **Chapter 3**. Next, we assess their healing and hearing outcomes in an animal model. We compare these observations to data obtained for fascia and Biodesign® Otologic Repair grafts (porcine small intestinal submucosa), which serve as controls for this study.

Two major features influence the ability of the TM to efficiently vibrate and conduct sound waves: mass and stiffness. TMs with greater mass exhibit lower sound-induced motion, particularly at high frequencies, as demonstrated by O'Connor *et al.* during computational modeling experiments [7]. TMs with lower stiffness can better match the impedance of air at low frequencies, resulting in higher middle ear gain (MEG), whereas stiff materials can better drive the umbo, as determined by Fay *et al.* [5]. However, as discussed in **Chapter 2**, anisotropic stiffness arising from the circumferential and radial collagen fiber arrangement of the lamina propria enables the TM to efficiently vibrate at low and high frequencies.

Our biomimetic TM grafts are produced by printing P-PEUU inks exhibit stiffnesses of 23.8 ± 1.49 MPa and 38.7 ± 2.75 MPa orthogonal and parallel to the print path, respectively. We have also incorporated circumferential and radial fiber features within these grafts via 3D printing. We now assess their ability for sound conduction using laser Doppler vibrometry (LDV) and digital opto-electronic holography (DOEH). Specifically, we compare the performance of biomimetic TM grafts to isotropic grafts (controls), whose patterned architecture has been "erased" by heating the grafts above the P-PEUU melting temperature and to isolated human cadaveric TMs that are separated from the ossicular chain for *in vitro* acoustic

assessment. A combination of these two techniques allow us to assess the effects of TM graft mass and architecture (anisotropic vs. isotropic) on their sound-induced motion prior to *in vivo* implantation.

To assess *in vivo* healing and hearing outcomes, our biomimetic TM grafts are implanted into chronic perforation models of gray Langeria chinchillas. Healing success is assessed by closure of the perforated region as well as TM graft remodeling *in vivo*. Perforation closure is determined using an endoscopic method, while graft remodeling is determined by histological sectioning of the TM following sacrifice of the chinchillas [16]. Specifically, the graft thickness and the ingrowth of native cells and deposition of extracellular proteins can be examined by hematoxylin and eosin (H&E) staining, whereby cell nuclei are stained blue and proteins are stained pink. Since P-PEUU degrades into small molecule byproducts, we must also assess ototoxicity in the form of damage to the hair cells of the organ of Corti and/or spiral ganglion neurons (SGNs) [454]. Using these methods, we find no ototoxic effects to the organ of Corti or SGNs following 3 months of implantation with P-PEUU or control graft materials.

In addition to assessing healing, we also evaluate the hearing outcomes of biomimetic and control TM grafts *in vivo*. Hearing outcomes are typically assessed in humans via behavioral audiometry. Since chinchillas cannot consciously indicate positive hearing thresholds to researchers, two electrophysiological measurement techniques (commonly used for hearing testing in human infants) are used before and after *in vivo* graft implantation to examine hearing threshold changes. The first measurement technique, evoked distortion product otoacoustic emissions (DPOAE), are collected to determine the ability of sound to reach and stimulate the cochlea. DPOAEs are weak sounds generated by nonlinear processes in the cochlea when it is stimulated simultaneously by two pure tone frequencies ($f_{dp} = 2f_1 - f_2$). These measurements have been successfully collected in chinchillas by other researchers [455-458]. DPOAE measurements give some information as to both the conductive and sensorineural hearing health of the animal. The second method of analyzing hearing restoration in chinchillas are auditory brainstem response (ABR) measurements, which determine the ability of sound to reach the auditory brainstem. ABR measurements have been successfully recorded in chinchillas to determine hearing loss from a variety of middle and inner ear pathologies [459-462]. Using these methods, we find that chinchillas that underwent tympanoplasty with biomimetic P-PEUU TM grafts restore hearing thresholds to closer to normal with an intact TM as compared to those that underwent tympanoplasty with control graft materials.

5.2   Experimental Methods

5.2.1   3D Printing of Biomimetic Tympanic Membrane Grafts

For *in vitro* acoustic testing, biomimetic TM grafts are designed to have an outer diameter of 16 mm with a microarchitecture of 100 circular lines (100C) followed by 50 radial lines (50R). The architecture is programmed in Aerobasic G-Code (Aerotech Inc., USA). For *in vivo* implantation, TM grafts are 3D printed via the HOT-DIW extrusion setup to have an outer diameter of 8 mm with a microarchitecture of 50C/50R. Custom polymeric inks are formulated from poly(ester urethane urea) (PEUU) with 25 wt% polyethylene glycol (PEG, MW = 1,500, Beantown Chemical, USA) as described in **Chapter 4**.

The custom HOT-DIW extrusion 3D printing setup in conjunction with the custom-designed 3D printer onto glass substrates is used to 3D print the grafts (**Figure 5.1**). Additionally, for exploring the impact of architecture versus mass on sound-induced motion, P-PEUU grafts are 3D printed into a 100C and 100C/50R architecture (50C and 50C/50R in the inner 8 mm). To remove the 3D printed structure and imparted anisotropy from the grafts, 100C and 100C/50R grafts are placed in an oven at 100°C for 1 hr. As this is above the melted temperature for the grafts, the structure is removed. Following 3D printing and/or melting, the grafts are removed from the glass substrates, plasma treated for 30 seconds per side (Femto PCCE plasma cleaner, Diener Electronic, Germany) and soaked in deionized water overnight to remove PEG and create porous PEUU (P-PEUU) grafts.
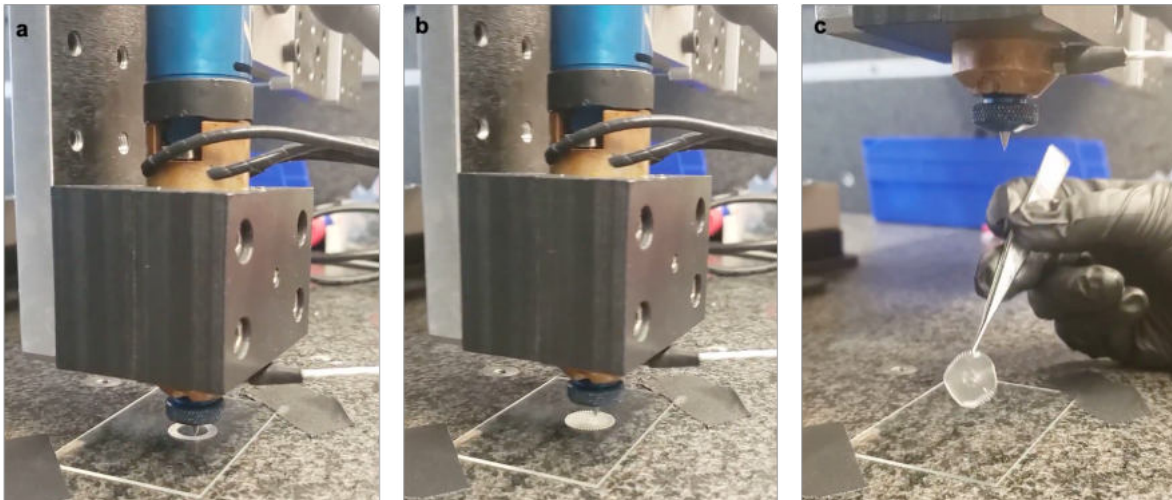
Figure 5.1. 3D printing of biomimetic TM grafts from P-PEUU ink using a custom HOT-DIW setup. 16 mm diameter grafts are printed for acoustic testing from 100 circular (100C) and 50 radial (50R) lines. When these grafts are mounted, only the inner 8 mm 50C/50R will be exposed for testing.

5.2.2 Preparation of Control Materials

For *in vitro* acoustic testing, control materials are prepared from cadaveric temporalis fascia and Biodesign® Otologic Repair Graft (acellular porcine small intestinal submucosa, Cook Medical, USA). Biodesign® is currently the only non-autologous graft on the market and has been shown to heal chronic TM perforations in humans. Grafts from both control materials are cut into 16 mm circular sections (n = 6). To isolate TM tissue for more relevant comparison in sound-induced motion, the TM is isolated from the annulus and ossicles of human cadaveric temporal bones in the Mass. Eye & Ear skills lab in the *Joseph B Nadol Surgical Skills Center*. All grafts are kept moist via phosphate buffered saline (PBS) soaks prior to all measurements and testing.

5.2.3 Quantifying Graft Thickness and Mass

A digital micrometer (Mitutoyo, Japan) with a circular clamping radius of 8 mm is used to measure the final thickness of both 3D-printed and melted grafts at the center 8 mm of different grafts (n = 6). These include biomimetic P-PEUU 100C and 100C/50R grafts (50C and 50C/50R in center), cadaveric temporalis fascia, and Biodesign® Otologic Repair Graft. The mean and standard deviation (SD) of graft thickness are calculated for each control and biomimetic group. A Student's t-test (JMP Pro 15, USA) is conducted to determine statistical significance between materials. Statistical significance is defined as $p < 0.05$.

To determine the TM graft mass, the center 8 mm region of each graft is biopsy punched after acoustic testing. The grafts are then soaked in phosphate buffered saline (PBS) for 5 min followed by patting the grafts with Kimwipes (Kimberly-Clark, USA) to remove water on their surface prior to weighing. Thermogravimetric analysis (TGA) (TA Instruments, USA) is used to weigh the grafts at accuracy up to 0.0001 mg. A Student's t-test (JMP Pro 15, USA) is conducted to determine statistical significance between materials. Statistical significance is defined as $p < 0.05$.

5.2.4 *In Vitro* Acoustic Testing

To determine *in vitro* sound-induced motion of biomimetic and control grafts, a series of custom holders is designed to clamp the grafts circumferentially to replicate the boundary condition of the TM inside the ear canal, where the TM is fixed along the tympanic annulus to the bony ear canal (**Figure 5.2**). A holder is designed using computer-aided design (SolidWorks, USA) with an inner diameter of 8 mm, containing a microphone input port, speaker input port, and a region for screwing in a metal rod for stability

of the holders. A vacuum seal ring is further adapted to ensure secure clamping of the graft to the holder. The holders are 3D printed using a high-resolution stereolithography 3D printer (HTM 140 resin, Aureus, EnvisionTEC, USA). The top and bottom portions of the holder are held together by 3 bolts spaced evenly at a diameter of 20 mm around the center of the holder.

For acoustic testing, the grafts are centered over the exposed 8 mm inner hole. A vacuum is applied via the vacuum hose to hold the grafts in place. Once the seal is established and we had a clear boundary, a cover is screwed on top in order to preserve that vacuum seal during the acoustic testing. The holders are mounted onto the respective acoustic testing setups, including mounting a speaker and a microphone in the designated holder ports. The speaker (CF1, Tucker-Davis Technologies, USA) is sealed into the sample holder with a sound coupler and rubber tube to deliver closed sound field stimuli. The microphone (ER-7C, Etymotic Research, USA) probe is inserted into the holder port until the tip of the probe is near the graft's surface in order to record sound pressure level (SPL) to normalize the data across frequencies, as different frequencies require different SPL values for effective stimulation. Prior to testing, DOEH is used to check the boundary conditions of each graft to ensure circumferential clamping at the boundary (no observed motion) prior to testing.
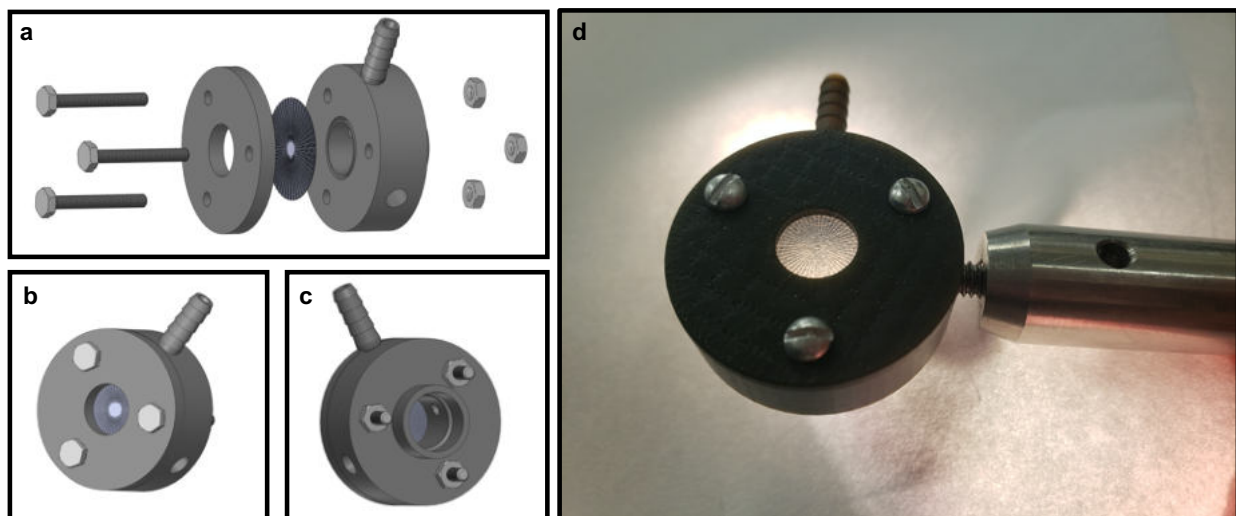
Figure 5.2. Custom holders for *in vitro* acoustic testing of TM grafts. (a-c) CAD assembly of components involved in holder. (d) Final assembly with 16 mm P-PEUU 100C/50C graft placed in the holder, exposing the circumferentially clamped inner 8 mm 50C/50R region.

The first acoustic test conducted on the grafts is LDV, as described in **Chapter 3**. LDV is conducted to gather sound-induced velocity at the center point of the grafts over high frequency-resolution with a custom setup (**Figure 5.3**). To capture the vibrations, a reflective bead (50 nm diameter polystyrene micro-beads) is placed in the center of each holder-mounted graft. To ensure that measured sound-induced velocity levels are above the noise produced by the holder, reflective beads are placed at various locations on the holder and tested. The sound stimuli for LDV measurements are broadband chirps containing continuous pure tones at frequencies of 20 – 20,000 Hz. The stimulus signals are delivered to the CF1 sound source to produce sound levels between 80 – 120 dB SPL near the membrane surface. At each measurement, the LDV and ER-7C microphone response signals to a series of repeated chirps are recorded through an A/D acquisition board running on a PXI system (National Instruments, USA) and averaged (n = 200). During post-processing of the data with a custom MATLAB® program (MathWorks, USA), the membrane velocity quantified by LDV is normalized by the sound pressure monitored by the ER-7C microphone. The sound-induced velocity of the surface of the graft holder is used to define a 'noise and artifact' level, which described the smallest discriminable velocity. The mean and SD of each group is calculated based on n = 6 of each sample type.
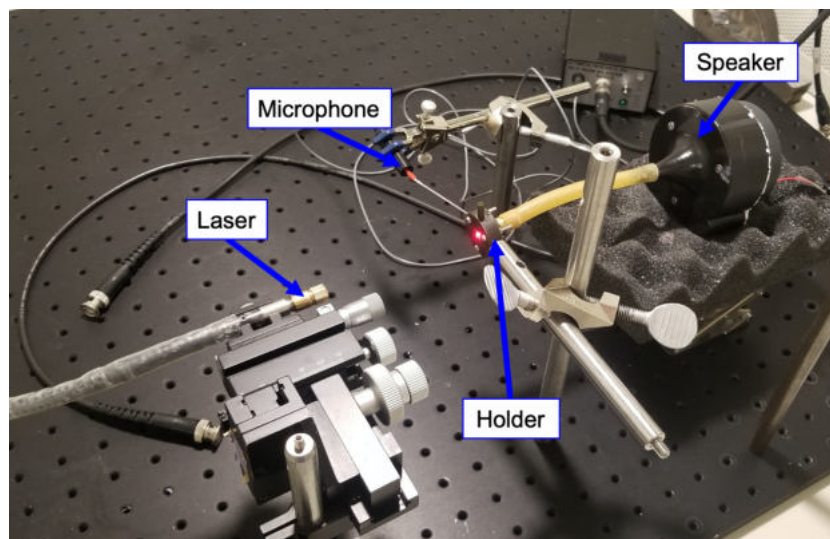
Figure 5.3. LDV setup for *in vitro* acoustic testing of TM grafts. TM grafts are mounted onto a custom holder. A speaker sound source is coupled to the holder to directly stimulate them. A microphone is placed adjacent to the graft through a hole in the holder to record sound pressure adjacent to the graft. A laser fiber interferometer records motion of grafts at the center via a reflective bead placed at the center of each graft.

The second acoustic test conducted is DOEH, as described in **Chapter 3**. Data acquisition techniques and hardware utilizes a custom setup (**Figure 5.4**). To increase the amount of reflected light from the TM graft surface, each graft is lightly painted with a solution of ZnO_2 powder and saline (Acros Organics, USA). This application of creating a reflective surface has previously been shown to not significantly change the acoustical/mechanical properties of the painted material [440]. Mounted TM grafts are subjected to continuous tones at 7 different frequencies across the human range of sound perception: (1) low frequencies of 400, 1000, and 3000 Hz, (2) mid frequency of 6000 Hz, and (3) high frequencies of 10,000, 15,000, and 20,000 Hz. SPL varied at different frequencies to produce DOEH measurable holographic fringes on the membrane surface. The sound stimulus levels used in this study are within the linear response range of the human TM and middle ear [441,442]. Displacement of the graft at each stimulus frequency is normalized by the stimulus sound pressure, monitored near the membrane surface. A custom MATLAB program is used to calculate displacement magnitude and phase, which are independently color mapped. For quantitative comparison between samples, consistent ranges are used for each frequency tested: (1) 0 – 64 nm/Pa for low frequencies of 400, 1000, and 3000 Hz, (2) 0 – 32 nm/Pa for the mid frequency of 6000 Hz, and (3) 0 – 8 nm/Pa for high frequencies of 10,000, 15,000, and 20,000 Hz.
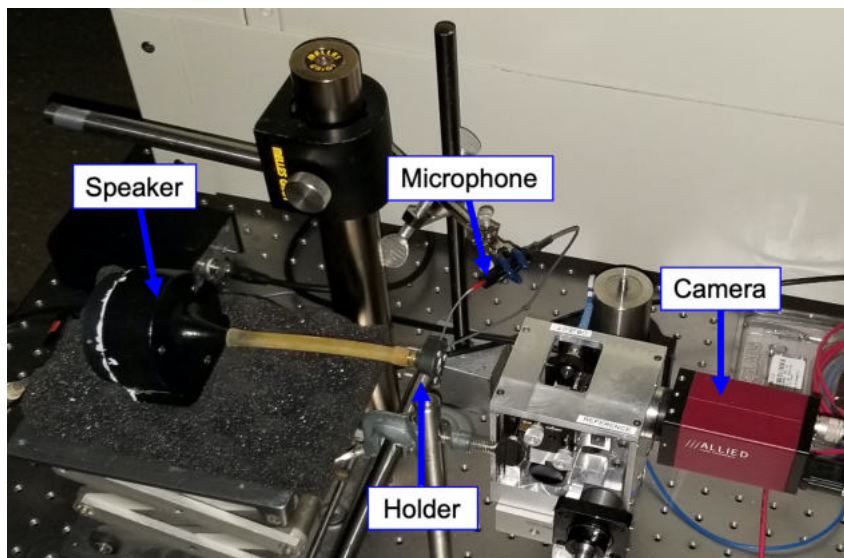
Figure 5.4. DOEH setup for *in vitro* acoustic testing of TM grafts. TM grafts are mounted onto a custom holder. A speaker sound source is placed behind the grafts to directly stimulate them. A microphone is placed adjacent to the graft through a hole in the holder to record sound pressure adjacent to the graft. A holographic camera records motion of surfaces painted with a reflective coating.

5.2.5 Chronic Perforation Creation and Tympanoplasty Procedures in Chinchilla Models

Approval for animal surgery is obtained and performed in accordance with the guidelines of the Institutional Animal Care and Use Committee (IACUC) at Massachusetts Eye & Ear. Chinchillas (*Chinchilla lanigera,* ~500 grams each, females) are anesthetized and monitored. Animals undergo baseline ABR and DPOAE testing in a sound treated booth as described in the below section. For control materials, fascia grafts are harvested from the superficial surface of the masticator muscle on chinchillas with a radius of approximately 8 mm. Biodesign® grafts are cut with a radius of approximately 8 mm as a second control material. Following hearing testing, the TM is visualized via using a rigid 0° and 30° Storz Hopkins® rod endoscope with a light source and camera (KARL STORZ, Germany). A low-temperature thermal myringotomy loop (Bovie Medical, USA) is used to create a 50% perforation on the inferior portion of the pars tensa [463]. The inner mucosal layer of the TM is removed using a 1 mm hook, and radial orientated incisions are made in the remnant TM. This process allows for infolding of epithelialized flaps. An identical procedure is then repeated on the contralateral ear. Weekly endo-otoscopy (weeks 1 – 4) is performed to ensure perforations remain stable and free of infection (**Figure 5.5a-e**).

The animals undergo transcanal endoscopic tympanoplasty utilizing biomimetic P-PEUU 50C/50R TM grafts in one ear (n = 20) with control autologous fascia grafts (n = 8) or Biodesign® grafts (n = 12) in the contralateral ear (**Figure 5.5f-h**). Grafts are placed in an underlay, transbullar fashion. Following graft placement, the middle ear is packed with absorbable Gelfoam® (Pfizer, USA) for graft stabilization during healing. Antibiotic ofloxacin drops are applied to both ears daily starting 1 week following the procedure. All treated and control ears undergo regular otoscopic evaluation to determine healing rates. After 3 months, a binary decision is made as to whether the tympanoplasty is successful in closing the perforation based on endoscopic examination.
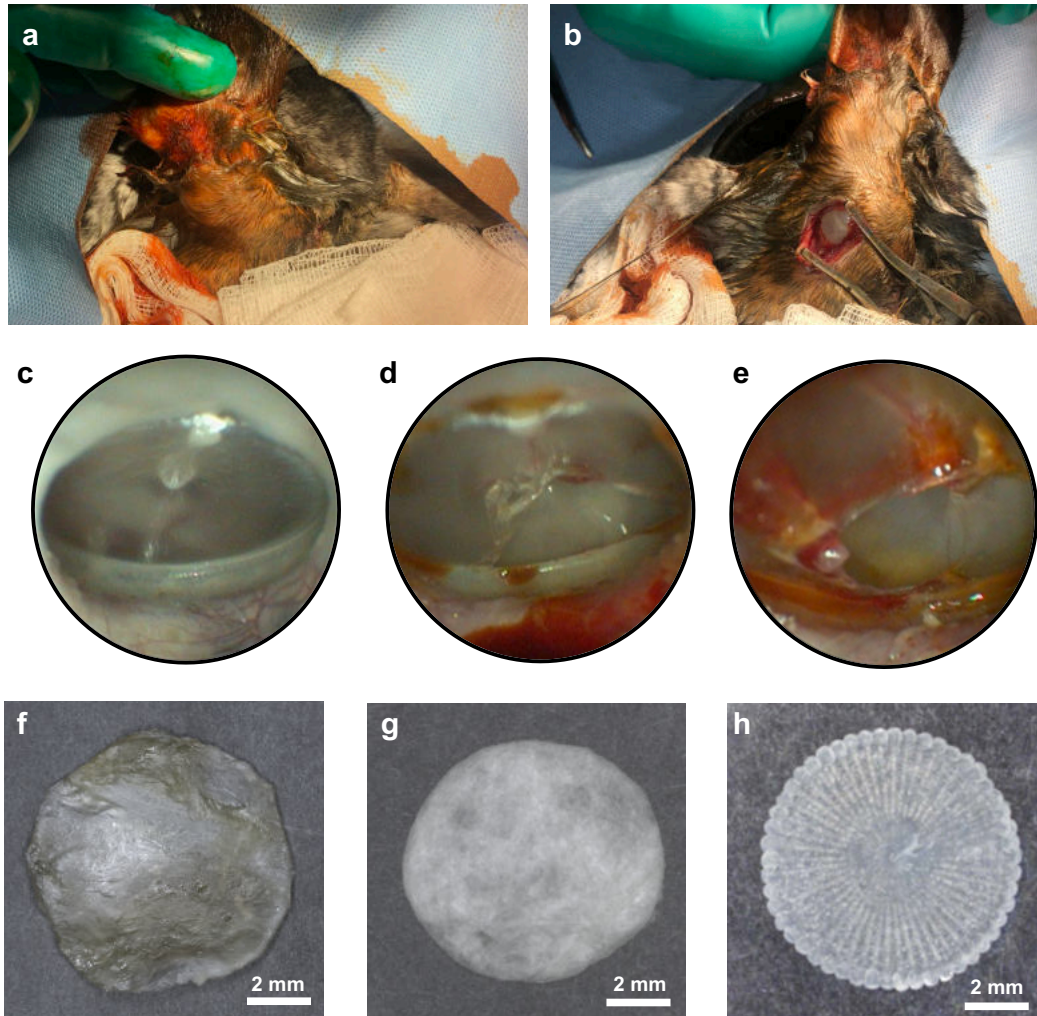
Figure 5.5. Creation and repair of chronic subtotal perforations. (a) An incision is made behind the bulla in a chinchilla, (b) exposing the middle ear space. (c) Normal chinchilla TM. (d) Chronic perforations are created using a thermal myringotomy loop. (e) These chronic perforations persist for 1 month without spontaneous healing. Underlay tympanoplasty is performed with (f) autologous fascia grafts, (g) Biodesign® grafts, and (h) biomimetic P-PEUU 50C/50R grafts with a diameter of 8 mm.

5.2.6   Auditory Testing in Chinchillas

Animals undergo baseline threshold DPOAE and ABR measurements in a sound treated booth in both ears under general anesthesia. Standard procedures are used for conducting these measurements, as used previously by researchers at Mass. Eye & Ear [464,465]. For DPOAE measurements, pure tones are delivered in pairs, and the otoacoustic emissions are recorded. Measurements are obtained at 500, 1000, 2000, 4000, 8000, and 16,000 Hz starting at 10 dB and advancing by 5 dB steps. ABR thresholds are obtained first by using a click stimulus starting at 20 dB SPL and progressing by 5 dB steps until a clear ABR wave V response is observed at three sequential runs. Tone bursts are delivered, and electrodes

143

measure activity from the auditory pathway. Pure tone ABR are obtained at 300, 1000, 2000, 4000, 8000, and 16,000 Hz starting at 10 dB and advancing by 5 dB steps. These electrical responses are analyzed, and the recordings are obtained in six to seven waveforms.

Hearing improvement following TM repair is determined by comparing the data before perforation (day 0) to post-perforation and 3 months following tympanoplasty. The mean and standard deviation (SD) of ABR and DPOAE threshold changes are calculated for each control and biomimetic group, using only data from successfully healed TMs to mitigate the pressure differential effect of residual perforations on non-healed TMs. A Student's t-test (JMP Pro 15, USA) is conducted to determine statistical significance of ABR and DPOAE threshold changes for each frequency between materials. A threshold difference greater than 10 dB is considered clinically significant. Statistical significance is defined as $p < 0.05$.

5.2.7 Histological Processing and Analysis

The chinchillas are sacrificed following hearing tests at approximately 3 months after the tympanoplasty procedure. Animals are perfused with 10% formalin through cardiac catheterization. Their temporal bones are harvested for histopathologic processing. The techniques for fixation, dehydration and embedding of ear tissues in celloidin are well described [466]. Decalcification of the skulls is performed with ethylenediaminetetraacetic acid (EDTA) over the course of 9 months. They are embedded in celloidin for sectioning. Celloidin provides a high level of anatomic detail over the entire auditory periphery and has demonstrated success in the preservation of the organ of Corti, enabling hair cell counts [467,468]. Histologic sections demonstrating reconstructed TMs and controls are analyzed using H&E staining and light microscopy. P-PEUU degradation is assessed by measuring thickness and presence of the remnant graft in comparison to pre-implanted dimensions. Established techniques permit evaluation of the ototoxicity of P-PEUU material through hair cell and neuronal counts [469-471].

5.3 Results

Biomimetic TM grafts (P-PEUU) are printed in both 100C (16 mm diameter) and 100C/50R architectures (50C and 50C/50R in the inner 8 mm) for acoustic testing. Control grafts composed of cadaveric temporalis fascia and Biodesign® controls are cut and prepared. Of these, temporalis fascia grafts have the highest mean thickness of 309 ± 93 µm and mass of 25.6 ± 5.1 mg (**Figure 5.6**). The

Biodesign® grafts are also significantly thicker and heavier (p < 0.05) than any of the printed P-PEUU grafts. P-PEUU 50C/50R grafts with 2 layers are slightly less than twice the thickness of P-PEUU 50C grafts (107 ± 4 μm vs. 57 ± 4 μm), likely due to the radial layer not covering the entire surface of the graft. The thickness of P-PEUU 50C/50R grafts is approximately 80 – 120 μm thick, which is close to that of the human TM in the pars tensa [15]. There is no statistically significant difference between the thickness or mass of printed biomimetic TM grafts (anisotropic or melted isotropic) with 50C single-layer or 50C/50R dual-layer architectures. Hence, the impact of their anisotropic architecture on sound-induced motion arises solely due to their anisotropic stiffness.
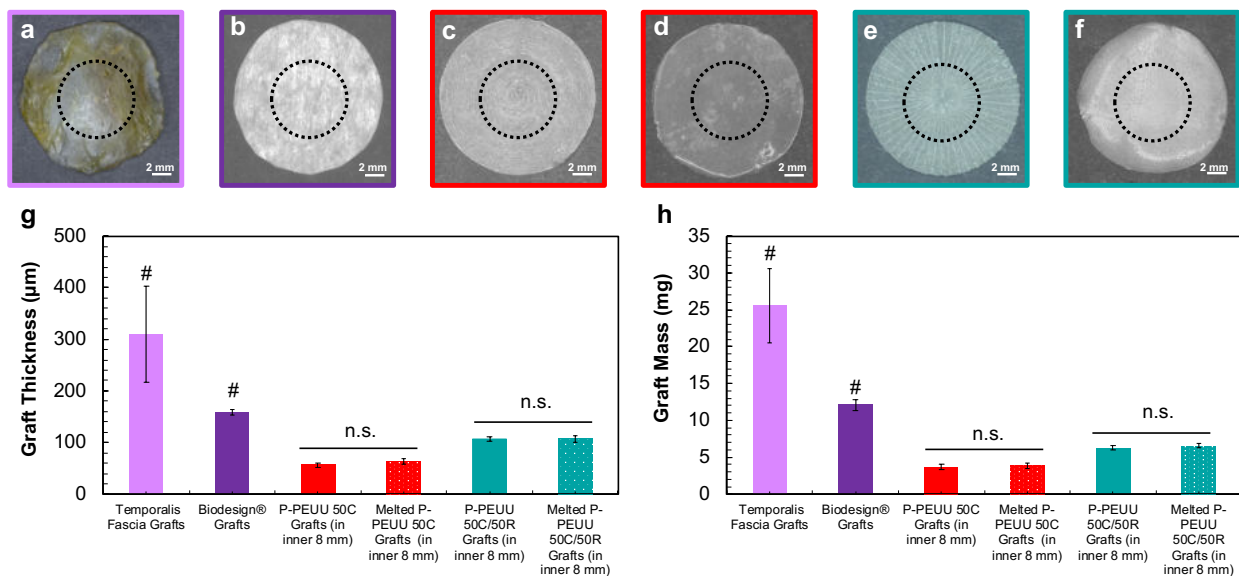
Figure 5.6. Characterization of grafts used for *in vitro* acoustic testing. Representative images of each graft type: (a) cadaveric temporalis fascia, (b) Biodesign® porcine intestinal submucosa, (c) P-PEUU 50C graft, (d) melted P-PEUU 50C graft, (e) P-PEUU 50C/50R graft, (f) melted P-PEUU 50C/50R graft. [Note: black dashed lines indicate biopsy punched 8 mm region.] (g) Thickness of moistened grafts at the center 8 mm as measured by digital micrometers. (h) Mass of moistened 8 mm biopsy punched center region of grafts as measured by a high accuracy thermal gravimetric analysis instrument. (n = 6, # p < 0.05 from all other groups, n.s. = no statistically significant difference).

We first investigate the sound-induced motion of biomimetic P-PEUU 50C/50R grafts compared to that of isolated cadaveric human TMs, fascia grafts, and Biodesign® grafts. The velocity at the center point of each graft, as determined by LDV, is above the noise floor of the holder at all frequencies tested (**Figure 5.7**). Across the range of frequencies (80 – 20,000 Hz) important for human hearing, the sound-induced motion P-PEUU 50C/50R grafts is greater than that of either the fascia of Biodesign® control materials. Additionally, these grafts have a higher sound-induced velocity than the unloaded human cadaveric TMs.

This difference is most pronounced at frequencies of 400 Hz – 4000 Hz. When comparing the two control graft materials, temporalis fascia grafts have greater sound-induced motion than Biodesign® grafts at low frequencies (<400 Hz); however, at mid frequencies and high frequencies, Biodesign® grafts exhibit higher sound-induced motion. All grafts exhibit a major resonant frequency of around 2000 – 3000 Hz. There is consistent motion among grafts in the same holder sizes, demonstrating fidelity between grafts of the same type. At high frequencies >10,000 Hz, P-PEUU 50C/50R grafts exhibit the highest sound-induced motion, followed by the human cadaveric TMs. It is important to note that the isolated TMs have a slight conical structure to them, even following isolation from the ossicular chain, which may impact their motion (see **Chapter 3**). Since the printed TM grafts are kept flat during *in vitro* acoustic testing, we may be underestimating their performance compared to implanted grafts that adopt a more conical shape.
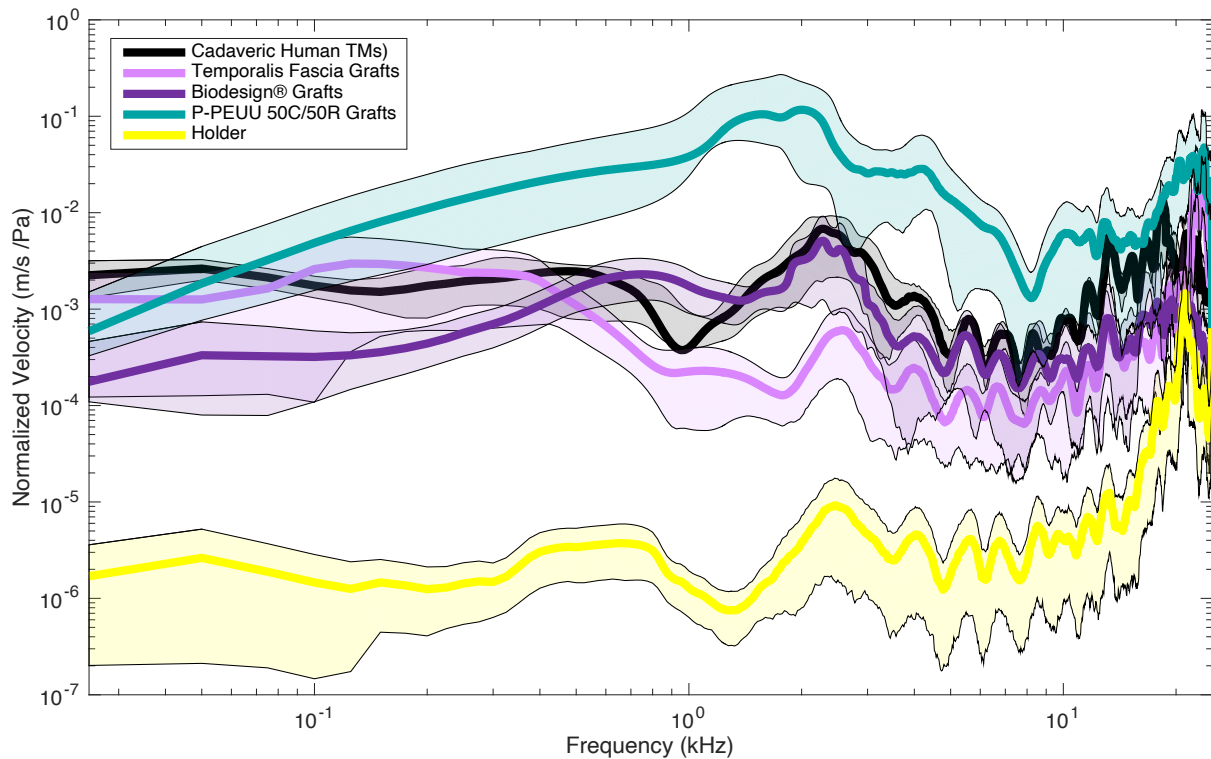
Figure 5.7. Impact of graft material architecture on *in vitro* sound-induced velocity of isolated cadaveric human TMs, control graft materials, and biomimetic P-PEUU 50C/50R TM grafts. Mean velocity normalized by stimulus sound pressure of biomimetic TM grafts and controls across human frequency range (n = 3 for unloaded human cadaveric TMs, n = 6 for all other groups). Shaded regions indicate ± SD. [Note: Noise-artifact level indicates background movement of the holder in yellow. Velocities at least a factor of 3 above the noise-artifact level are considered significant.]

DOEH data provides high spatial resolution image across the entire surface of the membrane, but it is limited in its frequency resolution. For DOEH, we test at 7 different frequencies within the range of human hearing. Displacements of representative grafts are shown for comparison between materials and holder sized (**Figure 5.8**). Motion is highest at low frequencies for human cadaveric TMs, although all grafts show movement in simple modal motion patterns. At frequencies above 400 Hz, the motion of the biomimetic P-PEUU 50C/50R graft becomes distinguished from that of control grafts, continuing strong modal motion at displacements of beyond 64 nm/Pa. At 6000 Hz and above, both the unloaded cadaveric human TM and the P-PEUU 50C/50R graft begin to exhibit complex motion patterns. These complex motion patterns have multiple areas of reduced displacement, with local displacement maxima and minima arranged like 'concentric rings'. For both the unloaded human cadaveric TM and the P-PEUU 50C/50R graft, there are 2 'rings' at 10,000 Hz and 3 rings at 15,000 Hz and 20,000 Hz.
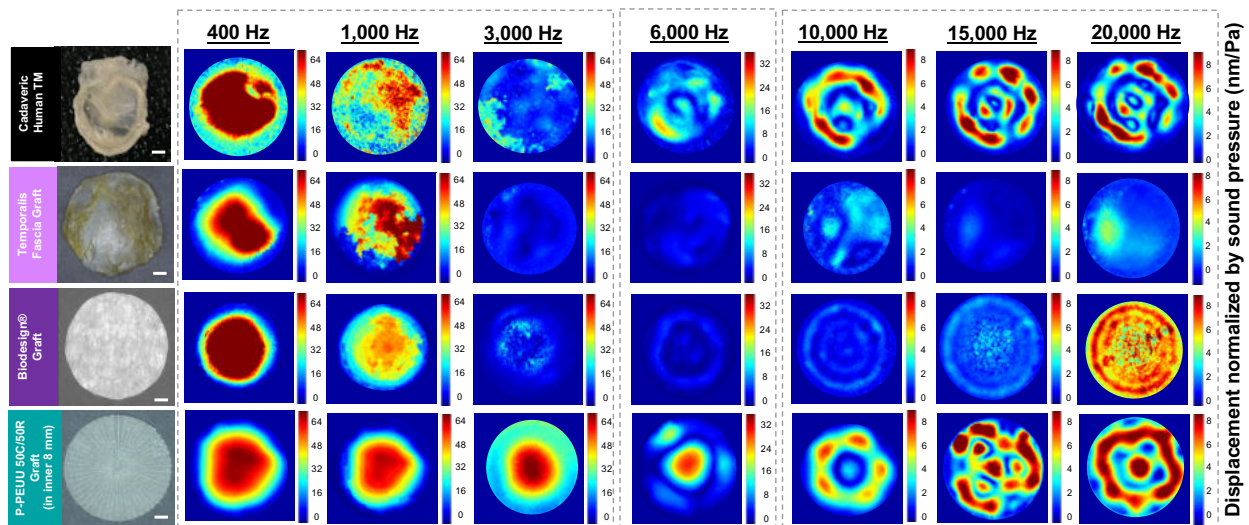
Figure 5.8. Impact of graft material architecture on *in vitro* sound-induced motion patterns of isolated cadaveric human TMs, control graft materials, and biomimetic P-PEUU 50C/50R TM grafts. Representative DOEH fringe patterns of representative human cadaveric TM tissue, control TM grafts, and biomimetic P-PEUU 50C/50R TM grafts. Displacement is normalized by sound pressure, and color bars were standardized across groups for each frequency range. Displacement is recorded in nm/Pa. Scale bars: 2 mm.

While this data suggests the importance of biomimetic architecture and anisotropic stiffness to sound conduction in the human TM, differences in material stiffness (described in **Chapter 4**) and thickness must be considered. Thus, melted, isotropic versions of both one-layer P-PEUU 50C grafts and two-layer P-PEUU 50C/50R grafts are compared. As anticipated, P-PEUU 50C/50R grafts, when melted and their

anisotropic structure is removed, exhibited lowered sound-induced motion as determined by LDV, around 1000-fold (**Figure 5.9**). Even though their thicknesses and composition are the same, the lack of biomimetic circular and radial architecture in these grafts highly affects their sound conduction. For comparison, single-layer circular-only P-PEUU 50C grafts and melted (isotropic) grafts are also measured. The only major difference between these grafts are observed at low frequencies <2000 Hz, where the latter grafts exhibit higher sound-induced motion. The melted (isotropic) P-PEUU 50C also exhibit higher sound-induced motion across most frequencies than the melted 50C/50R grafts (dashed lines). These differences become less significant at higher frequencies (>4000 Hz). Note, the melted P-PEUU 50C grafts have a lower thickness and mass compared to the melted 50C/50R P-PEUU grafts. Thus, for isotropic TM grafts, a higher sound-induced velocity is observed for thinner grafts than for thicker grafts, particularly for low frequency sound conduction.
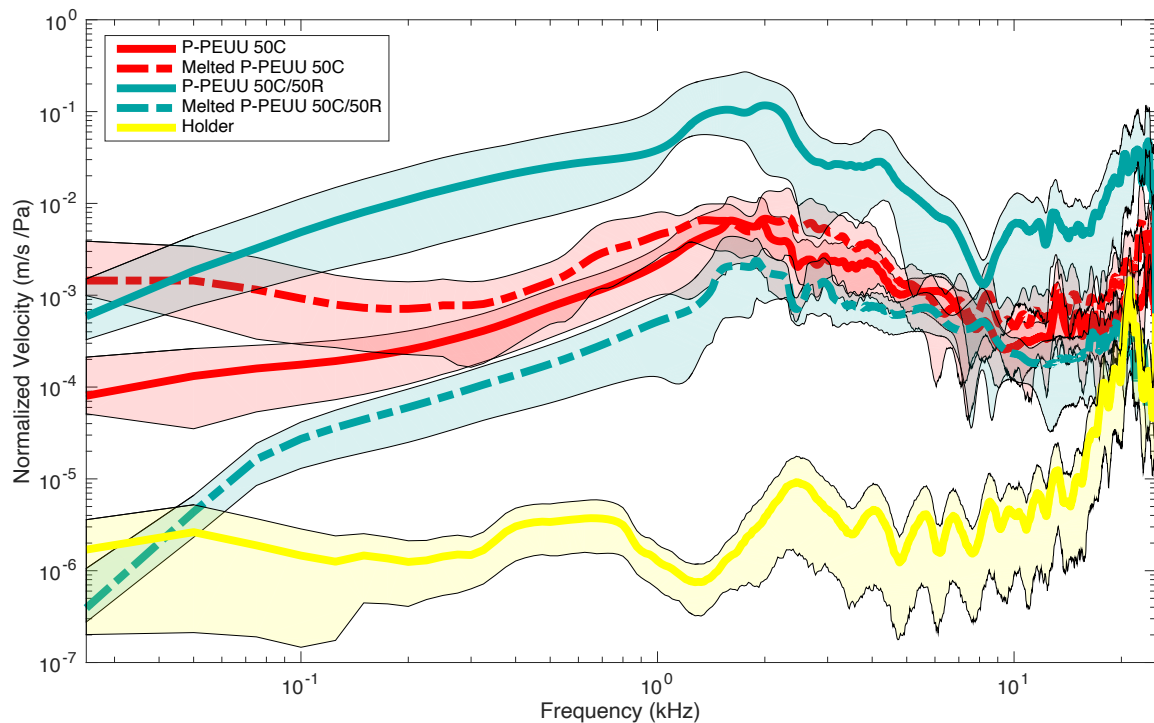
Figure 5.9. Impact of architecture on *in vitro* sound-induced velocity of P-PEUU grafts by comparing biomimetic (anisotropic) with melted (isotropic) grafts of the same thickness. Velocity normalized by stimulus sound pressure of biomimetic 3D printed (solid lines) and melted (dashed lines) P-PEUU TM grafts for both single-layer 50C and dual-layer 50C/50R grafts across human frequency range (n = 6). Shaded regions indicate ± SD. [Note: Noise-artifact level indicates background movement of the holder in yellow. Velocities at least a factor of 3 above the noise-artifact level are considered significant.]

The impact of "erasing" anisotropic architecture on sound-induced motion is captured via DOEH fringe patterns (**Figure 5.10**). Both P-PEUU 50C and 50C/50R grafts exhibit simple modal motion patterns at low frequencies, which increase in complexity with increasing frequency. The biomimetic P-PEUU 50C/50R grafts have a higher displacement magnitude than P-PEUU 50C grafts. When both grafts are melted, their motion patterns become more random and less organized, which could affect driving of the umbo, particularly at high frequencies.
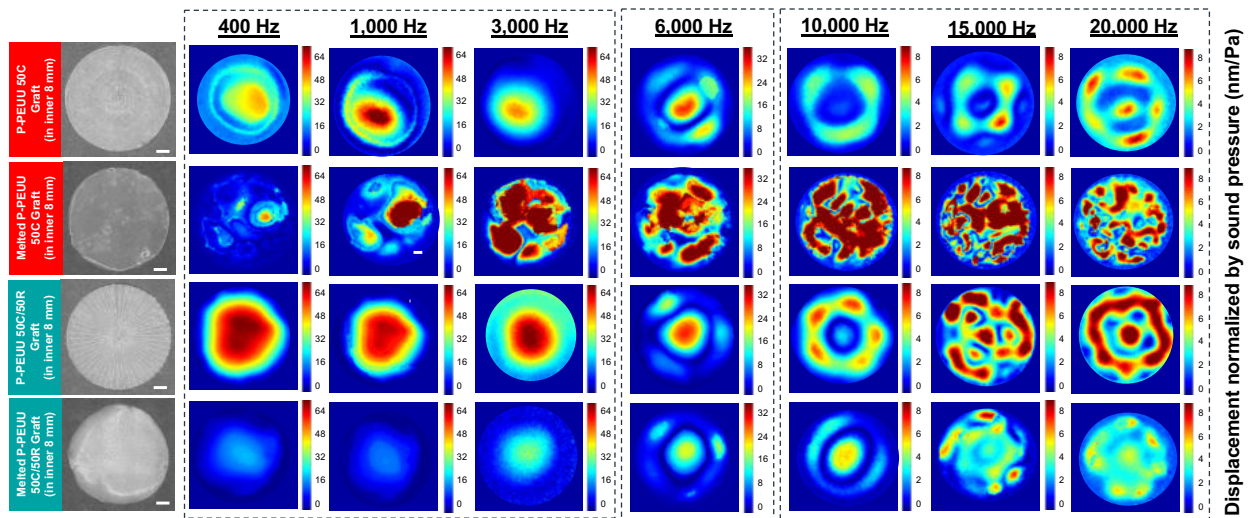
Figure 5.10. Impact of architecture on *in vitro* sound-induced motion patterns of P-PEUU grafts by comparing biomimetic (anisotropic) with melted (isotropic) grafts of the same thickness. Representative DOEH fringe patterns of representative single-layer 50C and dual-layer 50C/50R grafts. Displacement is normalized by sound pressure, and color bars were standardized across groups for each frequency range. Displacement is recorded in nm/Pa. Scale bars: 2 mm.

The phase angle between the displacement and stimulus sound pressure, an indication of the relative timing and directionality of membrane motion, is also measured by DOEH for biomimetic P-PEUU grafts, melted P-PEUU grafts, the human cadaveric TM tissue, and control grafts (**Figure 5.11**). Similar to displacement magnitude, the phase varied by frequency and material. At 400, 1000, and 3000 Hz, all grafts moved with adjacent areas of opposite phase (light blue with phase ~0 radians and dark blue and dark red with phases of ~ ±π radians). At higher frequencies, the spatial arrangement of the phase variations match the complexity of the measured DOEH magnitudes. All P-PEUU grafts and the cadaveric human TM and show more regular and cyclical variations in phase; whereas the fascia and Biodesign® grafts show fewer variations in phase across the graft surface.
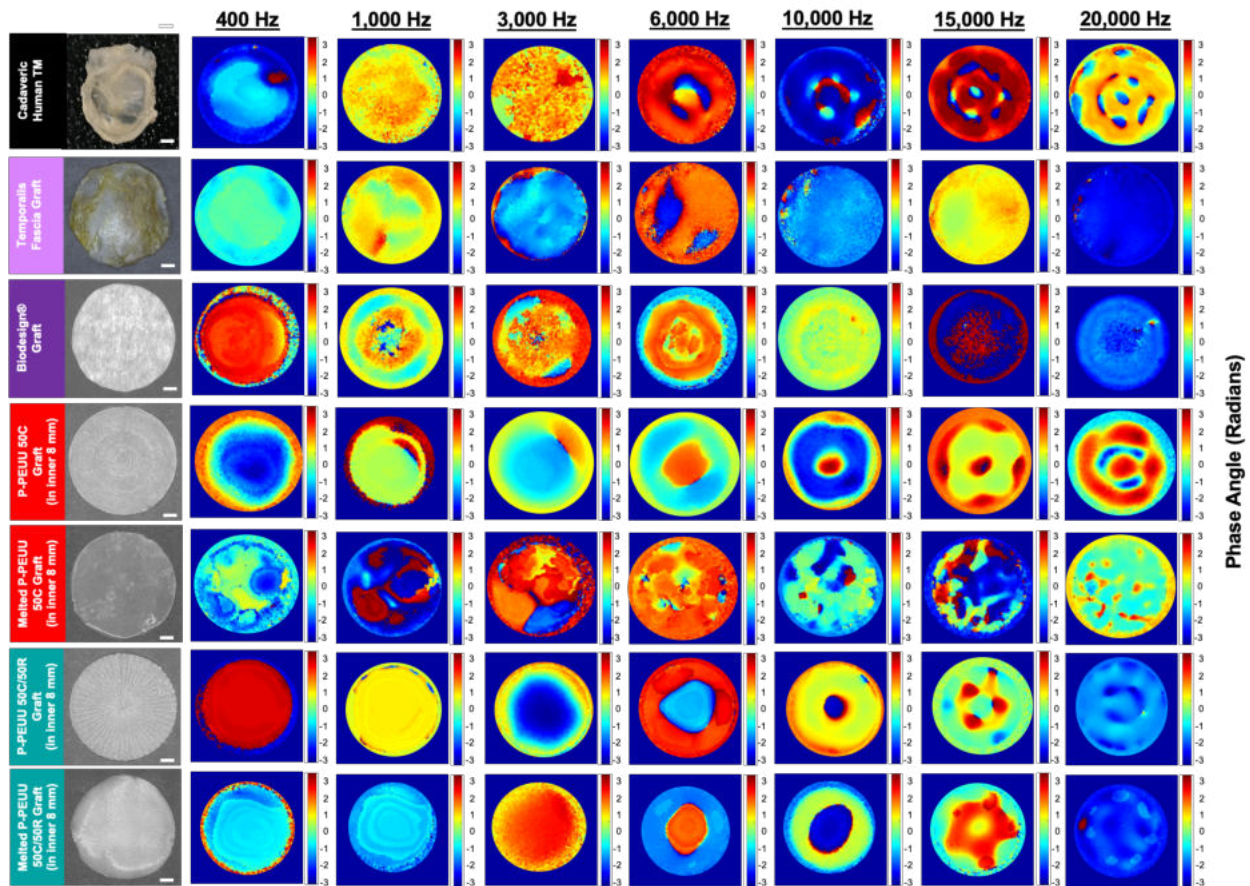
Figure 5.11. Phase angle of cadaveric human TMs, control graft materials commonly used in tympanoplasty, biomimetic (anisotropic) P-PEUU TM grafts, melted (isotropic) P-PEUU TM grafts. Representative DOEH images demonstrating the phase angle of the displacement relative to sound pressure in radians. [Note: Red represents a phase angle of ~ π radians, dark blue represents a phase angle of ~ -π radians, and light blue represents a phase angle of ~0 radians.]

Given the promising *in vitro* acoustic results for biomimetic P-PEUU 50C/50R grafts, we focused next on their healing and hearing outcomes in *in vivo* studies using chinchilla models for chronic TM perforations. Chinchillas with chronically perforated TMs successfully underwent transbullar underlay tympanoplasty procedures with biomimetic P-PEUU 50C/50R grafts and two controls: autologous temporalis fascia grafts and Biodesign® grafts. Notably, both the P-PEUU 50C/50R and Biodesign® grafts exhibit good mechanical properties and handling compared to temporalis fascia grafts, which must be completely desiccated to appropriately position the graft adjacent to the remnant TM (**Figure 5.12a-c**). Next, we explored the integration of the biomimetic P-PEUU 50C/50R, autologous temporalis fascia and Biodesign® grafts using serial oto-endoscopy. Representative otoscopic images of healed grafts (after 3 months) show their final TM structure (**Figure 5.12d-f**). While fascia and Biodesign® grafts are well

integrated, the original grafts are still readily identified without any indication of degradation or remodeling. By contrast, native tissue ingrowth is observed within the circular and radial architecture of the biomimetic P-PEUU 50C/50R grafts. This promising result indicates that native cells can remodel the biodegradable material into native tissue. Moreover, ingrowth of native vasculature via angiogenesis is observed, consistent with the vascular ingrowth seen in biodegradable polyurethanes by Apslund *et al.* [313]. The overall healing rate differs between graft types, with the biomimetic P-PEUU 50C/50R grafts (n = 20) exhibiting the highest rate of successful tympanoplasty, at 75% of implanted grafts (**Figure 5.12i**). By comparison, commonly used fascia (n = 8) and Biodesign® (n = 12) grafts for tympanoplasty had lower rates of perforation closure, at only 62.5% and 66.6%, respectively. Graft failures arose due to graft retraction, re-perforation, and infection of the chinchilla TM post-surgery.

Stained histological sections of representative biomimetic P-PEUU 50C/50R, fascia, and Biodesign® grafts are shown in **Figure 5.13**. While all sections show perforation closure and restoration of the boundary between the external auditory canal (EAC) and the middle ear space, the cross-sections of the remodeled TMs significantly differ. As native cells grow into the grafts to close the TM perforation, lack of graft material degradation leads to an increased thickness and thus lower sound-induced motion, particularly at low frequencies. Although it is difficult to make quantitative thickness measurements due to potential shearing of the grafts during histological slicing and absorbance of fixation solutions, their overall structure can be compared. While fascia grafts maintain a thin structure with a keratinocyzed epidermal layer adjacent to the EAC, there are no signs of remodeling into the lamina propria, with grafts retaining their original linear structure. Similarly, Biodesign® grafts show a keratinocyzed epidermal layer adjacent to the EAC; however, the thickness of these grafts is substantially greater than that of the native TM, at around 200 – 300 µm. In contrast, P-PEUU 50C/50R grafts show native cellular ingrowth on both the medial and lateral sides of the graft, with arranged collagen fibers being deposited. The partially degraded P-PEUU material has a measured thickness of 32 µm ± 11 µm (taken across 6 sections). Given their original thickness of 107 ± 4 µm, this represents a 70% reduction after 3 months of implantation. We expect this thickness to reduce further over time as the P-PEUU material fully degrades.
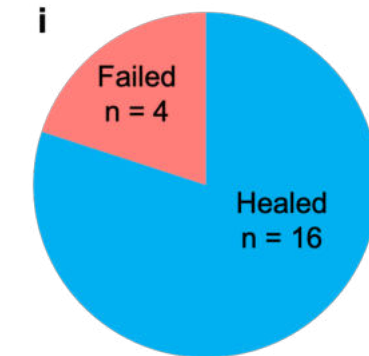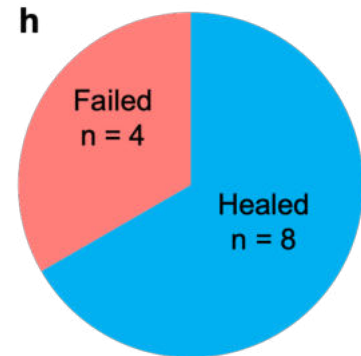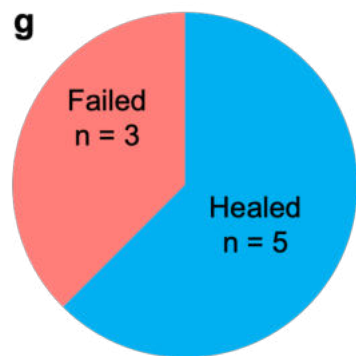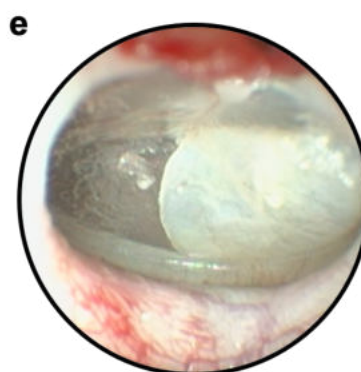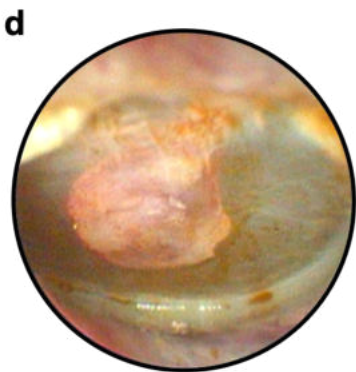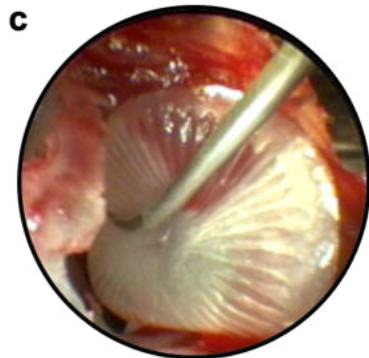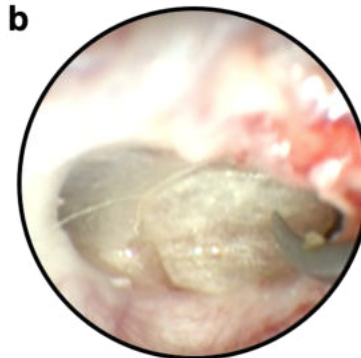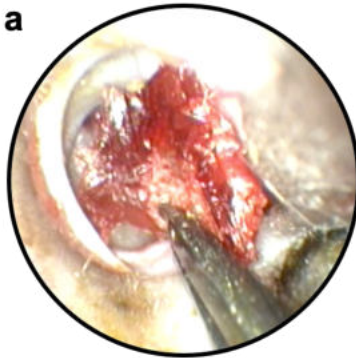
Figure 5.12. Repair and healing outcomes following underlay tympanoplasty of chronic subtotal perforations in chinchilla models. Endoscopic images of underlay tympanoplasty with (a) temporalis fascia graft, (b) Biodesign® graft, and (c) 3D-printed P-PEUU 50C/50R graft. Healed TMs 3 months post-implantation are endoscopically viewed for (d) temporalis fascia graft, (e) Biodesign® graft, and (f) 3D-printed P-PEUU 50C/50R graft. The number of failed grafts and healed grafts for (g) temporalis fascia grafts, (h) Biodesign® grafts, and (i) 3D-printed P-PEUU 50C/50R grafts.
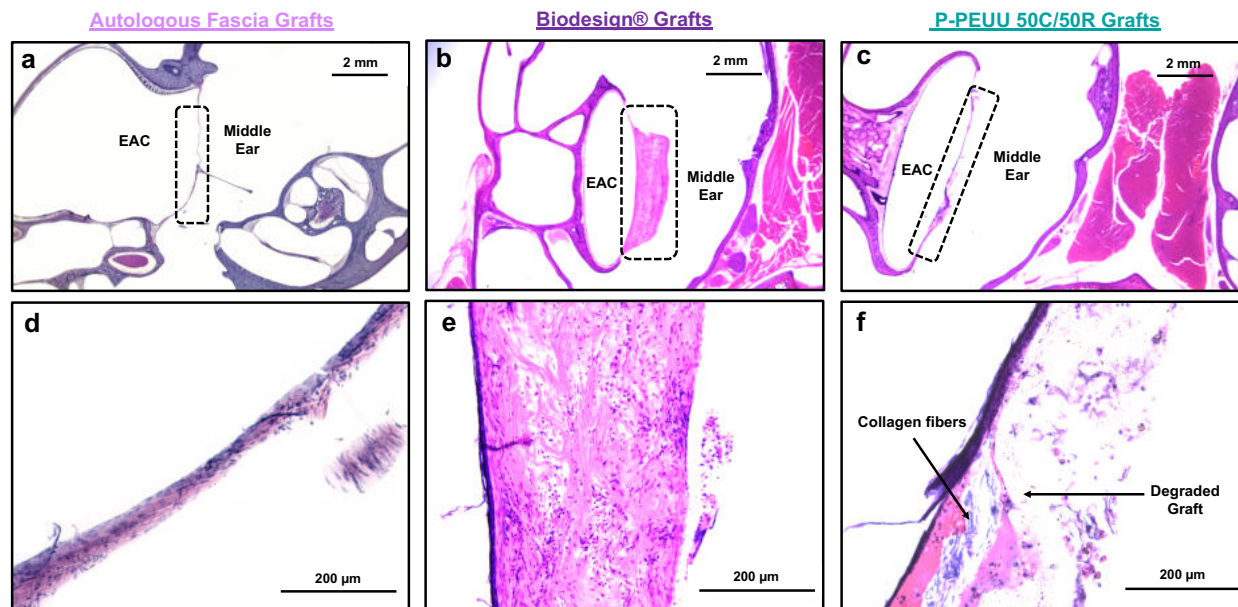
Figure 5.13. Histological sections of celloidin-fixed temporal bones showing the cross-section of the TM following underlay tympanoplasty of chronic subtotal perforations in chinchilla models with various graft materials. Hematoxylin and eosin (H&E) staining with light microscopy. Top row shows 1.25x magnification of TMs containing (a) healed fascia grafts, (b) healed Biodesign® grafts, (c) P-PEUU 50C/50R grafts. The location of the remodeled TM is indicated by black dashed boxes. Bottom row shows 20x magnification of TMs containing (d) healed fascia grafts, (e) healed Biodesign® grafts, (f) P-PEUU 50C/50R grafts. [Note: The left side of each image is the lateral side adjacent to the external auditory canal (EAC), while the right side of images is the medial side adjacent to the middle ear space.]

To complement the healing outcomes of biomimetic P-PEUU 50C/50R, fascia, and Biodesign® grafts, we also evaluated the hearing outcomes of these TM graft materials using DPOAE and ABR. Threshold values at 3 months following tympanoplasty are subtracted from initial hearing values with an intact TM (**Figure 5.14**). Since higher threshold values indicate higher sound pressure levels required for electrophysiological feedback indicating hearing, values closer to 0 indicate restoration of hearing close to baseline levels with an intact TM, whereas more negative values represent greater hearing loss following tympanoplasty. There is a large variation between animals due to anatomical differences and complexity of the surgical procedure. Thus, statistical comparisons are performed.

In chinchillas whose TMs are repaired with P-PEUU 50C/50R grafts, DPOAE hearing thresholds are restored closer to normal in a statistically significant ($p < 0.05$) amount compared to both fascia and Biodesign® grafts at all frequencies tested besides 16,000 Hz, whereby hearing threshold restoration is significantly better than fascia grafts but not significantly better than Biodesign® grafts, despite being better on average. Analysis of ABR results showed similar improvement in hearing restoration for biomimetic P-

PEUU 50C/50R grafts. In chinchillas whose TMs are repaired with those grafts, hearing is restored at a statistically significant and improved level (p < 0.05) compared with fascia grafts at lower frequencies of 1000 and 2000 Hz. Additionally, there is statistically significantly (p < 0.05) restored hearing in chinchillas whose TMs are repaired with P-PEUU 50C/50R grafts compared with outcomes for both fascia grafts and Biodesign® grafts at higher frequencies of 8,000 and 16,000 Hz. Interestingly, the average ABR thresholds at 3 months following tympanoplasty procedures for 16,000 Hz are better than those with the chinchilla's normal, intact TM prior to perforation, indicating an overall improvement (beyond baseline) of hearing function at high frequencies.

Control grafts exhibited no statistically significant difference (p < 0.05) between hearing outcomes for fascia and Biodesign® grafts in either ABR or DPOAE analysis, although as a general trend, average ABR hearing thresholds are restored closer to normal at lower frequencies (400, 1000, and 2000 Hz) for chinchillas undergoing tympanoplasty with Biodesign® grafts. In contrast, average ABR and DPOAE hearing thresholds are restored closer to normal at higher frequencies (4000, 8000, and 16,000 Hz) for chinchillas undergoing tympanoplasty with fascia grafts as compared to those with Biodesign® grafts. This may be due to the thinner remodeled TM with an overall lower mass, as seen in **Figure 5.13**.
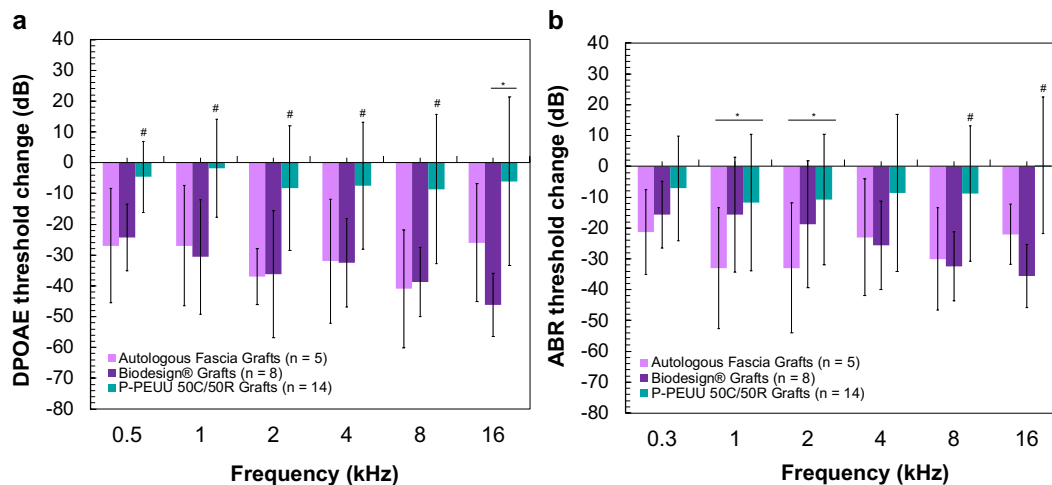
Figure 5.14. Hearing threshold changes (initial hearing thresholds minus 3 month post-tympanoplasty hearing thresholds) following underlay tympanoplasty of chronic subtotal perforations in chinchilla models with various graft materials. (a) Hearing thresholds detected by distortion product otoacoustic emissions (DPOAE) (b) Hearing thresholds detected by auditory brainstem response (ABR). Values shown are mean with error bars representing ± SD. (* p < 0.05 from one material group, # p < 0.05 from both material groups) [Note: Higher values closer to 0 indicate hearing restoration closer to normal and therefore improved tympanoplasty hearing outcomes.]

Additionally, histological sectioning of the cochlea 3 months following tympanoplasty with all three graft types show an intact organ of Corti and a healthy, normal population of SGN (**Figure 5.15**). Therefore, there is no reason to currently believe that the small molecule degradation products from either the control materials or P-PEUU are ototoxic. Indeed, the DPOAE and ABR results are similar to each other across the frequencies tested for P-PEUU grafts, suggesting a lack of ototoxicity. Due to the lack of ototoxicity observed in the cochlea following implantation with P-PEUU grafts and control materials, it is likely that the hearing thresholds changes seen by 3 months result from conductive hearing changes, not sensorineural hearing loss. During the surgical procedure, the ossicular chain is found to be fractured in several cases, which would indicate a conductive hearing loss stemming from the ossicular chain rather than the TM.
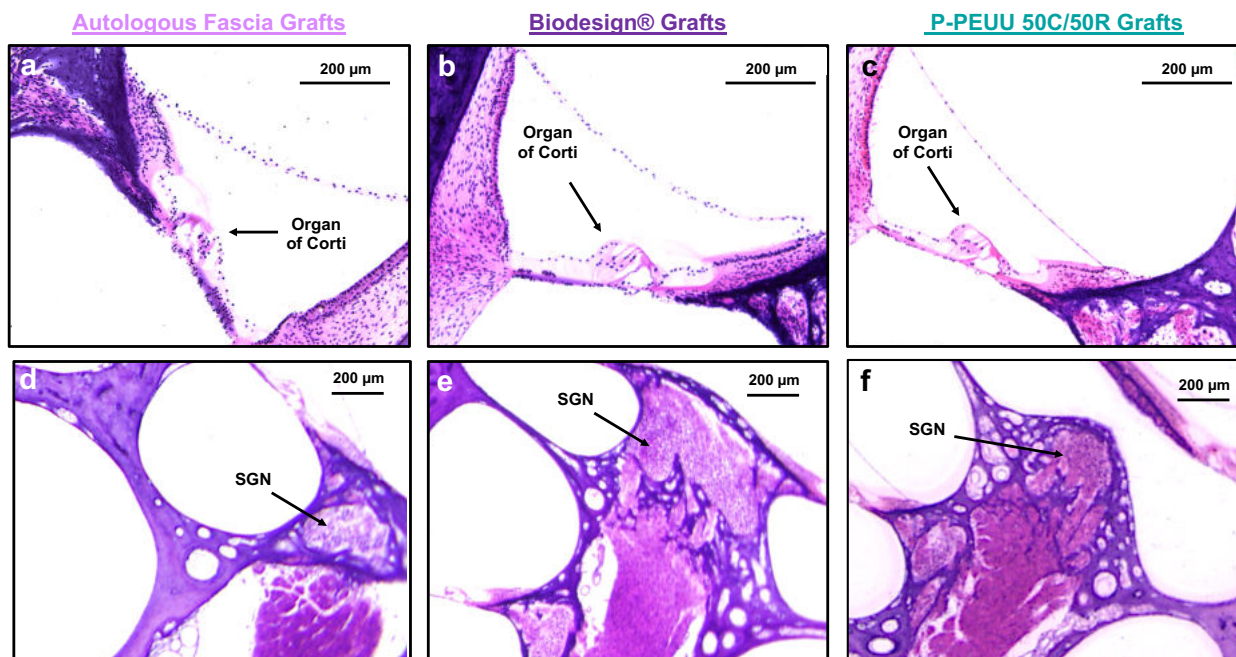
Figure 5.15. Histological sections of the cochlea to examine potential ototoxic effects following underlay tympanoplasty of chronic subtotal perforations in chinchilla models. Hematoxylin and eosin (H&E) staining with light microscopy of cochlear sections. The top row shows the organ of Corti visualized at 20x magnification following tympanoplasty with (a) healed fascia grafts, (b) healed Biodesign® grafts, (c) P-PEUU 50C/50R grafts. The bottom row shows the modiolus of the cochlea showing position of spiral ganglion neurons (SGN) following tympanoplasty with (d) healed fascia grafts, (e) healed Biodesign® grafts, (f) P-PEUU 50C/50R grafts. [Note: The locations of these features are designated by black arrows.]

5.4   Conclusions

We created biomimetic, biodegradable P-PEUU 50C/50R TM grafts that exhibit improved hearing and healing outcomes compared to both temporalis fascia and Biodesign® Otologic Repair Graft, These novel grafts, which recapitulate the circular and radial architecture of the native TM, were successfully used in tympanoplasty in chinchilla models for chronic TM perforations. Ideal tympanoplasty procedures resulted in a healed, closed TM perforation along with restoration of efficient sound conduction from the TM to the ossicles across the frequency range of human hearing. While further optimization of printed TM graft composition and architecture may be possible with computational modeling, our results are a promising indication of the value of biomimetic, biodegradable TM graft designs for tympanoplasty.

Chapter 6

Conclusions

My PhD dissertation focused on the design, fabrication, and *in vitro* and *in vivo* testing of novel biomimetic tympanic membrane (TM) grafts for use in tympanoplasty. To date, both autologous tissue and synthetic grafts have been used in tympanoplasty, but they do not remodel or recapitulate the circumferential and radial collagen fiber architecture present in the lamina propria of the native TM. As a consequence of imperfect graft materials, patient hearing and healing outcomes are variable and revision surgeries are often required. My research has addressed this important clinical need by (1) printing and characterizing biomimetic TM grafts with circumferential and radial features from commercially available polymers that mimic the sound-induced motion patterns and velocity of the native TM, (2) synthesizing, printing, and characterizing a biocompatible and resorbable poly(ester urethane urea) (PEUU), which was blended with a fugitive poly(ethylene glycol) (PEG) to simultaneously optimize their mechanical, biodegradation, and acousto-mechanical properties. We showed that these biomimetic TM grafts exhibited improved sound conduction as well as encouraged cell ingrowth onto the complex, biomimetic architecture. Finally, using a chinchilla animal model, we demonstrated that these grafts remodel into an anisotropic architecture *in vivo*, resulting in improved hearing outcomes as compared to control graft materials. The principal findings of my dissertation are summarized below:

1) Design, 3D printing, and properties of biomimetic TM grafts (commercial biomaterials)

Biomimetic TM grafts with circumferential and radial features were produced by printing PCL, PLA, and PDMS inks that mimic the architecture of the native TM. Grafts are infilled with a hydrogel blend of collagen and fibrinogen to create a confluent graft structure. A custom setup was designed for *in vitro* acoustic testing of both biomimetic and control TM grafts using laser Doppler vibrometry (LDV) and digital opto-electronic holography (DOEH). The sound-induced velocity is highly consistent between printed biomimetic grafts produced with the same material and architecture; however, altering these parameters led to significant differences in their performance. By comparison, temporalis fascia, the most widely used autologous TM graft, exhibits inconsistent sound-induced velocity— even between grafts harvested by the same surgeon.

2) Synthesis and printing of thermoplastic, biocompatible, and resorbable PEUU elastomers

A thermoplastic, biocompatible, and resorbable PEUU elastomer was synthesized, which can be printed via 3D printing (i.e., high operating temperature-direct ink writing, HOT-DIW) 3D. A decrease in the hard segment and chain extender content allowed for the creation of a PEUU material that melts at modest temperatures. The resultant filament width in the absence and presence of a fugitive porogen (PEG) to create porous PEUU (P-PEUU) inks were determined as a function of print speed to enable standardization in graft manufacturing.

3) Enhancement of biomimetic TM graft degradation via porogen incorporation

Biomimetic TM grafts in a 50C/50R architecture were created from PEUU and P-PEUU elastomers. In the latter case, the porosity arises from PEG leaching after printing. The grafts' degradation rates in saline solutions of varying lipase concentration were quantified. Porous TM grafts exhibited faster degradation rates by day 30 in PBS compared their solid counterparts (11.1% mass loss for PEUU grafts vs. 35.1% mass loss for P-PEUU grafts, 5.0% mass loss for PCL grafts vs. 23.1% mass loss for P-PCL grafts), likely due to increased surface area exposure for hydrolysis and enzymatic degradation processes.

4) Biomimetic TM grafts exhibit anisotropic mechanical properties

Biomimetic TM grafts printed from both PEUU and P-PEUU inks exhibited statistically significant higher stiffness parallel to the printing direction ($E_{\parallel}$) compared to the orthogonal direction ($E_{\perp}$). Importantly, both PEUU and P-PEUU grafts possess stiffness values (in both directions) that lie within the 10 – 100 MPa range of human TM tissue (PEUU: $E_{\parallel}$ = 72.6 ± 4.9 MPa, $E_{\perp}$ = 40.2 ± 4.2 MPa, P-PEUU: $E_{\parallel}$ = 33.7 ± 2.8 , $E_{\perp}$ = 23.8 ± 1.5 MPa).

5) Cellular alignment on biomimetic TM grafts

The fibroblast alignment and collagen I deposition on the top (patterned) and bottom (smooth) surfaces of biomimetic TM grafts were explored. P-PEUU grafts exhibits greater alignment compared to PEUU and control grafts (PCL and P-PCL). Alignment of fibroblasts and collagen I on P-PEUU grafts increased with increasing print speed. Upon melting the P-PEUU grafts to "erase" their stiffness anisotropy, no cellular alignment occurred along the original print path.

6) Acoustic properties of biomimetic TM grafts

The sound-induced motion of biomimetic TM grafts and two control grafts– human cadaveric temporalis fascia and Biodesign® Otologic Repair Graft – were measured on a custom optical-acoustic setup using LDV and DOEH. Biomimetic TM grafts (50C/50R, P-PEUU) exhibited superior sound-induced velocity compared to both control grafts and other biomimetic grafts (50C/0R, P-PEUU). Their velocity significantly decreased when melted into a mechanically isotropic graft of the same thickness. Biomimetic TM grafts (50C/50R, P-PEUU) show simple modal motion patterns at low frequencies and complex, organized motion patterns at high frequencies, similar to unloaded human cadaveric TMs.

7) I*n vivo* remodeling of biomimetic TM grafts

Biomimetic TM grafts (50C/50R, P-PEUU), autologous fascia grafts, and Biodesign® grafts were successfully implanted in chinchilla models with chronic TM perforations via an underlay tympanoplasty technique. Over a 4-week period, the perforation closure rate was highest for the P-PEUU 50C/50R grafts, in which ingrowth of native tissue, graft degradation, and vascular ingrowth into the graft material were observed both endoscopically and histologically. Importantly, the ingrowing native tissue appeared to be multi-laminar, mimicking the circumferential and radial fibrous collagen orientation in the native TM. By contrast, fascia and Biodesign® grafts appear endoscopically and histologically identical to their original pre-implanted structures and thicknesses.

8) Biomimetic TM grafts enable hearing restoration *in vivo* in animal models

Through distortion product otoacoustic emissions (DPOAE) and auditory brainstem response (ABR) testing, hearing thresholds were determined for normal, pre-implanted chinchilla ears as well as those healed after 3 months using biomimetic and control TM grafts. We found statistically significant hearing improvements for chinchillas implanted with biomimetic TM grafts (50C/50R, P-PEUU) compared to those implanted with either autologous fascia grafts or Biodesign® grafts. Overall, animals implanted with biomimetic TM grafts (50C/50R, P-PEUU) had threshold values restored closer to those with a normal, unperforated TM at all frequencies tested.

In summary, based on the above findings, we anticipate that these biomimetic TM grafts (porous PEUU) may have translational impact on the clinical otolaryngology community.

References

[1] Gennisson, J. L., Deffieux, T., Macé, E., Montaldo, G., Fink, M., & Tanter, M. (2010). Viscoelastic and anisotropic mechanical properties of in vivo muscle tissue assessed by supersonic shear imaging. *Ultrasound in medicine and biology*, *36*(5), 789-801.

[2] Mescher, A. L. (2013). *Junqueira's basic histology: text and atlas*. Mcgraw-hill. Chapter 10.

[3] Wright, G. J., Coombs, M. C., Hepfer, R. G., Damon, B. J., Bacro, T. H., Lecholop, M. K., ... & Yao, H. (2016). Tensile biomechanical properties of human temporomandibular joint disc: Effects of direction, region and sex. *Journal of biomechanics*, *49*(16), 3762-3769.

[4] Shimada, T., & Lim, D. J. (1971). The fiber arrangement of the human tympanic membrane: a scanning electron microscopic observation. *Annals of Otology, Rhinology & Laryngology*, *80*(2), 210-217.

[5] Fay, J. P., Puria, S., & Steele, C. R. (2006). The discordant eardrum. *Proceedings of the National Academy of Sciences*, *103*(52), 19743-19748.

[6] O'Connor, K. N., Tam, M., Blevins, N. H., & Puria, S. (2008). Tympanic membrane collagen fibers: a key to high-frequency sound conduction. *The Laryngoscope*, *118*(3), 483-490.

[7] O'Connor, K. N., Cai, H., & Puria, S. (2017). The effects of varying tympanic-membrane material properties on human middle-ear sound transmission in a three-dimensional finite-element model. *The Journal of the Acoustical Society of America*, *142*(5), 2836-2853.

[8] Dobie, R. A., Van Hemel, S., & National Research Council. (2004). Basics of Sound, the Ear, and Hearing. In *Hearing Loss: Determining Eligibility for Social Security Benefits*. National Academies Press (US).

[9] Blauert, J. (1997). *Spatial hearing: the psychophysics of human sound localization*. MIT press.

[10] Brant, L. J., & Fozard, J. L. (1990). Age changes in pure-tone hearing thresholds in a longitudinal study of normal human aging. *The Journal of the Acoustical Society of America*, *88*(2), 813-820.

[11] Lonsbury-Martin, B. L., Harris, F. P., Hawkins, M. D., Stagner, B. B., & Martin, G. K. (1990). Distortion product emissions in humans: I. Basic properties in normally hearing subjects. *Annals of Otology, Rhinology & Laryngology*, *99*(5_suppl), 3-14.

[12] Dempster, J. H., & Mackenzie, K. (1990). The resonance frequency of the external auditory canal in children. *Ear and hearing*, *11*(4), 296-298.

[13] Lim, D. J. (1970). Human tympanic membrane: an ultrastructural observation. *Acta oto-laryngologica*, *70*(3), 176-186.

[14] Heron, I. C. (1923). Measurements and observations upon the human auditory ossicles. *American Journal of Physical Anthropology*, *6*(1), 11-26.

[15] Van der Jeught, S., Dirckx, J. J., Aerts, J. R., Bradu, A., Podoleanu, A. G., & Buytaert, J. A. (2013). Full-field thickness distribution of human tympanic membrane obtained with optical coherence tomography. *Journal of the Association for Research in Otolaryngology*, *14*(4), 483-494.

[16] Trakimas, D. R., Ishai, R., Ghanad, I., Black, N. L., Kozin, E. D., Cheng, J. T., & Remenschneider, A. K. (2018). Otopathologic evaluation of temporalis fascia grafts following successful tympanoplasty in humans. *The Laryngoscope*, *128*(10), E351-E358.

[17] Tucker, A. S. (2017). Major evolutionary transitions and innovations: the tympanic middle ear. *Philosophical Transactions of the Royal Society B: Biological Sciences*, *372*(1713), 20150483.

[18] Lim, D. J. (1995). Structure and function of the tympanic membrane: a review. *Acta oto-rhino-laryngologica belgica*, *49*(2), 101-115.

[19] Alberti, P. W. R. M. (1964). Epithelial migration on the tympanic membrane. *The Journal of Laryngology & Otology*, *78*(9), 808-830.

[20] O'Donoghue, G. M. (1984). Epithelial migration on the tympanic membrane of children. *International journal of pediatric otorhinolaryngology*, *6*, 119-125.

[21] Yi, Z. X., Shi, G. S., & Huang, C. C. (1988). Age-related epithelial migration on the tympanic membrane of the Mongolian gerbil. *Otolaryngology—Head and Neck Surgery*, *98*(6), 564-567.

[22] Knutsson, J., Von Unge, M., & Rask-Andersen, H. (2011). Localization of progenitor/stem cells in the human tympanic membrane. *Audiology and Neurotology*, *16*(4), 263-269.

[23] Wang, W. Q., Wang, Z. M., & Tian, J. (2004). Epidermal stem cells in the tympanic membrane. *Zhonghua er bi yan hou ke za zhi*, *39*(12), 712-716.

[24] Frumm, S. M., Yu, K. S., Chang, J., Briscoe, J. A., Lee, K. P., Byrnes, L. E., ... & Tward, A. D. (2019). A hierarchy of migratory keratinocytes maintains the tympanic membrane. *bioRxiv*, 687947.

[25] Mozaffari, M., Jiang, D., & Tucker, A. S. (2019). Developmental aspects of the tympanic membrane: Shedding light on function and disease. *genesis*, e23348.

[26] Stenfeldt, K., Johansson, C., & Hellström, S. (2006). The collagen structure of the tympanic membrane: collagen types I, II, and III in the healthy tympanic membrane, during healing of a perforation, and during infection. *Archives of Otolaryngology–Head & Neck Surgery*, *132*(3), 293-298.

[27] Hentzer, E. (1969). Ultrastructure of the human tympanic membrane. *Acta oto-laryngologica*, *68*(1-6), 376-390.

[28] Hellström, S., Spratley, J., Eriksson, P. O., & Pais-Clemente, M. (2003). Tympanic membrane vessel revisited: a study in an animal model. *Otology & neurotology*, *24*(3), 494-499.

[29] Widemar, L., Hellström, S., Schultzberg, M., & Stenfors, L. E. (1985). Autonomic Innervation of the Tympanic Membrane An Immunocytochemical and Histofluorescence Study. *Acta oto-laryngologica*, *100*(1-2), 58-65.

[30] Earwood, J. S., Rogers, T., & Rathjen, N. A. (2018). Ear pain: diagnosing common and uncommon causes. *American family physician*, *97*(1), 20-27.

[31] Eriksson, P. O., & Hellström, S. (2001). Degranulation of mast cells provokes a massive inflammatory reaction in the tympanic membrane. *The Laryngoscope*, *111*(7), 1264-1270.

[32] Pauna, H. F., Monsanto, R. C., Schachern, P., Paparella, M. M., Chole, R. A., & Cureoglu, S. (2018). Evidence against the mucosal traction theory in cholesteatoma. *The Laryngoscope*, *128*(7), 1663-1667.

[33] Sadé, J., & Weissman, Z. (1977). Middle ear mucosa and secretory otitis media. *Archives of oto-rhino-laryngology*, *215*(3-4), 195-205.

[34] Daphalapurkar NP, Dai C, Gan RZ, Lu H. Characterization of the linearly viscoelastic behavior of human tympanic membrane. Journal of the Mechanical Behavior of Biomedical Materials. 2009 Jan 1;2(1):82-92.

[35] De Greef, D., Aernouts, J., Aerts, J., Cheng, J. T., Horwitz, R., Rosowski, J. J., & Dirckx, J. J. (2014). Viscoelastic properties of the human tympanic membrane studied with stroboscopic holography and finite element modeling. *Hearing research*, *312*, 69-80.

[36] Decraemer, W. F., Maes, M. A., & Vanhuyse, V. J. (1980). An elastic stress-strain relation for soft biological tissues based on a structural model. Journal of biomechanics, 13(6), 463-468.

[37] Aernouts J, Aerts JR, Dirckx JJ. Mechanical properties of human tympanic membrane in the quasi-static regime from in situ point indentation measurements. Hearing Research. 2012 Aug 1;290(1-2):45-54.

[38] Fay, J., Puria, S., Decraemer, W. F., & Steele, C. (2005). Three approaches for estimating the elastic modulus of the tympanic membrane. *Journal of biomechanics*, *38*(9), 1807-1815.

[39] Azhari, H. (2010). *Basics of biomedical ultrasound for engineers*. John Wiley & Sons.

[40] Mason, M. J. (2016). Structure and function of the mammalian middle ear. II: Inferring function from structure. Journal of anatomy, 228(2), 300-312.

[41] Withnell, R. H., & Gowdy, L. E. (2013). An analysis of the acoustic input impedance of the ear. *Journal of the Association for Research in Otolaryngology*, *14*(5), 611-622.

[42] Benade, A. H. (1968). On the propagation of sound waves in a cylindrical conduit. *The Journal of the Acoustical Society of America*, *44*(2), 616-623.

[43] Kringlebotn, M. (1988). Network model for the human middle ear. *Scandinavian audiology*, *17*(2), 75-85.

[44] Patel, A., & Groppo, E. (2010). Management of temporal bone trauma. *Craniomaxillofacial trauma & reconstruction*, *3*(02), 105-113.

[45] Magnuson, B. (2003). Functions of the mastoid cell system: auto-regulation of temperature and gas pressure. *The Journal of Laryngology & Otology*, *117*(2), 99-103.

[46] Merchant, S. N. (2010). *Schuknecht's Pathology of the Ear*. PMPH-USA.

[47] Kutz Jr, J. W., Mullin, G., & Campbell, K. C. M. (2012). Audiology pure-tone testing. *Medscape Reference.*

[48] Leonardelli, G. B. (1948). Contributo alla conoscenza dei sistemi di fibre a parabola della lamina propria della membrana del timpano umana. *Arch. ital. di otol*, *1*, 3-16.

[49] Fumagalli, Z. (1942). Contributio alla conscenza della structura della lamina propia della membrana del timpano umana. *Arch Ital Otol*, *54*, 211-219.

[50] Filogamo, G. (1949). Recherches sur la structure de la membrane du tympan chez les differents vertebres. *Cells Tissues Organs*, *7*(3), 248-272.

[51] Secondi, U. (1951). Structure and function of the lamina propria of the tympanic membrane in various mammals. *AMA archives of otolaryngology*, *53*(2), 170-181.

[52] Zhang, X., Guan, X., Nakmali, D., Palan, V., Pineda, M., & Gan, R. Z. (2014). Experimental and modeling study of human tympanic membrane motion in the presence of middle ear liquid. Journal of the Association for Research in Otolaryngology, 15(6), 867-881.

[53] Cheng, J. T., Hamade, M., Merchant, S. N., Rosowski, J. J., Harrington, E., & Furlong, C. (2013). Wave motion on the surface of the human tympanic membrane: holographic measurement and modeling analysis. *The Journal of the Acoustical Society of America*, *133*(2), 918-937.

[54] Saliba, I., & Froehlich, P. (2011). Hyaluronic acid fat graft myringoplasty: an office-based technique adapted to children. *Archives of Otolaryngology–Head & Neck Surgery*, *137*(12), 1203-1209.

[55] Powers R. Hearing - Military Medical Standards for Enlistment / Appointment. 2018 June 3. <https://www.thebalancecareers.com/military-medical-standards-for-enlistment-and-appointment-335399>.

[56] Enlisting Requirements – Ears. http://www.militaryspot.com/enlist/enlisting-requirements-ears

[57] Lim DJ, Bluestone CD, Casselbrant ML. Recent Advances in Otitis Media: Report of the Seventh Research Conference. Annals Publishing; 2002.

[58] Acuin J (2004) Chronic suppurative otitis media - Burden of Illness and Management Options. Geneva: World Health Organization.

[59] Rosenfeld, R. M., Schwartz, S. R., Pynnonen, M. A., Tunkel, D. E., Hussey, H. M., Fichera, J. S., ... & Haynes, D. S. (2013). Clinical practice guideline: tympanostomy tubes in children. *Otolaryngology—Head and Neck Surgery*, *149*(1_suppl), S1-S35.

[60] Wang, J. C., Hamood, A. N., Saadeh, C., Cunningham, M. J., Yim, M. T., & Cordero, J. (2014). Strategies to prevent biofilm-based tympanostomy tube infections. *International journal of pediatric otorhinolaryngology*, *78*(9), 1433-1438.

[61] Herzon, F. S. (1980). Tympanostomy tubes: infectious complications. *Archives of Otolaryngology*, *106*(10), 645-647.

[62] Golz, A., Netzer, A., Joachims, H. Z., Westerman, S. T., & Gilbert, L. M. (1999). Ventilation tubes and persisting tympanic membrane perforations. *Otolaryngology–Head and Neck Surgery*, *120*(4), 524-527.

[63] Holt, J. J. (2003). Cholesteatoma and otosclerosis: two slowly progressive causes of hearing loss treatable through corrective surgery. *Clinical medicine & research*, *1*(2), 151-154.

[64] Bhutta, M. F., Williamson, I. G., & Sudhoff, H. H. (2011). Cholesteatoma. *Bmj*, *342*.

[65] Cullis, I. G. (2001). Blast waves and how they interact with structures. *BMJ Military Health*, *147*(1), 16-26.

[66] Esquivel, C. R., Parker, M., Curtis, K., Merkley, A., Littlefield, P., Conley, G., ... & Stockinger, Z. (2018). Aural blast injury/acoustic trauma and hearing loss. *Military medicine*, *183*(suppl_2), 78-82.

[67] A.L. Dougherty, A.J. MacGregor, P.P. Han, E. Viirre, et al. J. Rehabil. Res. Dev. 50 (2013) 893–904.

[68] A.E. Ritenour, A. Wickley, J.S. Ritenour, et al. J. Trauma Inj. Infect. Crit. Care 64 (2008) S174–S178.

[69] Remenschneider, A. K., Lookabaugh, S., Aliphas, A., Brodsky, J. R., Devaiah, A. K., Dagher, W., ... & Tsai, A. C. (2014). Otologic outcomes after blast injury: the Boston Marathon experience. *Otology & Neurotology*, *35*(10), 1825-1834.

[70] O'Neill, O. J., & Murphy-Lavoie, H. M. (2019). Hyperbaric, Compressed Air Workers, Caissons, Tunneling, Bounce Diving, and Saturation Diving. In *StatPearls [Internet]*. StatPearls Publishing.

[71] Morris, S., Osborne, M. S., & McDermott, A. L. (2018). Will children ever learn? Removal of nasal and aural foreign bodies: a study of hospital episode statistics. *The Annals of The Royal College of Surgeons of England*, *100*(8), 632-634.

[72] Smith, M., Darrat, I., & Seidman, M. (2012). Otologic complications of cotton swab use: one institution's experience. *The Laryngoscope*, *122*(2), 409-411.

[73] Eleftheriadou, A., Chalastras, T., Kyrmizakis, D., Sfetsos, S., Dagalakis, K., & Kandiloros, D. (2007). Metallic foreign body in middle ear: an unusual cause of hearing loss. *Head & face medicine*, *3*(1), 23.

[74] O. A., Oyewole, E. A., & Mabifah, T. O. (2018). Traumatic tympanic membrane perforations: characteristics and factors affecting outcome. *Ghana medical journal*, *52*(1), 34-40.

[75] Voss, S. E., Rosowski, J. J., Merchant, S. N., & Peake, W. T. (2001). Middle-ear function with tympanic-membrane perforations. I. Measurements and mechanisms. *The Journal of the Acoustical Society of America*, *110*(3), 1432-1444.

[76] Mehta, R. P., Rosowski, J. J., Voss, S. E., O'Neil, E., & Merchant, S. N. (2006). Determinants of hearing loss in perforations of the tympanic membrane. *Otology & neurotology: official publication of the American Otological Society, American Neurotology Society [and] European Academy of Otology and Neurotology*, *27*(2), 136.

[77] Pannu, K. K., Chadha, S., & Kumar, D. (2011). Evaluation of hearing loss in tympanic membrane perforation. *Indian Journal of Otolaryngology and Head & Neck Surgery*, *63*(3), 208-213.

[78] Lerut, B., Pfammatter, A., Moons, J., & Linder, T. (2012). Functional correlations of tympanic membrane perforation size. *Otology & Neurotology*, *33*(3), 379-386.

[79] Gyo, K., Aritomo, H., & Goode, R. L. (1987). Measurement of the ossicular vibration ratio in human temporal bones by use of a video measuring system. *Acta oto-laryngologica*, *103*(1-2), 87-95.

[80] Stasche, N., Foth, H. J., Hörmann, K., Baker, A., & Huthoff, C. (1994). Middle ear transmission disorders—tympanic membrane vibration analysis by laser-Doppler-vibrometry. *Acta oto-laryngologica*, *114*(1), 59-63.

[81] Hornsby, B. W., & Ricketts, T. A. (2003). The effects of hearing loss on the contribution of high-and low-frequency speech information to speech understanding. *The Journal of the Acoustical Society of America*, *113*(3), 1706-1717.

[82] House, W. F., & Sheehy, J. L. (1960). Tympanosclerosis. *Archives of Otolaryngology*, *72*(3), 308-313.

[83] Park, J. H., Park, S. J., Kim, Y. H., & Park, M. H. (2014). Sensorineural hearing loss: a complication of acute otitis media in adults. *European Archives of Oto-Rhino-Laryngology*, *271*(7), 1879-1884.

[84] Mutlu, C., Odabasi, A. O., Metin, K., Basak, S., & Erpek, G. (1998). Sensorineural hearing loss associated with otitis media with effusion in children. *International journal of pediatric otorhinolaryngology*, *46*(3), 179-184.

[85] Margolis, R. H., & Nelson, D. A. (1993). Acute otitis media with transient sensorineural hearing loss: a case study. *Archives of Otolaryngology–Head & Neck Surgery*, *119*(6), 682-686.

[86] Taylor, M., & McMinn, R. M. (1967). Cytology of repair in experimental perforation of the tympanic membrane and its relationship to chronic perforations in man. *Transactions-American Academy of*

Ophthalmology and Otolaryngology. American Academy of Ophthalmology and Otolaryngology, *71*(5), 802.

[87] Mondain, M., & Ryan, A. (1994). Effect of basic fibroblast growth factor on normal tympanic membrane. *American journal of otolaryngology*, *15*(5), 344-350.

[88] Yeo, S. W., Kim, S. W., Suh, B. D., & Cho, S. H. (2000). Effects of platelet-derived growth factor-AA on the healing process of tympanic membrane perforation. *American journal of otolaryngology*, *21*(3), 153-160.

[89] Clymer, M. A., Schwaber, M. K., & Davidson, J. M. (1996). The effects of keratinocyte growth factor on healing of tympanic membrane perforations. *The Laryngoscope*, *106*(3), 280-285.

[90] Santa Maria, P. L., Redmond, S. L., McInnes, R. L., Atlas, M. D., & Ghassemifar, R. (2011). Tympanic membrane wound healing in rats assessed by transcriptome profiling. *The Laryngoscope*, *121*(10), 2199-2213.

[91] McMinn, R. M., & Taylor, M. (1966). The cytology of repair in experimental perforations of the tympanic membrane. *The British journal of surgery*, *53*(3), 222.

[92] Taylor, M., & McMinn, R. M. H. (1965). Healing of experimental perforations of the tympanic membrane. *The Journal of Laryngology & Otology*, *79*(2), 148-158.

[93] Boedts, D. (1978). The tympanic epithelium in normal and pathological conditions.

[94] Johnson, A., & Hawke, M. (1987). The function of migratory epidermis in the healing of tympanic membrane perforations in guinea-pig: a photographic study. *Acta oto-laryngologica*, *103*(1-2), 81-86.

[95] Clawson, J. P. (1971). The healing process of tympanic membrane perforations. *Trans Am Acad Ophthalmol Otalaryngol*, *75*, 1302-1312.

[96] O'Donoghue, G. M. (1983). Epithelial migration on the guinea-pig tympanic membrane: the influence of perforation and ventilating tube insertion. *Clinical otolaryngology and allied sciences*, *8*(5), 297.

[97] Gladstone HB, Jackler RK, Varav K. Tympanic membrane wound healing. An overview. Otolaryngol Clin North Am. 1995;28(5):913–932.

[98] Spandow, O., Hellström, S., & Dahlström, M. (1996). Structural characterization of persistent tympanic membrane perforations in man. *The Laryngoscope*, *106*(3), 346-352.

[99] Zajączkiewicz, H., Hassmann-Poznańska, E., Skotnicka, B., Chyczewski, L., Reszeć, J., & Winnicka, M. M. (2014). The healing process of tympanic membrane perforations in rats. Otolaryngologia polska= The Polish otolaryngology, 68(5), 244-251.

[100] de Araújo, M. M., Murashima, A. A. B., Alves, V. M., Jamur, M. C., & Hyppolito, M. A. (2014). Spontaneous healing of the tympanic membrane after traumatic perforation in rats. *Brazilian journal of otorhinolaryngology*, *80*(4), 330-338.

[101] Wang, W. Q., Wang, Z. M., & Chi, F. L. (2004). Spontaneous healing of various tympanic membrane perforations in the rat. *Acta oto-laryngologica*, *124*(10), 1141-1144.

[102] Kerr, A. G., & Byrne, J. E. T. (1975). Concussive effects of bomb blast on the ear. *The Journal of Laryngology & Otology*, *89*(2), 131-144.

[103] Orji, F. T., & Agu, C. C. (2008). Determinants of spontaneous healing in traumatic perforations of the tympanic membrane. *Clinical Otolaryngology*, *33*(5), 420-426.

[104] Lou, Z. C., & He, J. G. (2011). A randomised controlled trial comparing spontaneous healing, gelfoam patching and edge-approximation plus gelfoam patching in traumatic tympanic membrane perforation with inverted or everted edges. *Clinical Otolaryngology*, *36*(3), 221-226.

[105] Lou, Z. C., Tang, Y. M., & Yang, J. (2011). A prospective study evaluating spontaneous healing of aetiology, size and type-different groups of traumatic tympanic membrane perforation. *Clinical Otolaryngology*, *36*(5), 450-460.

[106] Lou, Z. C. (2012). Spontaneous healing of traumatic eardrum perforation: outward epithelial cell migration and clinical outcome. *Otolaryngology--Head and Neck Surgery*, *147*(6), 1114-1119.

[107] Sridhara, S. K., Rivera, A., & Littlefield, P. (2013). Tympanoplasty for blast-induced perforations: the Walter Reed experience. *Otolaryngology--Head and Neck Surgery*, *148*(1), 103-107.

[108] Jellinge, M. E., Kristensen, S., & Larsen, K. (2015). Spontaneous closure of traumatic tympanic membrane perforations: observational study. *The Journal of Laryngology & Otology*, *129*(10), 950-954.

aneous healing in traumatic perforations of the tympanic membrane. *Clinical Otolaryngology*, *33*(5), 420-426.

[109] Lou, Z. C., & He, J. G. (2011). A randomised controlled trial comparing spontaneous healing, gelfoam patching and edge-approximation plus gelfoam patching in traumatic tympanic membrane perforation with inverted or everted edges. *Clinical Otolaryngology*, *36*(3), 221-226.

[111] Lou, Z. C., Tang, Y. M., & Yang, J. (2011). A prospective study evaluating spontaneous healing of aetiology, size and type-different groups of traumatic tympanic membrane perforation. *Clinical Otolaryngology*, *36*(5), 450-460.

[112] Lou, Z. C. (2012). Spontaneo
us healing of traumatic eardrum perforation: outward epithelial cell migration and clinical outcome. *Otolaryngology--Head and Neck Surgery*, *147*(6), 1114-1119.

[113] Sridhara, S. K., Rivera, A., & Littlefield, P. (2013). Tympanoplasty for blast-induced perforations: the Walter Reed experience. *Otolaryngology--Headand Neck Surgery*, *148*(1), 103-107.

[115] Jellinge, M. E., Kristensen, S., & Larsen, K. (2015). Spontaneous closure of traumatic tympanic membrane perforations: observational study. *The Journal of Laryngology & Otology*, *129*(10), 950-954.

[116] Griffin Jr, W. L. (1979). A retrospective study of traumatic tympanic membrane perforations in a clinical practice. The Laryngoscope, 89(2), 261-282.

[117] Strohm, M. (1986). *Trauma of the middle ear*. Karger Publishers.

[118] Seonwoo, H., Kim, S. W., Kim, J., Chunjie, T., Lim, K. T., Kim, Y. J., ... & Chung, J. H. (2013). Regeneration of chronic tympanic membrane perforation using an EGF-releasing chitosan patch. *Tissue Engineering Part A*, *19*(17-18), 2097-2107.

[119] Petitjean, M., Martinez, S. A., O'daniel, T. G., Jones, S. C., Nolph, M. B., Zogg, J., & Schultz, G. S. (1990). Epidermal growth factor binding and action on tympanic membranes. *Annals of Otology, Rhinology & Laryngology*, *99*(1), 80-84.

[120] Dvorak, D. W., Abbas, G., Ali, T., Stevenson, S., & Welling, D. B. (1995). Repair of chronic tympanic membrane perforations with long-term epidermal growth factor. *The Laryngoscope*, *105*(12), 1300-1304.

[121] Lee, A. J., Jackler, R. K., Kato, B. M., & Scott, N. M. (1994). Repair of chronic tympanic membrane perforations using epidermal growth factor: progress toward clinical application. *Otology & Neurotology*, *15*(1), 10-18.

[122] Amoils, C. P., Jackler, R. K., & Lustig, L. R. (1992). Repair of chronic tympanic membrane perforations using epidermal growth factor. *Otolaryngology—Head and Neck Surgery*, *107*(5), 669-683.

[123] Mondain, M., Saffiedine, S., & Uziel, A. (1991). Fibroblast growth factor improves the healing of experimental tympanic membrane perforations. *Acta oto-laryngologica*, *111*(2), 337-341.

[124] Fina, M., Baird, A., & Ryan, A. (1993). Direct application of basic fibroblast growth factor improves tympanic membrane perforation healing. *The Laryngoscope*, *103*(7), 804-809.

[125] Fina, M., Bresnick, S., Bairp, A., & Ryan, A. (1991). Improved healing of tympanic membrane perforations with basic fibroblast growth factor. *Growth Factors*, *5*(4), 265-272.

[126] Mondain, M., & Ryan, A. (1993). Histological study of the healing of traumatic tympanic membrane perforation after basic fibroblast growth factor application. *The Laryngoscope*, *103*(3), 312-318.

[127] Vrabec, J. T., Schwaber, M. K., Davidson, J. M., & Clymer, M. A. (1994). Evaluation of basic fibroblast growth factor in tympanic membrane repair. *The Laryngoscope*, *104*(9), 1059-1064.

[128] Kaftan H, Herzog M, Miehe B, Hosemann W. Topical application of transforming growth factor-β1 in acute traumatic tympanic membrane perforations: an experimental study in rats. Wound repair and regeneration. 2006 Jul;14(4):453-6.

[129] DeLapp, N. W., & Dieckman, D. K. (1990). Effect of basic fibroblast growth factor (bFGF) and insulin-like growth factors type I (IGF-I) and type II (IGF-II) on adult human keratinocyte growth and fibronectin secretion. *Journal of investigative dermatology*, *94*(6).

[130] Kakigi, A., Uchida, A., Nishimura, M., Takeda, T., Takeda, S., & Nakatani, H. (2009). Expression of fibroblast growth factor receptors 1–4 in human chronic tympanic membrane perforation. *ORL*, *71*(Suppl. 1), 67-70.

[131] Liu, J., Agrawal, S. K., Ladak, H. M., & Wan, W. (2016). Fiber arrangement in the rat tympanic membrane. *The Anatomical Record*, *299*(11), 1531-1539.

[132] Browning, G. G., & Granich, M. S. (1978). Surgical anatomy of the temporal bone in the chinchilla. *Annals of Otology, Rhinology & Laryngology*, *87*(6), 875-882.

[133] Hakuba, N., Taniguchi, M., Shimizu, Y., Sugimoto, A., Shinomori, Y., & Gyo, K. (2003). A new method for closing tympanic membrane perforations using basic fibroblast growth factor. *The Laryngoscope*, *113*(8), 1352-1355.

[134] Bailey, B. J. (Ed.). (2001). *Atlas of Head & Neck Surgery--otolaryngology*. Lippincott Williams & Wilkins.

[135] Santos, F., Shu, E., Lee, D. J., Jung, D. H., Quesnel, A. M., Stankovic, K. M., ... & Welling, D. B. (2020). Topical fibroblast growth factor-2 for treatment of chronic tympanic membrane perforations. *Laryngoscope Investigative Otolaryngology*, *5*(4), 657-664.

[136] Röösli, C., von Büren, T., Gassmann, N. B., & Huber, A. M. (2011). The impact of platelet-derived growth factor on closure of chronic tympanic membrane perforations: a randomized, double-blind, placebo-controlled study. *Otology & Neurotology*, *32*(8), 1224-1229.

[137] Wang, A. Y., Shen, Y., Wang, J. T., Eikelboom, R. H., & Dilley, R. J. (2014). Animal models of chronic tympanic membrane perforation: in response to plasminogen initiates and potentiates the healing of acute and chronic tympanic membrane perforations in mice. *Clinical and Translational Medicine*, *3*(1), 1-3.

[138] Welling, B. (2013). *Fibroblast Growth Factor Regeneration of Tympanic Membrane Perforations*. OHIO STATE UNIV COLUMBUS.

[139] Lindeman, P., Edström, S., Granström, G., Jacobsson, S., von Sydow, C., Westin, T., & Åberg, B. (1987). Acute traumatic tympanic membrane perforations: cover or observe?. *Archives of Otolaryngology–Head & Neck Surgery*, *113*(12), 1285-1287.

[140] Patterson, M. E., Lockwood, R. W., & Sheehy, J. L. (1967). Temporalis fascia in tympanic membrane grafting: tissue culture and animal studies. *Archives of Otolaryngology*, *85*(3), 287-291.

[141] Wullstein, H. (1956). Theory and practice of tympanoplasty. *The Laryngoscope*, *66*(8), 1076-1093.

[142] Merkus, P., Kemp, P., Ziylan, F., & Yung, M. (2018). Classifications of mastoid and middle ear surgery: A scoping review. *The journal of international advanced otology*, *14*(2), 227.

[143] Inwood, J. L., Wallace, H. C., & Clarke, S. E. (2003). Endaural or postaural incision for myringoplasty: does it make a difference to the patient?. *Clinical Otolaryngology & Allied Sciences*, *28*(5), 396-398.

[144] Echelon Wealth Partners. ProMetic Life Sciences. (2019). Exhibit 6 – Revenue Forecasts, Plasminogen (Tympanic Membrane Repair).

[145] Kaftan, H., Noack, M., Friedrich, N., Völzke, H., & Hosemann, W. (2008). Prävalenz chronischer Trommelfellperforationen in der erwachsenen Bevölkerung. *HNO*, *56*(2), 145-150.

[146] Thomassin, J. M., Duchon-Doris, J. M., Emram, B., Rud, C., Conciatori, J., & Vilcoq, P. (1990). Endoscopic ear surgery. Initial evaluation. In *Annales d'oto-laryngologie et de chirurgie cervico faciale: bulletin de la Societe d'oto-laryngologie des hopitaux de Paris* (Vol. 107, No. 8, p. 564).

[147] Bottrill, I. D., & Poe, D. S. (1995). Endoscope-assisted ear surgery. *The American journal of otology*, *16*(2), 158-163.

[148] Migirov, L., Shapira, Y., Horowitz, Z., & Wolf, M. (2011). Exclusive endoscopic ear surgery for acquired cholesteatoma: preliminary results. *Otology & Neurotology*, *32*(3), 433-436.

[149] Bayram, A., Muluk, N. B., Cingi, C., & Bafaqeeh, S. A. (2020). Success rates for various graft materials in tympanoplasty–a review. *Journal of Otology*.

[150] Faramarzi, M., Shishegar, M., Tofighi, S. R., Sharouny, H., & Rajagopalan, R. (2019). Comparison of Grafting Success Rate and Hearing Outcomes between Primary and Revision Tympanoplasties. *Iranian Journal of Otorhinolaryngology*, *31*(102), 11.

[151] Attallah, M. S. (1996). Revision tympanoplasty: surgical findings and results in Riyadh. *ORL*, *58*(1), 36-38.

[152] Yurttas, V., Yakut, F., Kutluhan, A., & Bozdemir, K. (2014). Preparation and placement of cartilage island graft in tympanoplasty. *Brazilian Journal of Otorhinolaryngology*, *80*(6), 522-526.

[153] Indorewala, S., Adedeji, T. O., Indorewala, A., & Nemade, G. (2015). Tympanoplasty outcomes: a review of 789 cases. *Iranian journal of otorhinolaryngology*, *27*(79), 101.

[154] Ghanad I, Remenschneider A, Quesnel A. Long-term Otologic Outcomes Following Blast Injury: The Boston Marathon Bombings. AOS at COSM 2018.

[155] Yurttas, V., Ural, A., Kutluhan, A., & Bozdemir, K. (2015). Prognostic factors for graft success in tympanoplasty with mastoidectomy. *ENT Updates*, *5*(2), 68.

[156] Pignataro, L., Grillo della Berta, L., Capaccio, P., & Zaghis, A. (2001). Myringoplasty in children: anatomical and functional results. *Journal of laryngology and otology*, *115*(5), 369-373.

[157] Onal, K., Uguz, M. Z., Kazikdas, K. C., Gursoy, S. T., & Gokce, H. (2005). A multivariate analysis of otological, surgical and patient-related factors in determining success in myringoplasty. *Clinical Otolaryngology*, *30*(2), 115-120.

[158] Indorewala, S., Pagare, R., Aboojiwala, S., & Barpande, S. (2004). Dimensional stability of the free fascia grafts: A human study. *The laryngoscope*, *114*(3), 543-547.

[159] Cabra, J., & Moñux, A. (2010). Efficacy of cartilage palisade tympanoplasty: randomized controlled trial. *Otology & Neurotology*, *31*(4), 589-595.

[160] Polanik, M. D., Trakimas, D. R., Black, N. L., Cheng, J. T., Kozin, E. D., & Remenschneider, A. K. (2020). High-Frequency Conductive Hearing following Total Drum Replacement Tympanoplasty. *Otolaryngology–Head and Neck Surgery*, 0194599820907600.

[161] Hornsby, B. W., & Ricketts, T. A. (2006). The effects of hearing loss on the contribution of high-and low-frequency speech information to speech understanding. II. Sloping hearing loss. *The Journal of the Acoustical Society of America*, *119*(3), 1752-1763.

[162] McDermott, H. J., & Dean, M. R. (2000). Speech perception with steeply sloping hearing loss: effects of frequency transposition. *British Journal of Audiology*, *34*(6), 353-361.

[163] Li, B., Guo, Y., Yang, G., Feng, Y., & Yin, S. (2017). Effects of Various Extents of High-Frequency Hearing Loss on Speech Recognition and Gap Detection at Low Frequencies in Patients with Sensorineural Hearing Loss. *Neural plasticity*, *2017*.

[164] Hornsby, B. W., Ricketts, T. A., & Johnson, E. E. (2006). The effects of speech and speechlike maskers on unaided and aided speech recognition in persons with hearing loss. *Journal of the american academy of audiology*, *17*(6), 432-447.

[165] Carlile, S., & Schonstein, D. (2006, May). Frequency bandwidth and multi-talker environments. In *Audio Engineering Society Convention 120*. Audio Engineering Society.

[166] Psillas, G., Rizou, A., Rachovitsas, D., Tsiropoulos, G., & Constantinidis, J. (2019). Hearing outcome of low-tone compared to high-tone sudden sensorineural hearing loss. *International archives of otorhinolaryngology*, *23*(01), 065-069.

[167] Shim, H. J., Kim, S. K., Park, C. H., Lee, S. H., Yoon, S. W., Ki, A. R., ... & Yeo, S. G. (2009). Hearing abilities at ultra-high frequency in patients with tinnitus. *Clinical and experimental otorhinolaryngology*, *2*(4), 169.

[168] Bagger-Sjöbäck, D., Strömbäck, K., Hultcrantz, M., Papatziamos, G., Smeds, H., Danckwardt-Lillieström, N., ... & Fridberger, A. (2015). High-frequency hearing, tinnitus, and patient satisfaction with stapedotomy: A randomized prospective study. *Scientific reports*, *5*, 13341.

[169] Yung, M., Vivekanandan, S., & Smith, P. (2011). Randomized study comparing fascia and cartilage grafts in myringoplasty. *Annals of Otology, Rhinology & Laryngology*, *120*(8), 535-541.

[170] Sergi, B., Galli, J., De Corso, E., Parrilla, C., & Paludetti, G. (2011). Overlay versus underlay myringoplasty: report of outcomes considering closure of perforation and hearing function. *Acta otorhinolaryngologica italica*, *31*(6), 366.

[171] Röösli, C., Sim, J. H., Chatzimichalis, M., & Huber, A. M. (2012). How Does Closure of Tympanic Membrane Perforations Affect Hearing and Middle Ear Mechanics?—An Evaluation in a Patient Cohort and Temporal Bone Models. *Otology & Neurotology*, *33*(3), 371-378.

[172] D'Eredità, R. (2015). Porcine small intestinal submucosa (SIS) myringoplasty in children: a randomized controlled study. *International Journal of Pediatric Otorhinolaryngology*, *79*(7), 1085-1089.

[173] Yawn, R. J., Dedmon, M. M., O'Connell, B. P., Virgin, F. W., & Rivas, A. (2018). Tympanic membrane perforation repair using porcine small intestinal submucosal grafting. *Otology & Neurotology*, *39*(5), e332-e335.

[174] Basonbul, R. A., & Cohen, M. S. (2017). Use of porcine small intestinal submucosa for pediatric endoscopic tympanic membrane repair. *World Journal of Otorhinolaryngology-Head and Neck Surgery*, *3*(3), 142-147.

[175] Kozin, E. D., Lee, D. J., & Remenschneider, A. K. (2019). Bilayer Graft for Incisionless In-Office Endoscopic Repair of Tympanic Membrane Perforations: A Pilot Study. *OTO open*, *3*(3), 2473974X19869911.

[176] Merwin, G. E., & Boies Jr, L. R. (1980). Paper patch repair of blast rupture of the tympanic membrane. *The Laryngoscope*, *90*(5), 853-860.

[177] Laurent, C., Söderberg, O., Anniko, M., & Hartwig, S. (1991). Repair of chronic tympanic membrane perforations using applications of hyaluronan or rice paper prostheses. *ORL*, *53*(1), 37-40.

[178] Lee, J. H., Kim, D. K., Park, H. S., Jeong, J. Y., Yeon, Y. K., Kumar, V., ... & Park, C. H. (2016). A prospective cohort study of the silk fibroin patch in chronic tympanic membrane perforation. *The Laryngoscope*, *126*(12), 2798-2803.

[179] Mandour, Y. M. H., Mohammed, S., & Menem, M. A. (2019). Bacterial cellulose graft versus fat graft in closure of tympanic membrane perforation. *American Journal of Otolaryngology*, *40*(2), 168-172.

[180] Biskin, S., Damar, M., Oktem, S. N., Sakalli, E., Erdem, D., & Pakir, O. (2016). A new graft material for myringoplasty: bacterial cellulose. *European Archives of Oto-Rhino-Laryngology*, *273*(11), 3561-3565.

[181] Hakuba, N., Hato, N., Okada, M., Mise, K., & Gyo, K. (2015). Preoperative factors affecting tympanic membrane regeneration therapy using an atelocollagen and basic fibroblast growth factor. *JAMA Otolaryngology–Head & Neck Surgery*, *141*(1), 60-66.

[182] Hakuba, N., Iwanaga, M., Tanaka, S., Hiratsuka, Y., Kumabe, Y., Konishi, M., ... & Wada, T. (2010). Basic fibroblast growth factor combined with atelocollagen for closing chronic tympanic membrane perforations in 87 patients. *Otology & Neurotology*, *31*(1), 118-121.

[183] Tamae, A., & Komune, S. (2015). Clinical study of transcanal closure of tympanic membrane perforations using a collagen sponge. *The Journal of Laryngology & Otology*, *129*(S2), S21-S26.

[184] Aslan, G., & Uzun, L. (2011). Adhesive strip patching for tympanic membrane perforations. *Operative Techniques in Otolaryngology-Head and Neck Surgery*, *22*(2), 173-174.

[185] Park, M. K., Kim, K. H., Lee, J. D., & Lee, B. D. (2011). Repair of large traumatic tympanic membrane perforation with a Steri-Strips patch. *Otolaryngology--Head and Neck Surgery*, *145*(4), 581-585.

[186] Lou, Z. C., & Lou, Z. (2018). Efficacy of EGF and gelatin sponge for traumatic tympanic membrane perforations: a randomized controlled study. *Otolaryngology–Head and Neck Surgery*, *159*(6), 1028-1036.

[187] Wang, N., & Isaacson, G. (2020). Collagen matrix as a replacement for Gelfilm® for post-tympanostomy tube myringoplasty. *International Journal of Pediatric Otorhinolaryngology*, 110136.

[188] Ballivet de Régloix, S., Crambert, A., Salf, E., Maurin, O., Pons, Y., & Clément, P. (2018). Early tympanoplasty using a synthetic biomembrane for military-related blast induced large tympanic membrane perforation. *Military medicine*, *183*(11-12), e624-e627.

[189] Sayin, I., Kaya, K. H., Ekizoğlu, O., Erdim, İ., & Kayhan, F. T. (2013). A prospective controlled trial comparing spontaneous closure and Epifilm® patching in traumatic tympanic membrane perforations. *European Archives of Oto-Rhino-Laryngology*, *270*(11), 2857-2863.

[190] Prior, M., Gibbins, N., John, G., Rhys-Williams, S., & Scott, P. (2008). Hyaluronic acid ester in myringoplasty. *The Journal of Laryngology and Otology*, *122*(2).

[191] Alzahrani, M., & Saliba, I. (2015). Hyaluronic acid fat graft myringoplasty vs fat patch fat graft myringoplasty. *European Archives of Oto-Rhino-Laryngology*, *272*(8), 1873-1877.

[192] Saliba, I. (2008). Hyaluronic acid fat graft myringoplasty: how we do it. *Clinical Otolaryngology*, *33*(6), 610-614.

[193] Saliba, I., & Froehlich, P. (2011). Hyaluronic acid fat graft myringoplasty: an office-based technique adapted to children. *Archives of Otolaryngology–Head & Neck Surgery*, *137*(12), 1203-1209.

[194] Saliba, I., Alzahrani, M., Zhu, T., & Chemtob, S. (2014). Growth factors expression in hyaluronic acid fat graft myringoplasty. *The Laryngoscope*, *124*(6), E224-E230.

[195] Stenfors, L. E. (1989). Repair of tympanic membrane perforations using hyaluronic acid: an alternative to myringoplasty. *The Journal of Laryngology & Otology*, *103*(1), 39-40.

[196] Benecke Jr, J. E. (2001). Tympanic membrane grafting with alloderm. *The Laryngoscope*, *111*(9), 1525-1527.

[197] Ghanad, I., Polanik, M., Trakimas, D., Knoll, R., Castillo-Bustamante, M., Black, N.L., Kozin, E.D., & Remenschneider, A.K. A Systematic Review of Non-Autologous Graft Materials Used in Human Tympanoplasty. *The Laryngoscope*. Accepted in June 2020.

[198] Weber, D. E., Semaan, M. T., Wasman, J. K., Beane, R., Bonassar, L. J., & Megerian, C. A. (2006). Tissue-engineered calcium alginate patches in the repair of chronic chinchilla tympanic membrane perforations. *The Laryngoscope*, *116*(5), 700-704.

[199] Jang, C. H., Ahn, S., Lee, J. W., Lee, B. H., Lee, H., & Kim, G. (2017). Mesenchymal stem cell-laden hybrid scaffold for regenerating subacute tympanic membrane perforation. *Materials Science and Engineering: C*, *72*, 456-463.

[200] Shen, Y., Redmond, S. L., Teh, B. M., Yan, S., Wang, Y., Zhou, L., ... & Zheng, M. (2013). Scaffolds for tympanic membrane regeneration in rats. *Tissue Engineering Part A*, *19*(5-6), 657-668.

[201] Shen, Y., Redmond, S. L., Teh, B. M., Yan, S., Wang, Y., Atlas, M. D., ... & Marano, R. J. (2013). Tympanic membrane repair using silk fibroin and acellular collagen scaffolds. The Laryngoscope, 123(8), 1976-1982.

[202] Altuntaş, E. E., & Sümer, Z. (2013). Biocompatibility evaluation of cigarette and carbon papers used in repair of traumatic tympanic membrane perforations: experimental study. European Archives of Oto-Rhino-Laryngology, 270(1), 81-86.

[203] Wieland, A. M., Sundback, C. A., Hart, A., Kulig, K., Masiakos, P. T., & Hartnick, C. J. (2010). Poly (glycerol sebacate)-engineered plugs to repair chronic tympanic membrane perforations in a chinchilla model. Otolaryngology—Head and Neck Surgery, 143(1), 127-133.

[204] Williams, K. R., & Blayney, A. W. (1987). Tissue response of several polymeric materials implanted in the rat middle ear. *Biomaterials*, *8*(4), 254-258.

[205] Moscato, S., Rocca, A., D'Alessandro, D., Puppi, D., Gramigna, V., Milazzo, M., ... & Danti, S. (2020). Tympanic Membrane Collagen Expression by Dynamically Cultured Human Mesenchymal Stromal Cell/Star-Branched Poly (ε-Caprolactone) Nonwoven Constructs. *Applied Sciences*, *10*(9), 3043.

[206] Parekh, A., Mantle, B., Banks, J., Swarts, J. D., Badylak, S. F., Dohar, J. E., & Hebda, P. A. (2009). Repair of the tympanic membrane with urinary bladder matrix. *The Laryngoscope*, *119*(6), 1206-1213.

[207] Ort, S. A., Ehrlich, H. P., & Isaacson, J. E. (2010). Acellular porcine intestinal submucosa as fascial graft in an animal model: Applications for revision tympanoplasty. *Otolaryngology—Head and Neck Surgery*, *143*(3), 435-440.

[208] Browning, G. G., & Granich, M. S. (1978). Surgical anatomy of the temporal bone in the chinchilla. *Annals of Otology, Rhinology & Laryngology*, *87*(6), 875-882.

[209] Weber, D. E., Semaan, M. T., Wasman, J. K., Beane, R., Bonassar, L. J., & Megerian, C. A. (2006). Tissue-engineered calcium alginate patches in the repair of chronic chinchilla tympanic membrane perforations. *The Laryngoscope*, *116*(5), 700-704.

[210] Amoils, C. P., Jackler, R. K., Milczuk, H., Kelly, K. E., & Cao, K. (1992). An animal model of chronic tympanic membrane perforation. *Otolaryngology—Head and Neck Surgery*, *106*(1), 47-55.

[211] Ramalho, J. R., & Bento, R. F. (2006). Healing of subacute tympanic membrane perforations in chinchillas treated with epidermal growth factor and pentoxifylline. *Otology & Neurotology*, *27*(5), 720-727.

[212] Gao, T., Li, X., Hu, J., Ma, W., Li, J., Shao, N., & Wang, Z. (2017). Management of traumatic tympanic membrane perforation: a comparative study. *Therapeutics and clinical risk management*, *13*, 927.

[213] Spiegel, J. H., & Kessler, J. L. (2005). Tympanic membrane perforation repair with acellular porcine submucosa. *Otology & Neurotology*, *26*(4), 563-566.

[214] Miller, J. D. (1964). Auditory sensitivity of the chinchilla in quiet and in noise. *The Journal of the Acoustical Society of America*, *36*(10), 2010-2010.

[215] Heffner, R. S., & Heffner, H. E. (1991). Behavioral hearing range of the chinchilla. *Hearing research*, *52*(1), 13-16.

[216] Downey, T. J., Champeaux, A. L., & Silva, A. B. (2003). AlloDerm tympanoplasty of tympanic membrane perforations. *American journal of otolaryngology*, *24*(1), 6-13.

[217] Chen, E., & Harner, S. G. (1986). The effect of butyl 2-cyanoacrylate on the middle and inner ear of the chinchilla. *Otolaryngology—Head and Neck Surgery*, *95*(2), 187-192.

[218] Yadav, S. P. S., Malik, J. S., Malik, P., Sehgal, P. K., Gulia, J. S., & Ranga, R. K. (2018). Studying the result of underlay myringoplasty using platelet-rich plasma. The Journal of Laryngology & Otology, 132(11), 990-994.

[219] Lopez, I. A., Ishiyama, G., Hosokawa, S., Hosokawa, K., Acuna, D., Linthicum, F. H., & Ishiyama, A. (2016). Immunohistochemical techniques for the human inner ear. *Histochemistry and cell biology*, *146*(4), 367-387.

[220] O'malley, J. T., Burgess, B. J., Jones, D. D., Adams, J. C., & Merchant, S. N. (2009). Techniques of celloidin removal from temporal bone sections. *Annals of Otology, Rhinology & Laryngology*, *118*(6), 435-441.

[221] Koide, Y. (1965). LXXXIV Foreign Materials in Tympanoplasty. *Annals of Otology, Rhinology & Laryngology*, *74*(4), 1055-1072.

[222] Honings, J., & Dammeijer, P. F. (2013). Chronic otorrhea caused by myospherulosis in the middle ear after tympanoplasty. *Annals of Otology, Rhinology & Laryngology*, *122*(7), 461-463.

[223] Schacht, J. (1976). Biochemistry of neomycin ototoxicity. The Journal of the Acoustical Society of America, 59(4), 940-944.

[224] Daudet, N., Vago, P., Ripoll, C., Humbert, G., Pujol, R., & Lenoir, M. (1998). Characterization of atypical cells in the juvenile rat organ of corti after aminoglycoside ototoxicity. *Journal of Comparative Neurology*, *401*(2), 145-162.

[225] Theopold, H. M. (1977). Comparative surface studies of ototoxic effects of various aminoglycoside antibiotics on the organ of corti in the guinea pig a scanning electron microscopic study. *Acta Oto-laryngologica*, *84*(1-6), 57-64.

[226] Lang, H., Schulte, B. A., & Schmiedt, R. A. (2005). Ouabain induces apoptotic cell death in type I spiral ganglion neurons, but not type II neurons. *Journal of the Association for Research in Otolaryngology*, *6*(1), 63-74.

[227] Fu, Y., Ding, D., Wei, L., Jiang, H., & Salvi, R. (2013). Ouabain-induced apoptosis in cochlear hair cells and spiral ganglion neurons in vitro. *BioMed research international*, *2013*.

[228] Fu, Y., Ding, D., Jiang, H., & Salvi, R. (2012). Ouabain-induced cochlear degeneration in rat. *Neurotoxicity research*, *22*(2), 158-169.

[229] Ylikoski, J., Wersäll, J., & Björkroth, B. (1974). Degeneration of neural elements in the cochlea of the guinea-pig after damage to the organ of corti by ototoxic antibiotics. *Acta Oto-Laryngologica*, *78*(sup326), 23-41.

[230] Hamers, F. P., Wijbenga, J., Wolters, F. L., Klis, S. F., Sluyter, S., & Smoorenburg, G. F. (2003). Cisplatin ototoxicity involves organ of Corti, stria vascularis and spiral ganglion: modulation by αMSH and ORG 2766. *Audiology and Neurotology*, *8*(6), 305-315.

[231] Schweitzer, V. G. (1993). Cisplatin-induced ototoxicity: the effect of pigmentation and inhibitory agents. *The Laryngoscope*, *103*, 1-52.

[232] Laurell, G., & Bagger-sjöbäck, D. (1991). Degeneration of the organ of Corti following intravenous administration of cisplatin. *Acta oto-laryngologica*, *111*(5), 891-898.

[233] Rybak, L. P., & Ramkumar, V. (2007). Ototoxicity. *Kidney international*, *72*(8), 931-935.

[234] Selimoglu, E. (2007). Aminoglycoside-induced ototoxicity. *Current pharmaceutical design*, *13*(1), 119-126.

[235] Hawkins, J. E. (1976). Drug ototoxicity. In *Auditory system* (pp. 707-748). Springer, Berlin, Heidelberg.

[236] Powell, C. A., Smiley, B. L., Mills, J., & Vandenburgh, H. H. (2002). Mechanical stimulation improves tissue-engineered human skeletal muscle. *American Journal of Physiology-Cell Physiology*, *283*(5), C1557-C1565.

[237] Riehl, B. D., Park, J. H., Kwon, I. K., & Lim, J. Y. (2012). Mechanical stretching for tissue engineering: two-dimensional and three-dimensional constructs. *Tissue Engineering Part B: Reviews*, *18*(4), 288-300.

[238] Bono, N., Pezzoli, D., Levesque, L., Loy, C., Candiani, G., Fiore, G. B., & Mantovani, D. (2016). Unraveling the role of mechanical stimulation on smooth muscle cells: A comparative study between 2D and 3D models. *Biotechnology and bioengineering*, *113*(10), 2254-2263.

[239] Dan, P., Velot, É., Decot, V., & Menu, P. (2015). The role of mechanical stimuli in the vascular differentiation of mesenchymal stem cells. *J Cell Sci*, *128*(14), 2415-2422.

[240] Zhou, J., & Niklason, L. E. (2012). Microfluidic artificial "vessels" for dynamic mechanical stimulation of mesenchymal stem cells. *Integrative Biology*, *4*(12), 1487-1497.

[241] Chang, H. F., Lee, Y. S., Tang, T. K., & Cheng, J. Y. (2016). Pulsed DC Electric Field–Induced Differentiation of Cortical Neural Precursor Cells. *PloS one*, *11*(6), e0158133.

[242] Flaibani, M., Boldrin, L., Cimetta, E., Piccoli, M., Coppi, P. D., & Elvassore, N. (2009). Muscle differentiation and myotubes alignment is influenced by micropatterned surfaces and exogenous electrical stimulation. *Tissue Engineering Part A*, *15*(9), 2447-2457.

[243] Ahadian, S., Ramón-Azcón, J., Ostrovidov, S., Camci-Unal, G., Hosseini, V., Kaji, H., ... & Matsue, T. (2012). Interdigitated array of Pt electrodes for electrical stimulation and engineering of aligned muscle tissue. *Lab on a Chip*, *12*(18), 3491-3503.

[244] Sadeghian, R. B., Ebrahimi, M., & Salehi, S. (2017). Electrical Stimulation of Microengineered Skeletal Muscle Tissue, Effect of Stimulus Parameters on Myotube Contractility and Maturation. *Journal of tissue engineering and regenerative medicine*.

[245] Tandon, N., Cannizzaro, C., Chao, P. H. G., Maidhof, R., Marsano, A., Au, H. T. H., ... & Vunjak-Novakovic, G. (2009). Electrical stimulation systems for cardiac tissue engineering. *Nature protocols*, *4*(2), 155.

[246] Schmalenberg, K. E., & Uhrich, K. E. (2005). Micropatterned polymer substrates control alignment of proliferating Schwann cells to direct neuronal regeneration. *Biomaterials*, *26*(12), 1423-1430.

[247] He, S., Liu, C., Li, X., Ma, S., Huo, B., & Ji, B. (2015). Dissecting collective cell behavior in polarization and alignment on micropatterned substrates. *Biophysical journal*, *109*(3), 489-500.

[248] Aubin, H., Nichol, J. W., Hutson, C. B., Bae, H., Sieminski, A. L., Cropek, D. M., ... & Khademhosseini, A. (2010). Directed 3D cell alignment and elongation in microengineered hydrogels. *Biomaterials*, *31*(27), 6941-6951.

[249] Versaevel, M., Grevesse, T., & Gabriele, S. (2012). Spatial coordination between cell and nuclear shape within micropatterned endothelial cells. *Nature communications*, *3*, 671.

[250] Dunn, G. A., & Brown, A. F. (1986). Alignment of fibroblasts on grooved surfaces described by a simple geometric transformation. *Journal of cell science*, *83*(1), 313-340.

[251] Van Delft, F. C. M. J. M., Van Den Heuvel, F. C., Loesberg, W. A., te Riet, J., Schön, P., Figdor, C. G., ... & Jansen, J. A. (2008). Manufacturing substrate nano-grooves for studying cell alignment and adhesion. *Microelectronic Engineering*, *85*(5-6), 1362-1366.

[252] Zhou, X., Shi, J., Hu, J., & Chen, Y. (2013). Cells cultured on microgrooves with or without surface coating: Correlation between cell alignment, spreading and local membrane deformation. *Materials Science and Engineering: C*, *33*(2), 855-863.

[253] Sun, B., Xie, K., Chen, T. H., & Lam, R. H. (2017). Preferred cell alignment along concave microgrooves. *RSC Advances*, *7*(11), 6788-6794.

[254] Hu, J., Hardy, C., Chen, C. M., Yang, S., Voloshin, A. S., & Liu, Y. (2014). Enhanced cell adhesion and alignment on micro-wavy patterned surfaces. *PLoS One*, *9*(8), e104502.

[255] Suzuki, I., Sugio, Y., Moriguchi, H., Jimbo, Y., & Yasuda, K. (2004). Modification of a neuronal network direction using stepwise photo-thermal etching of an agarose architecture. *Journal of nanobiotechnology*, *2*(1), 7.

[256] Koppes, R. A., Park, S., Hood, T., Jia, X., Poorheravi, N. A., Achyuta, A. H., ... & Anikeeva, P. (2016). Thermally drawn fibers as nerve guidance scaffolds. *Biomaterials*, *81*, 27-35.

[257] Babakhanova, G., Krieger, J., Li, B. X., Turiv, T., Kim, M. H., & Lavrentovich, O. D. (2020). Cell alignment by smectic liquid crystal elastomer coatings with nanogrooves. *Journal of Biomedical Materials Research Part A*, *108*(5), 1223-1230.

[258] Riso, E. M., Kaasik, P., & Seene, T. (2016). Remodelling of Skeletal Muscle Extracellular Matrix: Effect of Unloading and Reloading. In *Composition and Function of the Extracellular Matrix in the Human Body*. InTech.

[259] Prockop, D. J., & Kivirikko, K. I. (1984). Heritable diseases of collagen. *New England Journal of Medicine*, *311*(6), 376-386.

[260] Lange, J. R., & Fabry, B. (2013). Cell and tissue mechanics in cell migration. *Experimental cell research*, *319*(16), 2418-2423.

[261] Kim, D. H., Khatau, S. B., Feng, Y., Walcott, S., Sun, S. X., Longmore, G. D., & Wirtz, D. (2012). Actin cap associated focal adhesions and their distinct role in cellular mechanosensing. *Scientific reports*, *2*, 555.

[262] Sandler, N., Salmela, I., Fallarero, A., Rosling, A., Khajeheian, M., Kolakovic, R., ... & Vuorela, P. (2014). Towards fabrication of 3D printed medical devices to prevent biofilm formation. *International journal of pharmaceutics*, *459*(1-2), 62-64.

[263] Morrison, R. J., Hollister, S. J., Niedner, M. F., Mahani, M. G., Park, A. H., Mehta, D. K., ... & Green, G. E. (2015). Mitigation of tracheobronchomalacia with 3D-printed personalized medical devices in pediatric patients. *Science translational medicine*, *7*(285), 285ra64-285ra64.

[264] Ricles, L. M., Coburn, J. C., Di Prima, M., & Oh, S. S. (2018). Regulating 3D-printed medical products. *Science Translational Medicine*, *10*(461).

[265] Chimento, J., Highsmith, M. J., & Crane, N. (2011). 3D printed tooling for thermoforming of medical devices. *Rapid Prototyping Journal*.

[266] Genina, N., Holländer, J., Jukarainen, H., Mäkilä, E., Salonen, J., & Sandler, N. (2016). Ethylene vinyl acetate (EVA) as a new drug carrier for 3D printed medical drug delivery devices. *European Journal of Pharmaceutical Sciences*, *90*, 53-63.

[267] Mohammed, M., Fitzpatrick, A., Malyala, S., & Gibson, I. (2016, August). Customised design and development of patient specific 3D printed whole mandible implant. In *Proceedings of the 27th Annual International Solid Freeform Fabrication Symposium* (pp. 1708-1717).

268 Bruyas, A., Lou, F., Stahl, A. M., Gardner, M., Maloney, W., Goodman, S., & Yang, Y. P. (2018). Systematic characterization of 3D-printed PCL/β-TCP scaffolds for biomedical devices and bone tissue engineering: Influence of composition and porosity. *Journal of materials research*, *33*(14), 1948.

[269] Guerra, A. J., Cano, P., Rabionet, M., Puig, T., & Ciurana, J. (2018). 3D-printed PCL/PLA composite stents: Towards a new solution to cardiovascular problems. *Materials*, *11*(9), 1679.

[270] Morrison, R. J., Hollister, S. J., Niedner, M. F., Mahani, M. G., Park, A. H., Mehta, D. K., ... & Green, G. E. (2015). Mitigation of tracheobronchomalacia with 3D-printed personalized medical devices in pediatric patients. *Science translational medicine*, *7*(285), 285ra64-285ra64.

[271] Barry III, R. A., Shepherd, R. F., Hanson, J. N., Nuzzo, R. G., Wiltzius, P., & Lewis, J. A. (2009). Direct-write assembly of 3D hydrogel scaffolds for guided cell growth. *Advanced materials*, *21*(23), 2407-2410.

[272] Hanson Shepherd, J. N., Parker, S. T., Shepherd, R. F., Gillette, M. U., Lewis, J. A., & Nuzzo, R. G. (2011). 3D microperiodic hydrogel scaffolds for robust neuronal cultures. *Advanced functional materials*, *21*(1), 47-54.

[273] Xu, M., Gratson, G. M., Duoss, E. B., Shepherd, R. F., & Lewis, J. A. (2006). Biomimetic silicification of 3D polyamine-rich scaffolds assembled by direct ink writing. *Soft Matter*, *2*(3), 205-209.

[274] Sun, L., Parker, S. T., Syoji, D., Wang, X., Lewis, J. A., & Kaplan, D. L. (2012). Direct-write assembly of 3D silk/hydroxyapatite scaffolds for bone co-cultures. *Advanced healthcare materials*, *1*(6), 729-735.

[275] Michna, S., Wu, W., & Lewis, J. A. (2005). Concentrated hydroxyapatite inks for direct-write assembly of 3-D periodic scaffolds. *Biomaterials*, *26*(28), 5632-5639.

[276] Zhang, L., Yang, G., Johnson, B. N., & Jia, X. (2019). Three-dimensional (3D) printed scaffold and material selection for bone repair. *Acta biomaterialia*, *84*, 16-33.

[277] Kolesky DB, Truby RL, Gladman AS, Busbee TA, Homan KA, Lewis JA. 3D bioprinting of vascularized, heterogeneous cell-laden tissue constructs. Advanced Materials. 2014 May;26(19):3124-30.

[278] Skylar-Scott, M. A., Uzel, S. G., Nam, L. L., Ahrens, J. H., Truby, R. L., Damaraju, S., & Lewis, J. A. (2019). Biomanufacturing of organ-specific tissues with high cellular density and embedded vascular channels. *Science advances*, *5*(9), eaaw2459.

[279] Kolesky, D. B., Homan, K. A., Skylar-Scott, M. A., & Lewis, J. A. (2016). Three-dimensional bioprinting of thick vascularized tissues. *Proceedings of the national academy of sciences*, *113*(12), 3179-3184.

[280] Homan, K. A., Kolesky, D. B., Skylar-Scott, M. A., Herrmann, J., Obuobi, H., Moisan, A., & Lewis, J. A. (2016). Bioprinting of 3D convoluted renal proximal tubules on perfusable chips. *Scientific reports*, *6*, 34845.

[281] Mandrycky, C., Wang, Z., Kim, K., & Kim, D. H. (2016). 3D bioprinting for engineering complex tissues. *Biotechnology advances*, *34*(4), 422-434.

[282] Norotte, C., Marga, F. S., Niklason, L. E., & Forgacs, G. (2009). Scaffold-free vascular tissue engineering using bioprinting. *Biomaterials*, *30*(30), 5910-5917.

[283] Truby, R. L., & Lewis, J. A. (2016). Printing soft matter in three dimensions. *Nature*, *540*(7633), 371-378.

[284] Gladman, A. S., Matsumoto, E. A., Nuzzo, R. G., Mahadevan, L., & Lewis, J. A. (2016). Biomimetic 4D printing. *Nature materials*, *15*(4), 413-418.

[285] Kotikian, A., Truby, R. L., Boley, J. W., White, T. J., & Lewis, J. A. (2018). 3D printing of liquid crystal elastomeric actuators with spatially programed nematic order. *Advanced materials*, *30*(10), 1706164.

[286] Kotikian, A., McMahan, C., Davidson, E. C., Muhammad, J. M., Weeks, R. D., Daraio, C., & Lewis, J. A. (2019). Untethered soft robotic matter with passive control of shape morphing and propulsion. *Sci. Robot*, *4*(33), 7044.

[287] Boley, J. W., Chaudhary, K., Ober, T. J., Khorasaninejad, M., Chen, W. T., Hanson, E., ... & Zhu, A. Y. (2017). High-Operating-Temperature Direct Ink Writing of Mesoscale Eutectic Architectures. *Advanced Materials*, *29*(7), 1604778.

[288] Kuo, C. Y., Wilson, E., Fuson, A., Gandhi, N., Monfaredi, R., Jenkins, A., ... & Reilly, B. (2018). Repair of tympanic membrane perforations with customized bioprinted ear grafts using chinchilla models. *Tissue Engineering Part A*, *24*(5-6), 527-535.

[289] Mota, C., Danti, S., D'Alessandro, D., Trombi, L., Ricci, C., Puppi, D., ... & Moroni, L. (2015). Multiscale fabrication of biomimetic scaffolds for tympanic membrane tissue engineering. *Biofabrication*, *7*(2), 025005.

[290] Ilhan, E., Ulag, S., Sahin, A., Ekren, N., Kilic, O., Oktar, F. N., & Gunduz, O. (2020, May). Production of 3D-Printed Tympanic Membrane Scaffolds as a Tissue Engineering Application. In *International Work-Conference on Bioinformatics and Biomedical Engineering* (pp. 175-184). Springer, Cham.

[291] Gentile, P., Chiono, V., Carmagnola, I., & Hatton, P. V. (2014). An overview of poly (lactic-co-glycolic) acid (PLGA)-based biomaterials for bone tissue engineering. *International journal of molecular sciences*, *15*(3), 3640-3659.

[292] Maurus, P. B., & Kaeding, C. C. (2004). Bioabsorbable implant material review. *Operative Techniques in Sports Medicine*, *12*(3), 158-160.

[293] Abdelwahab, M. A., Flynn, A., Chiou, B. S., Imam, S., Orts, W., & Chiellini, E. (2012). Thermal, mechanical and morphological characterization of plasticized PLA–PHB blends. *Polymer degradation and stability*, *97*(9), 1822-1828.

[294] Sundback, C. A., Shyu, J. Y., Wang, Y., Faquin, W. C., Langer, R. S., Vacanti, J. P., & Hadlock, T. A. (2005). Biocompatibility analysis of poly (glycerol sebacate) as a nerve guide material. *Biomaterials*, *26*(27), 5454-5464.

[295] Chen, Q. Z., Bismarck, A., Hansen, U., Junaid, S., Tran, M. Q., Harding, S. E., ... & Boccaccini, A. R. (2008). Characterisation of a soft elastomer poly (glycerol sebacate) designed to match the mechanical properties of myocardial tissue. *Biomaterials*, *29*(1), 47-57.

[296] Chen, Q. Z., Ishii, H., Thouas, G. A., Lyon, A. R., Wright, J. S., Blaker, J. J., ... & Harding, S. E. (2010). An elastomeric patch derived from poly (glycerol sebacate) for delivery of embryonic stem cells to the heart. *Biomaterials*, *31*(14), 3885-3893.

177

[297] Ravichandran, R., Venugopal, J. R., Sundarrajan, S., Mukherjee, S., & Ramakrishna, S. (2011). Poly (glycerol sebacate)/gelatin core/shell fibrous structure for regeneration of myocardial infarction. *Tissue Engineering Part A*, *17*(9-10), 1363-1373.

[298] Prabhakaran, M. P., Nair, A. S., Kai, D., & Ramakrishna, S. (2012). Electrospun composite scaffolds containing poly (octanediol-co-citrate) for cardiac tissue engineering. *Biopolymers*, *97*(7), 529-538.

[299] Sharma, A. K., Hota, P. V., Matoka, D. J., Fuller, N. J., Jandali, D., Thaker, H., ... & Cheng, E. Y. (2010). Urinary bladder smooth muscle regeneration utilizing bone marrow derived mesenchymal stem cell seeded elastomeric poly (1, 8-octanediol-co-citrate) based thin films. *Biomaterials*, *31*(24), 6207-6217.

[300] Jeong, C. G., Zhang, H., & Hollister, S. J. (2011). Three-dimensional poly (1, 8-octanediol–co-citrate) scaffold pore shape and permeability effects on sub-cutaneous in vivo chondrogenesis using primary chondrocytes. *Acta biomaterialia*, *7*(2), 505-514.

[301] Jeong, C. G., & Hollister, S. J. (2010). Mechanical and biochemical assessments of three-dimensional poly (1, 8-octanediol-co-citrate) scaffold pore shape and permeability effects on in vitro chondrogenesis using primary chondrocytes. *Tissue Engineering Part A*, *16*(12), 3759-3768.

[302] Zhu, L., Zhang, Y., & Ji, Y. (2017). Fabricating poly (1, 8-octanediol citrate) elastomer based fibrous mats via electrospinning for soft tissue engineering scaffold. *Journal of Materials Science: Materials in Medicine*, *28*(6), 93.

[303] Motlagh, D., Yang, J., Lui, K. Y., Webb, A. R., & Ameer, G. A. (2006). Hemocompatibility evaluation of poly (glycerol-sebacate) in vitro for vascular tissue engineering. *Biomaterials*, *27*(24), 4315-4324.

[304] Yi, F., & LaVan, D. A. (2008). Poly (glycerol sebacate) nanofiber scaffolds by core/shell electrospinning. *Macromolecular bioscience*, *8*(9), 803-806.

[305] Liang, S., Cook, W. D., & Chen, Q. (2012). Physical characterization of poly (glycerol sebacate)/Bioglass® composites. *Polymer international*, *61*(1), 17-22.

[306] Polymer Science Learning Center. Making polyurethane. http://pslc.ws/macrog/uresyn.htm

[307] Wong, C. S., & Badri, K. H. (2012). Chemical analyses of palm kernel oil-based polyurethane prepolymer. *Mater Sci Appl*, *3*(2), 78-86.

[308] McKee, C. T., Last, J. A., Russell, P., & Murphy, C. J. (2011). Indentation versus tensile measurements of Young's modulus for soft biological tissues. *Tissue Engineering Part B: Reviews*, *17*(3), 155-164.

[309] Covestro AG. Thermoplastic Polyurethanes. <https://www.tpu.covestro.com/en/Technologies/Properties/Mechanical-Properties/Stiffness>.

[310] Asefnejad, A., Khorasani, M. T., Behnamghader, A., Farsadzadeh, B., & Bonakdar, S. (2011). Manufacturing of biodegradable polyurethane scaffolds based on polycaprolactone using a phase separation method: physical properties and in vitro assay. *International journal of nanomedicine*, *6*, 2375.

[311] Eglin, D., Griffon, S., & Alini, M. (2010). Thiol-containing degradable poly (thiourethane-urethane) s for tissue engineering. *Journal of Biomaterials Science, Polymer Edition*, *21*(4), 477-491.

[312] Wen, Y. T., Dai, N. T., & Hsu, S. H. (2019). Biodegradable water-based polyurethane scaffolds with a sequential release function for cell-free cartilage tissue engineering. *Acta biomaterialia*, *88*, 301-313.

[313] Asplund, B., Aulin, C., Bowden, T., Eriksson, N., Mathisen, T., Bjursten, L. M., & Hilborn, J. (2008). In vitro degradation and in vivo biocompatibility study of a new linear poly (urethane urea). *Journal of Biomedical Materials Research Part B: Applied Biomaterials*, *86*(1), 45-55.

[314] Cheung, J. W., Rose, E. E., & Santerre, J. P. (2013). Perfused culture of gingival fibroblasts in a degradable/polar/hydrophobic/ionic polyurethane (D-PHI) scaffold leads to enhanced proliferation and metabolic activity. *Acta biomaterialia*, *9*(6), 6867-6875.

[315] Karchin, A., Simonovsky, F. I., Ratner, B. D., & Sanders, J. E. (2011). Melt electrospinning of biodegradable polyurethane scaffolds. *Acta biomaterialia*, *7*(9), 3277-3284.

[316] Childers, E. P., Peterson, G. I., Ellenberger, A. B., Domino, K., Seifert, G. V., & Becker, M. L. (2016). Adhesion of Blood Plasma Proteins and Platelet-rich Plasma on l-Valine-Based Poly (ester urea). *Biomacromolecules*, *17*(10), 3396-3403.

[317] Guan, J., Fujimoto, K. L., Sacks, M. S., & Wagner, W. R. (2005). Preparation and characterization of highly porous, biodegradable polyurethane scaffolds for soft tissue applications. *Biomaterials*, *26*(18), 3961-3971.

[318] Guan, J., Stankus, J. J., & Wagner, W. R. (2006). Development of composite porous scaffolds based on collagen and biodegradable poly (ester urethane) urea. *Cell transplantation*, *15*(1), 17-27.

[319] Sharifpoor, S., Simmons, C. A., Labow, R. S., & Santerre, J. P. (2010). A study of vascular smooth muscle cell function under cyclic mechanical loading in a polyurethane scaffold with optimized porosity. *Acta biomaterialia*, *6*(11), 4218-4228.

[320] Hidalgo-Bastida, L. A., Barry, J. J. A., Everitt, N. M., Rose, F. R. A. J., Buttery, L. D., Hall, I. P., ... & Shakesheff, K. M. (2007). Cell adhesion and mechanical properties of a flexible scaffold for cardiac tissue engineering. *Acta biomaterialia*, *3*(4), 457-462.

[321] Gao, Y., Childers, E. P., & Becker, M. L. (2015). l-Leucine-Based Poly (ester urea) s for Vascular Tissue Engineering. *ACS Biomaterials Science & Engineering*, *1*(9), 795-804.

[322] Guan, J., Sacks, M. S., Beckman, E. J., & Wagner, W. R. (2004). Biodegradable poly (ether ester urethane) urea elastomers based on poly (ether ester) triblock copolymers and putrescine: synthesis, characterization and cytocompatibility. *Biomaterials*, *25*(1), 85-96.

[323] Dailing, E. A., Nair, D. P., Setterberg, W. K., Kyburz, K. A., Yang, C., D'Ovidio, T., ... & Stansbury, J. W. (2016). Combined, independent small molecule release and shape memory via nanogel-coated thiourethane polymer networks. *Polymer chemistry*, *7*(4), 816-825.

[324] Gugerell, A., Kober, J., Laube, T., Walter, T., Nürnberger, S., Grönniger, E., ... & Keck, M. (2014). Electrospun poly (ester-urethane)-and poly (ester-urethane-urea) fleeces as promising tissue engineering scaffolds for adipose-derived stem cells. *PloS one*, *9*(3), e90676.

[325] Zhang, J. Y., Beckman, E. J., Hu, J., Yang, G. G., Agarwal, S., & Hollinger, J. O. (2002). Synthesis, biodegradability, and biocompatibility of lysine diisocyanate–glucose polymers. *Tissue engineering*, *8*(5), 771-785.

[326] Abdal-hay, A., Agour, M., Kim, Y. K., Lee, M. H., Hassan, M. K., El-Ainin, H. A., ... & Ivanovski, S. (2019). Magnesium-particle/polyurethane composite layer coating on titanium surfaces for orthopedic applications. *European Polymer Journal*, *112*, 555-568.

[327] Li, A., Dearman, B. L., Crompton, K. E., Moore, T. G., & Greenwood, J. E. (2009). Evaluation of a novel biodegradable polymer for the generation of a dermal matrix. *Journal of burn care & research*, *30*(4), 717-728.

[328] Valério, A., Conti, D. S., Araújo, P. H., Sayer, C., & da Rocha, S. R. (2015). Synthesis of PEG-PCL-based polyurethane nanoparticles by miniemulsion polymerization. *Colloids and Surfaces B: Biointerfaces*, *135*, 35-41.

[329] Condello, V., Dei Giudici, L., Perdisa, F., Screpis, D. U., Guerriero, M., Filardo, G., & Zorzi, C. (2019). Polyurethane scaffold implants for partial meniscus lesions: delayed intervention leads to an inferior outcome. *Knee Surgery, Sports Traumatology, Arthroscopy*, 1-8.

[330] Accadbled, F., Pham, T. T., Lemoine, C. T., & de Gauzy, J. S. (2020). Implantation of an Actifit® Polyurethane Meniscal Scaffold 18 Months After Subtotal Lateral Meniscectomy in a 13-Year-Old Male Adolescent. *The American Journal of Case Reports*, *21*, e920688-1.

[331] Toanen, C., Dhollander, A., Bulgheroni, P., Filardo, G., Zaffagnini, S., Spalding, T., ... & Pujol, N. (2020). Polyurethane Meniscal Scaffold for the Treatment of Partial Meniscal Deficiency: 5-Year Follow-up Outcomes: A European Multicentric Study. *The American Journal of Sports Medicine*, *48*(6), 1347-1355.

[332] Bonart, R. (1968). X-ray investigations concerning the physical structure of cross-linking in segmented urethane elastomers. *Journal of Macromolecular Science, Part B*, *2*(1), 115-138.

[333] Kim, T. R., Shin, J. K., Goh, T. S., Kim, H. S., Lee, J. S., & Lee, C. S. (2017). Modeling of elasto-viscoplastic behavior for polyurethane foam under various strain rates and temperatures. *Composite Structures*, *180*, 686-695.

[334] Kojio, K., Matsuo, K., Motokucho, S., Yoshinaga, K., Shimodaira, Y., & Kimura, K. (2011). Simultaneous small-angle X-ray scattering/wide-angle X-ray diffraction study of the microdomain structure of polyurethane elastomers during mechanical deformation. *Polymer journal*, *43*(8), 692.

[335] Hammond, P. T., Nallicheri, R. A., & Rubner, M. F. (1990). An examination of the strain-induced orientation of hard segment domains in 4, 4′-methylenebis (phenyl isocyanate)-based polyurethane-diacetylene segmented copolymers. *Materials Science and Engineering: A*, *126*(1-2), 281-287.

[336] Amitay-Sadovsky, E., Ward, B., Somorjai, G. A., & Komvopoulos, K. (2002). Nanomechanical properties and morphology of thick polyurethane films under contact pressure and stretching. *Journal of applied physics*, *91*(1), 375-381.

[337] Sakamoto, H., Asakawa, H., Fukuma, T., Fujita, S., & Suye, S. I. (2014). Atomic force microscopy visualization of hard segment alignment in stretched polyurethane nanofibers prepared by electrospinning. *Science and technology of advanced materials*, *15*(1), 015008.

[338] Chen, Q., Mangadlao, J. D., Wallat, J., De Leon, A., Pokorski, J. K., & Advincula, R. C. (2017). 3D printing biocompatible polyurethane/poly (lactic acid)/graphene oxide nanocomposites: anisotropic properties. *ACS applied materials & interfaces*, *9*(4), 4015-4023.

[339] Hung, K. C., Tseng, C. S., & Hsu, S. H. (2014). Synthesis and 3D Printing of Biodegradable Polyurethane Elastomer by a Water-Based Process for Cartilage Tissue Engineering Applications. *Advanced healthcare materials*, *3*(10), 1578-1587.

[340] Brunette, C. M., Hsu, S. L., & MacKnight, W. J. (1982). Hydrogen-bonding properties of hard-segment model compounds in polyurethane block copolymers. *Macromolecules*, *15*(1), 71-77.

[341] Zhang, C., Hu, J., Li, X., Wu, Y., & Han, J. (2014). Hydrogen-bonding interactions in hard segments of shape memory polyurethane: toluene diisocyanates and 1, 6-hexamethylene diisocyanate. A theoretical and comparative study. *The Journal of Physical Chemistry A*, *118*(51), 12241-12255.

[342] Touchet, T. J., & Cosgriff-Hernandez, E. M. (2016). Hierarchal structure–property relationships of segmented polyurethanes. In *Advances in polyurethane biomaterials* (pp. 3-22). Woodhead Publishing.

[343] Jiang, L., Ren, Z., Zhao, W., Liu, W., Liu, H., & Zhu, C. (2018). Synthesis and structure/properties characterizations of four polyurethane model hard segments. *Royal Society open science*, *5*(7), 180536.

[344] Yang, J. H., Chun, B. C., Chung, Y. C., & Cho, J. H. (2003). Comparison of thermal/mechanical properties and shape memory effect of polyurethane block-copolymers with planar or bent shape of hard segment. *Polymer*, *44*(11), 3251-3258.

[345] Arnold, S. M., Collins, M. A., Graham, C., Jolly, A. T., Parod, R. J., Poole, A., ... & Woolhiser, M. R. (2012). Risk assessment for consumer exposure to toluene diisocyanate (TDI) derived from polyurethane flexible foam. *Regulatory Toxicology and Pharmacology*, *64*(3), 504-515.

[346] Scheel, L. D., Killens, R., & Josephson, A. (1964). Immunochemical aspects of toluene diisocyanate (TDI) toxicity. *American Industrial Hygiene Association Journal*, *25*(2), 179-184.

[347] Kavlock, K. D., Pechar, T. W., Hollinger, J. O., Guelcher, S. A., & Goldstein, A. S. (2007). Synthesis and characterization of segmented poly (esterurethane urea) elastomers for bone tissue engineering. Acta biomaterialia, 3(4), 475-484.

[348] Spaans, C. J., De Groot, J. H., Dekens, F. G., & Pennings, A. J. (1998). High molecular weight polyurethanes and a polyurethane urea based on 1, 4-butanediisocyanate. *Polymer Bulletin*, *41*(2), 131-138.

[349] Santerre, J. P., Woodhouse, K., Laroche, G., & Labow, R. S. (2005). Understanding the biodegradation of polyurethanes: from classical implants to tissue engineering materials. *Biomaterials*, *26*(35), 7457-7470.

[350] Zhang, X., Battiston, K. G., McBane, J. E., Matheson, L. A., Labow, R. S., & Santerre, J. P. (2016). Design of biodegradable polyurethanes and the interactions of the polymers and their degradation by-products within in vitro and in vivo environments. In *Advances in polyurethane biomaterials* (pp. 75-114). Woodhead Publishing.

[351] Spaans, C. J., Belgraver, V. W., & Pennings, A. J. (1998). A new biomedical polyurethane with a high modulus based on 1, 4-butanediisocyanate and ε-caprolactone. *Journal of Materials Science: Materials in Medicine*, *9*(12), 675-678.

[352] Spaans, C. J., Belgraver, V. W., Rienstra, O., De Groot, J. H., Veth, R. P. H., & Pennings, A. J. (2000). Solvent-free fabrication of micro-porous polyurethane amide and polyurethane-urea scaffolds for repair and replacement of the knee-joint meniscus. *Biomaterials*, *21*(23), 2453-2460.

[353] Guan, J., Sacks, M. S., Beckman, E. J., & Wagner, W. R. (2002). Synthesis, characterization, and cytocompatibility of elastomeric, biodegradable poly (ester-urethane) ureas based on poly (caprolactone) and putrescine. *Journal of Biomedical Materials Research: An Official Journal of The Society for Biomaterials, The Japanese Society for Biomaterials, and The Australian Society for Biomaterials and the Korean Society for Biomaterials*, *61*(3), 493-503.

[354] Van Minnen, B., Van Leeuwen, M. B. M., Stegenga, B., Zuidema, J., Hissink, C. E., Van Kooten, T. G., & Bos, R. R. M. (2005). Short-term in vitro and in vivo biocompatibility of a biodegradable polyurethane foam based on 1, 4-butanediisocyanate. *Journal of Materials Science: Materials in Medicine*, *16*(3), 221-227.

[355] Zuidema, J., Van Minnen, B., Span, M. M., Hissink, C. E., van Kooten, T. G., & Bos, R. R. M. (2009). In vitro degradation of a biodegradable polyurethane foam, based on 1, 4-butanediisocyanate: A three-year study at physiological and elevated temperature. *Journal of Biomedical Materials Research Part A: An Official Journal of The Society for Biomaterials, The Japanese Society for Biomaterials, and The Australian Society for Biomaterials and the Korean Society for Biomaterials*, *90*(3), 920-930.

[356] Van Minnen, B., Van Leeuwen, M. B. M., Kors, G., Zuidema, J., Van Kooten, T. G., & Bos, R. R. M. (2008). In vivo resorption of a biodegradable polyurethane foam, based on 1, 4-butanediisocyanate: A three-year subcutaneous implantation study. *Journal of Biomedical Materials Research Part A: An Official Journal of The Society for Biomaterials, The Japanese Society for Biomaterials, and The Australian Society for Biomaterials and the Korean Society for Biomaterials*, *85*(4), 972-982.

[357] Gunatillake, P. A., Adhikari, R., & Felton, G. (2011). Biodegradable polyurethanes: Design, synthesis, properties and potential applications. *Biodegradable Polymers: Processing, Degradation and Applications*, 431-470.

[358] Zdrojewicz, Z., & Lachowski, M. (2014). The importance of putrescine in the human body. *Postepy Higieny i Medycyny Doswiadczalnej (Online)*, *68*, 393-403.

[359] Wang, F., Li, Z., Lannutti, J. L., Wagner, W. R., & Guan, J. (2009). Synthesis, characterization and surface modification of low moduli poly (ether carbonate urethane) ureas for soft tissue engineering. *Acta biomaterialia*, *5*(8), 2901-2912.

[360] Ma, Z., Hong, Y., Nelson, D. M., Pichamuthu, J. E., Leeson, C. E., & Wagner, W. R. (2011). Biodegradable polyurethane ureas with variable polyester or polycarbonate soft segments: Effects of crystallinity, molecular weight, and composition on mechanical properties. *Biomacromolecules*, *12*(9), 3265-3274.

[361] Hafeman, A. E., Li, B., Yoshii, T., Zienkiewicz, K., Davidson, J. M., & Guelcher, S. A. (2008). Injectable biodegradable polyurethane scaffolds with release of platelet-derived growth factor for tissue repair and regeneration. *Pharmaceutical research*, *25*(10), 2387.

[362] Jung, Y. S., & Ross, C. A. (2009). Solvent-Vapor-Induced Tunability of Self-Assembled Block Copolymer Patterns. *Advanced Materials*, *21*(24), 2540-2545.

[363] Frick, A., Borm, M., Kaoud, N., Kolodziej, J., & Neudeck, J. (2014, May). Microstructure and thermomechanical properties relationship of segmented thermoplastic polyurethane (TPU). In *AIP Conference Proceedings* (Vol. 1593, No. 1, pp. 520-525). American Institute of Physics.

[364] Lee, S. H., Teramoto, Y., & Shiraishi, N. (2002). Biodegradable polyurethane foam from liquefied waste paper and its thermal stability, biodegradability, and genotoxicity. *Journal of Applied Polymer Science*, *83*(7), 1482-1489.

[365] Zia, K. M., Barikani, M., Bhatti, I. A., Zuber, M., & Bhatti, H. N. (2008). Synthesis and characterization of novel, biodegradable, thermally stable chitin-based polyurethane elastomers. *Journal of Applied Polymer Science*, *110*(2), 769-776.

[366] Barikani, M., Honarkar, H., & Barikani, M. (2009). Synthesis and characterization of polyurethane elastomers based on chitosan and poly (ε-caprolactone). *Journal of applied polymer science*, *112*(5), 3157-3165.

[367] Guelcher, S. A., Srinivasan, A., Dumas, J. E., Didier, J. E., McBride, S., & Hollinger, J. O. (2008). Synthesis, mechanical properties, biocompatibility, and biodegradation of polyurethane networks from lysine polyisocyanates. *Biomaterials*, *29*(12), 1762-1775.

[368] Dinnes, D. L. M., Santerre, J. P., & Labow, R. S. (2005). Phospholipase A2 pathway association with macrophage-mediated polycarbonate-urethane biodegradation. *Biomaterials*, *26*(18), 3881-3889.

[369] Sheikh, Z., Brooks, P. J., Barzilay, O., Fine, N., & Glogauer, M. (2015). Macrophages, foreign body giant cells and their response to implantable biomaterials. *Materials*, *8*(9), 5671-5701.

[370] Labow, R. S., Meek, E., & Santerre, J. P. (2001). Hydrolytic degradation of poly (carbonate)-urethanes by monocyte-derived macrophages. *Biomaterials*, *22*(22), 3025-3033.

[371] Labow, R. S., Meek, E., & Santerre, J. P. (2001). Model systems to assess the destructive potential of human neutrophils and monocyte-derived macrophages during the acute and chronic phases of inflammation. *Journal of Biomedical Materials Research: An Official Journal of The Society for Biomaterials and The Japanese Society for Biomaterials*, *54*(2), 189-197.

[372] Matheson, L. A., Labow, R. S., & Santerre, J. P. (2002). Biodegradation of polycarbonate-based polyurethanes by the human monocyte-derived macrophage and U937 cell systems. *Journal of Biomedical Materials Research: An Official Journal of The Society for Biomaterials, The Japanese Society for Biomaterials, and The Australian Society for Biomaterials and the Korean Society for Biomaterials*, *61*(4), 505-513.

[373] Phua, S. K., Castillo, E., Anderson, J. M., & Hiltner, A. (1987). Biodegradation of a polyurethane in vitro. *Journal of biomedical materials research*, *21*(2), 231-246.

[374] Marchant, R. E., Zhao, Q., Anderson, J. M., & Hiltner, A. (1987). Degradation of a poly (ether urethane urea) elastomer: infra-red and XPS studies. *Polymer*, *28*(12), 2032-2039.

[375] Huang, S. J., & Edelman, P. G. (1995). An overview of biodegradable polymers and biodegradation of polymers. In *Degradable Polymers* (pp. 18-28). Springer, Dordrecht.

[376] Loredo-Treviño, A., García, G., Velasco-Téllez, A., Rodríguez-Herrera, R., & Aguilar, C. N. (2011). Polyurethane foam as substrate for fungal strains. *Advances in Bioscience and Biotechnology*, *2*(2), 52.

[377] Labow, R. S., Duguay, D. G., & Santerre, J. P. (1995). The enzymatic hydrolysis of a synthetic biomembrane: a new substrate for cholesterol and carboxyl esterases. *Journal of Biomaterials Science, Polymer Edition*, *6*(2), 169-179.

[378] Wang, G. B., Labow, R. S., & Santerre, J. P. (1997). Biodegradation of a poly (ester) urea-urethane by cholesterol esterase: Isolation and identification of principal biodegradation products. *Journal of Biomedical Materials Research: An Official Journal of The Society for Biomaterials and The Japanese Society for Biomaterials*, *36*(3), 407-417.

[379] Jiang, X., Li, J., Ding, M., Tan, H., Ling, Q., Zhong, Y., & Fu, Q. (2007). Synthesis and degradation of nontoxic biodegradable waterborne polyurethanes elastomer with poly (ε-caprolactone) and poly (ethylene glycol) as soft segment. *European Polymer Journal*, *43*(5), 1838-1846.

[380] Nelson, D. M., Baraniak, P. R., Ma, Z., Guan, J., Mason, N. S., & Wagner, W. R. (2011). Controlled release of IGF-1 and HGF from a biodegradable polyurethane scaffold. *Pharmaceutical research*, *28*(6), 1282-1293.

[381] Ma, Z., Hong, Y., Nelson, D. M., Pichamuthu, J. E., Leeson, C. E., & Wagner, W. R. (2011). Biodegradable polyurethane ureas with variable polyester or polycarbonate soft segments: Effects of crystallinity, molecular weight, and composition on mechanical properties. *Biomacromolecules*, *12*(9), 3265-3274.

[382] Bruin, P., Smedinga, J., Pennings, A. J., & Jonkman, M. F. (1990). Biodegradable lysine diisocyanate-based poly (glycolide-co-ϵ-caprolactone)-urethane network in artificial skin. *Biomaterials*, *11*(4), 291-295.

[383] Dias, R. C. M., Góes, A. M., Serakides, R., Ayres, E., & Oréfice, R. L. (2010). Porous biodegradable polyurethane nanocomposites: preparation, characterization, and biocompatibility tests. *Materials Research*, *13*(2), 211-218.

[384] Hafeman, A. E., Zienkiewicz, K. J., Zachman, A. L., Sung, H. J., Nanney, L. B., Davidson, J. M., & Guelcher, S. A. (2011). Characterization of the degradation mechanisms of lysine-derived aliphatic poly (ester urethane) scaffolds. *Biomaterials*, *32*(2), 419-429.

[385] Shen, Z., Lu, D., Li, Q., Zhang, Z., & Zhu, Y. (2015). Synthesis and characterization of biodegradable polyurethane for hypopharyngeal tissue engineering. *BioMed research international*, *2015*.

[386] Stankus, J. J., Freytes, D. O., Badylak, S. F., & Wagner, W. R. (2008). Hybrid nanofibrous scaffolds from electrospinning of a synthetic biodegradable elastomer and urinary bladder matrix. *Journal of Biomaterials Science, Polymer Edition*, *19*(5), 635-652.

[387] Van Tienen, T. G., Heijkants, R. G., Buma, P., de Groot, J. H., Pennings, A. J., & Veth, R. P. (2002). Tissue ingrowth and degradation of two biodegradable porous polymers with different porosities and pore sizes. *Biomaterials*, *23*(8), 1731-1738.

[388] Xu, C., Huang, Y., Tang, L., & Hong, Y. (2017). Low-Initial-Modulus Biodegradable Polyurethane Elastomers for Soft Tissue Regeneration. *ACS applied materials & interfaces*, *9*(3), 2169-2180.

[389] Ivanoska-Dacikj, A., Bogoeva-Gaceva, G., Krumme, A., Tarasova, E., Scalera, C., Stojkovski, V., ... & Ristoski, T. (2019). Biodegradable polyurethane/graphene oxide scaffolds for soft tissue engineering: in vivo behavior assessment. *International Journal of Polymeric Materials and Polymeric Biomaterials*, 1-11.

[390] Gao, Y., Yi, T., Shinoka, T., Lee, Y. U., Reneker, D. H., Breuer, C. K., & Becker, M. L. (2016). Pilot Mouse Study of 1 mm Inner Diameter (ID) Vascular Graft Using Electrospun Poly (ester urea) Nanofibers. *Advanced healthcare materials*, *5*(18), 2427-2436.

[391] Guo, X., Zhu, J., Zhang, H., You, Z., Morsi, Y., Mo, X., & Zhu, T. (2019). Facile preparation of a controlled-release tubular scaffold for blood vessel implantation. *Journal of colloid and interface science*, *539*, 351-360.

[392] Hong, Y., Huber, A., Takanari, K., Amoroso, N. J., Hashizume, R., Badylak, S. F., & Wagner, W. R. (2011). Mechanical properties and in vivo behavior of a biodegradable synthetic polymer microfiber–extracellular matrix hydrogel biohybrid scaffold. *Biomaterials*, *32*(13), 3387-3394.

[393] Hashizume, R., Hong, Y., Takanari, K., Fujimoto, K. L., Tobita, K., & Wagner, W. R. (2013). The effect of polymer degradation time on functional outcomes of temporary elastic patch support in ischemic cardiomyopathy. *Biomaterials*, *34*(30), 7353-7363.

[394] Burkoth, A. K., Burdick, J., & Anseth, K. S. (2000). Surface and bulk modifications to photocrosslinked polyanhydrides to control degradation behavior. *Journal of Biomedical Materials Research: An Official Journal of The Society for Biomaterials, The Japanese Society for Biomaterials, and The Australian Society for Biomaterials and the Korean Society for Biomaterials*, *51*(3), 352-359.

[395] von Burkersroda, F., Schedl, L., & Göpferich, A. (2002). Why degradable polymers undergo surface erosion or bulk erosion. *Biomaterials*, *23*(21), 4221-4231.

[396] Rothstein, S. N., Federspiel, W. J., & Little, S. R. (2009). A unified mathematical model for the prediction of controlled release from surface and bulk eroding polymer matrices. *Biomaterials*, *30*(8), 1657-1664.

[397] Göpferich, A. (1997). Polymer bulk erosion. *Macromolecules*, *30*(9), 2598-2604.

[398] Dorati, R., Colonna, C., Genta, I., Modena, T., & Conti, B. (2010). Effect of porogen on the physico-chemical properties and degradation performance of PLGA scaffolds. *Polymer Degradation and Stability*, *95*(4), 694-701.

[399] Reignier, J., & Huneault, M. A. (2006). Preparation of interconnected poly (ε-caprolactone) porous scaffolds by a combination of polymer and salt particulate leaching. *Polymer*, *47*(13), 4703-4717.

[400] Mistry, A. S., Cheng, S. H., Yeh, T., Christenson, E., Jansen, J. A., & Mikos, A. G. (2009). Fabrication and in vitro degradation of porous fumarate-based polymer/alumoxane nanocomposite scaffolds for bone tissue engineering. *Journal of Biomedical Materials Research Part A: An Official Journal of The Society for Biomaterials, The Japanese Society for Biomaterials, and The Australian Society for Biomaterials and the Korean Society for Biomaterials*, *89*(1), 68-79.

[401] Lu, L., Zhang, Q., Wootton, D., Lelkes, P. I., & Zhou, J. (2010). A novel sucrose porogen-based solid freeform fabrication system for bone scaffold manufacturing. *Rapid Prototyping Journal*.

[402] Mondrinos, M. J., Dembzynski, R., Lu, L., Byrapogu, V. K., Wootton, D. M., Lelkes, P. I., & Zhou, J. (2006). Porogen-based solid freeform fabrication of polycaprolactone–calcium phosphate scaffolds for tissue engineering. *Biomaterials*, *27*(25), 4399-4408.

[403] Kim, J., Yaszemski, M. J., & Lu, L. (2009). Three-dimensional porous biodegradable polymeric scaffolds fabricated with biodegradable hydrogel porogens. *Tissue Engineering Part C: Methods*, *15*(4), 583-594.

[404] Gong, Y., Ma, Z., Zhou, Q., Li, J., Gao, C., & Shen, J. (2008). Poly (lactic acid) scaffold fabricated by gelatin particle leaching has good biocompatibility for chondrogenesis. *Journal of Biomaterials Science, Polymer Edition*, *19*(2), 207-221.

[405] Willson, K., & Ratner, B. A Thin Porous Sheath to Mitigate the Foreign Body Response: Implications for Drug Delivery.

[406] Marshall, A. J., Maginness, M. G., Glaister, C. L., Woods, C., Metter, R. B., & Burdick, J. A. Sphere Templated Angiogenic Regeneration (STAR®) Scaffolds for Device Biointegration and Wound Repair.

[407] Columbus, S., Krishnan, L. K., & Kalliyana Krishnan, V. (2014). Relating pore size variation of poly (ε-caprolactone) scaffolds to molecular weight of porogen and evaluation of scaffold properties after degradation. *Journal of Biomedical Materials Research Part B: Applied Biomaterials*, *102*(4), 789-796.

[408] Courtois, J., Byström, E., & Irgum, K. (2006). Novel monolithic materials using poly (ethylene glycol) as porogen for protein separation. *Polymer*, *47*(8), 2603-2611.

[409] Yu, D., Sun, C., Zheng, Z., Wang, X., Chen, D., Wu, H., ... & Shi, F. (2016). Inner ear delivery of dexamethasone using injectable silk-polyethylene glycol (PEG) hydrogel. *International journal of pharmaceutics*, *503*(1-2), 229-237.

[410] Feng, L., A Ward, J., Kevin Li, S., Tolia, G., Hao, J., & I Choo, D. (2014). Assessment of PLGA-PEG-PLGA copolymer hydrogel for sustained drug delivery in the ear. *Current drug delivery*, *11*(2), 279-286.

[411] Zhang, Y., Zhang, W., Johnston, A. H., Newman, T. A., Pyykkö, I., & Zou, J. (2011). Comparison of the distribution pattern of PEG-b-PCL polymersomes delivered into the rat inner ear via different methods. *Acta oto-laryngologica*, *131*(12), 1249-1256.

[412] Kozin, E. D., Black, N. L., Cheng, J. T., Cotler, M. J., McKenna, M. J., Lee, D. J., Lewis, J.A, Rosowski, J.J, & Remenschneider, A. K. (2016). Design, fabrication, and in vitro testing of novel three-dimensionally printed tympanic membrane grafts. *Hearing Research*, *340*, 191-203.

[413] Kuypers, L. C., Decraemer, W. F., & Dirckx, J. J. (2006). Thickness distribution of fresh and preserved human eardrums measured with confocal microscopy. *Otology & Neurotology*, *27*(2), 256-264.

[414] Decraemer, W. F., Dirckx, J. J., & Funnell, W. R. J. (1991). Shape and derived geometrical parameters of the adult, human tympanic membrane measured with a phase-shift moire interferometer. *Hearing research*, *51*(1), 107-121.

[415] Monasta, L., Ronfani, L., Marchetti, F., Montico, M., Brumatti, L. V., Bavcar, A., ... & Tamburlini, G. (2012). Burden of disease caused by otitis media: systematic review and global estimates. *PloS one*, *7*(4), e36226.

[416] Strens, D., Knerer, G., Van Vlaenderen, I., & Dhooge, I. J. M. (2012). A pilot cost-of-illness study on long-term complications/sequelae of AOM. *B-ENT*, *8*(3), 153.

[417] Ruben, R. J. (1982). The disease in society-evaluation of chronic otitis media in general and cholesteatoma in particular. In *2nd International Conference of Cholesteatoma and Mastoide Surgery. Amsterdam: Kugler Publications* (pp. 111-6).

[418] Marquet, J. (1971). Human middle ear transplants. *The Journal of Laryngology & Otology*, *85*(6), 523-540.

[419] House, W. F., Patterson, M. E., & Linthicum, F. H. (1966). Incus homografts in chronic ear surgery. *Archives of otolaryngology*, *84*(2), 148-153.

[420] Pfaltz, C. R., & Grieseme, C. (1985). Pericard: a new biomaterial for tympanoplasty: preliminary report. *Otology & Neurotology*, *6*(3), 266-268.

[421] Kohn, F. E., Feijen, J., & Feenstra, L. (1984). New perspectives in myringoplasty. *The International journal of artificial organs*, *7*(3), 151-162.

[422] Levin, B., Rajkhowa, R., Redmond, S. L., & Atlas, M. D. (2009). Grafts in myringoplasty: utilizing a silk fibroin scaffold as a novel device. *Expert review of medical devices*, *6*(6), 653-664.

[423] Hiraide, F., Sawada, M., Inouye, T., Miyakogawa, N., & Tsubaki, Y. (1980). The fiber arrangement of the pathological human tympanic membrane. *Archives of oto-rhino-laryngology*, *226*(1-2), 93-99.

[424] Boedts, D., De, M. C., Andries, L., & Marquet, J. (1990). A scanning electron-microscopic study of different tympanic grafts. *The American journal of otology*, *11*(4), 274-277.

[425] Kaylie, D., Gardner, E. K., & Jackson, C. G. (2005). Revision Chronic Ear Surgery. *Otolaryngology-Head and Neck Surgery*, *2*(133), P177.

[426] Sun, C., Wang, X., Zheng, Z., Chen, D., Wang, X., Shi, F., ... & Wu, H. (2015). A single dose of dexamethasone encapsulated in polyethylene glycol-coated polylactic acid nanoparticles attenuates cisplatin-induced hearing loss following round window membrane administration. *International Journal of Nanomedicine*, *10*, 3567.

[427] Rousset, F., Kokje, V. B. C., Coelho, M. D. C., Mugnier, T., Belissa, E., Gabriel, D., ... & Senn, P. (2019). Poly-Lactic Acid-Based Biopolymer Formulations Are Safe for Sustained Intratympanic Dexamethasone Delivery. *Otology & Neurotology*, *40*(7), e739-e746.

[428] Ensari, N., Tutar, H., Ekinci, O., Ugur, M. B., Bayazıt, Y. A., Gokdogan, C., & Goksu, N. (2015). Effects of polylactic acid film on middle ear mucosa and cochlear function in Guinea pigs. *European Archives of Oto-Rhino-Laryngology*, *272*(5), 1091-1097.

[429] Lee, H., Jang, C. H., & Kim, G. H. (2014). A polycaprolactone/silk-fibroin nanofibrous composite combined with human umbilical cord serum for subacute tympanic membrane perforation; an in vitro and in vivo study. Journal of Materials Chemistry B, 2(18), 2703-2713.

[430] Jang, C. H., Cho, Y. B., Kim, J. S., Lee, H. J., & Kim, G. H. (2012). Regeneration of mastoid air cells using polycaprolactone/β-tricalcium phosphate biocomposites: An experimental study. *The Laryngoscope*, *122*(3), 660-664.

[431] Hohenhoff, G., Krauss, J. K., Schwabe, K., Nakamura, M., Haastert, K., & Hustedt, M. (2009). Laser generated scaffolds for regeneration of the auditory nerve and facial nerve. In *4th European Conference of the International Federation for Medical and Biological Engineering* (pp. 2161-2164). Springer, Berlin, Heidelberg.

[432] Abbasi, F., Mirzadeh, H., & Simjoo, M. (2006). Hydrophilic interpenetrating polymer networks of poly (dimethyl siloxane)(PDMS) as biomaterial for cochlear implants. *Journal of Biomaterials Science, Polymer Edition*, *17*(3), 341-355.

[433] Lee, J. H., Lee, S. M., Byeon, H. J., Hong, J. S., Park, K. S., & Lee, S. H. (2014). CNT/PDMS-based canal-typed ear electrodes for inconspicuous EEG recording. Journal of neural engineering, 11(4), 046014.

[434] Knutsson, J., Bagger-Sjöbäck, D., & von Unge, M. (2009). Collagen type distribution in the healthy human tympanic membrane. *Otology & Neurotology*, *30*(8), 1225-1229.

[435] Lim, D. J. (1968). Tympanic membrane: electron microscopic observation part I: pars tensa. *Acta oto-laryngologica*, *66*(1-6), 181-198.

[436] Geckil, H., Xu, F., Zhang, X., Moon, S., & Demirci, U. (2010). Engineering hydrogels as extracellular matrix mimics. *Nanomedicine*, *5*(3), 469-484.

[437] Seliktar, D. (2012). Designing cell-compatible hydrogels for biomedical applications. Science, 336(6085), 1124-1128.

[438] Cheng, J. T., Aarnisalo, A. A., Harrington, E., del Socorro Hernandez-Montes, M., Furlong, C., Merchant, S. N., & Rosowski, J. J. (2010). Motion of the surface of the human tympanic membrane measured with stroboscopic holography. *Hearing research*, *263*(1-2), 66-77.

[439] del Socorro Hernández-Montes, M., Furlong, C., Rosowski, J. J., Hulli, N., Harrington, E., Cheng, J. T., ... & Mendoza-Santoyo, F. (2009). Optoelectronic holographic otoscope for measurement of nano-displacements in tympanic membranes. *Journal of biomedical optics*, *14*(3), 034023.

[440] Rosowski, J. J., Cheng, J. T., Ravicz, M. E., Hulli, N., Hernandez-Montes, M., Harrington, E., & Furlong, C. (2009). Computer-assisted time-averaged holograms of the motion of the surface of the mammalian tympanic membrane with sound stimuli of 0.4–25 kHz. *Hearing research*, *253*(1-2), 83-96.

[441] Guinan Jr, J. J., & Peake, W. T. (1967). Middle-ear characteristics of anesthetized cats. *The Journal of the Acoustical Society of America*, *41*(5), 1237-1261.

187

[442] Goode, R. L., Killion, M., Nakamura, K., & Nishihara, S. (1994). New knowledge about the function of the human middle ear: development of an improved analog model. *The American journal of otology*, *15*(2), 145-154.

[443] Aarnisalo, A. A., Cheng, J. T., Ravicz, M. E., Hulli, N., Harrington, E. J., Hernandez-Montes, M. S., ... & Rosowski, J. J. (2009). Middle ear mechanics of cartilage tympanoplasty evaluated by laser holography and vibrometry. *Otology & neurotology: official publication of the American Otological Society, American Neurotology Society [and] European Academy of Otology and Neurotology*, *30*(8), 1209.

[444] Aarnisalo, A. A., Cheng, J. T., Ravicz, M. E., Furlong, C., Merchant, S. N., & Rosowski, J. J. (2010). Motion of the tympanic membrane after cartilage tympanoplasty determined by stroboscopic holography. *Hearing research*, *263*(1-2), 78-84.

[445] "Substance Name: Hexafluoroisopropanol." NIH, U.S. National Library of Medicine. <https://chem.nlm.nih.gov/chemidplus/rn/920-66-1>.

[446] "Substance Name: Toluene." NIH, U.S. National Library of Medicine. <https://chem.nlm.nih.gov/chemidplus/rn/108-88-3>.

[447] Fung, Y. C. B. (1972). Stress-strain-history relations of soft tissues in simple elongation. *Biomechanics its foundations and objectives*, 181-208.

[448] Fung, Y. C. (1984). Structure and stress-strain relationship of soft tissues. *American Zoologist*, *24*(1), 13-22.

[449] Rosowski, J. J., Cheng, J. T., Merchant, S. N., Harrington, E., & Furlong, C. (2011). New data on the motion of the normal and reconstructed tympanic membrane. *Otology & neurotology: official publication of the American Otological Society, American Neurotology Society [and] European Academy of Otology and Neurotology*, *32*(9), 1559.

[450] Aabel, P., Utheim, T. P., Olstad, O. K., Rask-Andersen, H., Dilley, R. J., & Von Unge, M. (2018). Transcription and microRNA profiling of cultured human tympanic membrane Epidermal Keratinocytes. Journal of the Association for Research in Otolaryngology, 19(3), 243-260.

[451] Levin, B., Rajkhowa, R., Redmond, S. L., & Atlas, M. D. (2009). Grafts in myringoplasty: utilizing a silk fibroin scaffold as a novel device. *Expert review of medical devices*, *6*(6), 653-664.

[452] Puszko, A. K., Sosnowski, P., Pułka-Ziach, K., Hermine, O., Hopfgartner, G., Lepelletier, Y., & Misicka, A. (2019). Urea moiety as amide bond mimetic in peptide-like inhibitors of VEGF-A165/NRP-1 complex. *Bioorganic & medicinal chemistry letters*, *29*(17), 2493-2497.

[453] Chieng, B. W., Azowa, I. N., Wan Md Zin, W. Y., & Hussein, M. Z. (2014). Effects of graphene nanopletelets on poly (lactic acid)/poly (ethylene glycol) polymer nanocomposites. In *Advanced Materials Research* (Vol. 1024, pp. 136-139). Trans Tech Publications Ltd.

[454] Blausen.com staff. *Medical gallery of Blausen Medical.* (2014.)

[455] Clark, W. W., Kim, D. O., Zurek, P. M., & Bohne, B. A. (1984). Spontaneous otoacoustic emissions in chinchilla ear canals: correlation with histopathology and suppression by external tones. *Hearing Research*, *16*(3), 299-314.

[456] Hamernik, R. P., Ahroon, W. A., & Lei, S. F. (1996). The cubic distortion product otoacoustic emissions from the normal and noise-damaged chinchilla cochlea. *The Journal of the Acoustical Society of America*, *100*(2), 1003-1012.

[457] Hamernik, R. P., & Qiu, W. (2000). Correlations among evoked potential thresholds, distortion product otoacoustic emissions and hair cell loss following various noise exposures in the chinchilla. *Hearing research*, *150*(1-2), 245-257.

[458] Shera, C. A., Guinan, J. J., & Oxenham, A. J. (2010). Otoacoustic estimation of cochlear tuning: validation in the chinchilla. *Journal of the Association for Research in Otolaryngology*, *11*(3), 343-365.

[459] Kakigi, A., Hirakawa, H., Harel, N., Mount, R. J., & Harrison, R. V. (1998). Comparison of distortion-product and transient evoked otoacoustic emissions with ABR threshold shift in chinchillas with ototoxic damage. *Auris Nasus Larynx*, *25*(3), 223-232.

[460] Henry, K. S., Kale, S., Scheidt, R. E., & Heinz, M. G. (2011). Auditory brainstem responses predict auditory nerve fiber thresholds and frequency selectivity in hearing impaired chinchillas. *Hearing research*, *280*(1-2), 236-244.

[461] Cowper-Smith, C. D., Dingle, R. N., Guo, Y., Burkard, R., & Phillips, D. P. (2010). Synchronous auditory nerve activity in the carboplatin-chinchilla model of auditory neuropathy. *The Journal of the Acoustical Society of America*, *128*(1), EL56-EL62.

[462] Wang, X., & Gan, R. Z. (2018). Surface Motion of Tympanic Membrane in a Chinchilla Model of Acute Otitis Media. *Journal of the Association for Research in Otolaryngology*, *19*(6), 619-635.

[463] Amoils CP, Jackler RK, Milczuk H, Kelly KE, Cao K. An animal model of chronic tympanic membrane perforation. Otolaryngology—Head and Neck Surgery. 1992 Jan;106(1):47-55.

[464] Rosowski, J. J., Dobrev, I., Khaleghi, M., Lu, W., Cheng, J. T., Harrington, E., & Furlong, C. (2013). Measurements of three-dimensional shape and sound-induced motion of the chinchilla tympanic membrane. *Hearing research*, *301*, 44-52.

[465] Slama, M. C., Ravicz, M. E., & Rosowski, J. J. (2010). Middle ear function and cochlear input impedance in chinchilla. *The Journal of the Acoustical Society of America*, *127*(3), 1397-1410.

[466] Schuknecht HF, Merchant SN, Nadol JB. Schuknecht's pathology of the ear. People's Medical Pub. House-USA, Shelton. 2010.

[467] Quesnel AM, Nakajima HH, Rosowski JJ, Hansen MR, Gantz BJ, Nadol Jr JB. Delayed loss of hearing after hearing preservation cochlear implantation: human temporal bone pathology and implications for etiology. Hearing research. 2016 Mar 1;333:225-34.

[468] Nadol Jr JB, Burgess BJ, Gantz BJ, Coker NJ, Ketten DR, Kos I, Roland Jr JT, Shiao JY, Eddington DK, Montandon P, Shallop JK. Histopathology of cochlear implants in humans. Annals of Otology, Rhinology & Laryngology. 2001 Sep;110(9):883-91.

[469] Liberman MC, Kiang NY. Acoustic trauma in cats: cochlear pathology and auditory-nerve activity. Acta oto-laryngologica. 1978.

[470] Sugawara M, Corfas G, Liberman MC. Influence of supporting cells on neuronal degeneration after hair cell loss. Journal of the Association for Research in Otolaryngology. 2005 Jun 1;6(2):136-47.

[471] Wang Y, Hirose K, Liberman MC. Dynamics of noise-induced cellular injury and repair in the mouse cochlea. Journal of the Association for Research in Otolaryngology. 2002 Sep 1;3(3):248-68.